Universitat Autònoma de Barcelona

Two-dimensional Engineering of Molecular Nanoparticles for Biological Applications

Witold Ireneusz Tatkiewicz

Doctoral Thesis

PhD Programme in Materials Science

Directors:

Jaume Veciana i Imma Ratera

Tutor:

Cristina Palet Ballús

Departament de Química

Facultat de Ciències

- 2014 -

Declaration

I hereby declare that the work carried out in this Doctoral Thesis has not been previously submitted for any degree and is no currently being submitted in candidature for any other degree.

Signed ……..
Witold Ireneusz Tatkiewicz
Candidate

The work of this Doctoral Thesis was carried out by the candidate at the Institut de Ciéncia de Materials de Barcelona (ICMAB). Also, we certify that we have read this Doctoral Thesis and that, in our opinion, it is fully adequate in scope and quality as a Doctoral Thesis for the degree of PhD in Materials Science.

Signed ……..
Imma Ratera Bastardas
Research Scientist – ICMAB
Thesis Director

Signed ……..
Jaume Veciana Miró
Research Professor – ICMAB
Thesis Director

Signed ……..
Cristina Palet Ballús
Research Scientist – ICMAB
Thesis Tutor

Lecz marzyć każdemu jest wolno, marzenie rzecz prosta.

J. Sienkiewicz "Na krzywy ryj"

Acknowledgements

It is said that success has many fathers, this thesis is no different – it is the culmination of work which was contributed by many people and institutions. I hereby would like to express my thanks to all of those to whom I have an unspeakable debt of gratitude.

Firstly, I would like to thank Prof. Jaume Veciana for taking me under his wing and generously allowing the completion of this work in his group.

Dr. Imma Ratera. I simply cannot imagine that this work could have been supervised by someone else, who could both give freedom to explore intuition and set an example of the responsibility for the choices taken.

I owe to thank the Consejo Superior de Investigaciones Científicas for the financial support through the JAE-Predoc predoctoral fellowship.

The presented work wouldn't have been completed without multiple and fruitful collaborations. Therefore I would like to express my deep gratitude to the group of Dr. Ralf Richter from Biosurfaces Unit, CIC biomaGUNE from San Sebastian, Spain that made investigation with QCM-D possible and contributed vastly in proper data interpretation. Similarly, I would like to thank Prof. Milan Mrksich for hosting me in his group, giving me a unique opportunity to have an unforgettable experience of working at Northwestern University in Chicago, Illinois.

I would like to acknowledge the collaboration with the Nanobiotechnology group headed by Prof. Antonio Villaverde from Applied Proteomics and Protein Engineering Unit, Instituto de Biotecnología y Biomedicina, UAB. At least 70% of this book is related to Inclusion Bodies produced within this group by Quim. My thanks also go to Elena and Esther for their contribution - none of the results would have been published without a thoughtful discussion with you.

Important part of this work is dependent on vesicles generously provided by Supercritics group lead by Dra. Nora Ventosa. I especially would like to thank Lidia Ferrer for their meticulous preparation and Dra. Evelyn Moreno for discussion on liposomes properties.

There would be no experiments with cells without help of people from Servei de Cultius Cel·lulars, UAB: Paqui García Haro, Fran Cortés López, Silvia Rayo Luengo and Olga Garreta Guerra. Thank You for Your support.

I would like to thank Mònica Roldán Molina and Meritxell Vendrell Flotat from Servei Microscopia UAB for hours and hours spent in the dark realm of confocal microscopy in order to discover the mysteries of cell movement.

I want to express sincere and warm appreciation to all of actual and past peers from NANOMOL group for their company, example, patience, councils and every day little gestures that made a research group out of individual investigators. Particularly I would like to commemorate César, who was my guide from the first moment I passed the Institute´s doorstep and Laura, for whom I was guide during my last months in the Institute.

Special thanks go to “Club San Quintin”. People patient enough to share with me not only their work time, but also spare time, particularly permanent residents of club’s headquarter: Jose-Luis, Carlos and Maria Victoria.

This piece of science would not exist without numerous people that have shaped my mind along my educational path. I am most grateful to Librarians from Gimnazjum Publiczne Nr. 1 w Siedlcach for broadening my horizons. I am much obliged to director Adam Owczarczyk and Anita Woźnica from I LO im. Bogusława Prusa w Siedlcach. I can never thank enough to Anna Frączkiewicz and Krzysztof Wolski and of course their families for their time, patience and care during my exchange stay in France.

A very special place in my heart is dedicated for Wojtek and his wife Cathia, for their support in the harsh journeys through emigration as well as Pyrenees.

Among friends I cannot permit myself to forget to mention Maria and Jordi that rescued me and Anna, so many times, from both psychological and cultural distresses, while giving support and the comfort of knowing other souls share similar burdens.

And there is Liściu. There is always Liściu. Saying, that it is thanks to him this piece of text is readable, would be a great underestimation.

Finally, the most important people in my life: my parents, grandparents and my beautiful wife. The joy and satisfaction from finishing this work would have been incomplete without seeing your smiling faces. Thank you for everything, against all odds and distances.

Summary

In the past decades, the rapid growth in the field of nanotechnology has promoted many innovations for therapeutic applications, which are currently revolutionizing the delivery of biologically active compounds. In order to contribute to this trend, the work presented in this Thesis is focused on two systems of molecular nanoparticles that have a prospective use in nanomedicine. These systems are:

- Lipidic vesicles – supramolecular entities that are already used as drug delivery systems
- Inclusion Bodies (IBs) - proteic nanoaggregates, that are emerging as a new tool in the light of tissue engineering

The first part of this work is focused on the comparison of a vesicular system prepared by DELOS - susp, a compressed fluid-based single-step method previously developed in our group, and conventional multi-step processes that are usually employed for vesicle production, like thin film hydratation or sonication followed by extrusion. We have compared also two different vesicle compositions: one system is based on DOPC phospholipid and cholesterol (liposome) and the other contain a quaternary ammonia amphiphile, CTAB, and cholesterol (quatsomes). To study the structural characteristics of both systems we have used the combination of two non-labelling methods: Surface Plasmon Resonance (SPR) and Quartz Crystal Microbalance with Dissipation (QCM-D) in order to obtain complementary data. From the data analysis it has been possible to conclude that both investigated vesicular systems form layers of vesicles when interacting with gold surfaces. Basing on the monitored data of these interactions and using an iterative calculation pipeline it has been possible to calculate the mass uptake, thickness, density and mechanical properties of the studied vesicular systems. From this analysis it has been possible to conclude, that the influence of the preparation method is negligible in the case of quatsomes. That is, the internal architecture, once achieved, determines the mechanical properties of these supramolecular entities. On the other hand, the impact of the composition of vesicles on their mechanical properties has been confirmed. Thus, vesicles formed by quaternary salts and cholesterol have demonstrated to be more rigid than the liposomes based on phospholipid and cholesterol.

The work developed in next three Chapters of this thesis has been focused on the use of a new kind of proteic nanoparticulate biomaterial, known as inclusion bodies (IBs), for surface

engineering. In this part we have characterized and evaluated IBs decorated surfaces as supports for cell cultivation and guidance.

The second Chapter of this thesis is centred on the formation of two-dimensional microscale patterns of IBs using a soft lithography technique and evaluation of cell behaviour when cultivated on them. We have successfully prepared high resolution geometrical IBs patterns and cultivated cell on them. Basing on a deep, statistical analysis of data derived from optical and confocal microscopy images it has been possible to derive conclusions about the influence of the IBs pattern geometry on cell´s behaviour. The orientation, morphology and positioning of cells clearly depends on the geometry of IBs patterns proving the usefulness of IBs for cell guidance. Moreover, the synergy between biological activity and topographical stimuli of cells by IBs has been confirmed.

In the third Chapter, in order to move a step forward and to study cell motility induced by IBs, we have focused on the design and engineering of a device allowing deposition of surface-bound IBs gradients from colloidal suspensions. The developed technique is based on the widely known coffee drop effect. A deposition device was constructed, calibrated and successfully used in order to prepare substrates with the desired, fully customizable and easy to modify patterns, which can be obtained in a fast (up to 1 mm per 1 min) and cost-effective manner. Also, a robust protocol for gradient deposition was proposed and implemented. The obtained gradients were characterized, confirming the presence of linear changes of IBs concentration over broad areas (c.a. 500 μm) as needed to perform cell motility studies.

The last Chapter describes how we have used the IBs gradients developed in the previous Chapter, to study cell motility. A complex substrate with 80 different environments for high-throughput cell culture was successfully engineered. Individual cell movement assay were carried out using confocal microscopy time-lapse acquisition. Cell movement descriptors such as average travelled distance, directionality, etc. were quantified, enabling us to investigate in detail how factors such as the gradient slope or the concentration of IBs influence cell motility. As an overall conclusion of this part we can confirm the control over cell motility by the IBs gradient patterns.

In general we have proved that IBs as well as the different two-dimensional engineering methods used are interesting and useful approaches with a prospective use in the control of cell guidance as well as a promising tools in regenerative medicine and tissue engineering.

Contents

List of abbreviations

µCP – Microcontact Printing

AU – Arbitrary Unit

BSA – Bovine Serum Albumin

et al. – et alii (and others)

DELOS – Depressurisation of an Expanded Liquid Organic Solution

DDS – Drug Delivery Systems

DLVO – Derjaguin and Landau, Verwey and Overbeek theory

EAPD – Evaporaion Assised Pattern Deposition

ECM – Extra Cellular Matrix

EtOH – Ethanol

FGF – Fibroblast Growth Factor

GFP – Green fluorescence Protein

HDMS – Hexamethyldisilazane (CAS: 999-97-3)

IBs – Inclusion Bodies

NPs – Nanoparticles

PdI – Polydispersity Index

PDMS – Polydimethylsiloxane

SDS – Sodium Dodecyl Sulfate

SUVs – Single Unilamellar Vesicles

TEM – Trensmission Electron Microscopy

TFH – Thin Film Hydratation (vesicle preparation method)

US – Ultra Sonic (vesicle preparation method)

v/v – Volume to Volume

wt. – wild type

w/w – Weight to Weight

Introduction

Living organisms are multi-scale constructs. However, whether we consider gigantic mammals or unicellular *Paramecium caudatum*, all the behaviours they present are to some extent direct effects of the processes that occur at cellular level. It is at the nanoscale, with all its specification and limitations, where basic activities as genome proliferation, breeding, organ formation, tissue maintenance etc. have its origin. Because this world is alien to our senses and intuition humankind had a little curiosity in exploring it. Indeed, our interest in what happens at the nanoscale started recently with the Richard Feynman´s famous lecture "There's Plenty of Room at the Bottom" from the year 1959. Visionaries of that time theorised about worlds being filled with nanoscale robots constantly changing man´s environment. Some prophesied "The Diamond Age" - as Neal Stephenson titled his work.

Despite the passage of time, nanosciences are still regarded as the ultimate goal of control over matter. It is not yet explored entirely, and still has a great potential for research development. We have realised that "subduing earth" (Gen 1:28) means not only controlling with elan vast energies and amounts of matter, but the challenge lays also in operating with painstakingly precision and efficacy. A perfect example of dealing with such complexity is the miniaturisation trend that affected consumers electronics, resulting in an emergence of new technologies and tools. Nanotechnology has truly gone long way from the theory, through the scientific research, to its application in our daily lives. Electronic devices are becoming continuously and relentlessly more and more present in virtually every aspect of our lives.

Little by little these innovations are arriving also into the field of medicine. New tools originating from various scientific fields, such as: material science, biotechnology, chemistry, physics, engineering or medicine are appearing and find their real-life application. The scientific method, applied to interdisciplinary fields, enables studying, taming and finally utilizing natural biological processes to cure diseases, extend lifespan and enhance the quality of life.

The work presented in this thesis aims to contribute to these efforts. Within its scope are two nanoscopic systems that have their prospective use in medicine. They are nanometric lipidic vesicles and protein nanoparticles named Inclusion Bodies (IBs).

In the first part of the thesis we will focus on characterization of vesicular systems that have prospective use as drug delivery systems (DDS). Proprietary solutions based on closed compartments made of lipidic bilayer already exist. However this rich field is vast and there is still plenty to discover. Specifically, we will focus on characterization of mechanical properties of vesicles comparing two systems: liposomes (based on phospholipids) and quatsomes (based on quaternaty ammonia amphyphiles). We will also inquire into how the preparation route influences their mechanical properties studying their interactions with substrates by instrumental analysis. Those properties have a vital impact on key processes that determine drug´s efficacy: assimilation, circulation and internalization.

The second part of this work will focus on a novel particulate biomaterial, Inclusion Bodies (IBs), in the light of tissue engineering. This new material is very promising, as IBs are pure, highly hydrated and mechanically stable protein nanoparticles. They are easy to produce and commonly formed in recombinant bacteria enabling production on a scale up to the industrial level. They are porous, highly hydrated and insoluble in water. Their properties, such as size or biological activity can be easily fine tuned modifying the genetic background of the producing bacteria. As it is a fully biocompatible material we will use them to engineer surfaces and explore their interactions with model cells by quantifying their impact on various aspects of cell behaviour.

The accomplishments presented in this thesis may be considered minor, especially in comparison with the visions unfolded in the first paragraph of this introduction. Nevertheless, the progress they represent is, even if humbly, yet firmly aiming towards the foreseen direction.

General Objectives

The objectives of this thesis will be focused on the two-dimensional engineering of molecular nanoparticles for biological applications. Specifically we will be interested in the characterization of supramolecular systems to study their impact on model cells. In order to do that, we will make use of a large variety of instrumental analytical methods and its subsequent data analysis.

In the first part of the thesis (Chapter 1) our efforts will be directed to characterize the mechanical properties of lipidic vesicles. In the scope of our research there will be two systems with different composition: one based on quaternary ammonia anions (CTAB-cholesterol) and the other one on phospholipids (DOPC-cholesterol). The influence of the internal composition on their mechanical properties will be pursued. Moreover, three methods of vesicle preparation will be applied in order to compare their influence on the properties of the produced vesicles.

The second part of the research work (Chapters 2, 3 and 4) will concentrate on application of bacterial proteic nanoparticles, namely Inclusion Bodies (IB), in the surface modification for cell cultivation and guidance. Parameters such as cell orientation, morphology, positioning and motility will be not only qualitatively but also quantitatively studied based on microscopy images and their careful treatment. In order to reach these goals novel protocols for the controlled deposition of nanoparticles on surfaces will be proposed.

The general goal of this thesis will be to explore different aspects of the proposed systems in order to get closer to their potential opportunities in medical applications and tissue engineering.

1.Adsorption of lipidic vesicles on gold: influence of internal structure on vesicular rigidity

1.1. Objectives

This Chapter will be devoted to the study of the influence of the internal structure of lipidic vesicles on their mechanical properties. Specifically, we will be interested in obtaining reliable, qualitative descriptors for these materials which might have significant implications in nanomedicine and drug delivery. Towards this aim, we used Quartz Crystal Microbalance with Dissipation (QCM-D) and Surface Plasmon Resonance (SPR) techniques to monitor the deposition of model vesicular systems, named quatsomes and liposomes, on a gold surface in order to investigate which is the influence of its preparation route and/or composition on the vesicle rigidity during the deposition process. Thus, the main objectives of the Chapter are:

1. Determination of the type of deposit formed by investigating vesicular systems in contact with a gold surface.
2. Develop a robust data treatment that enables the coupling of data from two different techniques: SPR and QCM-D.
3. Determine the mechanical properties of vesicular systems obtained with different preparation routes.
4. Determine the mechanical properties of vesicular systems obtained with the same preparation route, but with different internal structure; i.e. comparing quatsomes with liposomes.

1.2. Introduction

Membranes are important components of biological systems. They constitute cellular and nuclei boundaries. Cellular respiration depends on proteins of electron transport chain embedded in them. Organelles formed from membranes, such as endosomes or Golgi apparatus are spatially separate cell compartments in which various, often antagonistic processes take place. Lizosomes enable the existence of enzymes within the cell that can be lethal when released. Transport vesicles protect their content until translated into the desired part of cells, etc. [1,2]. In all these processes mechanical properties of membranes are important factors that are determined by the membranes composition like the presence of functional carbohydrates and/or proteins [2].

Recently, the mechanical properties of membranes have gained more attention as vesicles are more widely used as drug delivery systems (DDS) where the membrane is not only a compartment for cargo, but can actively influence the overall outcome of a treatment [3,4]. Membranes used in drug delivery systems are relatively simple, compared with cell membranes, that are dynamic and contain many specific regions with various properties [1,5]. Their role is however quite different – instead of adjusting to dynamic environment, membranes used in drug delivery systems should be stable over prolonged periods of time (shelf-life) with unchanged properties.

Vesicles constitute one of the most developed and already commercially used systems for drug delivery. A better comprehension of these bilayered vehicles as pharmaceutical carriers requires understanding of the way in which supramolecular chemistry influences other properties. In this Chapter mechanical properties are going to be studied in the light of how vesicle´s internal architecture influence them.

1.2.1. Vesicular systems as self-assembled moieties

Molecular self-assembly is a bottom-up, spontaneous and reversible process of association of molecular moieties into larger and more complex supramolecular entities.

The concept of self-assembly emerged from researches of natural processes. In biological systems one of the most basic emanations of self-assembly is the folding of nucleic acids and polypeptides into higher order functional forms [6,7]. Examples of other naturally occurring molecular self-assembled supramolecular entities are molecular crystals [8], colloids [9],

phase-separated polymers [10], self-assembled monolayers [11] and lipid bilayers [12]. Many artificial supramolecular systems are inspired by their biological analogues.

The driving force of self assembly is based on the minimisation of free energy. In general, aggregated components (crystal, macromolecule, etc.) should be in a more energetically favourable state than their correspondent dispersed forms (solution, suspension, random coil, etc).

The majority of naturally occurring self-assemblyed molecules have amphiphilic character, meaning that they contain both hydrophobic and hydrophilic domains. In case of membrane forming lipids, the hydrophobic part is usually constituted of one or more long hydrocarbon "tails" and the hydrophilic "head" is constituted by polar groups (e.g. phosphate). In aqueous phase this dual character leads to the association of its components by weak interactions into assemblies (see Figure 1.1). It is driven by intermolecular association of hydrophobic parts shielding them from the aqueous environment by the protecting hydrophilic head groups. This so called hydrophobic effect is a result of a tendency to minimize the contact of hydrophobic parts with water molecules [13].

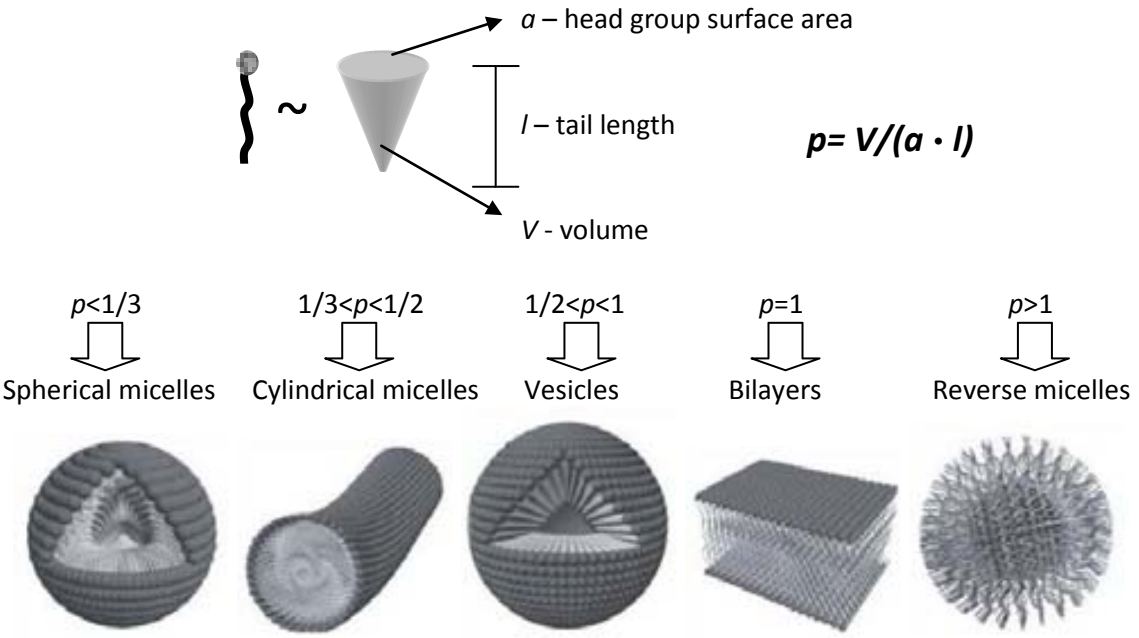

Figure 1.1. Various morphologies of self-assembled aggregates. The final morphology depends on the geometrical properties of the amphiphilic molecule (*p* parameter).

The final aggregates can have different aspects and sizes from nanometric to micrometric range [14,15,16,17]. Their actual form depends on the geometry of their molecular components. As a rule of thumb their final morphology depends on the packing parameter *p*, defined as:

$p=V/(a \cdot l)$

where V, a and l denote the hydrophobic volume, the head group area and the chain length, respectively [18]. The p parameter determines the curvature of the formed aggregates (see Figure 1.1).

When appropriate geometrical requirements are met bilayers are formed. Bilayers are composed of two layers, each of which presents a hydrophilic head groups towards the bulk medium and protecting the hydrophobic tails from the contact with aqueous environment. The spontaneous curvature of the bilayers is caused by the geometrical properties of the assembled molecules, thermal fluctuations, etc. which can lead to the closing of the bilayer and formation of a vesicle. Another factor that promotes vesicle formation is the tendency of bilayers to minimise their perimeter length, as those are areas with excess of energy. A schematic view of a vesicular system is presented in Figure 1.2.

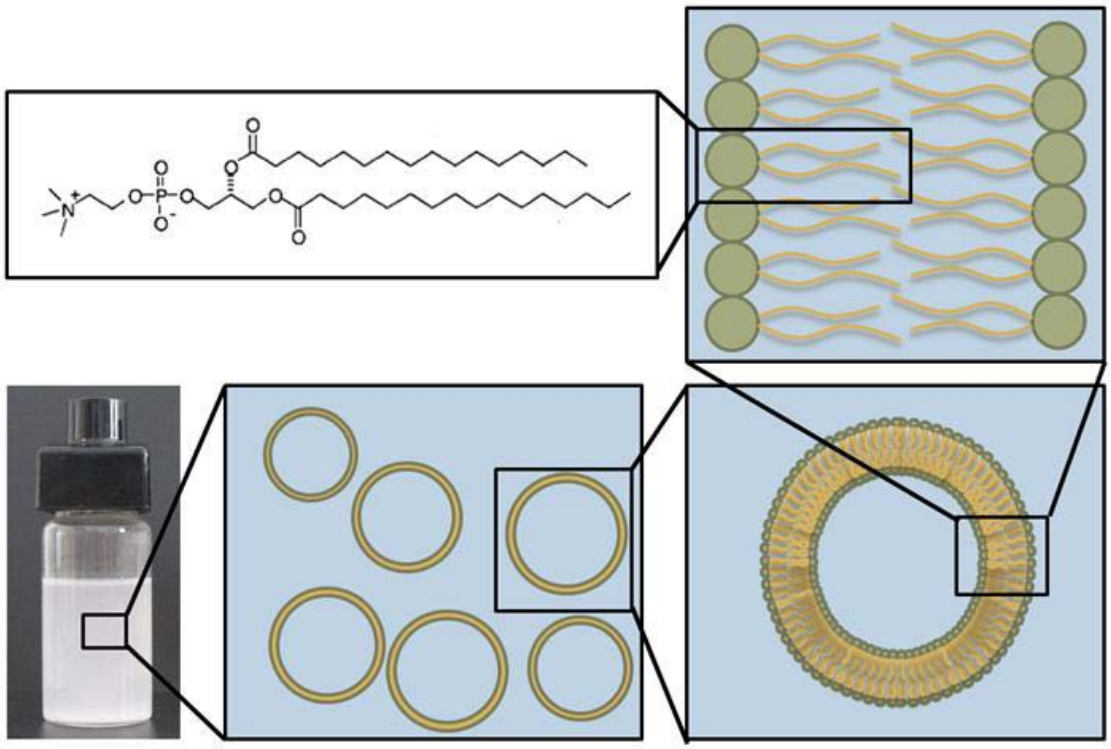

Figure 1.2. Schematic view of the internal architecture of lipidic vesicles from micro- to macroscopic scale. Amphiphilic particles in aqueous environment form supramolecular bilayers exposing hydrophilic "heads" (symbolized as green circles) to the bulk and shielding hydrophobic tails (presented as orange lines) inside the bilayer. Curved bilayers form the vesicles´ walls.

Bilayer membranes are often regarded as two-dimensional liquids, since the movement of molecules is limited in the bilayer. However, they are free to move laterally across the entire supramolecular structure and rotate. Also translation from one monolayer to another monolayer can occur which is called a flip-flop event.

1.2.2. Vesicles as Drug Delivery Systems

The versatility of vesicles comes from the possibility to modify their membranes which can be realised in many ways. Therefore, it comes as no surprise that much interest is put into the development of vesicle-based drug delivery systems (DDS). These approaches aim to produce new formulations by combining therapeutic drugs with agents that play an auxiliary role in order to enhance drug´s effectiveness, selectivity or alleviate side effects. There are many ways of tuning this carrier, making it a very versatile tool as presented in Figure 1.3.

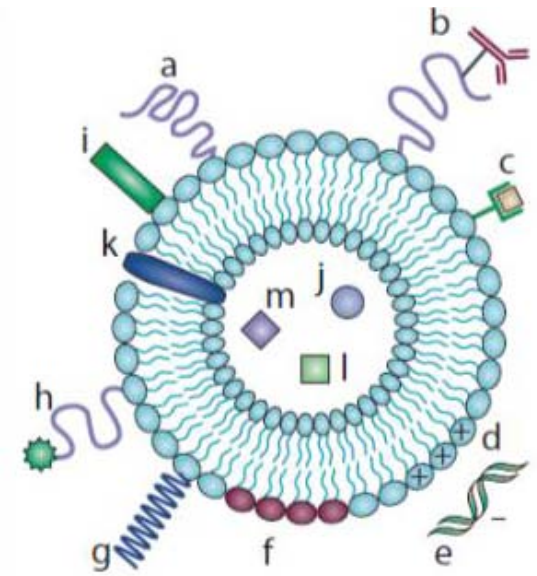

Figure 1.3. Schematic representation of different modifications that can be performed on a vesicle for drug delivery and diagnosis purposes. Among these modifications are: a) the attachment of protective polymer or b) protective polymer and targeting ligand, such as an antibody; c) the attachment/incorporation of the diagnostic label; d) the incorporation of positively charged lipids e) allowing for the complexation with DNA; f) the incorporation of stimuli - sensitive lipids; g) the attachment of stimuli - sensitive polymer; h) the attachment of cell - penetrating peptide; i) the incorporation of viral components or k) hydrophobic drug itself. Vesicles can be loaded by j) hydrophilic drug as well as with l) magnetic particles for magnetic targeting or m) with colloidal gold or silver particles for electron microscopy. Illustration adapted from [19].

Vesicles have various qualities that can promote synergistic effects [20]. The incorporation of drugs into the vesicles´ lumen may shield them from deterioration (by e.g. enzymes) present in physiological conditions. Moreover vesicles are considered a promising approach in nanomedicine in order to overcome the inability of most conventional therapies to deliver drugs without provoking severe toxic effects on normal organs or tissues. Vesicles can circulate longer in blood vessels than free drugs, prolonging the therapeutic effect of the drug. Similarly, vesicles can be also prepared to slowly release entrapped compounds, also enhancing drug´s therapeutic activity. As clearance is longer, also lower (less toxic) doses of drugs are often required. Furthermore, interaction of vesicles with cells can enable the internalization of the

cargo, that would not enter into cell in its free (non capsulated) form. Finally vesicles can also be targeted to specific body regions/cell types enhancing its therapeutic efficacy (site-specific delivery).

Membranes used in drug delivery systems are relatively simple compared with cell´s membranes that are dynamic and contain many specific regions with various properties [1,21]. Among the different types of vesicular systems used for DDS, liposomes (constituted by phospholipids) and vesicles containing ionic, non-ionic, or both surfactants are the most investigated ones. Some examples of surfactants used in order to produce vesicles are presented in Figure 1.4.

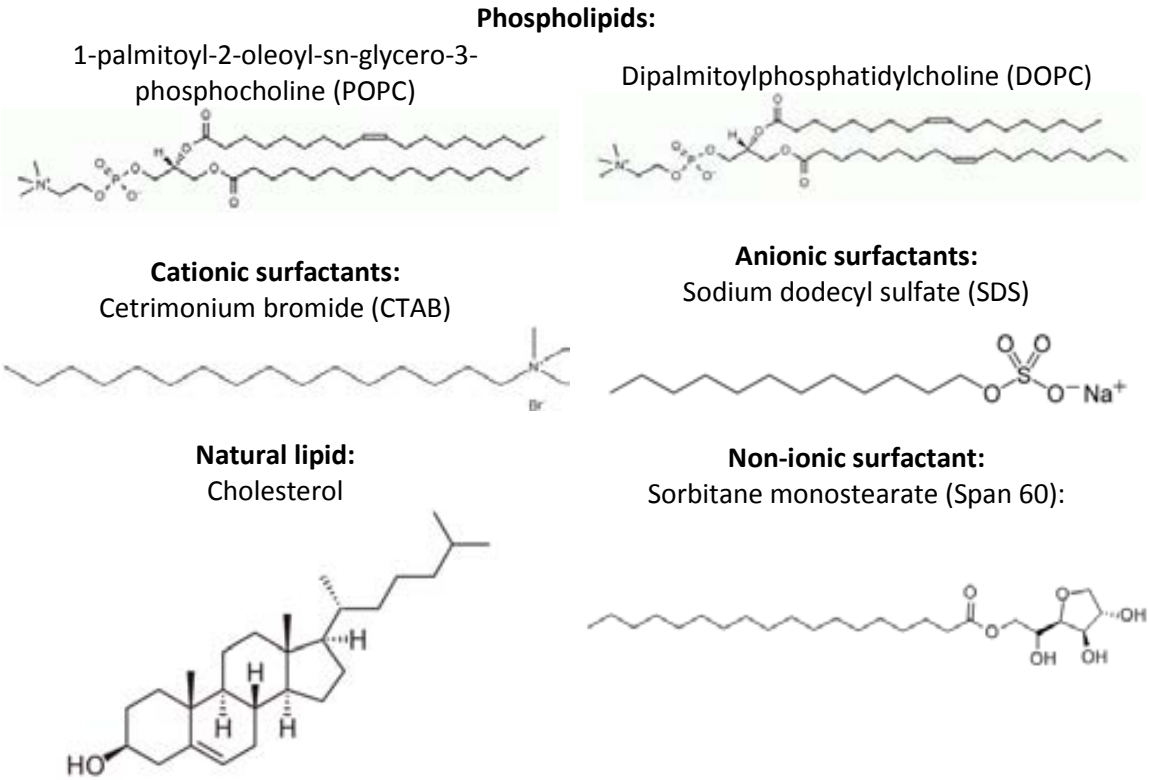

Figure 1.4 Examples of phospholipids, neutral and ionic surfactants used for the preparation of model vesicles.

1.2.3. Vesicle preparation

In order to achieve optimal performance of these self-assembled objects as functional materials a high grade of structural homogeneity is required. For example, the behaviour of vesicles as DDS is highly affected by their homogeneity, not only in size or morphology, but also in the membrane composition and supramolecular organization. Specifically, vesicle membrane plays an important role not only in terms of their stability and permeability but also their rigidity, the property in which we have centred the objective of this Chapter.

Protocols of vesicle preparation vary depending on the scale of production and on the materials used. In this Chapter we will consider two standard approaches: thin film hydration (THF) and ultrasounication (US) as well as a novel method named DELOS-susp. This new method for the preparation of homogeneous vesicles was developed in the Nanomol group due to the unsatisfactory quality of vesicles often obtained by the other two conventional methods. A schematic representation of each method is presented in Figure 1.5.

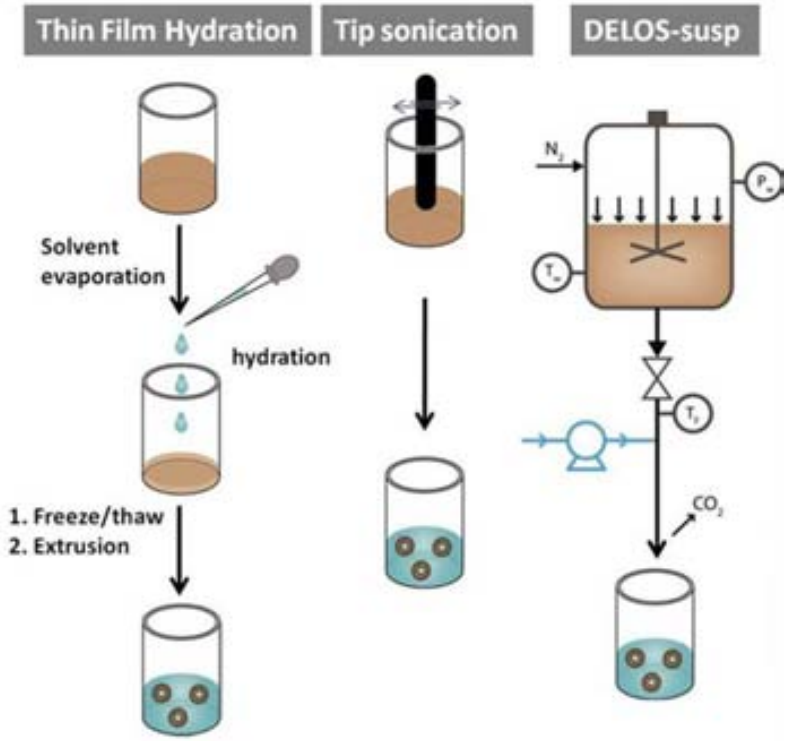

Figure 1.5. Scheme of vesicle production methods. Thin film hydration (TFH): a solution of the precursor components is evaporated and the deposits remaining on the glass walls of a recipient are repeatedly hydrated, frozen and thawed and at the end extruded. Tip sonication (US) consists in the preparation of precursors and delivering energy to the system through an oscillating tip. The DELOS-susp procedure involves the depressurisation of compressed fluids (mixture of CO_2 and ethanol) with dissolved hydrophobic compounds over aqueous solution of hydrophilic compounds.

1.2.3.1. Thin Film Hydration (TFH)

Thin Film Hydration (THF) is a conventional method in which vesicles are prepared following a multi-step procedure [22]. It starts with dissolving the precursor compounds in a chlorinated solvent (e.g. CH_2Cl_2, $CHCl_3$) and is followed by solvent evaporation under a flow of nitrogen and vacuum in order to obtain a lipidic film on the bottom and walls of the flask. Then, this film is hydrated and cycles of freezing and thawing are repeated a desired number of times. At this stage an heterogeneous mixture of multilayered lipid vesicles (MLVs) is obtained. The final step is the extrusion in order to homogenize sizes and morphologies resulting in small unilamellar vesicles (SUVs).

1.2.3.2. Ultra Sonic (US) method

Ultra Sonic (US) method, called also "tip sonication", is a methodology where a probe is introduced into a solution of the precursors and set to oscillate at high frequencies. This technique provides to the system with an additional energy that facilitates the vesicle formation. Vesicle size distribution and morphologies are more homogenous than the ones obtained by THF. However, this method is prone to contaminations coming from the probe (metal particles).

1.2.3.3. DELOS-susp

DELOS-susp is a compressed fluid-based procedure for the one-step production of vesicles that was developed in the Nanomol group at ICMAB-CSIC [23,24]. It is based on the DELOS (Depressurisation of an Expanded Liquid Organic Solution) process which is a crystallization technique based on the use of CO_2-expanded solutions [25]. The driving force of crystallization in this process is the large, sudden and extremely homogeneous temperature drop caused by the rapid evaporation of compressed CO_2, which was previously dissolved, in an organic liquid solution containing the compound to be crystallized. This abrupt and homogeneous temperature reduction produced during the depressurization of the CO_2-expanded solution generates a pronounced and very uniform increase of the supersaturation in every point of the solution, favouring the assembling of solute molecules through homogeneous nucleation rather than by crystal growth, and promoting the formation of micron (or submicron) sized particles with narrow particle size distributions and with an exceptional supramolecular structural homogeneity. DELOS methodology was later on adapted for the obtaining of dispersed systems, such as vesicular formulations, by performing the depressurization step of the CO_2-expanded solution over an aqueous flow (see Figure 1.5). It results in high quality and very homogenous systems that can omit post-formation processing such as extruding. This new CF-based method for the production of dispersed systems was named DELOS-susp.

1.2.4. Vesicular adsorption characterization

As mentioned before, research on the mechanical properties of vesicles is gaining more attention due to the use of these nano-objects in DDS, where the membrane is not merely a compartment for cargo, but can actively influences the overall outcome of the treatment [3,4].

Direct measurements of mechanical properties of lipidic layers have been studied mainly by means of indentation techniques (see Figure 1.6). Nanoindentation experiments relay on the identification of the measured vertical displacement of the membrane caused by a probe and the applied load required to translate the probe along the displacement using Atomic

Force Microscopy (AFM). Nanomechanical properties or elastic behaviours in the environs of the host molecules can thereafter be deduced from the relation between the harmonic contact stiffness and the infinitesimal displacement [26]. This technique have been also used to study properties of cell membranes in biological contexts [27,28]. More details on this technique can be found in Reference [29].

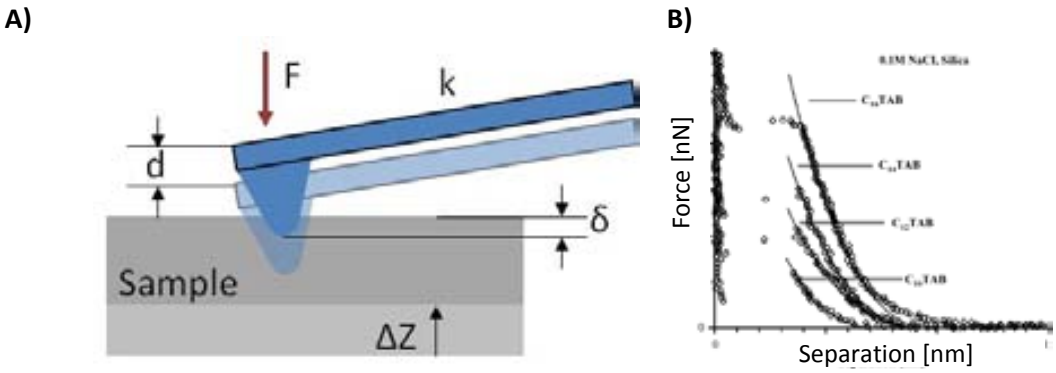

Figure 1.6. Principles of nanoindentation experiments with AFM. A) Force curve parameters that are used for quantitative estimation of elastic properties of a material. F - load of cantilever, d - cantilever displacement, k - cantilever spring constant, δ - indentation depth, ΔZ - sample displacement. B) Example of an experimental force-distance curves (circles) measured between an AFM tip and monolayers of cetyltrimethylammonium bromide with various tail lengths (10-16) that are deposited on a silica substrate. Image adapted from Ref. [29a].

Other experimental techniques are based on rheological studies in flow chambers, for example microscopic observation of giant vesicles (see Figure 1.7). Quantification of the large-scale circulation patterns induced inside vesicles adhered to a solid surface and subjected to simple shear flow in a microfluidics device enables calculation of viscoelastic properties of the membrane [30].

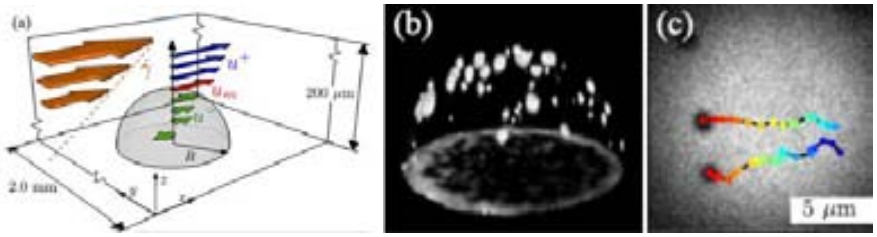

Figure 1.7 Microfluidic shear experiment. a) Schematic view of the chamber (not to scale). b) Confocal imaging reconstruction of an adhering hemispherical vesicle with small domains visible on its surface. (c) Tracking of gel domains, flowing across the vesicle apex (tracks colour-coded in time over 2.6s). Image adapted from Ref. [30].

Other techniques that allow the extraction of mechanical properties of materials are the Quartz Crystal Microbalance with Dissipation (QCM-D) technique and the Surface Plasmon Resonance (SPR) technique, both allowing to perform label-free and real time measurements.

1.2.4.1. Quartz Crystal Microbalance with Dissipation technique

Quartz Crystal Microbalance with Dissipation (QCM-D) enables measurements of mass of material adhering to an acoustic sensor and have emerged as another technique useful in this field. Mass is directly calculated from changes of its frequency (ΔHz) using the Sauerbrey relation [47]. Dissipation factor (also measured in Hz) can be related with viscoelastic properties of the deposited material [49] and by applying an appropriate model (e.g. Voigt model) physically meaningful properties of the material, such as shear stress and viscosity, can be determined. Schematic cartoon of the QCM-D principle is presented in Figure 1.8.

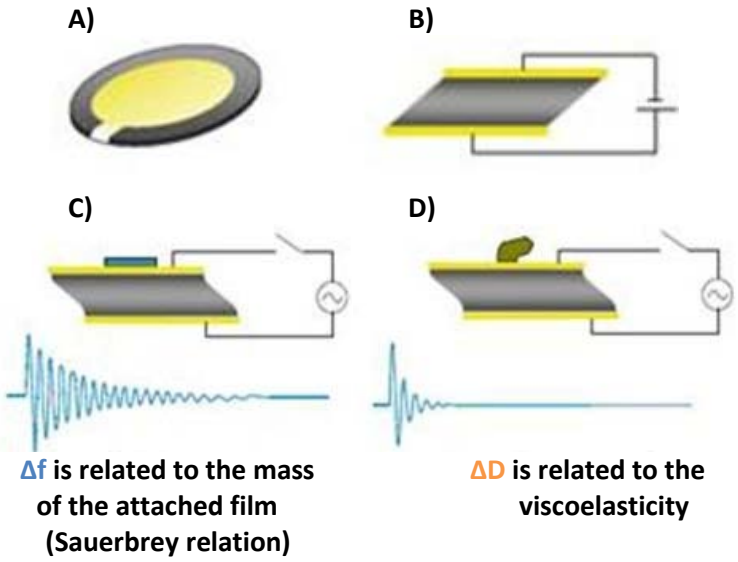

Figure 1.8 QCM-D principle. A) view of the sensor: circular tile of quartz with deposited gold. B) Upon electrical stimuli the quartz crystal undergoes a share deformation. C) Resonance frequency, Δf, of crystal oscillation under alternating stimuli depends on the total mass of material absorbed on the sensor. D) Dissipation, ΔD, depends on the viscoelastic properties of the absorbed material. Image adapted from Ref. [31].

This technique has proven its usefulness in measuring cells-substrate interactions [32], or exploring mechanisms that occur on various substrates while exposed to lipid vesicles [33]. For example, the mode how vesicles deposit on a surface can be easily determined having data on the mass and its mechanical properties evolution during the absorption (see Figure 1.9). Example of recent applications of this technique on vesicle research include studying the influence of temperature on deposition mechanism [34], study bacteria outer membrane components glycosphingolipids and lipopolysaccharides) [35] or development of new bilayer deposition protocols [36].

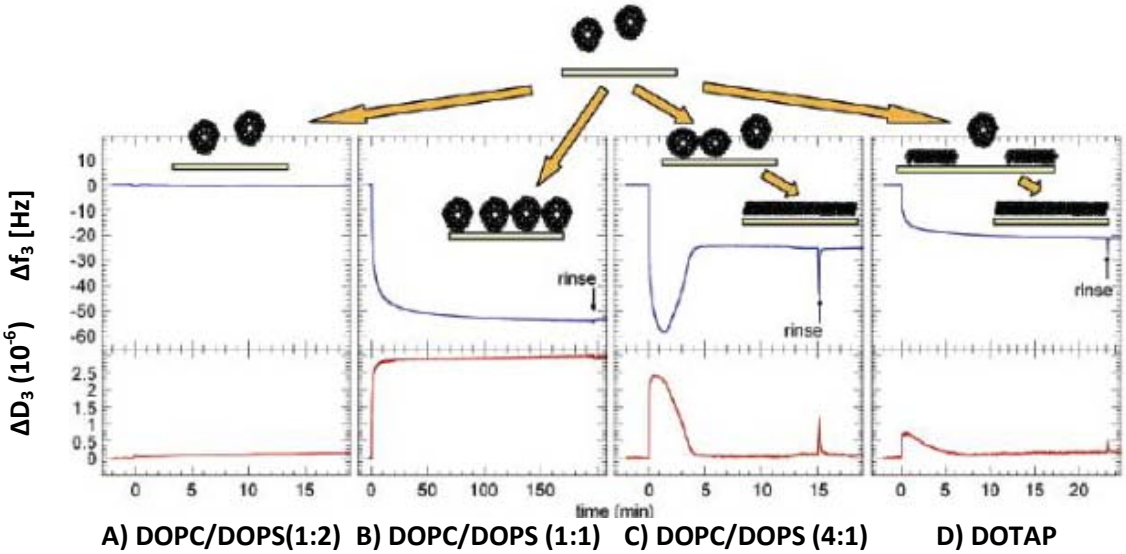

Figure 1.9 Lipid deposition pathways measured by QCM-D on silica. (A) Vesicles do not adsorb and no changes in both *Δf* and *ΔD* is observed. (B) Vesicles adsorb and remain intact, forming a vesicular layer. High mass of deposited layers is signalised by high *Δf* change and increase in *ΔD* indicates that layer dissipates energy. (C) Vesicles adsorb and remain initially intact as signalised by initial changes of both *Δf* and *ΔD*. At high vesicular coverage a supported lipid bilayer (SLB) is formed - vesicles burst and as SLB mass and dissipation is lower *Δf* reflects lower mass uptake. *ΔD* returns to initial state, as SLB almost no dissipates energy. (D) Vesicles adsorb and rupture instantaneously, to form an SLB. Practically no change *ΔD* is observed and *Δf* change is less than in case of vesicular layer deposition (example B). The legends indicate the lipids used dioleoyltrimethylammonium-propane (DOTAP), dioleoylphosphatidylcholine (DOPC), and dioleoylphosphatidylserine (DOPS)s with their molar mixing ratios. Image taken from Reference [33].

1.2.4.2. Surface Plasmon Resonance

Electromagnetic waves that propagate at the metal/dielectric interface in a direction parallel to this surface are called surface plasmon polaritons (surface plasmons). These oscillations are very sensitive to any change on the boundary of the metal and the external medium (e.g. liquid or gaseous medium) such as the adsorption of material to the metal surface, refractive index changes of medium or temperature changes.

SPR quantifies changes in direct proximity of the sensor's surface (up to ~300 nm) using an optic sensor (Figure 1.10). For a given laser incidence angle to the conductor-dielectric surface, a resonance between the laser photons and plasmons occurs leading to decrease of reflected laser light intensity. The angle of minimum intensity of reflected laser can quantified and used to study phenomena occurring on the sensor surface, such as vesicle or protein absorption. These phenomena change its local refractive index and it influences the electric field called evanesced wave that is formed close to the sensor surface by surface plasmons. As the evanesced field decays exponentially with distance from the sensor, SPR is extremely sensitive to small and local changes on the properties of the metal-liquid interface. It changes the angle

of incident light at which the resonance of plasmons occurs and therefore it can be quantified. By measuring changes of resonant angle we are able to gain insight into local changes of refractive index at close proximity of the sensor surface. Schematic illustration of the used setup is presented in Figure 1.10.

The number of phenomena able to generate an SPR response is quite numerous, from conformational changes, to modifications of the colorimetric or fluorescent properties of the substrate, nevertheless the adsorption of molecules is the most common of all of them. This technique is therefore used as a tool to study kinetic and affinity of binding events. Recent studies of vesicles by SPR are i.e. protein binding with fatty acids kinetics [37], binding of modified, amphiphilic DNA strains to the lipid bilayer membrane [38] or the interaction between vesicle membrane embedded protein (proteoliposome) and free protein in solution [39].

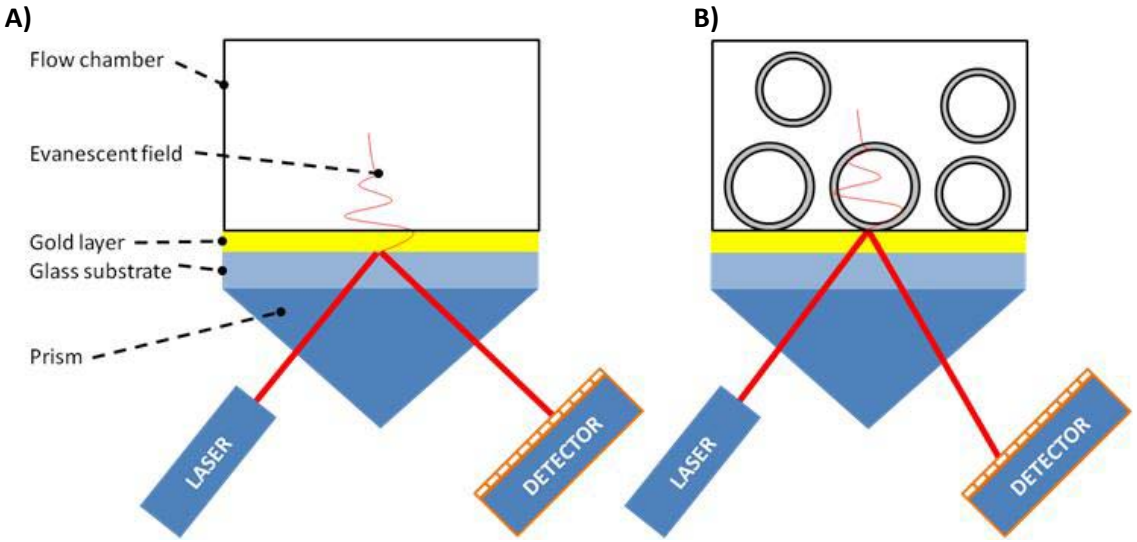

Figure 1.10 Schematic view of SPR setup based on a continuous flow system. A) The device consists of a monochromatic light source (LASER), an optical detector, a prism of controlled refractive index, a gold coated glass slide and a flow chamber. B) In the case of interaction of the sensor with an analyte, the variations of the local refraction index, change the incidence angle that is monitored while the solution is pumped over the gold layer.

1.2.4.3. Coupling SPR and QCM-D techniques

Although both techniques bring valuable data on their own, coupling them enables one to access a rich source of data. Since one technique is designed to measure acoustic and the other optical properties, they can complement each other (see Figure 1.11).

Coupling QCM-D with SPR has been previously applied to research in areas such as: the study of the interactions between various vesicle concentration and sensor [40], the study of

DNA multilayer's mechanical properties [41] or to incorporate kinetics of integral membrane protein to tethered lipid bilayer membrane [42].

Some researchers instead using SPR as optical sensor are using ellipsometry in order to complement QCM-D data. Such combination was used for example to evaluate the mass or the calculation and deposition layer thickness in for example protein-membrane interaction study [36,43]. Also the combination of the three techniques (SPR, QCM-D and ellipsometry) simultaneously has been reported [44].

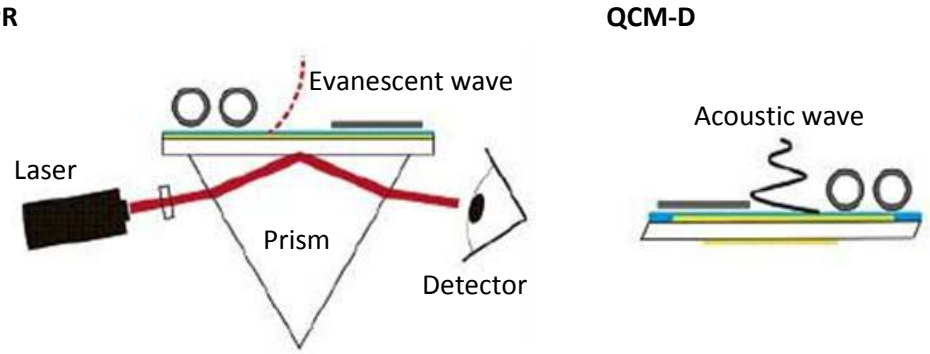

Figure 1.11 Schematic illustration of the measurements configuration. Coupling both techniques enables to obtain optical (SPR) and sonic (QCM-D) sensors/properties. Image adapted from Ref. [45].

1.2.5. QCM-D principles

In order to properly explain the calculation protocol that we will apply to determine mechanical properties from experimental values, we need to cast light on details of the QCM-D principles.

QCM is based on the inverse piezoelectric effect. When voltage is applied to a certain crystalline materials, they yield in mechanical deformation [46]. Quartz has been broadly used for this purpose due to its stability and low energy dissipation. Usage of alternating voltage leads to oscillations. In special cases, when the voltage frequency matches the crystal's resonance frequency a mechanical standing wave is generated in the crystal. This resonant frequency f_0 is denominated as "fundamental" in opposition to overtones, that is, harmonic partials (frequencies that are integer multiples of the fundamental one), that also exists in such case. We will denote the overtone order by *n*.

The use of a quartz crystal as microbalance is due to the linear dependence found by Sauerbrey [47] that binds the change of the resonance frequency and the change of the mass of the resonator:

$$\Delta f_n = -\frac{n}{C}\Delta m_a = -\frac{n}{C}\rho_f h_f \qquad \text{EQ. 1}$$

Where Δm_a is the acoustic aerial mass change (note: the "mass" is expressed in mass per surface unit [ng/cm^2]), ρ_f and h_f are the density and thickness of the adsorbed film, respectively, which as we see are not independent values. The constant *C* depends only on the fundamental resonance frequency, f_0, and the material properties of the sensor (quartz crystal shear modulus and density). For f_0 this "Sauerbrey constant" is approximately 18ng cm^{-2} Hz^{-1} [48].

An extension of the QCM is the so-called QCM-D which has been developed by Rodal *et al.* [49]. In this approach, the external alternating voltage is turned on and off intermittently. While off, crystal´s oscillations are decaying freely (see Figure 1.12). Since the quartz is piezoelectric, a voltage is generated and recorded during this period. This results in registration of two parameters per overtone: the resonance frequency f_n and bandwidth Γ_n., which is imminently connected with the dissipation *D* (those terms are often used interchangeably) by the relation:

$$D_n = \frac{2\Gamma_n}{f_n} \qquad \text{EQ. 2}$$

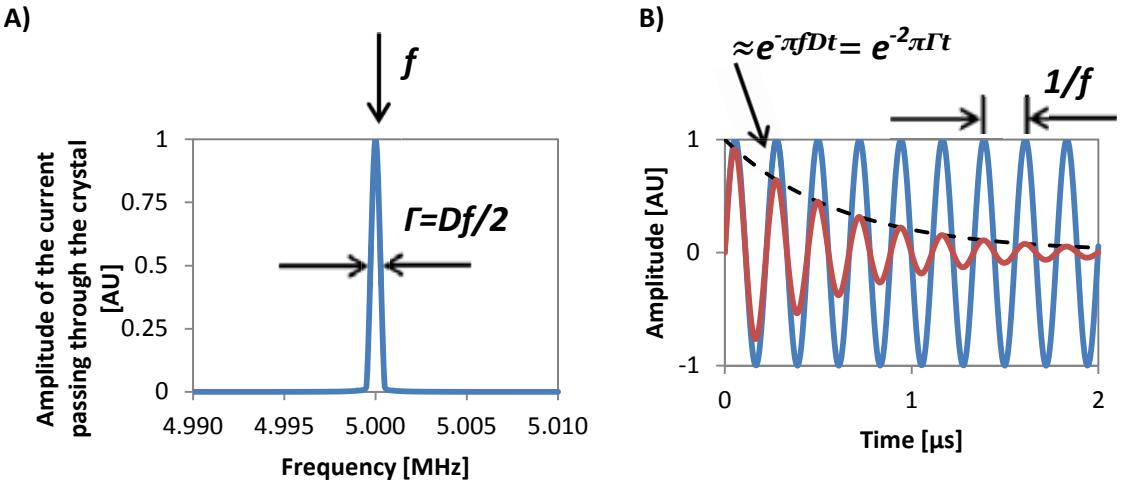

Figure 1.12 Schematics of QCM-D principles: A) The typical crystal resonance spectra obtained with impedance analysis. In the y-axis can be, equivalently, the amplitude of the crystal's shear motion. Two parameters are used to characterize the resonance: its frequency *f* and its bandwidth *Γ*. B) In QCM-D the driving voltage is intermittently switched off and the decay in time of the oscillation is monitored. From the decay curve, the resonance frequency *f* and the energy dissipation *D=2Γ/f* are extracted. Image adapted from Ref. [48].

There are various approaches used to quantitatively interpret the QCM-D data [48]. The analysis done within this Thesis work is based on the methodology described by Reviakine *et al.* [48] that uses the laterally homogenous film approximation. In that model layers with

ΔD>0 are assumed to have viscoelastic properties, meaning that the model has to take into account both elastic and viscous (dissipative) behavior of real materials. In general viscoelastic properties can be expressed as a complex modulus:

$$\boldsymbol{G = G' + iG''} \qquad \text{EQ. 3}$$

Where *i* is an imaginary unit (square root of -1), *G´* is a storage modulus describing the layer´s elasticity (spring constant) and *G´´* is the loss modulus describing viscous energy dissipation in the material subjected to the deformation.

Viscoelastic properties can be also modeled as linear combinations of springs and dashpot elements. The elastic modulus of a spring stores energy and the viscosity of a dashpot dissipates energy. Each model differs in the arrangement of these elements. We will apply the Voigt model where spring and dashpot elements are connected in parallel, as shown in Figure 1.13. This model represents a solid undergoing reversible, viscoelastic strain. Upon application of a constant stress, the material deforms at a decreasing rate, asymptotically approaching the steady-state strain. When the stress is released, the material gradually relaxes to its initial state. At constant stress (creep), the model is quite realistic as it predicts strain to tend to σ/G' as time continues to infinity.

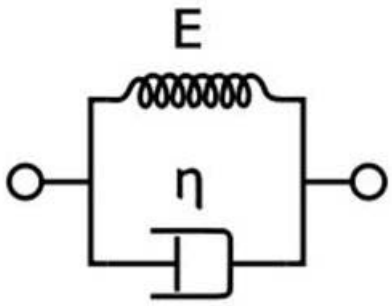

Figure 1.13 Schematic representation of the Voigt Model. Spring and dashpot element are joined in parallel.

This model applied to QCM-D assumes also a frequency-independent storage modulus G´, viscosity *η* and linear dependence:

$$\boldsymbol{G'' = 2\pi f \eta} \qquad \text{EQ. 4}$$

The viscosity *η* can be viewed as a friction coefficient that relates the applied force to the rate of deformation.

For such a model, the areal mass density of the film, m_f, and its viscoelastic properties are related to frequency and bandwidth shifts of QCM-D as follows:

$$\boldsymbol{\Delta f_n \approx -\frac{n}{C} m_f \left(1 - n\omega_0 \rho_l \eta_l \frac{G_f''}{\rho_f \left(G_f'^2 + G_f''^2\right)}\right)} \qquad \text{EQ. 5}$$

$$\Delta\Gamma \approx \frac{n}{C} m_f n\omega_0 \rho_l \eta_l \frac{G'_f}{\rho_f\left(G'^2_f + G''^2_f\right)} \qquad \text{EQ. 6}$$

Where $\omega_0 = 2\pi f_0$ is the angular fundamental resonance frequency and subscripts *l* and *f* refer to liquid and film, respectively.

Fitting QCM-D experimental data with the proposed model enables estimation of viscoelastic properties of laterally homogeneous viscoelastic thin films, if the film thickness is much thinner than the wavelength of the shear-acoustic wave in the film. However, laterally homogeneous, acoustically thin films whose density and mechanical properties continuously vary in the vertical direction can also be treated with this approach. In such case we obtain equivalent thickness and z-averaged viscoelastic properties.

The application of the viscoelastic model requires a certain amount of care. An assumption about film density ρ_f is required to obtain film thickness (or *vice versa*) and independent knowledge of some of the film properties is helpful, if not essential, for a model to provide meaningful results.

1.2.6. Frequency vs. Dissipation (F/D): deposition trajectories

In case of thin films that are stiffer than the surrounding liquid and much thinner than the penetration depth of the shear wave in liquid[*] the dispersion in $\Delta f_n/n$ is small and the second term in the brackets of equation 5 can be neglected and the ratio between bandwidth and frequency gives a direct insight into mechanical properties of the deposited film:

$$\frac{\Delta\Gamma_n}{\Delta f_n} \approx \frac{\rho_l}{\rho_f} n\omega_0 \eta_l \frac{G'_f}{\left(G'^2_f + G''^2_f\right)} \qquad \text{EQ. 7}$$

This equation rationalizes how the ratio between $\Delta\Gamma$ (or ΔD) and Δf can provide useful information. To perform this analysis one has to construct $\Delta D/\Delta f$ plots, which are called also "fingerprints", as they are characteristic of processes that occur during deposition. Subsequent analysis of such "deposition trajectories" can reveal mechanisms that occur during depositions as this ratio increases with particle size and decreases with surface coverage [50]. Examples of these trajectories obtained from subject literature are presented in Figure 1.14. Despite being

[*] For water, at 5MHz, and for fundamental frequency n = 1, penetration depth is ≈250 nm.

informative and enabling comparison between systems, those plots do not bring quantitative data.

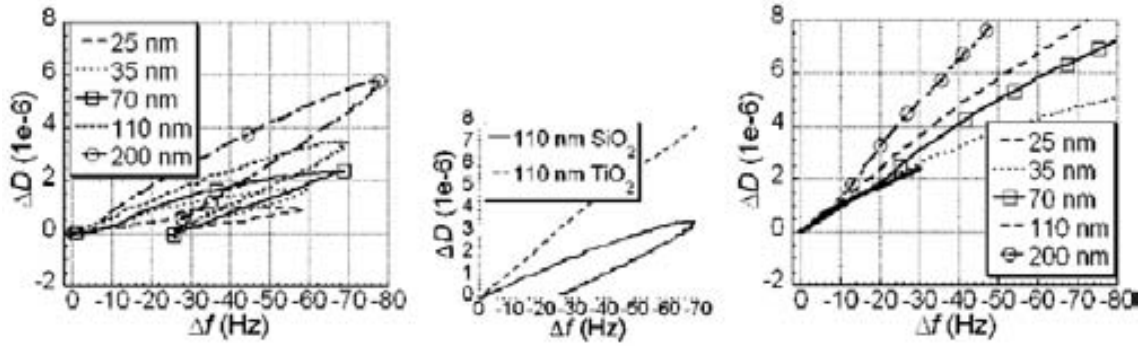

Figure 1.14 *ΔD* displayed versus *Δf* for the adsorption process on SiO_2 (left) and TiO_2 (right) surface of vesicles of different sizes. In the middle the juxtaposition of data for same vesicle and both substrates is presented. Image adapted from Reference [51]

1.2.7. Model independent particle size calculation based on QCM-D data

Another type of analysis, proposed by Tellechea *et al.* [50] enables calculation of the size of the adsorbed colloidal particles basing on gathered QCM-D data without fitting them to any model.

A) **B)**

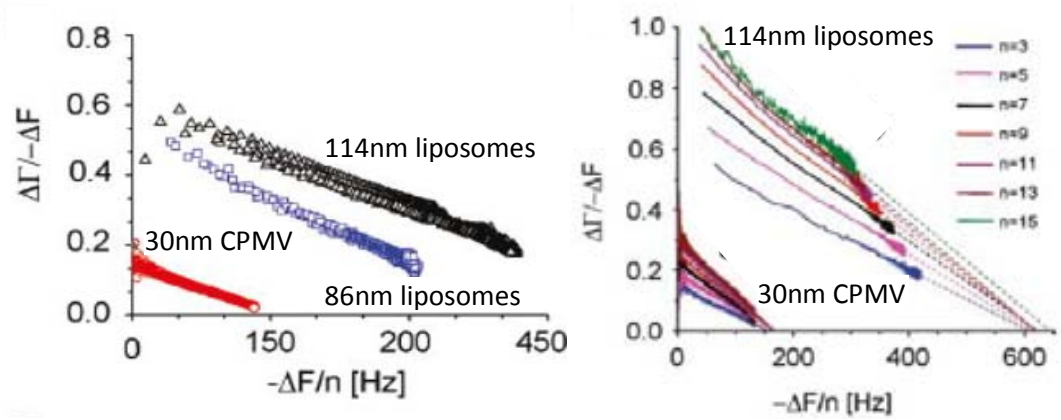

Figure 1.15 Dependence of the *ΔΓ/-Δf* ratio on the particle size and coverage. A) The effect of surface coverage on the bandwidth shift to the frequency shift ratio, *ΔΓ/-Δf*, can be separated from that of the particle size. Three curves are shown: black triangles, representing 114nm liposomes; blue squares, representing 86nm liposomes; and red circles, representing icosahedral cowpea mosaic virus (CPMV) particles of approximately 30nm. Only the 3rd overtone data are plotted. The ratio increases with the particle size but decreases with increasing magnitude of the frequency shift. B) Plotting the bandwidth shift to the frequency shift ratio, *ΔΓ/-Δf*, as a function of the scaled frequency shift for several overtones, reveals a common intercept with the *-Δf/n* axis. Data for the 114nm liposomes and for CPMV particles are shown. Dashed lines are linear regression fits to the data. Image reproduced from [50].

They showed, that the decrease of the $\Delta\Gamma/-\Delta f$ ratio is linear with Δf over a large range of frequency shifts Δf (Figure 1.15). These linear portions can be extrapolated to frequency-independent intercept with the $-\Delta f$ axis for different overtones. Such overtone-independent frequency shift value at zero of $\Delta\Gamma/-\Delta f$ by definition corresponds to the previously mentioned Sauerbrey mass [47] that can be calculated from Equation 1. Based on the Sauerbrey mass value and knowing the aerial density of the layer, its thickness (denominated "Sauerbrey thickness") can be calculated. For rigid particle deposition (virus particles and vesicles) a good agreement have been found between "Sauerbrey thickness" and particle diameter as measured by DLS.

1.2.8. Quatsomes vs. Liposomes

The rich field of supramolecular chemistry recognizes many molecules that can form curved bilayers and, effectively, vesicles. There is actually a large interest in the search of nonlipid components that self-assemble into stable vesicles as well as to satisfy the quality standards required in pharmaceutical formulations [52,53]. Examples of such substances are: amphiphilic polymers that form "polymersomes" [54,55,56], polypeptides that form "peptosomes" [57], rod−coil polymers [53], dendrimers [53], amphiphilic fullerene derivatives [53] or mixtures of cationic and anionic surfactants forming "catanionic vesicles" [58,59,60].

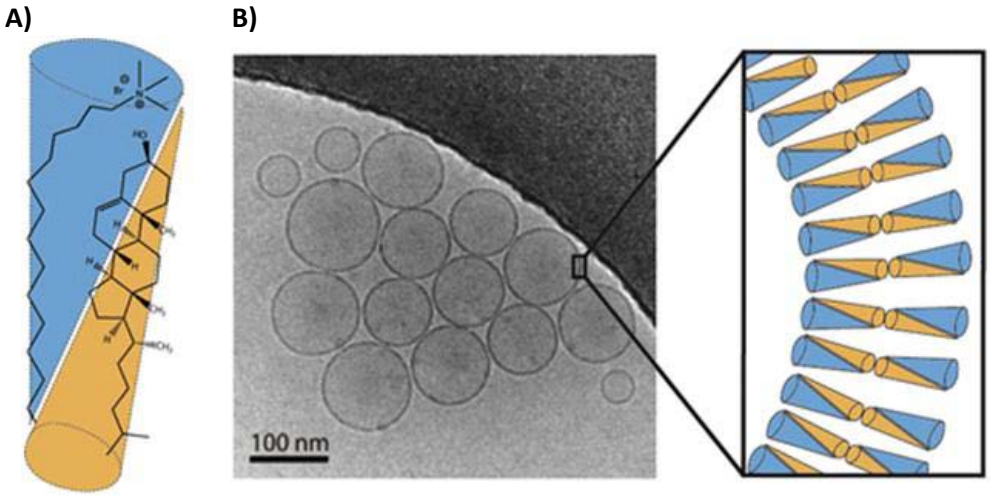

Figure 1.16 Schematic illustration of the tectome. A) A Chol/CTAB bimolecular amphiphile (tectome). B) Chol/CTAB tectomes self-assembling into bilayer vesicles. Figure adapted from Reference [62].

It has already been observed by our research group (Nanomol, ICMAB-CSIC), that cholesterol-rich cationic vesicles obtained by the DELOS-susp technique (Chol:CTAB, 1:1 mol:mol) present unique physicochemical characteristics compared to those prepared by a conventional mixing method [23]. Such spontaneous, single-walled, equilibrium, nanoscopic

vesicles of controllable size and surface charge are stable for periods as long as several years. Moreover, their morphologies do not change upon rising temperature or dilution. They show outstanding vesicle to vesicle homogeneity regarding size, lamellarity, and membrane supramolecular organization [23,61].

It is worth mentioning also, that none of the components of a quatsome spontaneously aggregate into vesicular structures separately. In water the quaternary ammonium surfactant form micelles and the insoluble sterol species form crystals. Therefore, the self-assembly of sterol/quaternary ammonium surfactant mixtures into exceptionally homogeneous bilayer vesicles has to be attributed to a synergy between both molecular entities. Indeed, a bimolecular amphiphile was proven both experimentally and by molecular dynamics simulation to form only when cationic surfactant is mixed with sterole at a 1:1 ratio [62]. Their formation results apparently from the production of an anion - cation surfactant pair which then acts like a double-tailed surfactant. This entity is called tectome (Figure 1.16).

Due to their unique internal architecture, these quatsomes have a great potential in the development of new drugs in nanomedicine [63]. They have also shown to be effective nanostructures to enhance specific bioactivity of proteins, and to protect them against premature degradation in topical pharmaceutical formulations [64,65].

Although there are numerous studies of differences and similarities of vesicular systems based on various lipids, there are relatively few research papers devoted to the influence of membrane supramolecular architecture and/or preparation method on membrane mechanics within the same system [66]. However, there are reports indicating that vesicles produced with the same precursors by different preparation routes may have present differences [61].

It is of paramount importance for the development of more efficient drug and gene delivery systems to characterize this new building block. The understanding of mechanisms of their self-assembly and its impact on mechanical properties is very important and may improve its functionalities.

This Chapter endeavours to explore if the highly homogeneous organization achieved using DELOS-susp also gives place to a different mechanical properties of quatsomes in comparison to vesicles obtained with other methodologies, like TFH or US. Moreover, we will study the influence of the components (CTAB-Chol vs. DOPC-Chol) of vesicles obtained with the same methodology (DELOS-susp). Thus, using a data treatment based on the combination of SPR and

QCM-D techniques we will make a comparison of not only the thickness and mass but also the mechanical properties of quatsomes obtained from different preparation routes and also of vesicular systems obtained with the same preparation route but with different internal composition/structure (quatsomes vs liposomes). So, the DOPC-Chol-based liposome will be included as a model into this comparison.

1.3. Results and Discussion

Cholesterol rich vesicles (1:1 ratio of cholesterol:other sufractant) with CTAB (CTAB-Chol quatsomes) and DOPC (DOPC-Chol liposomes) have been prepared by Lidia Ferrer from the Nanomol Group (ICMAB-CSIC). Quatsomes have been prepared by sonication, thin film hydration and DELOS-susp methodology. In this way we will be able to compare the influence of the preparation method on the same material. Liposomes have been prepared by DELOS-susp to enable a comparison between liposomes and quatsomes obtained using the same methodology.

As a buffer we have chosen phosphate buffer saline (PBS) in order to test vesicles properties in a context resembling physiological conditions as much as it was possible. Final concentration of the studied cholesterol – rich vesicles depended on the maximal solubility of precursor surfactant that could be used in DELOS-susp methodology. In this approach cholesterol and DOPC should be dissolved in an organic phase (ethanol) before introduction to supercritical reactor. Since CTAB did not require to be dissolved in ethanol, final concentration of surfactant for quatsomes is higher (5.4mg/ml) than in case of liposomes (2.1mg/ml). For measurements we have been using 10-fold and 100-fold dilution of this concentrations. Other techniques for quatsomes preparation (TFH and US) were preformed in order to obtain a similar concentration of the surfactants. Also, in order to maintain the same medium composition in all batches of quatsomes, 10.8% v/v of EtOH was added, as this is the minimal quantity that is needed in DELOS-susp protocol. Details on these preparations can be found in the Appendix in the Section A.1 (“Vesicle preparation”).

1.3.1. Characterization of the vesicles

Morphology and size are proven to have a non negligible impact on mechanical properties of vesicles. So, in order to properly compare mechanical properties of deposits resulting from interactions of vesicles with sensors (SPR and QCM-D), we have to ensure that vesicles are very similar in terms of size. To provide such requirements we have fully characterized all samples with DLS and cryo-TEM. This step is crucial in order to be able to compare the resulting data [51]. With a lot of efforts in the preparation step it has been possible to obtain similar sizes for all of them, thus, being not far from the ideal situation. More details are available in see Section A.1 (“Vesicle preparation”).

Table 1.1 Average vesicle size and polydispersity index (PdI) measured by DLS for quatsomes and liposomes prepared by different methods. The particle size distribution measurement is based on intensity of light scattered.

Vesicle composition	Preparation route	Medium diameter [nm]	PdI
Cholesterol/CTAB	DELOS-susp	118.7	0.134
Cholesterol/CTABB	US	116.0	0.179
Cholesterol/CTAB	TFH	121.4	0.056
Cholesterol/DOPC	DELOS-susp	94.77	0.262

The measured hydrodynamic sizes and the corresponding polydispersity index are given in Table 1.1. We have obtained vesicles with very similar average sizes around 120 nm in diameter.

CRYO-TEM images confirmed that the obtained vesicles are single unilamellar vesicles (SUV´s) regardless of the preparation route (see Figure 1.17). However, it is worth to note, that vesicles prepared by the TFH methodology (Figure 1.17b) show oval shape, probably caused by the extrusion procedure used to homogenize sizes of crude vesicles. Taking into account that the light scattering intensity in DLS is proportional to the 6-th power of the particle´s hydrodynamic diameter, the slightly lower vesicle diameter observed in the cryo-TEM images agrees with the reported DLS measurements. More details on this technique can be found in Section A.2 ("Cryogenic Transmission Electron Microscopy").

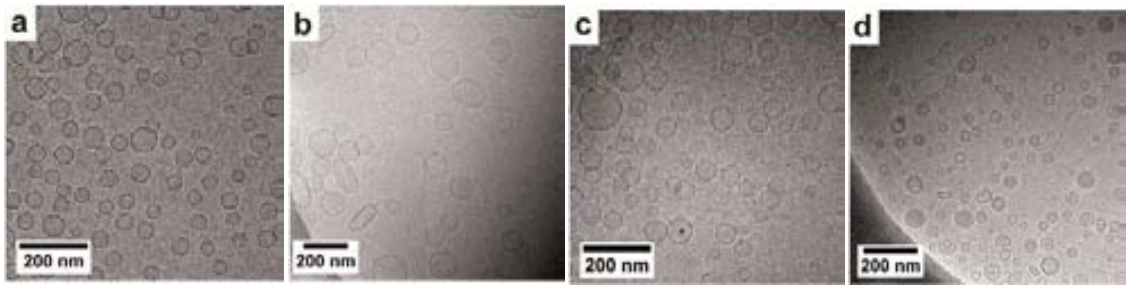

Figure 1.17 Cryo-TEM images of Chol/CTAB quatsomes prepared by a) sonication (US), b) thin film hydration (TFH) and c) DELOS-susp. d) Chol/DOPC liposomes prepared by DELOS-susp.

1.3.2. SPR and QCM-D measurements

All QCM-D measurements were performed in the Laboratory of Biosurfaces at the Centre for Cooperative Research in Biomaterials-CIC biomaGUNE, located in San Sebastian (Spain) under the supervision of Dr Ralf Richter.

Representative QCM-D and SPR data is presented in Figures 1.18 and 1.19, respectively. Injections of highly concentrated vesicles (0.54 and 0.21mg/ml of surfactants for quatsomes and liposomes, respectively) were useful to establish the saturation values for the two sensors

that are approximately 7500 μRU for SPR and -200 Hz for QCM-D frequency. Then, experiments with low concentration (0.054 and 0.021mg/ml of surfactants for quatsomes and liposomes, respectively) samples were performed since they provide a better insight of the kinetics (curve shape) of the process allowing to have more data points before the formation of a complete vesicle layer.

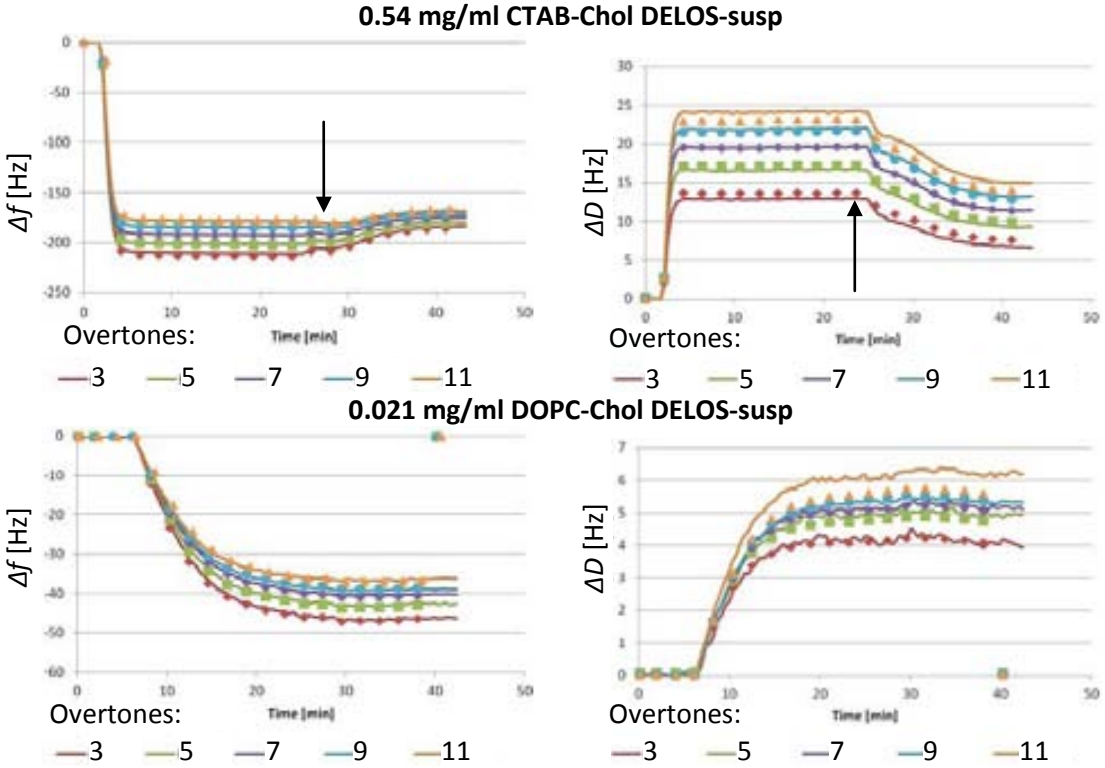

Figure 1.18 Representative frequency (left) and dissipation (right) curves for QCM – D overtones 3 to 11 recorded during vesicle deposition. Continuous lines represent raw data points. Dots are selected points form the fitting curve as explained in the Section 1.3.4 ("Coupling data from QCM-D and SPR"). Arrows indicate injection of buffer solution to promotea desorption. For more details see Section A.3 ("Quartz Crystal Microbalance with Dissipation (QCM-D)").

In the QCM-D frequency and dissipation plots we can see monotonous changes until achieving stable plateaus. This is a clear indication of the interaction between vesicles and the sensor surface, as the final value of both signals is different with respect to the initial, when the sensor was exposed to the buffer solution directly before vesicle containing sample was injected. The decrease of the frequency signal is indicative for a continuous accumulation of mass on the substrate. The increase of dissipation signal proves that with the deposited layer the sensor dissipates more energy than in buffer. The monotonic changes of both signals until the injection of buffer solution indicate that the formed layer does not undergo any conformational changes once adsorbed on the gold surfaces. Therefore, we can conclude, that the deposition mechanism is similar to the one presented in Figure 1.9.B and is indicative of

the deposition of a stable vesicular layer without breaking upon contact with the gold sensor surface; neither undergo any conformational change when achieving a "critical" concentration.

The SPR signals obtained for the vesicle deposition also present a monotonic increase of signal until reaching a stable plateau. Absolute values of saturation for all CTAB-Chol quatsomes were very similar. On the other hand, DOPC-Chol liposomes presented qualitatively very similar deposition curve, but with lower values indicating that less material was deposited in this case. Thus, SPR sensograms support the conclusions drawn from the analysis of QCM-D data. Indeed, vesicles interact with the sensor surface and accumulate steadily until full saturation of the sensor is achieved.

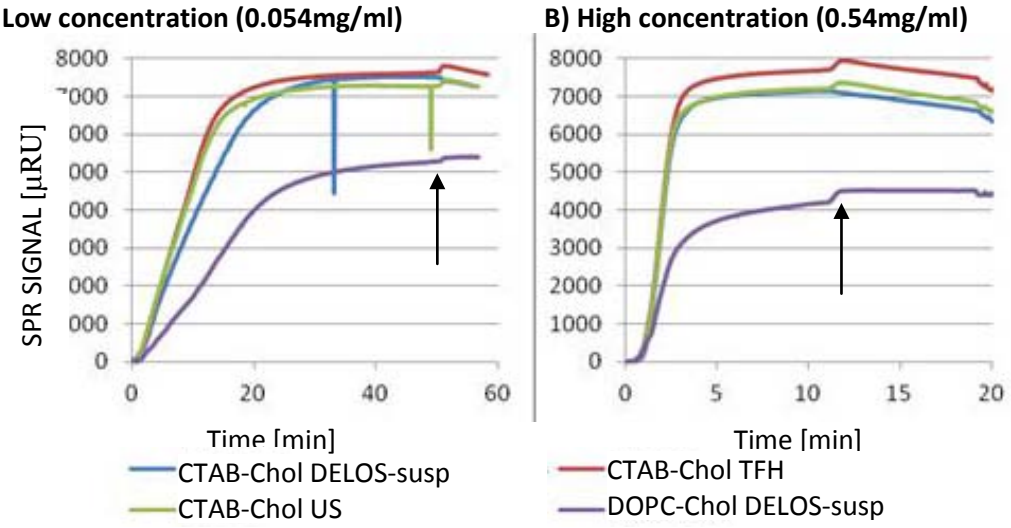

Figure 1.19 SPR sensograms obtained during deposition of CTAB-Chol quatsomes prepared using three different methodologies and DOPC-Chol liposomes formed by DELOS-susp. A) Low concentration of lipids (0.054mg/ml) B) High concentration of lipids (0.54 mg/ml). For more details see Section A.4 ("Surface Plasmon Resonance"). Arrow indicates injection of buffer solution to promote of vesicle desorption.

More details about data acquisition with these techniques can be found in Sections A.3 ("Quartz Crystal Microbalance with Dissipation (QCM-D)") and A.4 ("Surface Plasmon Resonance").

1.3.3. Frequency vs. Dissipation (F/D): deposition trajectories analysis

Figure 1.20.A shows examples of $\Delta D/\Delta F$ trajectories calculated for various QCM-D overtones originating from the experimental measurements described in the previous Section. In Figure 1.20.B trajectories for the same, 3rd, overtone but from different systems are juxtaposed. It is worth noting that data obtained for lower concentration of vesicles is more

trustworthy. This is due to the fact that curves for low concentration of vesicles have more valuable data points (see Figure 1.18).

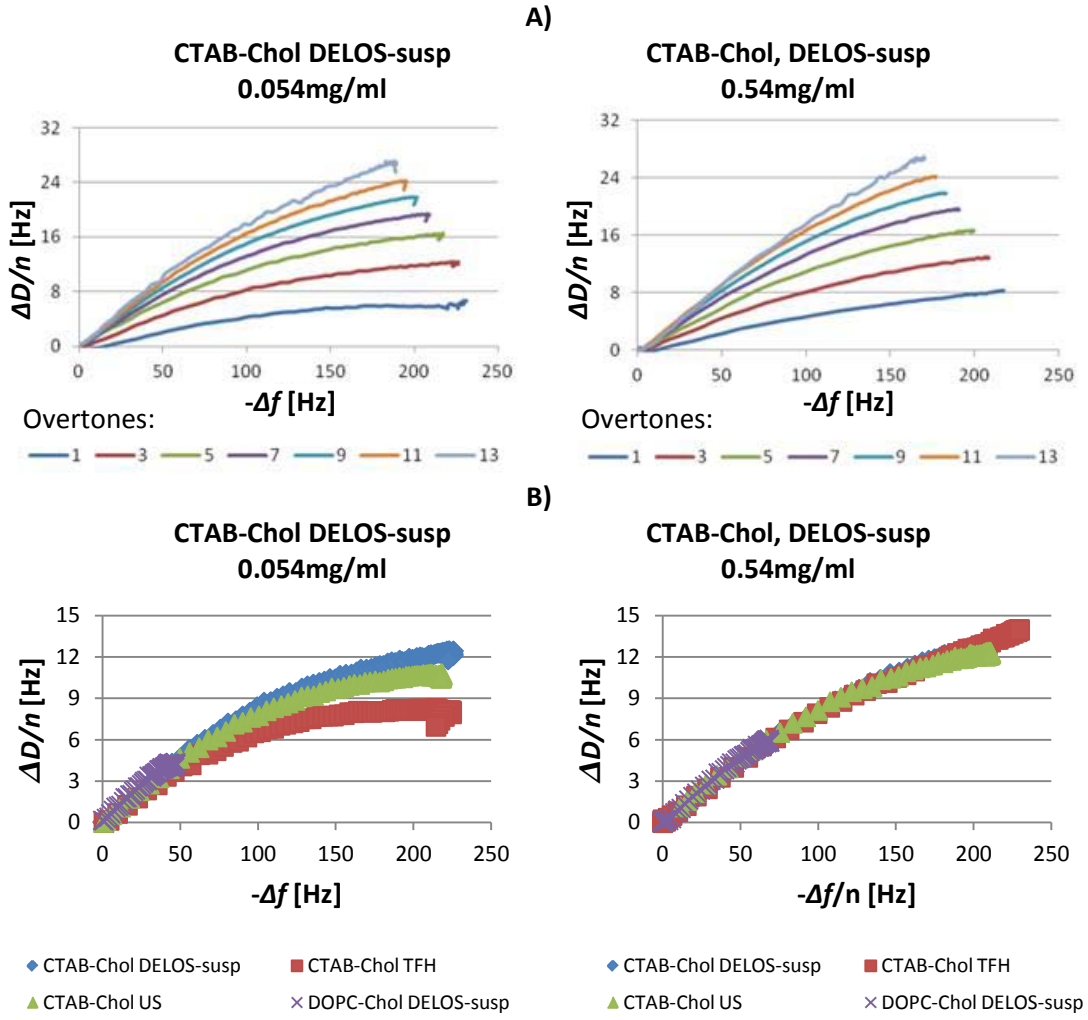

Figure 1.20 Deposition "fingerprint" plots. A) Trajectories for different overtones of the same experiment (vesicle type and concentration) B) 3-rd overtone trajectories of experiments from different vesicular systems.

The resemblances of the deposition "fingerprints" obtained for quatsomes from all preparation methodologies are indicating that in those vesicular systems the deposition mechanism and therefore dissipation/frequency ratio is similar during the whole process. Therefore we can assume, that the mechanical properties will be similar for all of them. This is especially visible for small values of both frequency and dissipation – that is in the first instants of deposition when the first vesicles arrive to the surface. Only vesicles formed by TFH present a slightly different trajectory for higher $-\Delta f$ values. This region describes later stages of vesicular layer formation when the sensor surface is fairly filled and close to saturation. Such a difference may be indicative of slight morphological differences of THF vesicles in comparison

with the vesicles prepared by DELOS-susp and US methods due to extrusion process they underwent.

In order to verify the "fingerprint" values we obtained for our vesicular systems, we have compared our results with ones previously described in the literature. In Figure 1.21 experimental data from the present work is given together with data reported by Reimhult *et al.* [51]. The F/D trajectories obtained for our vesicles are very similar to referenced data, and a reasonable agreement is achieved especially for small vesicles (110 nm) indicating similarities between the vesicles discussed here and the egg-yolk phosphatidylcholine unilamellar lipid model vesicles used in the referenced publication.

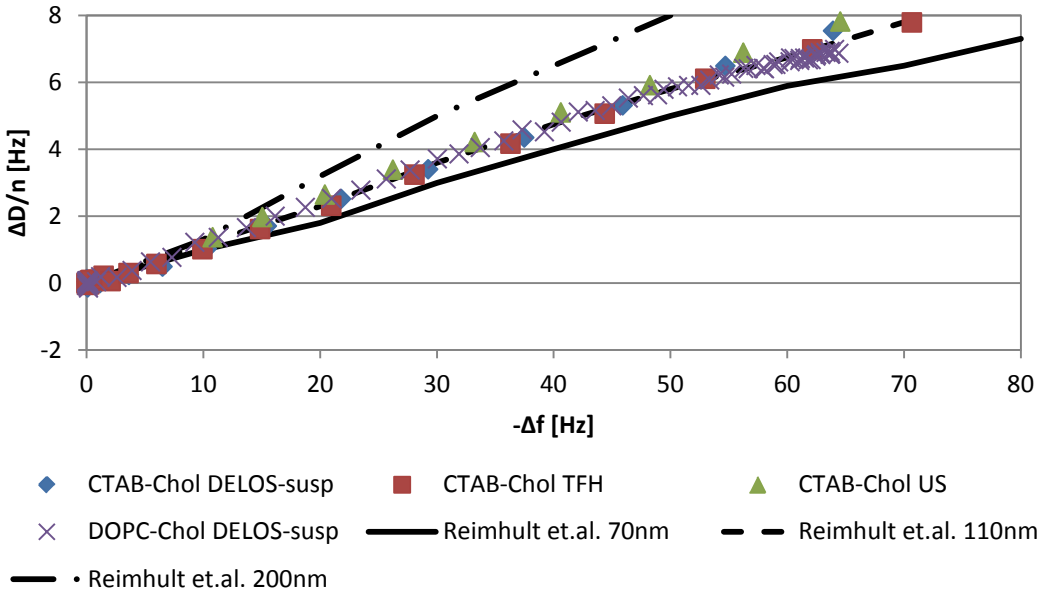

Figure 1.21 Juxtaposition of QCM-D fingerprints of the analysed systems (0.54mg/ml) and literature data for deposition of egg-yolk phosphatidylcholine unilamellar lipid vesicles from Ref. [51]. Good agreement is achieved with vesicles of 110 nm size. Other trajectories for 200nm and 70nm vesicles differ probably due to variations in vesicle size.

1.3.4. Coupling data from QCM-D and SPR

Vesicular layers have significant dissipation ($\Delta D>0$) and the acoustic mass measured by QCM-D takes into account both layer density and thickness. Thus, being not independent variables. Furthermore, the mechanism of energy dissipation in case of non - homogenous layers of separated soft particles is rather different from the mechanism occurring in a continuous and homogenous layer of adsorbates [48,67]. The measured changes in sensor frequency is not only due to the deposition of vesicles, but it takes also into account the buffer entrapped between vesicles, their hydratation layer, the buffer inside the vesicle lumen, etc.

Calculations of viscoelastic properties of deposited layers (such as viscosity or elastic modulus) based on the Voigt model in such cases are therefore burdened with errors.

However, combining QCM-D with SPR brings complementary data, which enables to calculate the thickness of material deposited. Thus, knowing the layer thickness from SPR data, one can use the QCM-D data to calculate the layer density (or *vice versa*). Since layer thickness and density are no longer dependent variables one can use both values to estimate the mechanical properties of vesicular layers basing on QCM-D data. In our case, the combination of both techniques is possible because much care was taken to conduct experiments always in the same conditions (temperature, flow rates, buffer, etc.). Moreover, the gold-covered sensors were the same in both cases as it is well known, that the nature of the substrate also strongly influences the vesicle adsorption mechanism [68].

In order to correctly calculate some properties of the vesicular layers such as density or thickness based on experimental values to further get information about its mechanical properties, an iterative protocol, similar to the one proposed by Reimhult *et al.* [45], was applied. Although we are conscious, that this methodology can be burdened with errors due to the nature of the systems we are investigating, we have decided to use this methodology for illustrative reasons. Also, as we wish to compare similar systems, systematic error would bias equally for all results presented below. Additionally such analysis will give valuable data on deposited layer properties that can be compared with other data sources such as DLS measurements or the model independent methodology suggested by Tellechea [50].

In the following Sections we will present the basic mechanisms and assumptions used for these calculations.

1.3.4.1. SPR data treatment

For the analysis of the SPR data we assume that the buffer inside and outside the vesicles has the same refractive index (n_b) as well as density and only the refractive index of the vesicle bilayer (n_s) changes locally the refractive index of the adsorbed material. Therefore, SPR measurements will detect only the mass of adsorbed lipids of the vesicle bilayer. For geometric simplification of the system we will treat the adsorbed vesicular layer as a continuous and homogenous layer that occupies a fraction *f* of the flat gold sensor surface. We will also assume that the thickness of the layer is the same as the thickness of the adsorbed vesicles, d (quatsomes or liposomes). This approach is widely used for the interpretation of data for vesicle layers with optical sensors [69,70] However, it is important to note that these values

may differ from the real ones, due to possible changes of geometry of the vesicles, heterogeneity of the layer, bilayer imperfections etc. (see Figure 1.22).

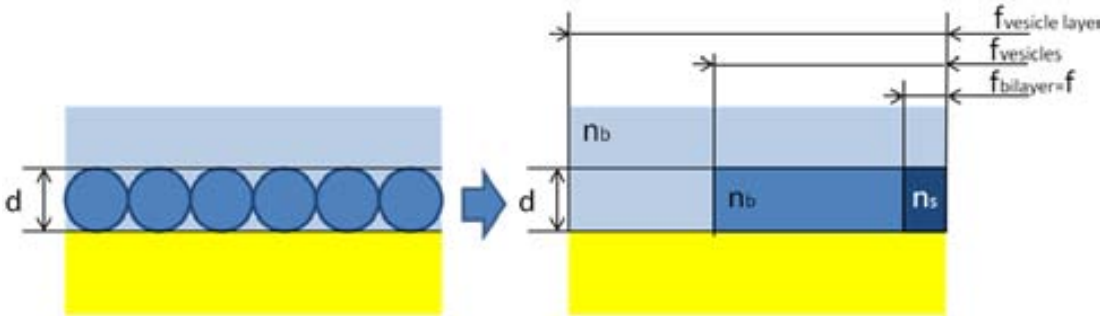

Figure 1.22 Schematic view of adsorbed vesicles layer on gold. Ideal layer and ways of treating it.

Given that the layer thickness *d* changes, plasmon resonance angle $\Delta\Theta$ recorded by the SPR spectrometer can be used to calculate the change of refractive index Δn of a thin layer deposited directly on the optic sensor [45,70]:

$$\boldsymbol{\Delta n = \kappa \frac{\Delta\Theta}{1-e^{\left(\frac{-2d}{l_{decay}}\right)}}} \qquad \text{EQ. 8}$$

Where κ is the sensitivity factor of the instrument, *d* is the thickness of the adsorbed layer and l_{decay} is the decay length of evanescent field. The value of κ was estimated to be 970250 μRU as found by calibrating the change of SPR response using different solutions of EtOH mixed in MiliQ water of known refractive index (method according to Reference [45]). For more details see Section A.5 ("Origin of values used for iterative protocol for coupling SPR and QCM-D data"). The decay length of evanescent field l_{decay} is defined as:

$$\boldsymbol{l_{decay} = \frac{\lambda}{2\pi}\sqrt{\frac{\epsilon_{r,Au}+\epsilon_{r,m}}{\epsilon_{r,m}^{\,2}}}} \qquad \text{EQ. 9}$$

Where λ is wavelength of the instrument, $\epsilon_{r,m}$ is the dielectric constant of the medium and ϵ_r the real part of complex refractive index of gold for a given wavelength. The values used for our calculations are as follow:

- λ is 780 nm according to the SPR equipment manual (model SR7000DC, Reichert)
- Since $\epsilon_{r,m}=n_s^2$ we have measured the value of n_s with a refractometer. The measured value is n_s=1.339, and therefore $\epsilon_{r,m}$ = 1.79
- ϵ_r for 780 nm was established to be -22.95 according to Reference [71]

It is worth noting, that the value of n_s measured with the refractometer is close to the predicted value of refractive index of 10.8% EtOH in water (1.3386) according to data from Reference [72]. For these values l_{decay} results in 318 nm. More details about the origin of these

values can be found in Section A.5 (“Origin of values used for iterative protocol for coupling SPR and QCM-D data”).

The absolute value of effective refractive index of an adsorbed layer can be calculated as follows:

$$\boldsymbol{n_{layer} = n_s + \Delta n} \qquad \text{EQ. 10}$$

The optical mass of absorbed material on a substrate is related to the refractive index and can be calculated by the modified Lorenz-Lorenz equation [73] with:

$$\boldsymbol{m_{\Delta n} = \frac{3d(n_{layer}{}^2 - n_s^2)}{(n_{layer}{}^2 + 2)[r(n_s^2 + 2) - v(n_s^2 - 1)]}} \qquad \text{EQ. 11}$$

Where *r* is the specific refractivity of the bilayer and *v* is the partial specific volume and it is equal to the inverse of the density. Based on geometrical considerations and data from other characterization techniques (DLS) *v* was calculated to be 0.8558 ml/g and the value of *r* used in further calculation was 0.304 ml/g. For more details see Section A.5 (“Origin of values used for iterative protocol for coupling SPR and QCM-D data”). For calculations we have assumed, that the density of the bilayer in the vesicle layer is the same as the density of the bilayer of the vesicle not adhered to the surface.

1.3.4.2. QCM-D data treatment

Data of frequency and dissipation shifts from QCM-D measurements are fitted (see Figure 1.18) assuming the Voigt viscoelastic model for a deposited layer [70]. Calculations are preformed using the QTools software package (a generous gift from Dr Ralf Richter, head of research laboratory, where the experiments were conducted). As fitting parameters this program uses the bulk buffer viscosity η_S and the density ρ_S. Values used for this purpose are 0.0014192 kg/ms and 983.8 kg/m^3, respectively. More details are available in Section A.5 (“Origin of values used for iterative protocol for coupling SPR and QCM-D data”).

1.3.4.3. Iterative protocol for coupling SPR and QCM-D data

The fitting algorithm uses layer density $\rho_{effective}$ and layer thickness $d_{effective}$ as parameters. However, as mentioned before, in our case, where dissipation is not negligible (D>0), these are not independent variables. Thus, in order to calculate these values, an iterative calculation process has been applied. A schematic illustration of the iterative calculations is presented in Figure 1.23.

To initiate iterations, we first must assume a reasonable value of $d_{effective}$ based on the size of vesicles measured by DLS, as explained in Section A.5 ("Origin of values used for iterative protocol for coupling SPR and QCM-D data"). We will use this value as a fixed parameter in order to fit the QCM-D data with the QTools software choosing the Voigt model mode. From the fitted data we obtain the effective density $\rho_{effective}$. With such values, the acoustic mass m_{Voigt} absorbed on the substrate can be calculated [45] using:

$$\boldsymbol{m_{Voigt} = d_{effective}\rho_{effective}} \qquad \text{EQ. 12}$$

Taking into account Eq. 11 and assuming that $d=d_{effective}$, the updated value of $\rho_{effective}$ was approximated [45] to:

$$\boldsymbol{\rho_{effective} = \frac{m_{Voigt}}{\frac{m_{\Delta n}}{\rho_B}+\frac{(m_{Voigt}-m_{\Delta n})}{\rho_S}}} \qquad \text{EQ. 13}$$

Then, the new value of $\rho_{effective}$ is used to fit the QCM-D data using the Voigt model once again, but this time as a fixed parameter, and from the new fit an updated effective thickness $d_{effective}$ is obtained. Based on SPR data and applying equations Eq. 11 and Eq. 13, the values of $m_{\Delta n}$ and $\rho_{effective}$, are found respectively. Finally, a new value of d was calculated from Eq. 14:

$$\boldsymbol{d = \frac{m_{Voigt}}{\rho_{effective}}} \qquad \text{EQ. 14}$$

With this new value of layer thickness d the procedure is let to iterate until values d and $d_{effective}$ converge.

Finally, in the last step (Figure 1.23), the values of thickness and density obtained from the iterative calculation are used to fit the QCM-D experimental data with the QTools software assuming Voigt model, from which values of mechanical properties like viscosity and storage modulus can be reliably obtained. The data obtained from this iterative process is presented in the Section 1.3.6 ("Results and discussion of mechanical properties").

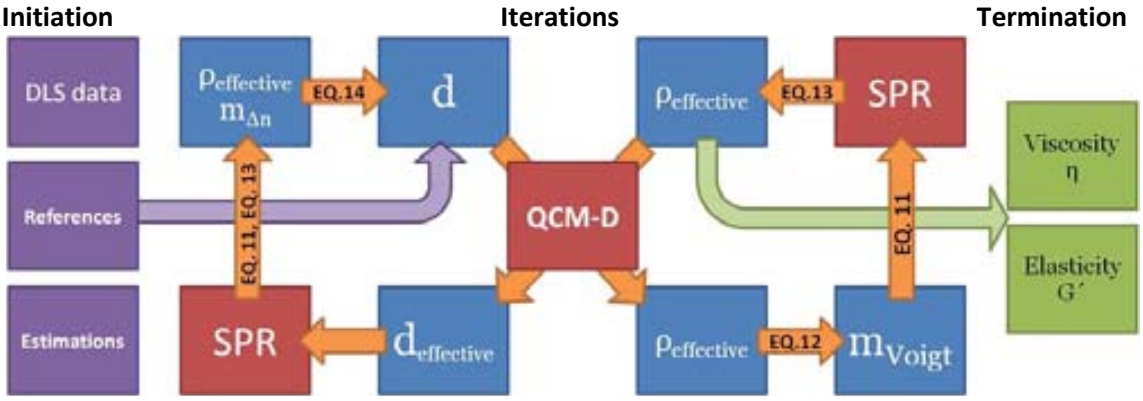

Figure 1.23 Scheme of the iterative protocol developed to calculate mechanical properties of adsorbed materials from data obtained with QCM-D and SPR techniques. The protocol consists of three steps. First, to initiate we use reference or experimental data to estimate the layer thickness *d,* as explained in the main text and in Section A.5 ("Origin of values used for iterative protocol for coupling SPR and QCM-D data"). Then, we initiate the iterative calculations to calculate density *ρ.* We proceed to calculate updated value of *d* using data generated by both experimental techniques (QCM-D and SPR). We repeat this step until these values converge. To terminate, we use both *d* and *ρ* as constants to fit QCM-D experimental data in order to calculate viscoelastic properties of vesicular layer: viscosity and elastic modulus. Colour explanation: violet – data to initiate iterative process, red – iterative calculations, that take into account experimental data from SPR and QCM-D, blue – values calculated using presented equations, green – values obtained in the last iteration of QCM-D data fitting when values *d* and $d_{effective}$ converge.

1.3.5. Model independent mass calculation based on QCM-D

Although with the iterative process explained in previous Section it is possible to get reliable data on the mass and thickness, as it has been previously explained in Section 1.2.7 ("Model independent particle size calculation based on QCM-D data"), from the QCM-D data it is also possible to use a model-independent analysis in order to calculate those values of an adsorbed vesicular layer. In order to do so, the linear portions of the *ΔD/-Δf* ratio versus *-Δf/n* curves obtained at different overtones 3 to 11 were extrapolated to find the intercept with the *-f/n* axis according to Ref. [50]. Example plots with its corresponding QCM-D input data are presented in Figure 1.24.

The found interception values multiplied by the Sauerbrey constant: 18ng cm^{-2} Hz^{-1}, see Section 1.2.5 ("QCM-D principles"), resulted in the hypothetical masses of the adsorbed vesicles (Eq. 1). The obtained mass value, divided by the density $\rho_{effective}$, calculated previously with the iterative process, as explained in Section 1.3.4.3 ("Iterative protocol for coupling SPR and QCM-D data"), for each layer gives the "Sauerbrey thickness" which describes the thickness of whole layer.

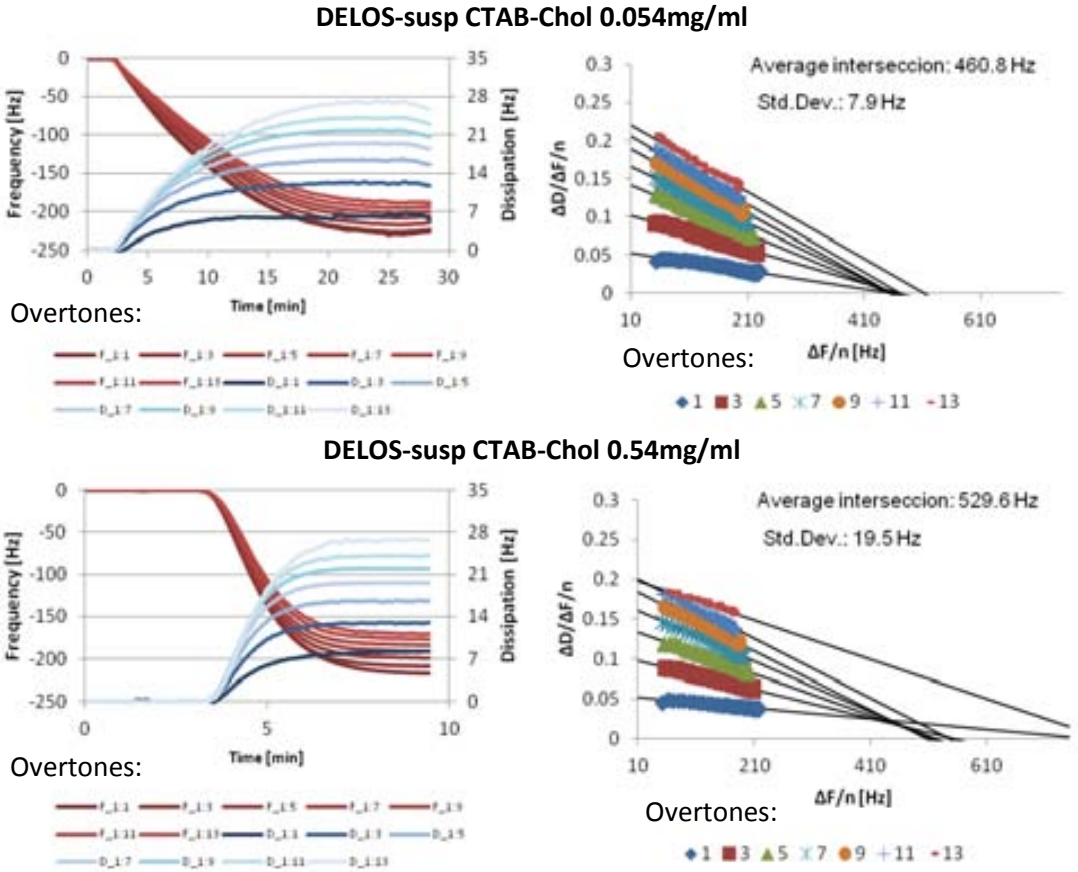

Figure 1.24 Example plots of two concentrations of CTAB-Chol vesicles. Left: original QCM-D data plots of frequency (red) and dissipation (blue). Right: Dependence of -ΔD/ΔF ratios on frequency shift for overtones 1 to 13 with linear extrapolations revealing the intercept with the ΔF /n axis. All plots are very similar, despite that the time to achieve surface saturation of signal in case of low density is ~20min whereas for high concentration it is ~5min.

The "Sauerbrey thickness" values obtained from such model-independent analysis are presented in following Section and compared with values calculated from the iterative approach.

1.3.6. Results and discussion of mechanical properties

In Figure 1.25 the calculated $d_{effective}$, from iterative calculations as explained in Section 1.2.4 ("Vesicular adsorption characterization"), the "Sauerbrey thickness" defined in Section 1.3.5 ("Model independent mass and particle size calculation based on QCM-D") and the initial vesicle sizes in the colloidal suspension, measured by DLS (see Table 1.1), are presented for all the analysed systems.

The values of layer thickness $d_{effective}$ found after the iterative process for the CTAB-Chol quatsoms are around 60-70 nm and there is no significant differences between thicknesses

($d_{efffective}$) of quatsomes obtained from different preparation routes or from two different vesicle dilutions.

As expected, vesicles are soft molecular materials and undergo deformation upon adsorption on a substrate giving place to a final vesicle layer thickness much smaller than the size of the vesicles measured with DLS in suspension. In fact, the thickness of CTAB-Chol vesicle layer is ca. 58% of the initial vesicle mean diameter in suspension for the three different preparation techniques. In case of DOPC-Chol vesicles, the final vesicular layer thickness is only ca. 50% of the initial vesicles mean diameter size.

The calculated "Sauerbrey thickness" is higher than the value of $d_{effective}$ for all the quatsomes (CTAB-Chol) but is equal or lower than the $d_{effective}$ values for the liposomes (DOPC-Chol) as depicted in Figure 1.25. This can be attributed to the difference in internal interaction between molecules that form bilayers in quatsomes or liposomes. Lower rigidity of liposomes may be the reason for underestimation of values of "Sauerbrey thickness" in comparison with $d_{effective}$.

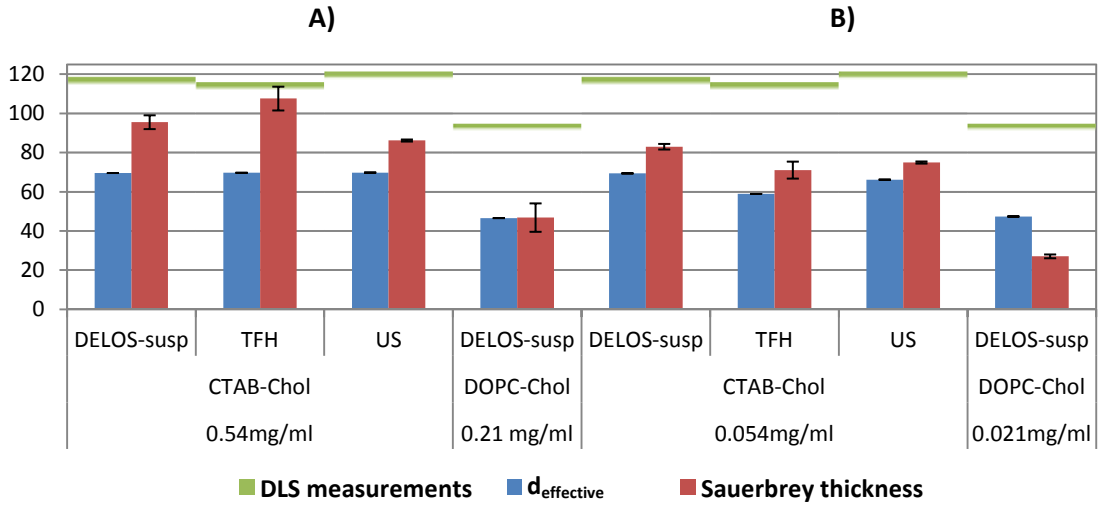

Figure 1.25 Comparison of layer thicknes: blue - thickness calculated by iterative protocol $d_{effective}$, red - Sauerbrey height, green - size of vesicles reported by DLS measurements (see Table 1.1). CTAB-Chol quatsomes and DOPC-Chol liposomes. Results for both concentrations: high (A) and low (B) are very similar.

It is worth noting that the data obtained for lower concentration of vesicles is more trustworthy, as there are more data points gathered by QCM-D during the deposition. This is due to the fact, that it takes longer for the sensor surface to reach the saturation (see Figure 1.18 and Figure 1.19) and therefore the subsequent data fitting during the iterative protocol has a better quality. Therefore, differences between Sauerbrey thickness and $d_{effective}$ are smaller in case of more diluted vesicle suspensions.

The thickness of vesicle layer calculated by the presented iterative process is in the range of 60-70 nm and 40-50 nm for CTAB-Chol and DOPC-Chol, respectively. The density obtained from iterative calculations for all cases is close to the density of the buffer ~1000kg/m^3 as presented in Table 1.2. Based on the DLS data regarding the size of the vesicles in bulk (suspension) we can state that CTAB-Chol vesicles are much more rigid than DOPC-Chol because vesicles undergo smaller deformation upon adsorption (see Figure 1.26).

Table 1.2 Viscoelastic properties of quatsomes layer calculated via iterative fitting of SPR and QCM-D data with the Voigt model.

Vesicle type	**CTAB-Chol**			**DOPC-Chol**	**CTAB-Chol**			**DOPC-Chol**
Concentration of surfactants [mg/ml]	0.54			0.21	0.054			0.021
Preparation route	**DELOS-susp**	**TFH**	**US**	**DELOS-susp**	**DELOS-susp**	**TFH**	**US**	**DELOS-susp**
Total layer density ρ [kg/m^3]	998	999	998	1018	972	1001	998	1019
Viscosity η [kg/ms · 10^{-3}]	3.95	4.75	4.06	2.23	3.97	5.61	4.43	1.84

The higher rigidity of the CTAB-Chol vesicles is confirmed with the viscosity values calculated based on experimental data and calculated with iterative protocol. The DOPC-Chol liposome layer present lower values of viscosity, than the CTAB-Chol quatsomes prepared using the three different methodologies indicating, that they are less deformed and therefore less constrained layer.

However, our methodology failed to calculate reasonable values of elastic properties (G') of vesicular layers as the obtained results varied over 4 orders of magnitude. This fact is beyond our capacities of interpretation. We attribute this outcome to the used approximations that inaccurately model the vesicular layers of our vesicles.

Such extensive description of a vesicle layer can be supplemented by additional data. For example, knowing masses and densities of adsorbed bilayers ($m_{\Delta n}$, ρ_S) and vesicle layers (m_{Voigt}, ρ_B) it is possible to calculate the partial volumetric occupancy of lipidic bilayer $f_{bilayer}$ in the vesicle layer (see Figure 1.22). We have found $f_{bilayer}$ values to be ~7.9% and ~4.4% for CTAB-Chol and DOPC-Chol vesicles respectively. Those values fit with viscosity data, as we can expect, that vesicular layer richer in surfactant material is more viscous.

The apparent superiority of quatsomes over liposomes can be attributed to the unique properties of quaternary ammonium surfactants and steroles, that form stable bilayers only when mixed in equimolar proportions. Various methods can facilitate achievement of this

state. Also fingerprint analysis evidences once again that all the systems are very similar independently of the preparation route. Therefore our findings support conclusions from Reference [62].

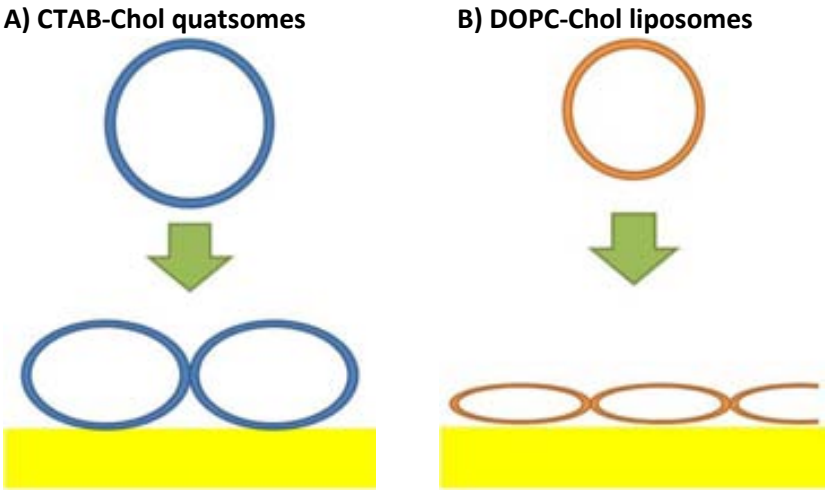

Figure 1.26. Comparison of deformation of vesicles upon deposition on gold. CTAB-Chol quatsomes behave as much more rigid objects than DOPC-Chol liposomes. Sizes of vesicles before and after deposition are scaled according to data from Figure 1.25.

1.3.7. Dynamic considerations of the model-independent analysis

Up to now no one had paid attention to the possibility of extracting dynamic information from the model-independent analysis according to the Tellechea model [50]. However, we have noticed, that this approach enables to study the process of layer formation. In order to do so, instead of approximating the whole linear range we have splitted it into ranges of frequencies (or times) and then the same methodology is applied to each portion of data separately. As it can be seen in Figure 1.27 each range give different intersection point corresponding to different masses and different “Sauerbrey thicknesses” of vesicular layers.

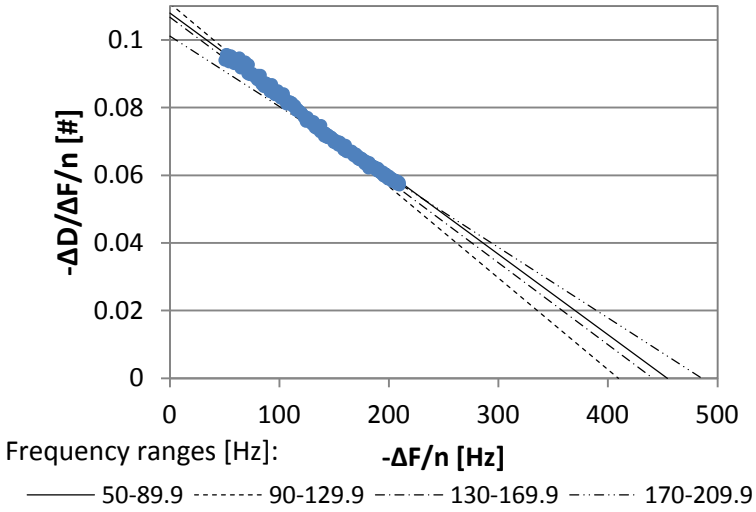

Figure 1.27 Representative example of frequency splitting into ranges for Tellechea model analysis. The 3-rd overtone of QCM-D data (blue points) for adsorption of 0.054mg/ml CTAB-Chol vesicles (DELOS-susp) was spitted into 4 ranges: 50-89.9 Hz, 90-129.9 Hz, 130-169.9 Hz and 170-209.9 Hz, and approximated with straight lines (black lines) to obtain different intersection points.

Repeating this operation for all of the overtones we can calculate the "Sauerbrey thickness" for the different stages of vesicular layer formation as depicted in Figure 1.28.

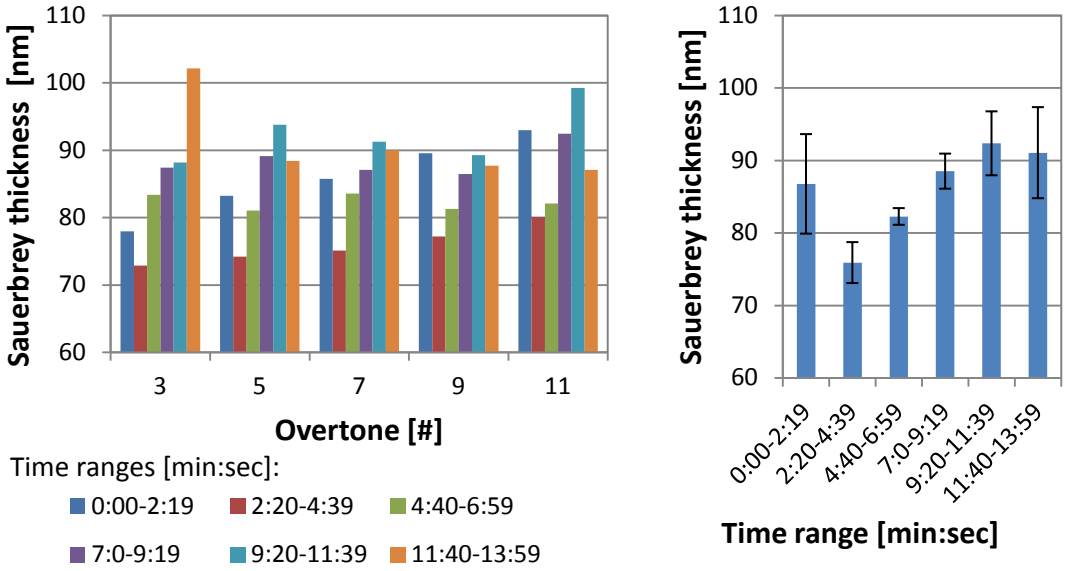

Figure 1.28 Analysis of overtones arbitrarily split in time ranges. Deposition of vesicles that lasted 14 minutes was arbitrarily divided into 6 periods of 140 seconds each. "Sauerbrey thickness" was calculated, for each overtone and each range of frequencies (left panel). As we can see, a common pattern emerges. After averaging "Sauerbrey thickness" for each overtone (right panel), the pattern becomes even better distinguishable. Values are relatively high at the beginning, in the next period they decrease significantly, to subsequently increases steadily over period of approximately 8 minutes to finally stabilize.

The obtained data for all overtones is consistent. These data suggest that at the beginning of the adsorption process vesicles are less flattened with heights of the vesicular layer close to the size measured by DLS found for vesicles in the colloidal suspension. After this initial stage, the thickness of the vesicle layer decrease getting a minimum value after 3 - 5 minutes after injection which is indicative for flattening of vesicles. This is possible, since they have more space to interact with the substrate. After this stage, as the surface is being filled with more vesicles they have less space to deform and thicknesses of the vesicle layer increases again to reach the initial values. This can be attributed to a deformation of vesicles in the vertical direction in order to fill the surface with the maximum number of vesicles (Figure 1.29).

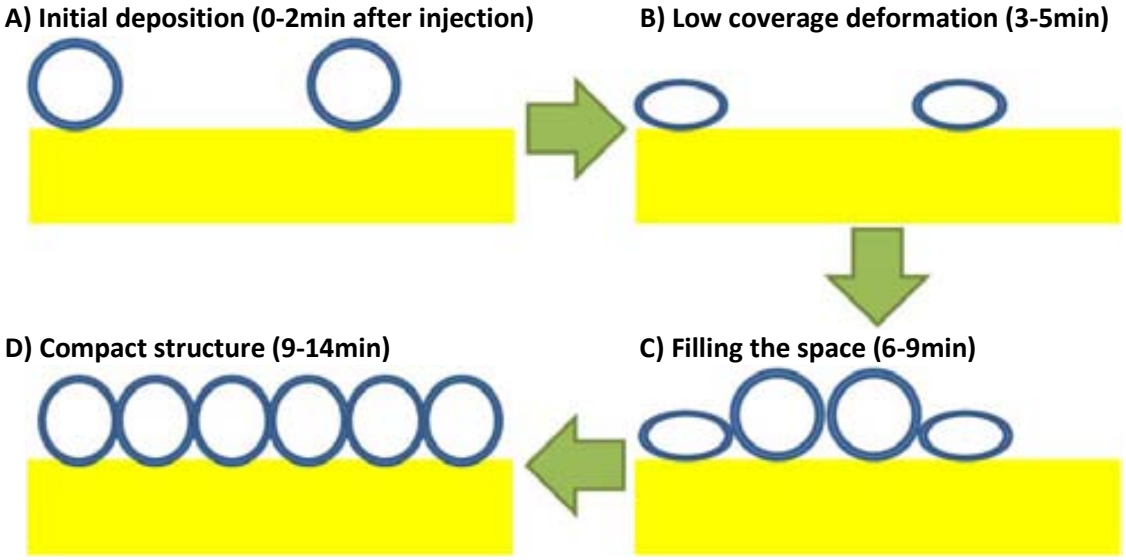

Figure 1.29. Scheme of vesicle deformational changes upon deposition on gold according to data obtained from Tellechea model considerations. A) Vesicles adsorb and in initial instances of data acquisition their original size is captured by QCM-D. B) With time vesicles deform (flatten) resulting lower values of averaged thickness of layer. C) New vesicles do not have enough space to accommodate after deposition and as a result average height of deposited vesicular layer increases.

This type of behavior might be explained by the type of interactions that are predominant in each stage of vesicle deposition. In the initial instances the vesicle-substrate interactions are dominant, while in later stages vesicle-vesicle interactions overweight them. Further evidences are needed in order to support or deny this hypothesis, but such analysis is beyond the scope of this Thesis.

1.4. Conclusions

In this work we have investigated the process of vesicles absorption on gold using QCM-D and SPR techniques. Two types of vesicles were investigated: CTAB-Chol quatsomes and DOPC-Chol liposomes in order to investigate the influence of their internal structure on their mechanical properties. Also three routes of quatsomes production were applied in order to compare the influence of the preparation methodology on the vesicle´s properties. In particular:

1. We have determined that vesicles from all the investigated systems form stable vesicular layers on gold. Furthermore, using model-independent analysis we have obtained the "Sauerbrey thickness" at different times after injection and we have found that vesicles deform upon deposition and these deformations depend on the surface coverage.
2. We have implemented a data treatment procedure that enabled us joining data from QCM-D and SPR techniques and calculate reliable mechanic properties of deposited vesicular layers.
3. This treatment enabled us also to calculate the mechanical properties of the deposited material and a subsequent comparison between vesicles obtained from various methodologies. Analysing these values we can state that from the mechanical standpoint there is no difference between vesicles obtained by different reparation routes for the three methodologies used. It seems that once the two components of the CTAB-Chol vesicles get its optimal internal structure, independently of the applied methodology, this singular supramolecular structure is the one that determines its mechanical properties.
4. Finally, we have found that DOPC-Chol liposomes are less viscous and deform more upon adsorption than CTAB-Chol quatsomes. This observation is a clear evidence of the influence of the internal supramolecular structure of the bilayer on the mechanical properties of vesicles.

1.5. Bibliography

[1] Janmey P.A., Kinnunen P.K.J. “Biophysical properties of lipids and dynamic membranes”; *Trends in Cell Biology* **2006**, Vol. 16(10), 538-546

[2] Chernomordik L.V., Kozlov M.M. "Mechanics of membrane fusion"; *Nature Structural & Molecular biology* **2008**, Vol. 15, 675-683

[3] Wenk M.R. “The emerging field of lipidomics”; *Nature Reviews Drug Discovery* **2005**, Vol. 4(7), 594-610

[4] Ganta S., Devalapally H., Shahiwala A., Amiji M. “A review of stimuli-responsive nanocarriers for drug and gene delivery”; *Journal of Controlled Release* **2008**, Vol. 126(3), 187-204

[5] Radmacher M., Fritz M., Kacher C.M., Cleveland J.P., Hansma P.K. “Measuring the viscoelastic properties of human platelets with the atomic force microscope”; *Biophysical Journal* **1996**, Vol. 70, 556-567

[6] Neidle S. “Oxford handbook of nucleic acid structure”; *Oxford Univ. Press* **1999**, Oxford (U.K.)

[7] Grantcharova V., Alm E.J., Baker D., Horwich A.L. “Mechanisms of protein folding”; *Current Opinion in Structural Biology* **2001**, Vol. 11, 70-82

[8] Desiraju G.R. “Crystal engineering: The design of organic solids”; *Elsevier* **1989**, New York (U.S.A.)

[9] Evans D.F., Wennerstrom H. “The colloidal domain: Where physics, chemistry, biology, and technology meet”; *Wiley* **1999**, New York, (U.S.A.)

[10] Thomas E.L. “Materials science: Enhanced: The ABCs of self assembly”; *Science* **1999**, Vol. 286, 1307

[11] Kumar A., Abbott N.L., Kim E., Biebuyck H.A., Whitesides G.M. “Patterned self assembled monolayers and mesoscale phenomena”; *Accounts of Chemical Research* **1995**, Vol. 28, 219-226

[12] Jones M.N., Chapman D. “Micelles, monolayers and biomembranes”; *Wiley-Liss* **1995**, New York (U.S.A.)

[13] Tanford C. “The hydrophobic effect: Formation of micelles and biological membranes”; *Wiley* **1980**, New York (U.S.A.)

[14] Ekwall P., Mandell L., Fontell K. “Solubilization in micelles and mesophases and transition from normal to reserved structures”; *Molecular Crystals and Liquid Crystals* **1969**, Vol. 8, 157-213

[15] Wennerström H., Lindman B. “Micelles. Physical chemistry of surfactant association”; *Physics Reports* **1979**, Vol. 52, 1-86

[16] Tu R.S., Tirrell M. “Bottom-up design of biomimetic assemblies”; *Advanced Drug Delivery Reviews* **2004**, Vol. 56, 1537-1563

[17] Chevalier Y., Zemb T. “The structure of micelles and microemulsions”; *Reports on Progress in Physics* **1990**, Vol. 53, 279-371

[18] Israelachvili J.N., Mitchell D.J., Ninham B.W. “Theory of selfassembly of hydrocarbon amphiphiles into micelles and bilayers”; *Journal of the Chemical Society-Faraday Transactions II* **1976**, Vol. 72, 1525-1568

[19] Torchilin V.P. “Recent advances with liposomes as pharmaceutical carriers”; *Nature Reviews Drug Discovery* **2005**, Vol. 4,145-160

[20] Storm G., Crommelin D.J.A. “Liposomes: quo vadis?”; *Pharmaceutical Science &Technology Today* **1998**, Vol. 1, 19-31

[21] Radmacher M., Fritz M., Kacher C.M., Cleveland J.P., Hansma P.K. “Measuring the Viscoelastic Properties of Human Platelets with the Atomic Force Microscope”; *Biophysical Journal* **1996**, Vol. 70, 556-567

[22] Olson F., Hunt C.A., Szoka F.C., Vail W.J., Papahadjopoulos D. “Preparation of liposomes of defined size distribution by extrusion through polycarbonate membranes”; *Biochimica Et Biophysica Acta* **1979**, Vol. 557, 9-23

[23] Cano-Sarabia M., Ventosa N., Sala S., Patino C., Arranz R., Veciana J. “Preparation of uniform rich cholesterol unilamellar nanovesicles using CO2 expanded solvents” *Langmuir* **2008**, Vol. 24, 2433-2437

[24] Cano-Sarabia M. “Preparación de materiales moleculares nanoparticulados y dispersos vesículas y microemulsionesempleando fluidos comprimidos”; *PhD Thesis* **2009** (July)

[25] (a) Ventosa N., Sala S., Veciana J., Torres J., Llibre J. “Depressurization of an expanded liquid organic solution (DELOS): A new procedure for obtaining submicronor micronsized crystalline particles”; *Crystal Growth & Design* **2001**, Vol. 1, 299-303; (b) Munto M., Gomez-Segura J., Campo J., Nakano M., Ventosa N., Ruiz-Molina D., Veciana J. “Controlled crystallization of Mn12 single molecule magnets by compressed CO2 and its influence on the magnetization relaxation”; *Journal of Materials Chemistry* **2006**, Vol. 16, 2612-2617; (c) Sala S., Elizondo E., Moreno E., Calvet T., Cuevas - Diarte M.A., Ventosa N., Veciana J. “Kinetically driven crystallization of a pure polymorphic phase of stearic acid from CO2expanded solutions”; *Crystal Growth & Design* **2010**, Vol. 10, 1226-1232;

Munto M., Ventosa N., Veciana J. “Synergistic solubility behaviour of a polyoxyalkylene block copolymer and its precipitation from liquid CO2expanded ethanol as solid microparticles”; *Journal of Supercritical Fluids* **2008**, Vol. 47, 290-295; (d) Ventosa N., Sala S., Veciana J. “DELOS process: a crystallization technique using compressed fluids 1. Comparison to the GAS crystallization method”; *Journal of Supercritical Fluids* **2003**, Vol. 26, 33-45; (e) Sala S., Gimeno M., Cano M., Munto M., Elizondo E., Ventosa N., Veciana J. “DELOS compressed fluid technology for the preparation of micro and nanoparticulate molecular materials: Main features and scaleup”; *Afinidad* **2007**, Vol. 64, 415-419

[26] Yang Y.T., Liao J.D., Lee Y.L., Chang C.W., Tsai H.J. “Ultra-thin phospholipid layers physically adsorbed upon glass characterized by nano-indentation at the surface contact level”; *Nanotechnology* **2009**, Vol. 20, 195702

[27] Yang Y.T., Liao J.D., Lin, C.C.K., Chang C.T., Wang S.H., Ju M.S "Characterization of cholesterol-depleted or -restored cell membranes by depth-sensing nano-indentation"; *Soft Matter* **2012**, Vol. 8(3), 682-687

[28] Hoh J.H., Schoenenberger C.A. “Surface morphology and mechanical properties of MDCK monolayers by atomic force microscopy”; *Journal of Cell Science* **1994**, Vol. 107, 1105-1114

[29] (a) Butt H.J., Cappell B., Kappl M. "Force measurements with the atomic force microscope: Technique, interpretation and applications"; *Surface Science Reports* **2005**, Vol. 59(1–6), 1–152; (b) ButtH.J., Awizio A.K. "Chapter 7 Atomic Force Microscopy of Lipid Bilayers", "Advances in Planar Lipid Bilayers and Liposomes", *Elsevier Inc.* **2006**, Vol. 3

[30] Honerkamp-Smith A.R., Woodhouse F.G., Kantsler V., Goldstein R.E. “Membrane Viscosity Determined from Shear-Driven Flow in Giant Vesicles”; *Phys. Rev. Lett.* **2013**, Vol. 111, 038103

[31] Image from http://soft.ifs.hr/procurement-contract-signed/ 29/09/2014

[32] Wegener J., Janshoff A., Steinem L. “The quartz crystal microbalance as a novel means to study cell-substrate interactions in situ”; *Cell Biochemistry and Biophysics* **2001**, Vol. 34, 121-151

[33] Richter R.P., Bérat R., Brisson A.R. “Formation of Solid-Supported Lipid Bilayers: An Integrated View”; *Langmuir* **2006**, Vol. 22(8), 3497–3505

[34] Lind T.K., Cardenas, M., Wacklin, H.P. "Formation of supported lipid bilayers by vesicle fusion: Effect of deposition temperature"; *Langmuir* **2014**, Vol. 30(25), 7259-7263

[35] Gutman J., Kaufman Y., Kawahara K., Walker S.L., Freger V., Herzberg, M. "Interactions of glycosphingolipids and lipopolysaccharides with silica and polyamide surfaces: Adsorption and viscoelastic properties"; *Biomacromolecules* **2014**, Vol. 15(6), 2128-2137

[36] Tabaei S.R., Choi J.H., Haw Zan G., Zhdanov V.P., Cho N.-J. "Solvent-assisted lipid bilayer formation on silicon dioxide and gold"; *Langmuir* **2014**, Vol. 30(34), 10363-10373

[37] Tan M.C., Matsuoka S., Ano H., Ishida H., Hirose M., Sato F., Sugiyama S., Murata M. "Interaction kinetics of liposome-incorporated unsaturated fatty acids with fatty acid-binding protein 3 by surface plasmon resonance"; *Bioorganic and Medicinal Chemistry* **2014**, Vol. 22(6), 1804-1808

[38] Makishi S., Shibata T., Okazaki M., Dohno C., Nakatani K. "Modulation of binding properties of amphiphilic DNA containing multiple dodecyl phosphotriester linkages to lipid bilayer membrane"; *Bioorganic and Medicinal Chemistry Letters* **2014**, Vol. 24(15), 3578-3581

[39] Olguin Y., Carrascosa L.G., Lechuga L.M., Young M. "The effects of lipids and surfactants on TLR5-proteoliposome functionality for flagellin detection using surface plasmon resonance biosensing"; *Talanta* **2014**, Vol. 126, 136-144

[40] Reimhult E., Zach M., Hook F., Kasemo B. "A Multitechnique Study of Liposome Adsorption on Au and Lipid Bilayer Formation on SiO2"; *Langmuir* **2006**, Vol. 22, 3313-3319

[41] Sun L., Svedhem S., Akerman, B. "Construction and modeling of concatemeric DNA multilayers on a planar surface as monitored by QCM-D and SPR"; *Langmuir* **2014**, Vol. 30(28), 8432-8441

[42] Coutable A., Thibault C., Chalmeau J., Franciois J.M., Vieu C., Noireaux V., Trevisiol E. "Preparation of tethered-lipid bilayers on gold surfaces for the incorporation of integral membrane proteins synthesized by cell-free expression"; *Langmuir* **2014**, Vol. 30(11), 3132-3141

[43] Edvardsson M., Svedhem S., Wang G., Richter R., Rodahl M., Kasemo B. "QCM-D and Reflectometry Instrument: Applications to Supported Lipid Structures and Their Biomolecular Interactions"; *Anal. Chem.* **2009**, Vol. 81, 349–361

[44] Höök F., Kasemo B., Nylander T., Fant C., Sott K., Elwing H. "Variations in Coupled Water, Viscoelastic Properties, and Film Thickness of a Mefp-1 Protein Film during Adsorption and Cross-Linking: A Quartz Crystal Microbalance with Dissipation Monitoring, Ellipsometry, and Surface Plasmon Resonance Study"; *Anal. Chem.* **2001**, Vol. 73(24), 5796–5804

[45] Reimhult E., Larsson C., Kasemo B., Hook F. “Simultaneous Surface Plasmon Resonance and Quartz Crystal Microbalance with Dissipation Monitoring Measurements of Biomolecular Adsorption Events Involving Structural Transformations and Variations in Coupled Water”; *Anal. Chem.* **2004**, Vol. 76, 7211-7220

[46] Ward M.D., Buttry D.A. "In situ interfacial mass detection with piezoelectric transducers"; *Science* **1990**, Vol. 249(4972), 1000-1007

[47] Sauerbrey G."Verwendung von Schwingquarzen zur Wägung dünner Schichten und zur Mikrowägung", *Zeitschrift für Physik* **1959**, Vol. 155(2), 206–222

[48] Reviakine I., Johannsmann D., Richter R.P. “Hearing What You Cannot See and Visualizing What You Hear: Interpreting Quartz Crystal Microbalance Data from Solvated Interfaces”; *Anal. Chem.* **2011**, Vol. 83, 8838–8848

[49] Rodahl M., Hook F., Krozer A., Brzezinski P., Kasemo B. "Quartz crystal microbalance setup for frequency and Q-factor measurements in gaseous and liquid environments"; *Review of Scientific Instruments* **1995**, Vol. 66(7), 3924-3930

[50] Tellechea E., Johannsmann D., Steinmetz N.F., Richter R.P., Reviakine I. “Model-Independent Analysis of QCM Data on Colloidal Particle Adsorption”; *Langmuir* **2009**, Vol. *25*(9), 5177–5184

[51] Reimhult E., Hook F., Kasemo B. “Vesicle adsorption on SiO2 and TiO2: Dependence on vesicle size”; *Journal of Chemical Physics* **2002**, Vol. 117, 7401-7404

[52] http://ncl.cancer.gov/

[53] Antonietti M., Forster S. “Vesicles and liposomes: A self assembly principle beyond lipids”; *Adv. Mater.* **2003**, Vol. 15(16), 1323−1333

[54] Zhang L.F., Eisenberg A. “Multiple morphologies of crew-cut aggregates of polystyrene-b-poly(acrylic acid) block-copolymers”; *Science* **1995**, Vol 268(5218), 1728−1731

[55] LoPresti C., Lomas H., Massignani M., Smart T., Battaglia G. “Polymersomes: Nature inspired nanometer sized compartments”; *J. Mater. Chem.* **2009**, Vol. 19(22), 3576−3590

[56] Discher B.M., Won Y.Y., Ege D.S., Lee J.C.M., Bates F.S., Discher D.E., Hammer D.A. “Polymersomes: Tough vesicles made from diblock copolymers” *Science* **1999**, Vol. 284(5417), 1143−1146

[57] Kukula H., Schlaad H., Antonietti M., Forster S. “The formation of polymer vesicles or “peptosomes” by polybutadieneblock-poly(L-glutamate)s in dilute aqueous solution”; *J. Am. Chem. Soc.* **2002**, Vol. 124(8), 1658−1663

[58] Fukuda H., Kawata K., Okuda H., Regen S.L. “Bilayer-forming ion-pair amphiphiles from single-chain surfactants”; *J. Am. Chem. Soc.* **1990**, Vol. 112(4), 1635−1637

[59] Kaler E.W., Herrington K.L., Murthy A.K., Zasadzinski J.A.N. “Phase-behavior and structures of mixtures of anionic and cationic surfactants”; *J. Phys. Chem.* **1992**, Vol. 96(16), 6698−6707

[60] Marques E.F. “Size and stability of catanionic vesicles: Effects of formation path, sonication, and aging”; *Langmuir* **2000**, Vol. 16(11), 4798−4807

[61] Elizondo E., Larsen J., Hatzakis N.S., Cabrera I., Bjornhorn T., Veciana J., Stamou D., Ventosa N. “Influence of the preparation route on the supramolecular organization of lipids in a vesicular system”; *J. Am. Chem. Soc.* **2012**, Vol. 134(4), 1918−1921

[62] Ferrer-Tasies L., Moreno-Calvo E., Cano-Sarabia M., Aguilella-Arzo M., Angelova A., Lesieur S., Ricart S., Faraudo J., Ventosa N., Veciana J. "Quatsomes: Vesicles Formed by Self-Assembly of Sterols and Quaternary Ammonium Surfactants"; *Langmuir* **2013**, Vol. 29(22), 6519-6528

[63] Elizondo E., Veciana J., Ventosa N. “Nanostructuring molecular materials as particles and vesicles for drug delivery, using compressed and supercritical fluids”; *Nanomedicine* **2012**, Vol. 7(9), 1391−1408

[64] Ventosa N., Cabrera I., Veciana J., Santana H., Martinez E., Berlanga J.A. “Vesicles comprising epidermal growth factor and compositions that contain them”; Patent PCT-WO **2014** 019555

[65] Cabrera I., Elizondo E., Esteban O., Corchero J.L., Melgarejo M., Pulido D., Córdoba A., Moreno E., Unzueta U., Vazquez E., Abasolo I., Schwartz S., Villaverde A., Albericio F., Royo M., García-Parajo M.F., Ventosa N., Veciana J. "Multifunctional nanovesicle-bioactive conjugates prepared by a one-step scalable method using CO2-expanded solvents"; *Nano Letters* **2013**, Vol. 13(8), 3766-3774

[66] Rodahl M., Hook F., Fredriksson C., Keller C.A., Krozer A., Brzezinski P., Voinova M., Kasemo B. “Simultaneous frequency and dissipation factor QCM measurements of biomolecular adsorption and cell adhesion” *Faraday Discuss.* **1997**, Vol. 107, 229-246

[67] Johannsmann D., Reviakine I., Richter R.P. “Dissipation in Films of Adsorbed Nanospheres Studied by Quartz Crystal Microbalance (QCM)” *Anal. Chem* **2009**, Vol. 81, 8167–8176

[68] Anderluh G., Besenicara M., Kladnik A., Lakey J.H., Macek P. “Properties of nonfused liposomes immobilized on an L1 Biacore chip and their permeabilization by a eukaryotic pore-forming toxin”; *Anal. Biochem.* **2005**, Vol. 344(1), 43–52

[69] Matsuzaki K., Murase O., Sugishita K., Yoneyama S., Akada K., Ueha M., Nakamura A., Kobayashi S. “Optical characterization of liposomes by right angle light scattering and turbidity measurement”; *Biochimica et Biophysica Acta* **2000**, Vol. 1467, 219-226

[70] Jung L.S., Campbell C.T., Chinowsky T.M., Mar M.N., Yee S.S. “Quantitative Interpretation of the Response of Surface Plasmon Resonance Sensors to Adsorbed Films”; *Langmuir* **1998**, Vol. 14, 5636-5648

[71] Innes R.A., Sambles J.R. “Optical characterisation of gold using surface plasmon-polariton”; *J. Phys. F: Met. Phys*. **1987**, Vol. 17, 277-287

[72] Lide D.R. “CRC Handbook of Chemistry and Physics”; *CRC Press* **2005**, Boca Raton (U.S.A.), internet version downloaded from: http://www.hbcpnetbase.com

[73] Cuypers P.A., Corsel J.W., Janssen M.P., Kop J.M.M., Hermens W.T., Hemkerg H.C. “The Adsorption of Prothrombin to Phosphatidylserine Multilayers Quantitated by Ellipsometry”; *The Journal of Biological Chemistry* **1983**, Vol 258, 2426-2431

2.Engineering nanoparticle-decorated surfaces for cell guidance

2.1. Objectives

In this Chapter we will investigate the use of proteic nanoparticles (NPs), named Inclusion Bodies (IBs), as a new biomaterial for the two dimensional engineering of substrates for tissue engineering. Furthermore, we will establish what is the influence of IBs structuration on the cell guidance. This main objective can be divided into the following five specific ones:

1. Optimization of the nanoparticle deposition technique to enable a selective decoration of surfaces with proteic NPs in order to obtain various geometric patterns in a reproducible way.
2. Optimization of the density of proteic nanoparticles on the surface for cell growth.
3. Study the influence of the IBs pattern geometry on cell´s proliferation, positioning, orientation and morphology.
4. Comparison of the influence of IBs derived from functional (FGF) or non functional (GFP) proteins on cell guidance.
5. Development of a new statistical method for image treatment in order to quantitatively evaluate the cell guidance on the different geometrical IBs patterns.

2.2. Introduction

Cell responses, such as positioning, migration, morphological changes, proliferation, and apoptosis, are the result of a complex network of stimuli transmitted by the extracellular matrix (ECM). Among them, mechanical (topography, internal constrains), chemical (presence and concentration of different effector molecules) and biological (influence of other cells, growth factors, and signal transducers) factors predetermine the cellular fate. Mimicking the physiological conditions and environmental topography of natural systems at the cell scale is one of the basic aims of tissue engineering and will definitely open new opportunities in regenerative medicine.

The control of cell positioning and spatial orientation is crucial in tissue engineering. It is vital especially when attempting the generation of complex structures such as aligned axonal circuits, blood vessels or stable multilayered artificial tissues [1,2]. Both biological and mechanical stimuli seem to be the best approach to the mimicry of real cell environments [3]. The use of patterned substrates permits the control of the expression of cell adhesion proteins [4], the distribution of focal adhesions [5] and the orientation of whole cells, as well as their morphological appearance [6,7]. Grooved or pitted surfaces offer valuable models offered by top-down lithography techniques, while the bottom-up surface decoration protocols with, for example, carbon nanotubes [8], nanocrystalline ceramics [9] or other nano- or microstructured materials [10,11,12] are methodologically simpler and aims to determine cell responses to their environment. Unfortunately, a further application of these approaches to *in vivo* situations is bottlenecked by methodological constraints and biocompatibility issues.

2.2.1. Surface modification for cell guidance

There are several techniques that are being applied to investigate the influence of various stimuli on cells in order to gain the necessary know-how and control over tissue culture. Among them, microcontact printing (μCP) [13] is recognized as a cost-effective, fast and versatile technique to control surface chemistry at the microscale over considerably large areas (up to hundreds of mm^2). The range of materials that can be used to cover surfaces using this method is very broad [14,15]: from self assembled monolayers (SAM´s)[16], proteins [17,18], and nucleic acids [19] to complex architectures [20] giving rise to functional surfaces [21] which are obtained by multistep protocols. Although in most cases the “ink” used in this printing procedure consists of a solution of the molecules of interest, such soft-

lithographic method can also be extended to pattern colloidal particles [22] or even bacteria [23].

The µCP technique uses a polydimethylsiloxane (PDMS) stamp with well defined geometry to transfer material ("ink") from a solution onto a substrate. Firstly, the surface of the stamp is cleaned. Then the stamp is conditioned inside the "ink" solution. During this step, the material (molecules, particles, etc.) are absorbed on the stamp surface. After this, the stamp is removed from the ink solution and it is washed to remove the excess of material. Then, it is gently pressed against the surface to be functionalized. While in contact, the material is transferred from the stamp to the substrate reacting or self-assembling on it. If successful, the final pattern reflects the geometrical features of the stamp. A schematic illustration of this process is presented in Figure 2.1.

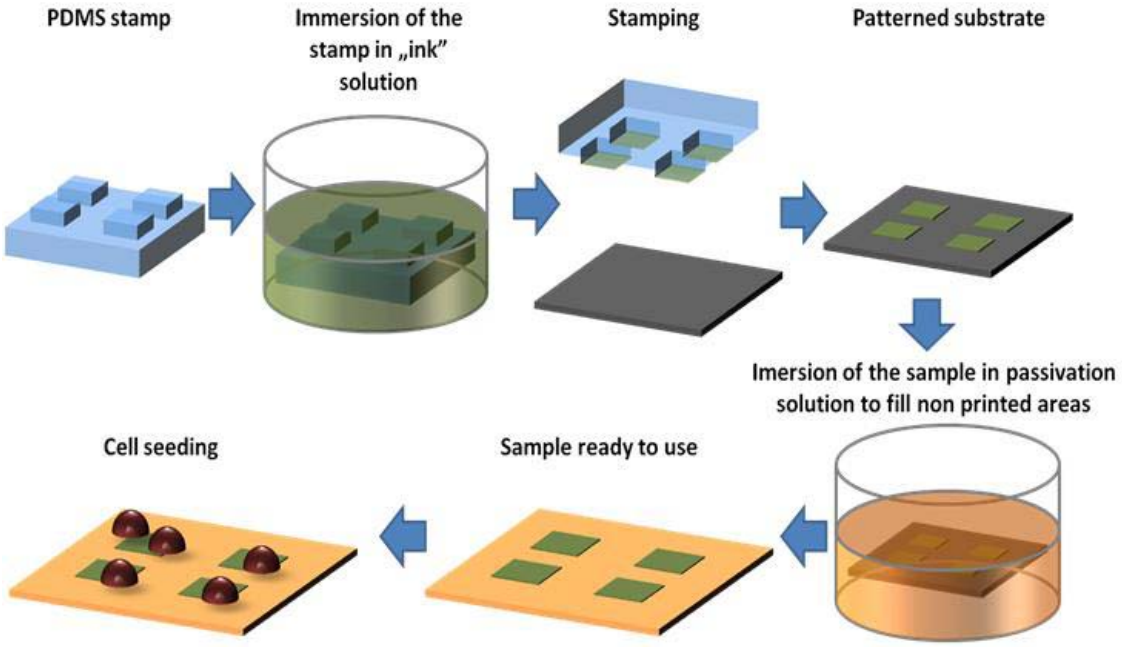

Figure 2.1 Scheme of the µCP protocol for the pattern-selective modification of a surface with a determined material for the enhancement of protein or cell adhesion. Image adapted from Reference [24].

Other approaches in tissue engineering use hard lithography techniques to study cell responses to topography [25,26]. Using these methods cell orientation and morphological changes in response to surface topography modification has been explored [27], and the relationship between the substrate topography and the formation of filopodia, lamellipodia and focal adhesion points, has been evaluated [28,29]. Cells have also been shown to follow carbon nanotubes [30] and to positively react to subtle differences induced by the presence of nanobeads on the surface [31].

Recently, approaches that focus on two or more of the previously described strategies have been reported. Thus, Charest *et al.* applied hot embossing to control the topography and μCP for a chemical patterning to obtain substrates with grooves covered with perpendicular stripes of proteins (see Figure 2.2) [32]. Feinberg *et al.* presented a similar architecture but with parallel patterns also using a multistep protocol [33]. An interesting study was presented by Recknor *et al.* where astrocytes cocultured with adult rat hippocampal progenitor cells over chemically modified micropatterned polystyrene substrates were shown to preferentially acquire neuronal morphology depending on the microstructuration of the substrate [34]. There are examples indicative that substrate topography, in synergy with chemical modification and biological guidance cues, facilitates the cell differentiation.

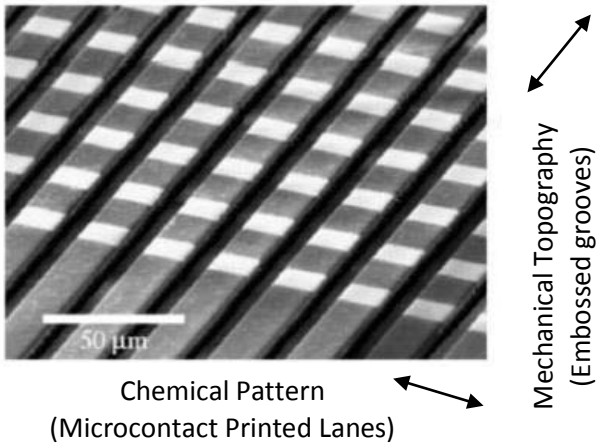

Figure 2.2 An example of a substrate with combined topographical and chemical patterns. After etching, the areas that were protected with microcontact-printed SAM became white. Unprotected areas (that have been etched) are grey. Mechanical pattern is clearly visible as embossed darker grooves. Image adapted from Reference [32].

2.2.2. Inclusion Bodies as functional biomaterials

The term "inclusion body" was coined to describe optically opaque moieties present in cell lumen. They have aspect of refractile particles of up to a few hundred nanometers [35] and about 2 μm^3 of size when observed by optical microscopy [36]. They appear as electron-dense aggregates without a defined organisation by transmission electron microscopy [37]. Scanning electron microscope images of these purified particles reveal ovoid or cylindrical shapes [37,38]. Representative images of IBs produced in *E. Coli* are presented in Figure 2.3.

IBs can occur naturally in eukaryotes, however their presence is deleterious [39] and is often connected with pathological changes accompanying diseases and other dysfunctions on

a cellular level. They are symptomatic of many illnesses such as rabies (Negri bodies), small pox (Guarnieri bodies), molluscum contagiosum (Henderson-Peterson bodies), etc.

Much more interest in IBs arose from their formation during recombinant protein expression in bacteria, especially in recombinant *E. coli*. As IBs were considered to be biologically inert and composed of unfolded or misfolded polypeptide aggregates [40] they were regarded as unwanted by-product or an obstacle in the process of obtaining pure, water soluble, native proteins [40], and therefore useless.

However, more recently it has been discovered that these aggregates are highly hydrated and chemically pure, containing up to 95% of proteic material [36,37] that is, at least partially, well-folded and functional [41]. The remaining mass is constituted from other cell components such as nucleic acids (DNA, RNA) and lipids [42].

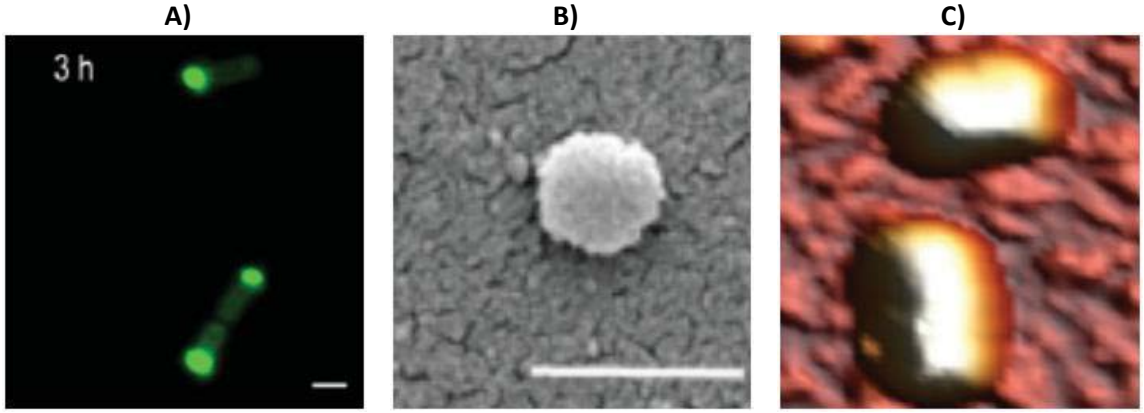

Figure 2.3 Representative images of IBs. A) Confocal microscopy images of w.t. (wild type) *E. Coli* cells producing green fluorescence protein (GFP) derived IBs 3 h after the plasmid introduction. Scale bar: 1µm. B) SEM images of the same IBs, extracted and purified. Scale bar: 500nm C) AFM characterization of the same IBs. 600nm X 600nm 3D zoom image of randomly deposited wt IBs on a mica surface. Images reproduced from Reference [43].

The history of IBs turned when they were recognized as a prospective biomaterial with desirable biological properties. Being a product derived from biological synthesis, it is fully biocompatible [44] and preserves the functionality of the embedded protein [45]. In a course of investigation it was revealed that IBs size, geometry, stiffness, wettability, z-potential, bio-adhesiveness, density/porosity etc. can be easily fine tuned by control over basic parameters during their production, like harvesting time, host genetic background and production conditions (e.g. temperature, pH) [45,46]. In addition, their production and downstream processes are fully scalable, cost effective and methodologically simple [47,48,49,50].

IBs derived from proteins such as β-galactosidase, D-amino acid oxidase, maltodextrin phosphorylase, sialic acid aldolase, and polyphosphate kinase [51,52,53,54] are functional

particles with enzymatic capabilities that can be used as catalysers in various processes. Their use on a broader scale is also prospected in the field of tissue engineering. Green Fluorescence Protein (GFP) derived IBs are convenient markers of IBs formation as this process can be easily followed by means of optical and confocal microscopy. These particles inherit properties of GFP and emit bright green light while excited with laser.

IBs measuring few hundred nanometers are within the range of topology features of extracellular matrix (ECM) making them prospective materials for developing surface roughness by surface decoration for cell culture. As totally biocompatible particles IBs may find their application in regenerative medicine. It has indeed been shown that when IBs are used to engineer the nanoscale topography of surface they have a positive impact on cell proliferation [43,55]. As they are highly bioadhesive materials, a mammalian cell expansion on IB-decorated surfaces is synergistically enhanced by both biological and mechanical stimulation of cell division as proved by the dramatic emission of filopodia in their presence [56]. Furthermore, it has been shown that cultured mammalian cells respond differentially to distinct IB variants obtained from bacteria with different genetic background, proving that the actual range of referred mechanical properties is sensed and discriminated by biological living systems [55]. So, it opened exciting possibilities for the fine tailoring of protein nanoparticles properties that are relevant in tissue engineering.

Although it is recognised that IBs are promising nanomaterials for tissue engineering, because they combine biofunctionality and the nanoscopic topography, little is known about the influence of surface modification with these nanoparticles on the global spatial organization of cells.

2.2.3. Inclusion Bodies Production

IBs production by biotechnology can be divided in three distinct steps: vector engineering, *in vivo* protein expression and IBs purification. Those are standard biotechnological procedures that can be adapted depending on the type of protein the IBs are derived from, their physicochemical properties and the genetic background of the used microbial factory. Details about the preparation of inclusion bodies used during this work are presented in detail in Section A.6 (“IBs production and purification”). All the IBs used in this work have been produced and purified in the group of Prof. Villaverde at the Institut de Biotecnologia i Biomedicina (IBB), Universitat Autònoma de Barcelona.

1. Vector engineering

The genetic information carrier, called vector, apart from preserving the desired DNA sequence influences other characteristics such as the possibility of multiplication, ease of introducing into the desired microbial factory and reliability of expression. Most commonly used vectors are plasmids, based on circular molecules of DNA. They are constructed by stitching sequence that codes a desired polypeptide with the rest of a construct that contains the origin of replication site and multiple cloning sites.

2. Protein expression

Engineered vectors are introduced into microbial factories; that is biological systems that will translate the DNA information and secrete polypeptides. Bacteria are the most preferred organism for such applications but yeast, filamentous fungi and animal cells are also among the used platforms [35]. The most common bacteria used as platform for gene expression are *E. coli*, but lactic bacteria are also becoming more and more popular due to the less toxicological risks of these lineages.

The *in vivo* formation of IBs is a fast and efficient process, since they are observed a few minutes after the induction of gene expression and with longer protein production times can represent around 50% of the total cell biomass. The final form of the expressed polypeptide depends on posttranslational machinery of microbial factory e.g. aggregation process is controlled by proteases and proper folding by chaperones. This enables fine tuning of IBs properties by changing the genetic background of producing bacteria [57,58].

3. IBs purification

After protein expression, IBs are harvested and purified. Bacterial cells are destroyed and IBs are extracted from lysate by standard purification procedures, such as washing with detergents, freeze-thaw cycles, centrifuging etc.

2.3. Results and Discussion

2.3.1. Optimisation of the microcontact printing

Our group has used bacterial IBs derived from the *Aequorea victoria* green fluorescence protein (GFP) as biologically inert nanobiomaterials. Fluorescence of obtained material enabled an easy detection and quantification of those nanoparticles.

The first task we had to perform was to establish a protocol for μCP of nanoparticles in order to selectively deposit IBs on surfaces in a controllable and efficient way.

Initial attempts conducted under the classical assumptions using the standard μCP technique to print IBs on silicon substrates were rather unsatisfactory (a scheme of the standard protocol used for μCP is presented in Figure 2.2.). We have obtained poor quality samples with discontinuous IBs pattern and very low fluorescence indicating the presence of very little biomaterial on the substrate. We have attributed these problems to the fact that μCP is generally applied to deposit soluble molecules and it is not an optimized technique for printing particulate material, such as IBs.

Therefore, we have tried to modify the μCP protocol in order to enhance the IBs transfer from the colloidal suspension to the stamp and from the stamp to the sample. Based on the work of Chang *et al.* [59] we have added some preparation steps to clean and condition the stamp surface before the inking. Stamp surface is thoroughly cleaned by sonication in acetone and dried in vacuum. Then, it is soaked in an aqueous solution of sodium dodecyl sulphate (SDS). The presence of surfactants (SDS) on the stamp surface enhanced the IBs adhesion during prolonged soaking in the IBs suspension and also improved the subsequent transfer of IBs to the surface during the printing procedure. With this new protocol we have achieved our intended goal, which was to obtain reproducible and continuous patterns of IBs on silicon substrates. A schematic cartoon of the developed protocol is presented in Figure 2.4. A detailed protocol description can be found in Section A.7 (“Microcontact printing of IBs”).

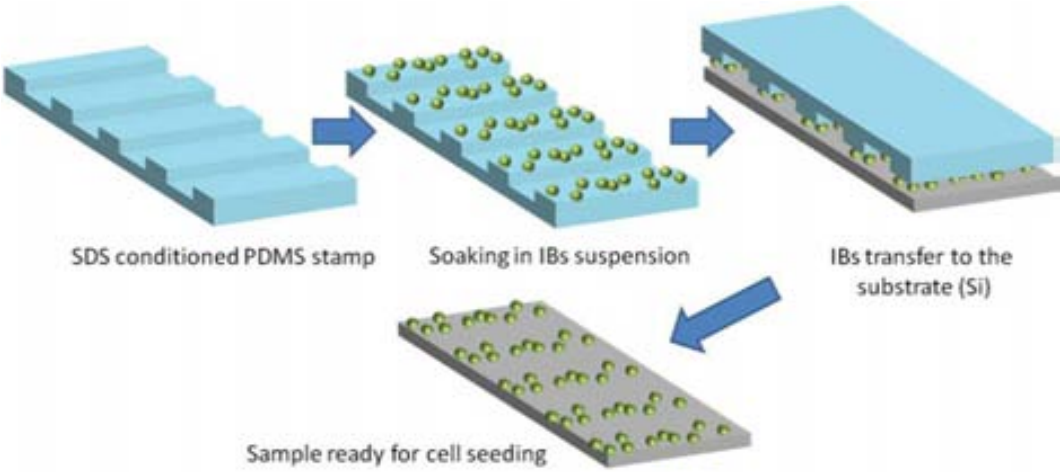

Figure 2.4. Schematic cartoon of µCP procedure optimized for IBs. Cleaned and conditioned in SDS solution PDMS stamp is soaked in IBs suspension. Next, IBs adhering to the geometrical features of stamp are transferred to cleaned and modified Si substrate. Finally, sample with deposited IBs in a geometrical pattern is obtained.

In order to enhance the IBs adhesion on the surface, the substrate surface has been also modified. We have used silicon substrate that is natively covered with a nanometric SiO_2 layer. There were two main reasons for surface modification: to enhance the IBs transfer and to prevent cells from unspecific binding. In order to do so, we decided to cover samples with a self assembled monolayer (SAM) of silanes functionalized with amino groups. The SAM deposition took place in gas phase as schematized in Figure 2.5. Detailed protocol description can be found in Section A.7.4 ("Substrates preparation").

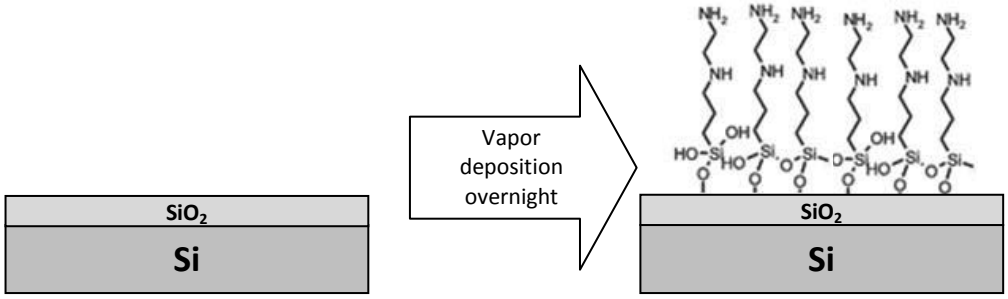

Figure 2.5 SAM deposition on Si substrates. Clean Si wafers are left under low pressure in presence of N-[3-(trimethoxysilyl)propyl]ethylenediamine (Aldrich) vapours overnight. This treatment deposits a well organized self assembled monolayer (SAM) over the surface that exposes neutral amino groups for cell neutral cultivation. This treatment aims to prepare surface with controlled chemical propeties.

The overall scheme of the final protocol used for the two-dimensional microscale structuration of IBs on surfaces is presented in Figure 2.6. Using this optimized µCP protocol we have been able to successfully print GFP IBs in a controlled and reproducible manner, as shown in Figure 2.7.

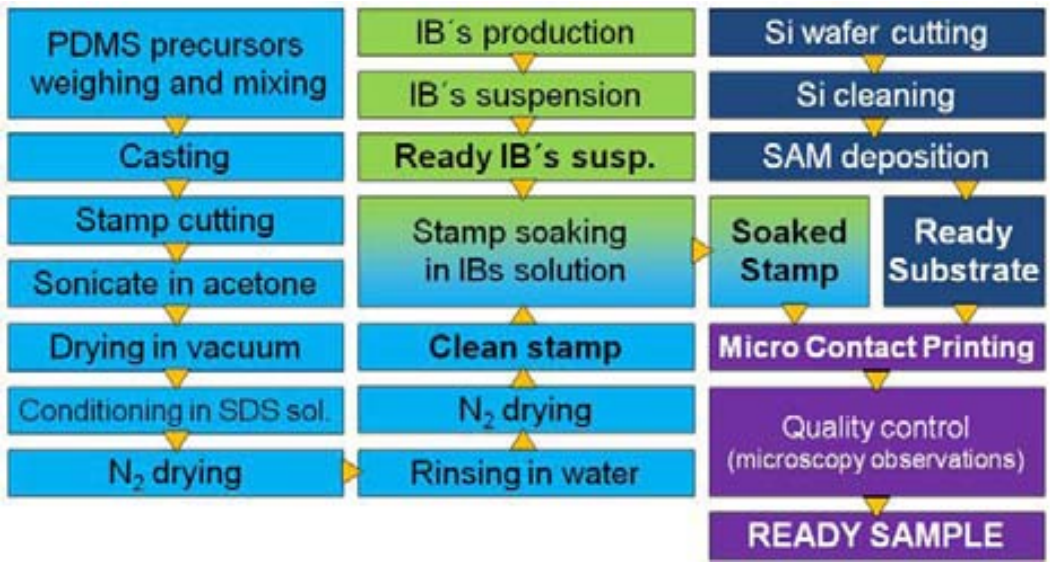

Figure 2.6 Overall flow chart of the two-dimensional microscale structuration of IBs on surfaces. Each block represents an operation and arrows visualize the flow direction. Operations regarding PDMS stamp, IBs suspension, silicon substrate and µCP sample are marked in turquoise, green, blue and purple, respectively. Detailed description of protocol is given in Section A.7 ("Microcontact printing of IBs").

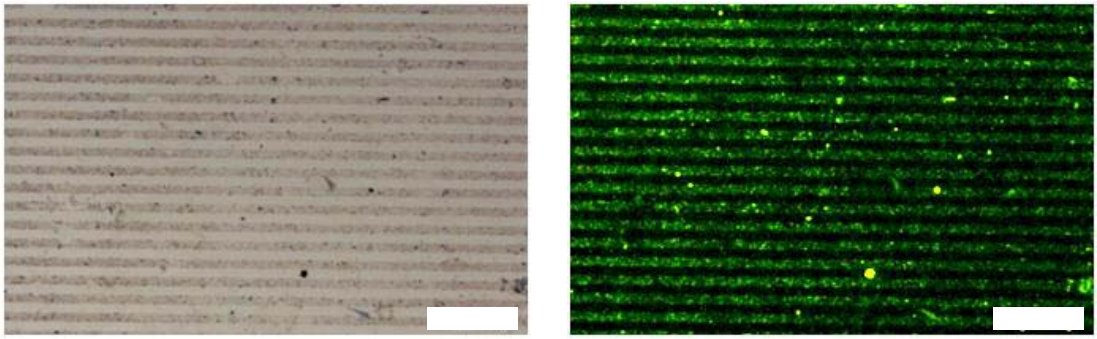

Figure 2.7 Representative microscopy images of µCP surfaces with GFP IBs. Bright field (left) and corresponding fluorescence (right) images are presented. Scale bars indicate 200 µm.

2.3.2. Influence of IBs density on cell growth

Having established the optimal protocol for the IBs deposition we proceeded to examine which is the optimal IBs density on surfaces for cell cultivation and guidance experiments. In order to do so, we have performed microcontact printing using various concentrations of IBs suspensions. This allowed us to prepare substrates with different surface coverage to achieve weaker or stronger interaction with cells. This interaction has been quantified in order to choose the optimal IBs density for cell guidance experiments. This is a crucial optimisation step because working with too high concentrations of a IBs suspension would imply a high demand of expensive IBs. On the other hand, too low concentration would not make the cell–IBs interaction strong enough to be quantified.

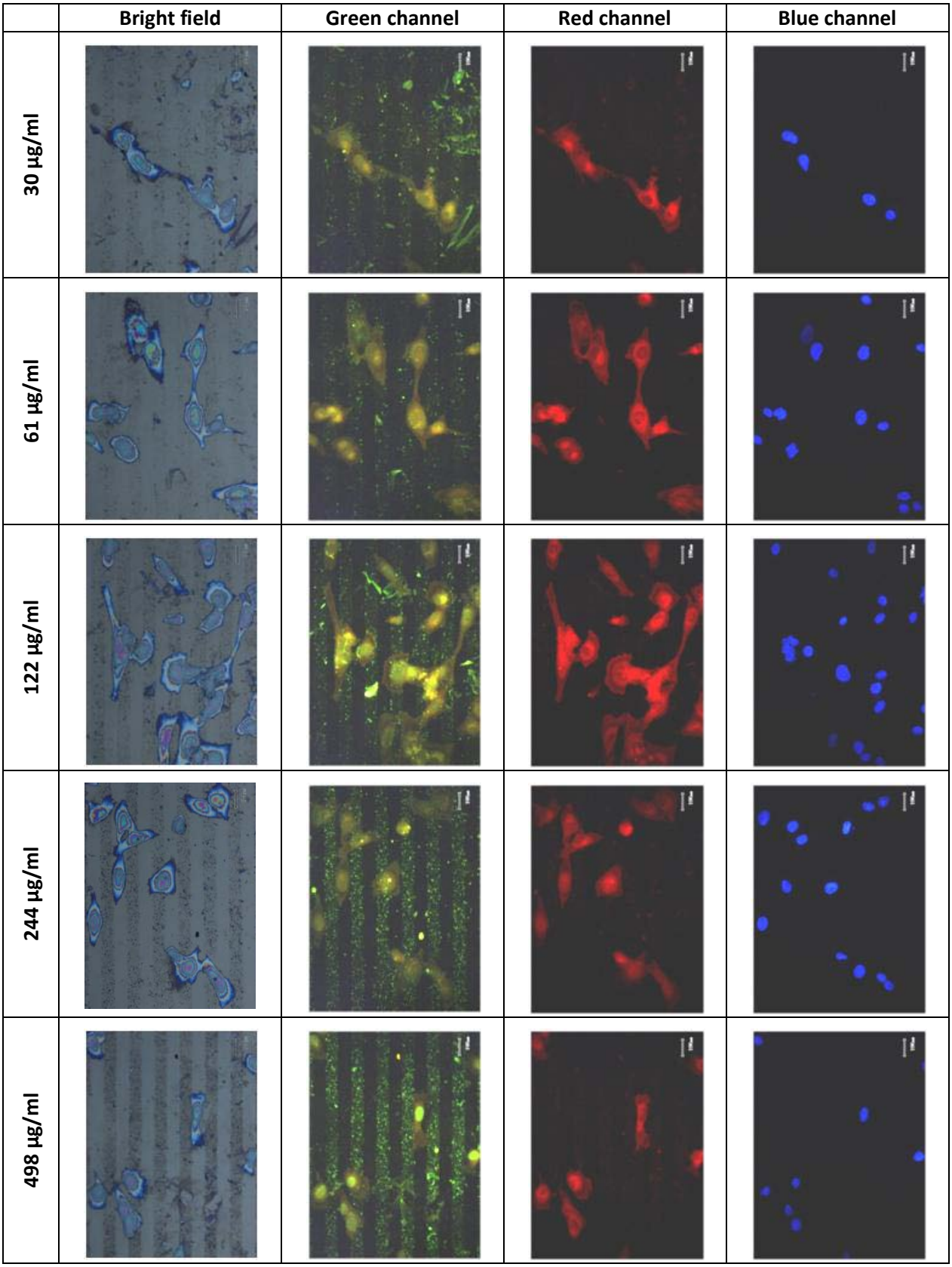

Figure 2.8 Microscopy images of cells cultivated over patterned surfaces with various IB´s densities. From left to right: Bright field, overall view; green channel, IBs; red channel, cell membrane and blue channel, cell nuclei. Images sizes are 260 x 350µm.

Micro contact printing was performed following the protocol described in Section A.7 ("Microcontact printing of IBs"). As a pattern we used simple stripes of 20μm wide (separated accordingly) and the IBs concentration in the suspension of a phosphate buffer saline (PBS) solution was set to 489, 244, 122, 61 and 30 μg/ml. We succeeded in obtaining, in a reproducible manner, supports with the same geometric pattern (20μm stripes) but with different density of IB particles. Moreover, it proved that the modification of the μCP protocol was successful. In Figure 2.8. it can be clearly seen that with rising IBs concentration there is more fluorescence coming from the pattern in the green channel.

In order to study the influence of IBs density on cell guidance we performed a preliminary statistical analysis of the IBs influence on cell (nuclei and membrane) orientation. Patterned surfaces with different IBs densities were introduced into standard flat-bottom 24-well plate. Human skin fibroblasts (1BR3.G) were seeded at density of 3×10^4 per well and cultured for 48 hours, stained and fixed, as described in Section A.8 ("Cell culture and dying for microscopy analysis"). Images of optical microscopy were captured for all samples, as described in Section A.9 ("Optical microscopy"). Representative images are given in Figure 2.8.

Using the above described protocol different IBs densities on surfaces were achieved. They were quantified by determining the average intensity of the green fluorescence emitted by the GFP-derived IBs. The dependence between the intensity of total green fluorescence emitted by the IBs on the patterned substrates and the particle concentration used in the "ink" suspension is shown in Figure 2.9A. The total green fluorescence increases with increasing the proteic material concentration in the soaking suspension. However, one can see from this graph, that the amount of IBs that can be transferred by the modified μCP technique reaches a saturation around 250 μg/ml. At higher concentrations an augment of the IBs concentration in the ink does not lead to a significant increase of the amount of deposited biomaterial on the surface.

We have quantified cell orientations using image treatment software as described in the Section A.10 ("Image analysis"). In short, each cell was approximated with ellipse and angle between ellipse´s long axis and the direction of patterned stripes was established. We have then assigned cells to three populations depending on their relative orientation along the stripped pattern: 0^0-30^0 (well-oriented), 30^0-60^0 (medium-oriented) and 60^0-90^0 (misoriented). Figure 2.9B shows the dependence of each population size depending on the surface density of IBs. Each data point corresponds to a different IB´s concentration used for the stamp soaking.

We have found that cells growing on substrates rich in IB´s align better to patterns. As the density of IBs on the stripped pattern increases we observe an increase of the well oriented cells (blue) as well as decrease of the medium and badly oriented ones (red and green respectively). This happens because cells respond positively to nano- and micro- topography.

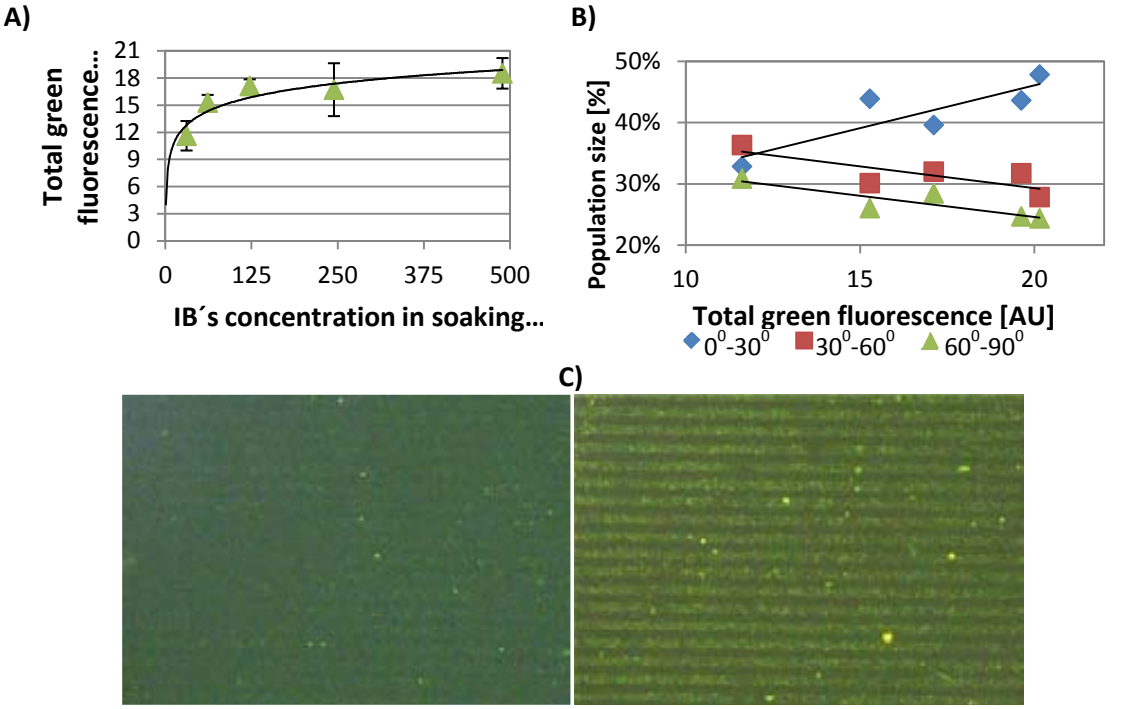

Figure 2.9 Optimization of the IBs coverage. A) Total green fluorescence intensity emitted by substrates patterned with 20µm stripes using PDMS stamps inked with suspensions of GFP-derived IBs at different concentrations (489, 244, 122, 61, and 30 µg·ml^{-1}) in PBS solutions. Note that acquired images were taken under the same exposure conditions. Logarithmic fitted curve is shown as guidance. B) Comparison between the resulting cell populations with well, medium, and wrong orientation of their membranes with respect to stripe direction, appearing with 0-30^0 (blue), 30-60^0 (red), and 60-90^0 (green) angles (see main text) obtained for 20µm stripe patterned substrates with increasing IB densities. Straight lines are shown as guidance. C) Images of patterned substrates with 20µm stripes using concentrations of GFP-derived IBs of 30 (left) and 489 µg·ml^{-1} (right).

From these plots, it was can be concluded that cells are better oriented when cultured on patterns with high IB densities. In addition, from these preliminary experiments, we also conclude that the optimal working density of IBs on surfaces is the one obtained by soaking the stamps in the suspension of IBs with a concentration of 240µg/ml. In fact, surfaces obtained from higher concentrations do not yield significantly higher densities of IBs on the surfaces due to saturation effects, and on the other hand, surfaces with lower densities of IBs show significantly poorer cell guidance properties.

2.3.3. Proliferation analysis

Once the optimal density of IBs was determined, the next step was to quantify the cell proliferation dependence on the geometry of IBs patterns. For this purpose 6×10^4 human skin

fibroblasts (1BR3.G) were seeded per well in a 24-well polystyrene plate containing the patterned substrates and cultured as described in Section A.8 ("Cell culture and dying for microscopy analysis") for 24, 48 and 72 hours. The patterns used for μCP were stripes with width of 50μm, and 5μm (spaced correspondingly) and dots with diameter of 50μm and 5 μm (spaced correspondingly). Also we used samples with randomly distributed IBs and IBs free substrates noted as "random" and "blank", respectively. Samples were prepared as explained in Section A.7 ("Microcontact printing of IBs"). In order to quantify only cells growing on patterned substrates and avoid the influence of cells growing on well´s bottom and walls, after the incubation substrates were transported to a new plate.

Then, cell proliferation was determined with a colorimetric assay using the EZ4U kit (Biomedica GmbH), following the manufacturer's instructions, and analyzed in the multilabel reader VICTOR3 V 1420 (PerkinElmer). The absorbances were measured at wavelengths of 450nm and 620nm, as reference, and the resulting values were standardized with respect to wells containing only cultivation medium (no living cells) and normalized so that the maximal value is equal to 1. All assays were done in triplicate. Data was expressed as the mean (+/- standard error) of the values obtained per condition and are presented in Figure 2.10.

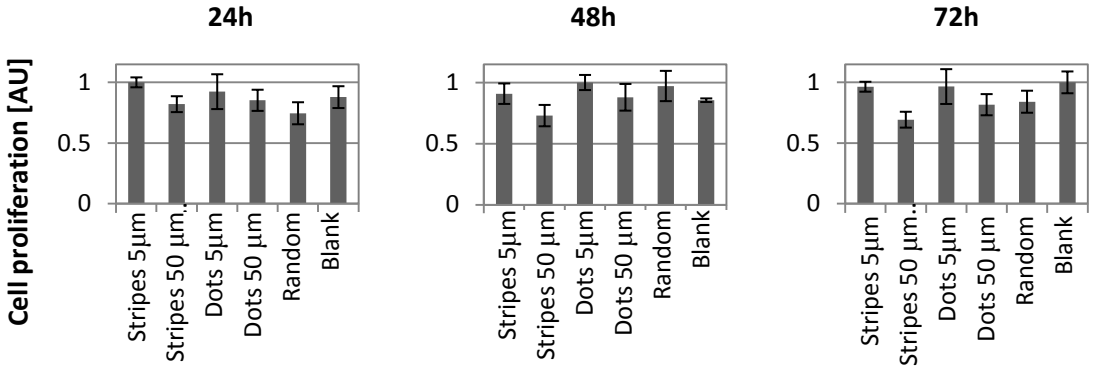

Figure 2.10 Cell proliferation data obtained from the colorimetric assay. Mind that cells were free to grow over the whole surface of the sample, whereas only 50% and 19% of the surface was printed with IB for stripes and dots respectively.

This experiment proved that IBs do not have any toxic impact on cell proliferation as it has already been observed. However, no significant variation in proliferation rates induced by the patterns was found, in agreement with the findings of Charest *et al.* [60].

2.3.4. Cell positioning, orientation and morphology

Once the optimal density of IBs was established as well as the non-toxic impact on cell proliferation was confirmed, we focused on the investigation of pattern induced changes in cells behaviour. Specifically we aimed to examine the influence of pattern geometry on cell

guidance, that is the impact of IBs pattern on: a) cell positioning; b) cell orientation and c) cell morphology.

In order to do so we have developed a new protocol based on cell staining, image acquisition and their subsequent treatment. Regarding the quantification of the complex cell substrate interactions, to the best of our knowledge, there are no widely available methods that deliver statistically relevant results. Most previous, image-based assays were limited by the use of a few cell images or just by eye counting. One pioneering study in this context was an innovative cell counting assay using quantum dots to compare cell adhesion data by means of an automated image recognition software developed by Parak *et al.* [61].

The geometries of patterns we have used were: stripes of 5, 20, and 50µm width (spaced with the same distances) and dots of 20µm diameter (spaced correspondingly from their borders). We also added two controls to our array of substrates, namely, a surface with randomly distributed IBs, obtained with the optimal IB density, and a IB-free surface, denoted as "Random" and "Blank", respectively. IBs concentration in the "ink" suspension was set to the optimal IBs density of 244 µg ml^{-1}. Samples were introduced to 24-well flat-bottom plates and 3 x 10^4 1BR3.G fibroblast seeded per well and cultured on these microstructures for 24, 48 and 72 hours. All experiments for all cultivation times and pattern geometries were triplicate. Nuclei and membrane were stained for and fixed. Finally, bright field, fluorescence and confocal microscopy images were acquired.

Unlike many other related researchers in the field, we have not changed the local wettability of the supports, letting cells adhere freely all over the sample surface, a fact that enabled us to determine the specific influence of IB patterns on cell guidance.

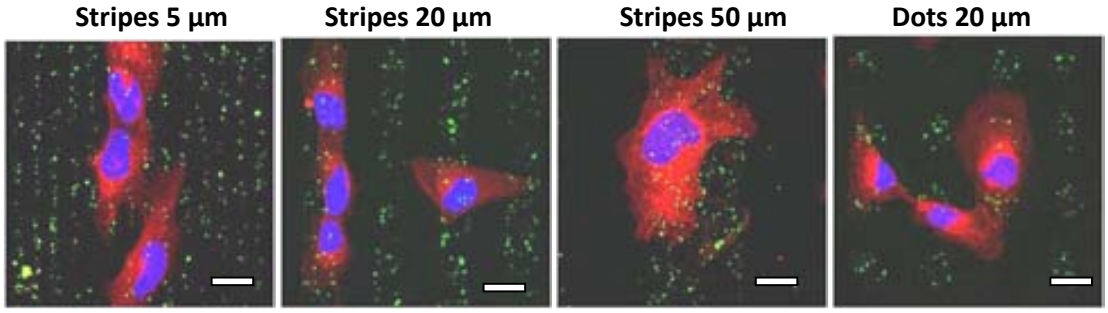

Figure 2.11 Example of confocal microscopy images (after 24 h of cultivation). Color legend: red - cellular membrane (stained with CellMask), blue - cellular nuclei (stained with Hoechst), green - IB (GFP). Bar lengths indicate 20 µm.

Confocal images of particular cells were captured in order to visualize details. Representative images are given in Figure 2.11. Cell proliferation and morphological changes are observed in all cases, evidencing the biocompatibility of the nano-patterned material.

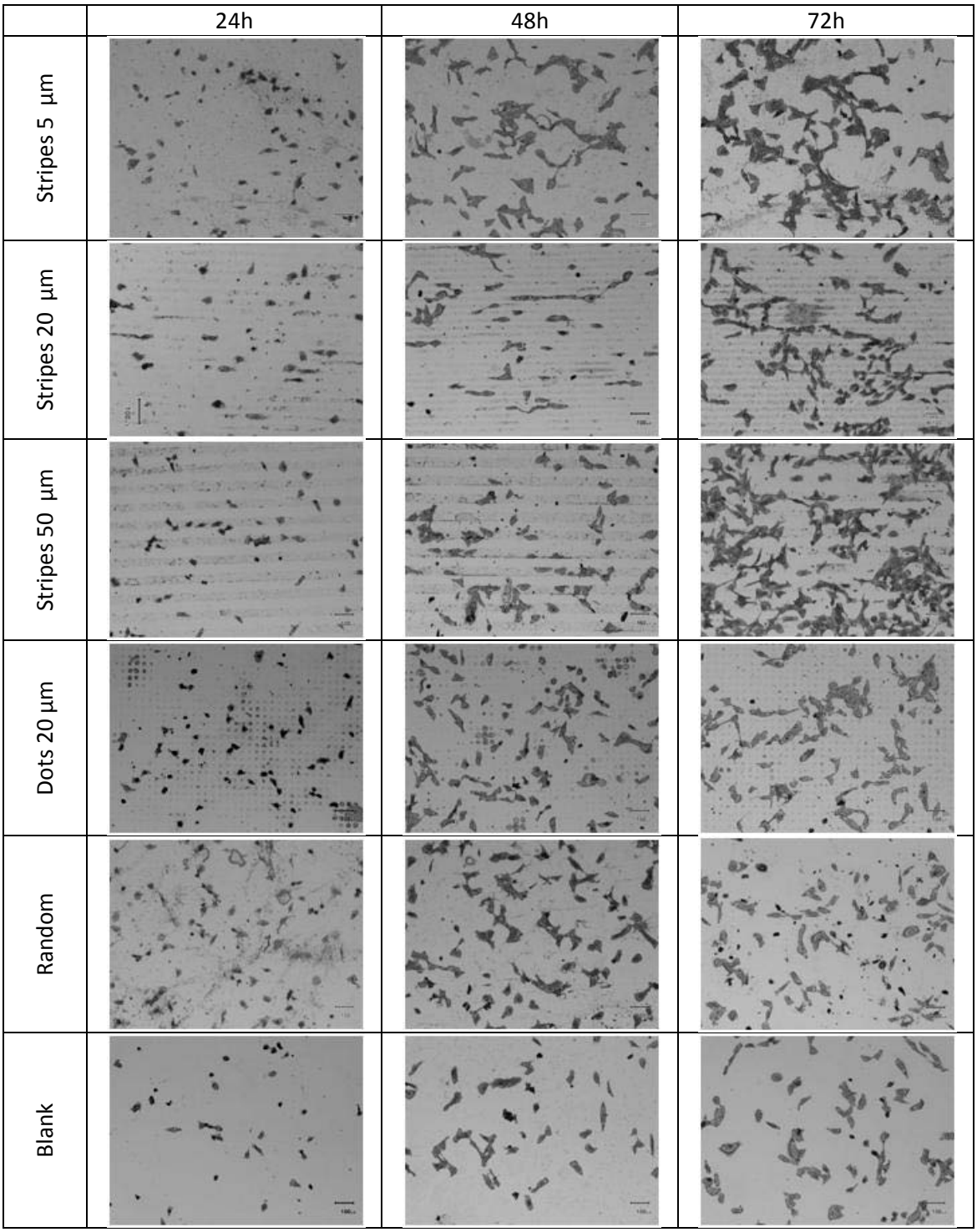

Figure 2.12 Representative bright field optical microscopy images of the analyzed regions taken for the 1BR3.G fibroblast cells cultured on the different IBs patterned substrates for 24, 48 and 72h. Images represent an area of 1400µm x 1000µm.

Representative bright-field optical microscopy images of 1BR3.G human skin fibroblasts cultured for 24, 48, and 72 hours on the different IB patterned are shown in Figure 2.12. As GFP-derived IB patterns emitted sufficient green fluorescence, we could investigate in detail the statistical correlation between the occurrence of IBs and cells. In fact, each image was taken in bright field as well as under an UV light with blue, red and green filters for visualizing nuclei, membrane and IBs, respectively. Images were the subject of further data treatment and statistic analysis in order to obtain quantitative data on the cell guidance.

Detailed descriptions of all the protocols used here can be found in Sections from A.7 ("Microcontact printing of IBs") to A.11 ("Confocal microscopy").

2.3.4.1. Cell positioning

To gain insight into cell positioning, we determined for each colour channel the average intensity of all pixels along analyzed vertical lines of the pattern. Then we represented these data as fluorescent intensity versus distance, obtaining the so-called "fluorescence profiles". We have preformed this for the green, red, and blue fluorescence channels that were originated from the IBs, cell membrane, and cell nuclei, respectively. Details of the data treatment are presented in Figure 2.13. Actual fluorescence profiles based on experimental data are presented in Figure 2.14. For more details see Section A.10 ("Image analysis").

A good correlation between the occurrence of IBs and the presence of cells (membrane and/or nuclei) can be seen for patterns with 20 and 50μm stripes and to a lesser extent for 20μm dots. In contrast for the 5μm stripes, peaks of blue (nuclei) and red (membrane) fluorescence were much wider than the green peaks of the IB pattern, due to the wider size of the cell in comparison with the patterned IB stripes. In the random control sample, it can be observed that, even without any pattern, a higher concentration of IBs leads to an increased concentration of cells.

In order to compare the efficacy of cell positioning for the different patterns, we calculated the ratio between the fluorescence coming from inside the patterned areas and the fluorescence from outside of such areas for every channel of emitted fluorescence (red, blue and green), separately (see Figure 2.13). This ratio, named *advantage ratio*, enables a quantitative estimation of the amounts of IBs deposited on the patterned surfaces as well as the amount of cells growing on the IB-covered regions in comparison with those on the IB-free ones (see Figure 2.15).

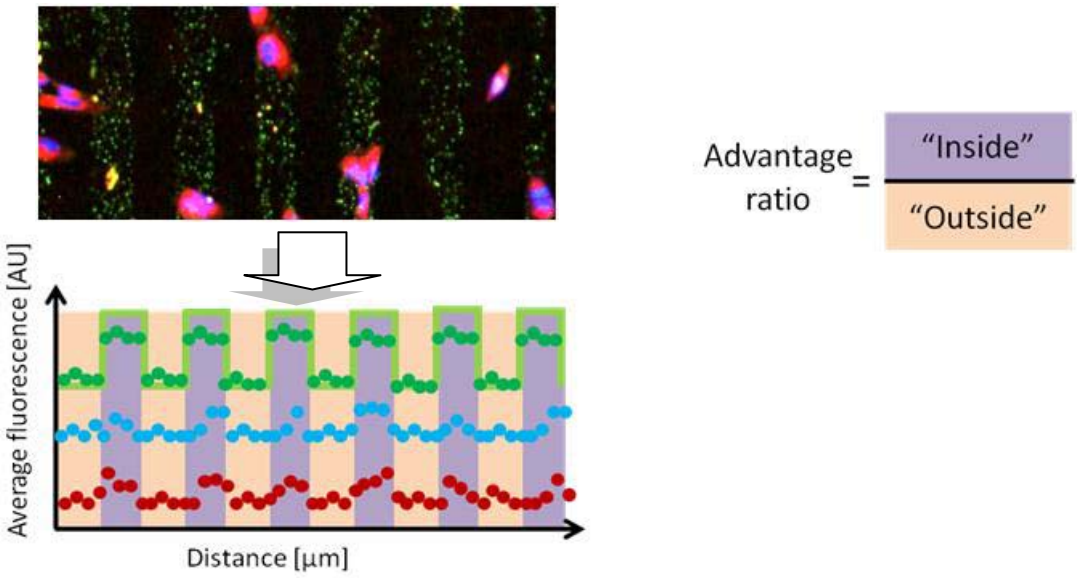

Figure 2.13 Fluorescence profiles based on fluorescence data from images. Images were split into three colour channels: green (IBs), red (membrane) and blue (nuclei). Averaged intensity of all pixels along analysed vertical lines were calculated. Values from every analysed vertical line versus the distance form the fluorescence profile of each channel (colour dots). Knowing the stamp pattern (shape and dimensions) an ideal pattern can be fitted to experimental data (continuous pale continuous green lines). Based on that, the total fluorescence intensity from "inside" (violet) and "outside" (peach) can be calculated. Advantage ratio is the ratio between the total inside to total outside fluorescence. For more details see Section A.10 ("Image analysis").

The advantage ratio calculated for green fluorescence enables us to perform a pattern validation. All patterns were correctly prepared, as there is at least 2 times more green fluorescence inside than outside the "idealized pattern". The higher values of advantage ratios obtained for the wider patterns suggest that such patterned areas are much better defined than the smaller ones. This result can be explained by the fact that wider patterns facilitate the adhesion of IBs to the stamp, improving the transfer to the silicon supports prefunctionalized with NH_2–terminated SAMs. More on pattern validation can be found in Section A.12 ("Quality control").

The values of advantage ratio obtained from the red channel corresponding to stained membranes of cells cultured at different times on distinct patterned surfaces clearly show, that for the 5µm stripes, the ratio of red fluorescence between the inside and outside of the patterned areas is close to 1. This is in good agreement with the fact that cells are much bigger than the size of such stripes and consequently they adhere to more than one stripe at the same time, covering the areas between the stripes of IBs (see Figure 2.11). High values of the advantage ratio observed for the 20µm striped patterns and even higher for the 50µm patterns suggest that the areas with IBs are preferred by the cells, especially after the first 24 hours of culture.

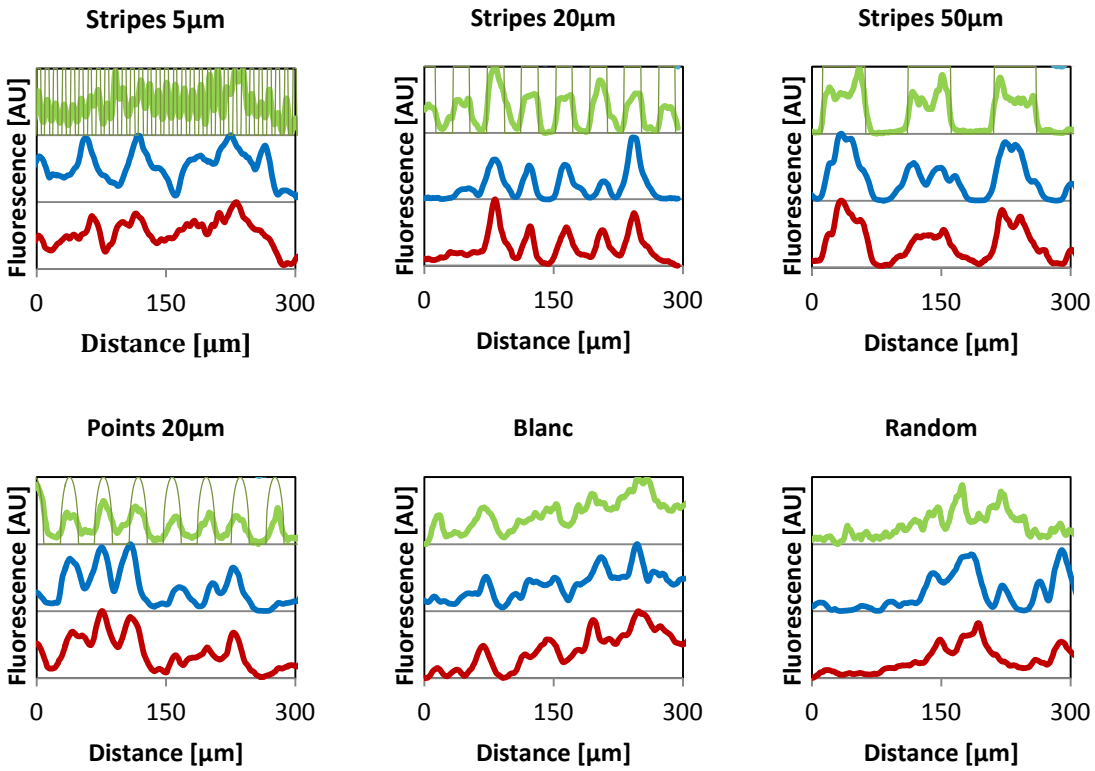

Figure 2.14 Impact of patterned geometry of IBs on the cell positioning. Representative fluorescence profiles of IBs (in dark green), cell membrane (in red) and cell nuclei (in blue) after 48h of cultivation of 1BR3.G cells on the six different substrates used for the analysis. Thin, light green lines represent the "ideal" IB profiles. Profiles are normalized so that maximal value is 1 and minimal is 0.

Another interesting observation is that the advantage ratio values decrease with time as an effect of the limited available space for cells on the patterned areas and proliferation of cells also occurs over undecorated areas. Thus, after 72 hours, the advantage ratio is close to 1 for most of the cases, indicating that all regions are almost equally covered with cells due to saturation (see also Figure 2.12). Such data is in agreement with previous studies in which nanotopographies generated by colloidal lithographic methods significantly favouring the attachment of fibroblasts at early culture times [62]. Interestingly, not only the size of nanocues but also their stiffness, chemical composition, and distribution have been shown to affect cell responses [63,64]. Thus, irregular distribution of the nanomechanical stimuli provided by IBs would enhance cell adhesion upon seeding, prompting higher cell coverage of the IB-patterned areas, a result that is most evident at 24 hours of cultivation and that progressively fades out at longer culture times.

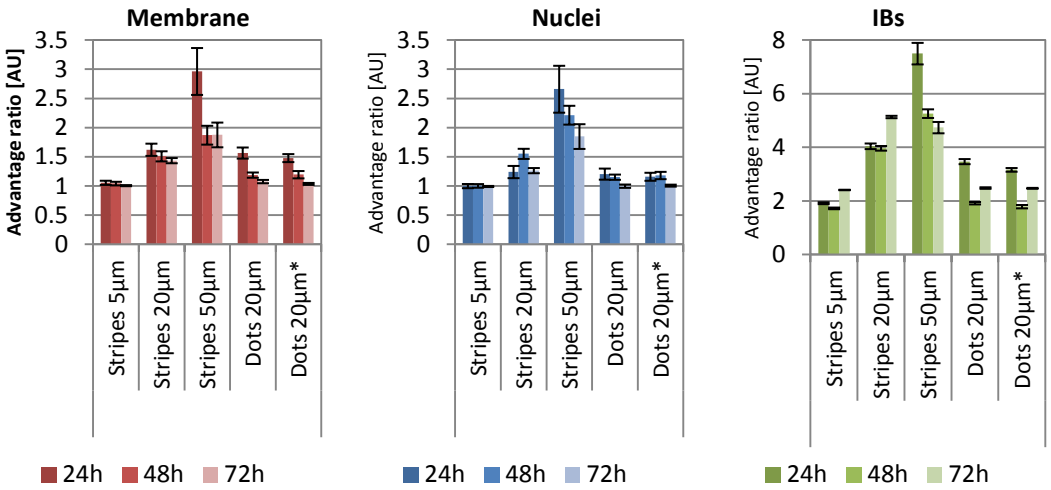

Figure 2.15 Influence of IBs-modified substrates on cell positioning. Advantage ratios of fluorescence signals inside and outside the IB-patterned regions coming from the red, blue and green fluorescence of stained cells (red: membrane, blue: nuclei, green: IBs). Dots were analyzed in both horizontal and vertical (marked with an asterisk) directions. An advantage ratio of 1 is an indication that cells are localized equally over patterned and unpatterned regions. The higher the values, the bigger the concentration of cell membranes over the patterned regions. It has to be taken into account the fact that IBs patterned in stripes cover 50% while dots only 19.6% of the whole surface.

2.3.4.2. Cell orientation

In order to extract orientation data of cells, the aligned images were turned into black and white (binarised) with the image threshold tools. Then, geometrical parameters of each cell were automatically calculated with the ImageJ "Analyze particles" procedure. Each region corresponding to the investigated feature (cell membrane or nuclei) was approximated to an ellipse. The angle between the long-axis of the ellipse and the x-axis of the image (direction of stripe or dot lines) was calculated. Moreover, the area of each region was measured, and only areas with surface greater than 100µm^2 were considered in the further analysis. Data corresponding to the same growth conditions but from different images were pooled. The frequencies of angle orientation were divided into 10^0 wide bins from 0^0 to 180^0. Values between 180^0 and 360^0 are symmetric repetition of data added for convenience on radial plots. Principles of angle calculation are explained in Figure 2.16. For more details see Section A.10 ("Image analysis").

Radial distributions of orientation angles of the cell membrane are presented in Figure 2.17. For all striped patterns, it can be clearly observed that the angular distributions present an unambiguous tendency to align along the stripes (horizontal direction). It can be observed that, after the first 24 hours, there is a broader distribution of membrane orientations on the 50µm stripes. This is indicative that cells still have some degree of freedom to orient

themselves perpendicularly to stripes direction, because the width of patterned area exceeds average cell size (see also confocal image in Figure 2.11). Contrary to that, the 20µm stripes almost match the cell size and, therefore, a narrower distribution of orientations of cells is observed in this case at all proliferation times. Surprisingly, despite the fact that on the 5µm striped pattern the cells grow over more than one stripe (see Figure 2.11), the distribution of orientations in this case is kept very narrow and well-pronounced at early times. However, this tendency changes with time, and a broadening of the orientation distribution is progressing. The distribution for the 5µm stripes broadens faster than for the 20µm and for the 50µm ones, in which it remains constant. It is worth mentioning that, after 72 hours, cells growing over the 20µm patterns still maintain their orientation.

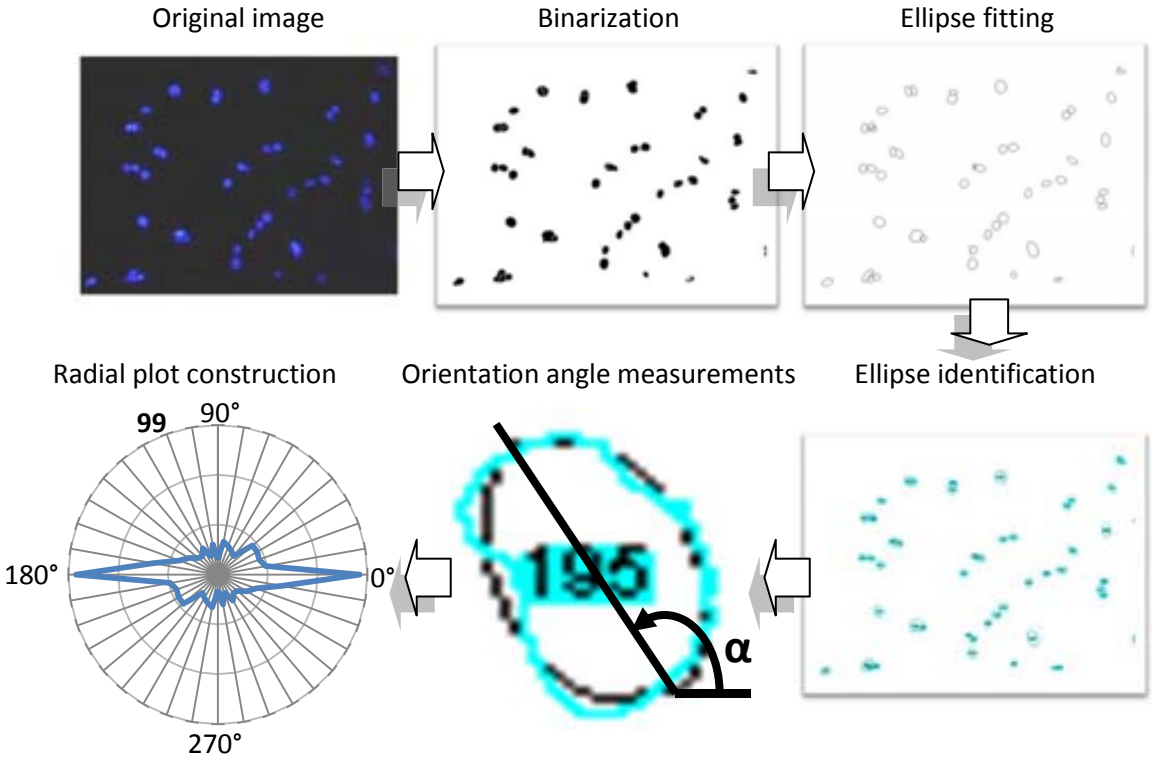

Figure 2.16 Scheme of cell orientation calculation based on microscopy images. First, the original image (in this case the nuclei image) is converted into black-white image (binarised). Black spots corresponding to nuclei are analyzed and each nucleus is approximated with the best fitting ellipse. Angle α between the ellipse´s long axis and the reference direction (horizontal line) is the nucleus orientation angle. Finally, a radial plot of angle distribution is constructed based on pooled data of all the nuclei orientation angles of cells cultured in similar conditions. 0° angle corresponds to horizontal line and is the same for all radial plots. Radial scale corresponds to the number of cells in each orientation and its maximal number is shown (in bold) to enable comparison between different conditions. The same analysis has been preformed for the red channel (cell´s membrane). For more details see Section A.10 ("Image analysis").

Similar analysis performed for the nuclei shows that the orientation of this cellular compartment follows the same orientation as the whole cell (see Figure 2.18).

Membrane	24 hours	48 hours	72 hours
Stripes 5µm	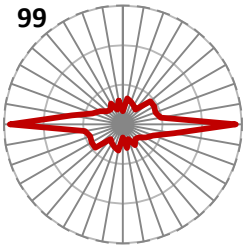	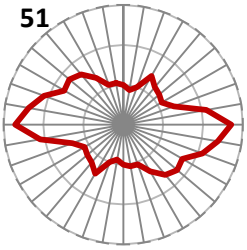	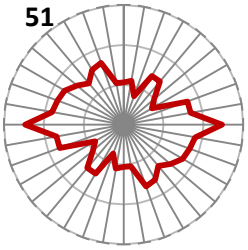
Stripes 20µm	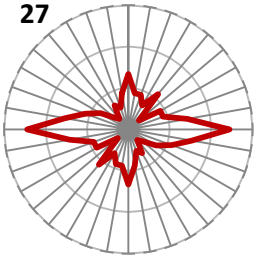	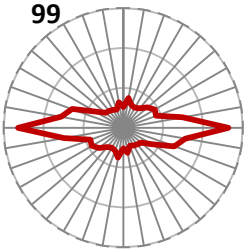	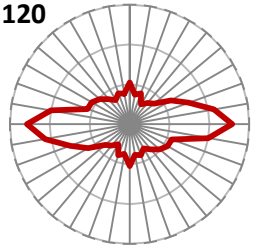
Stripes 50µm	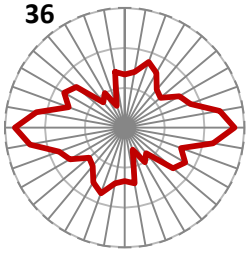	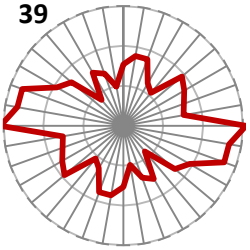	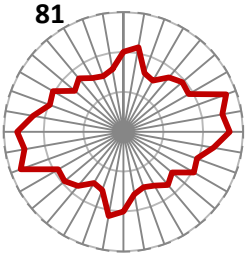
Dots 20µm	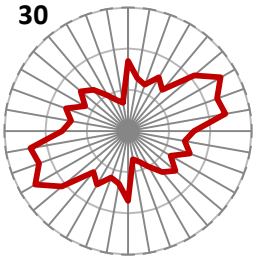	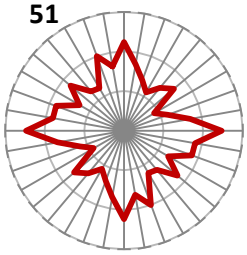	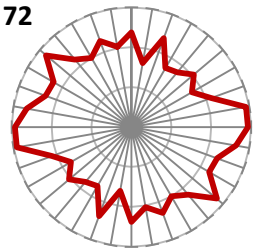
Random	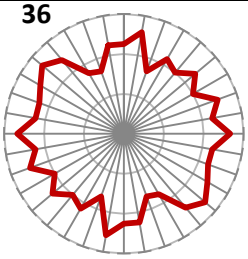	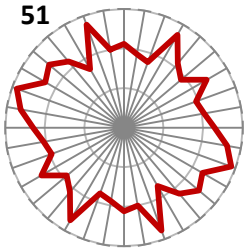	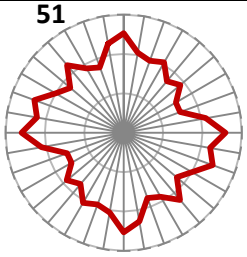
Blank	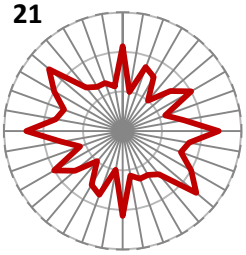	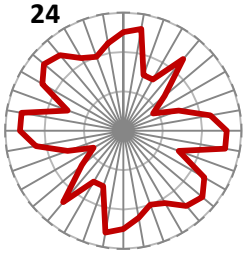	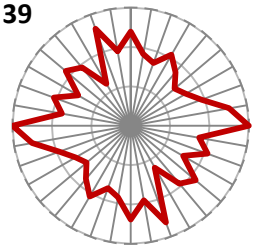

Figure 2.17 Radial plots of cell's membrane orientation (red fluorescence) versus occurrence frequency for every experimental condition. For all the stripped patterns spindle-like distribution indicating cells´ aligning is observed. The gradual broadening with the time of the "spindle" indicates a decay of cell orientation. Cross-like distribution of cells growing over the dotted pattern after 48h can be observed. Numbers indicate the maximal value of the radial axis.

Nuclei	24 hours	48 hours	72 hours
Stripes 5µm	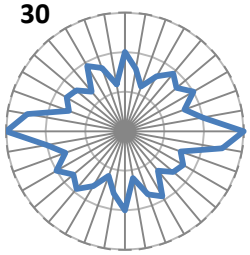	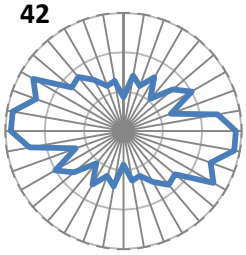	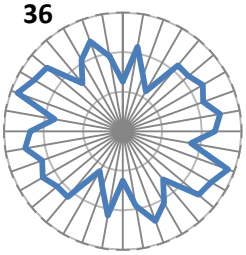
Stripes 20µm	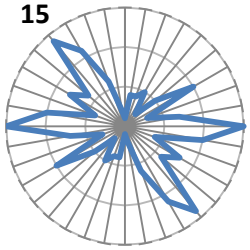	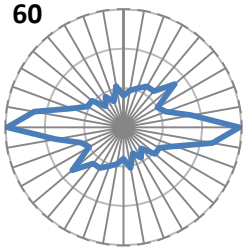	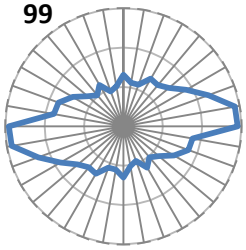
Stripes 50µm	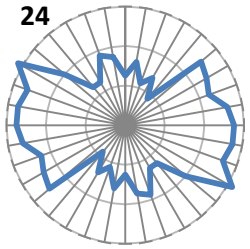	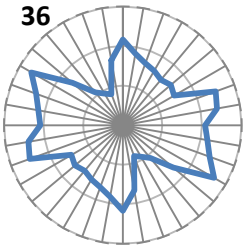	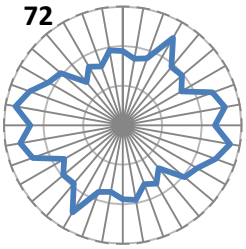
Dots 20µm	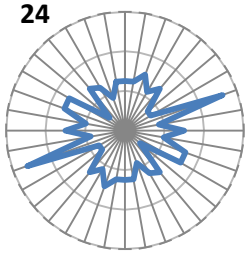	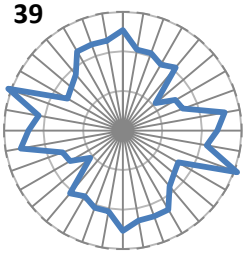	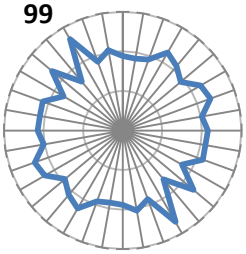
Random	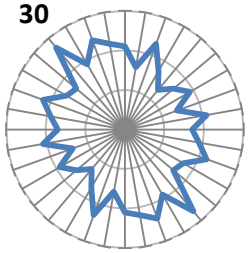	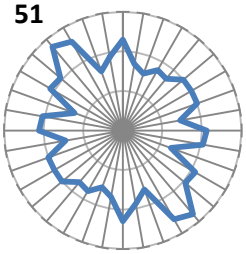	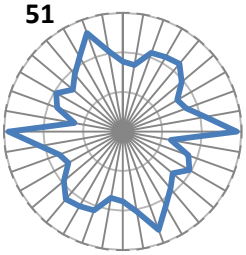
Blanc	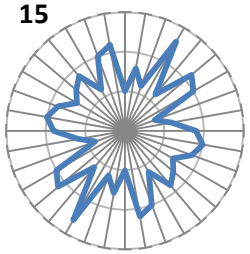	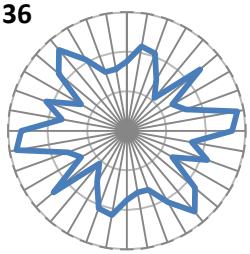	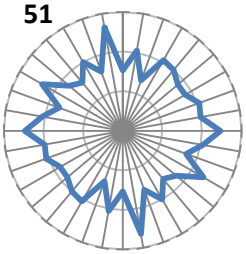

Figure 2.18 Radial plots of cell's nuclei orientation versus cell frequency for every experimental condition calculated for the blue fluorescence (cell´s nuclei). Observations are similar as for the membrane. Values between 180° and 360° are symmetric repetition of data from 0° to 180°. Numbers indicate maximal value of the radial axis.

Regarding the cells growing on dotted patterns, it is observed that at early experimental times they do not show any preferential direction. However, after 48 hours of culture, directions close to 0^0 and 90^0 became more pronounced (see Figure 2.17 and Figure 2.18). We attribute this bimodal distribution to the fact that cells elongate to reach neighbouring dots, spending less effort directing along dot rows and columns, as similarly reported by Charest *et al.* [60]. A coarse-grained analysis of these data highlights this event even more (marked with arrow in Figure 2.19). Similar analysis performed for the nuclei shows that the orientation of this cellular compartment follows the same orientation as the whole cell.

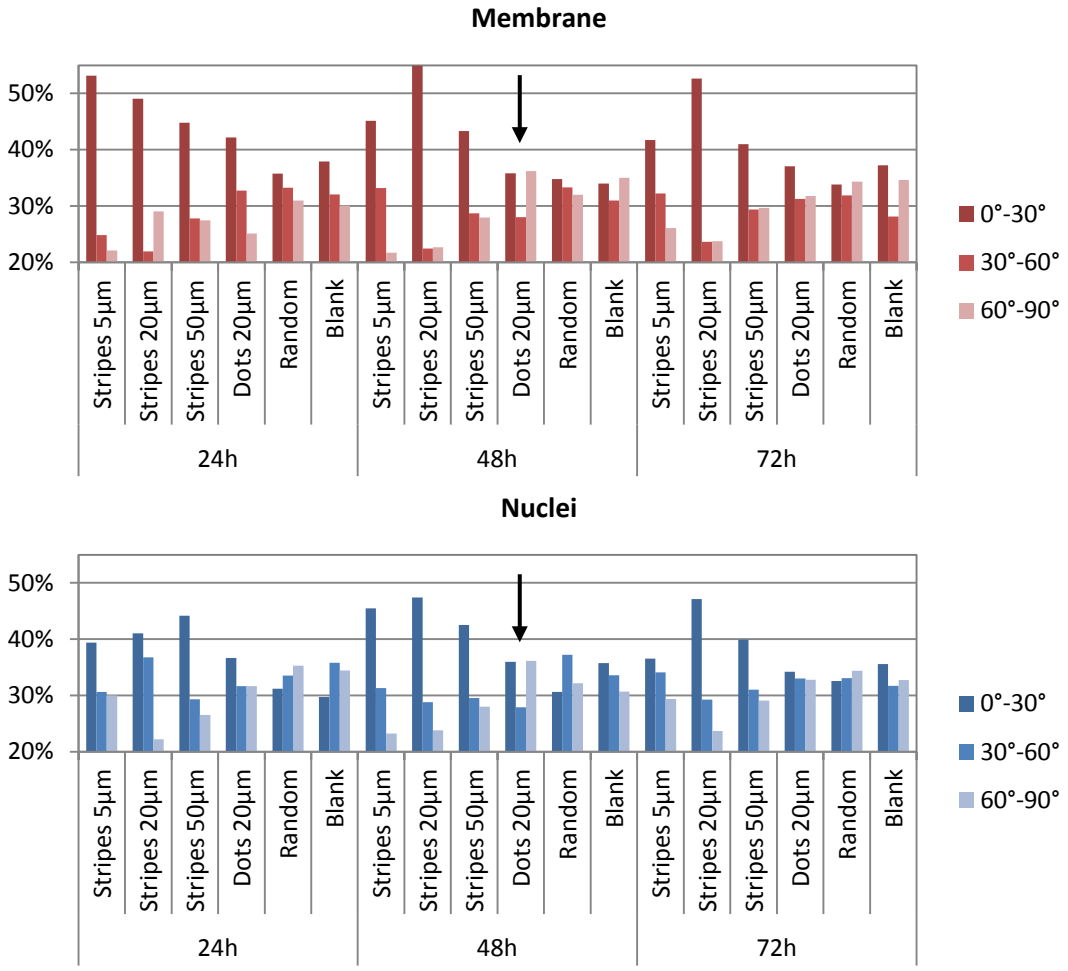

Figure 2.19 Coarse distribution of membrane and nuclei orientation. Cells were divided in three categories: cells with orientations 0 to 30^0, 30^0 to 60^0 and 60^0 to 90^0 with respect to the direction of stripes (dot´s rows) from the patterned substrates. Percentage of cells in each bin was calculated as a percentage of total number of cells for pattern and condition. For random orientation a value of 33.3% is expected (as the same orientation is obtained for each direction). In this representation, the "cross-like" orientation of cells cultivated over dotted pattern is very clear (see arrows). Narrower stripes have better pronounced impact on cells orientation at early times. However, 20µm stripes maintain high population of well-oriented cells even after 72 hours. The orientation of nuclei follows the orientation of the membrane and the whole cell.

2.3.4.3. Cell morphology

Apart from the cell positioning and its orientation, IB-patterned substrates also govern the morphology of cells. In Figure 2.20 the average elongation of cell membranes, named aspect ratio, is presented. For our purposes this value is calculated as the ratio between the cell's largest and smallest dimension minus one, attained from cells cultured on the different patterned substrates. Fibroblasts growing on striped supports for a short period of time presented a high aspect ratio that decreases with the course of cultivation. On the other hand, cells growing on supports without patterns showed an initially round membrane morphology (low values of aspect ratio) that progressively became more elongated. Moreover, after 72 hours, cells present similar elongations in all the supports. Interestingly, cells growing over randomly distributed IBs showed a more elongated initial morphology than those growing on bare supports without IBs. This fact is an indication that IBs are acting as efficient focal adhesion points, as evidenced in Figure 2.21 by the clear formation of filopodia and lamellipodia in contact with the IBs on the surface. This result confirms our previous observations that the cellular adhesion to IBs is stronger than that attained on standard supports [56].

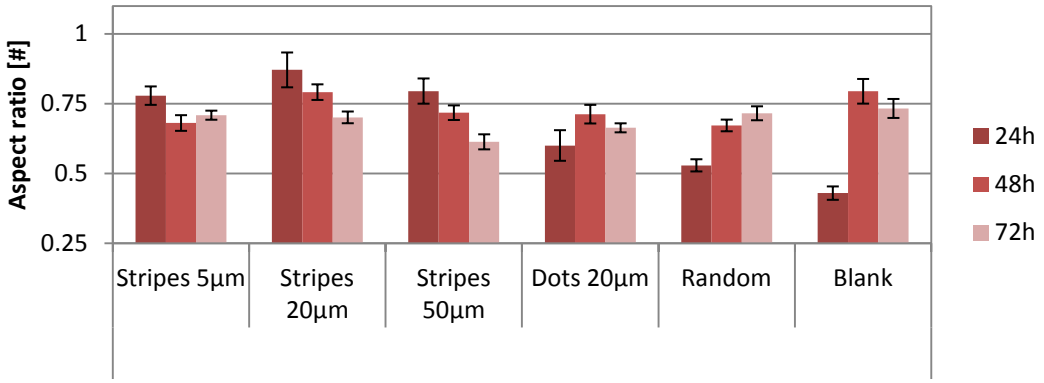

Figure 2.20 Influence of IBs-modified substrates on the cell morphology. Average aspect ratio of cells membrane growing on the different IBs patterned substrates with error bars indicating +/- standard errors. The evolution of cell's membrane elongation with time can be traced for each pattern.

To analyze the effect of the patterns on the cell elongation, we also analyzed the correlation between the aspect ratio and the orientation angles of cells as well as its evolution in time (see Figure 2.22). From the resulting plots, it can be concluded that in all cases cells were more elongated in the direction of the patterns, which is an indication of pattern-mediated cell morphology guidance. Also, in the case of the dotted pattern, a bimodal distribution of morphology emerged as previously described. Therefore, the combination of nanoscale features of IBs that provide a highly adhesive environment with the morphological

guidance determined by the microscale patterns clearly affects cell behaviour. Control of cell responses at nano/microscales has proved to be a powerful tool in order to trigger mechano-transductive events as well as direct tensegrity processes able to lead a gene expression shift with implications in such diverse cell responses such as adhesion, proliferation, spreading, differentiation, or apoptosis [65].

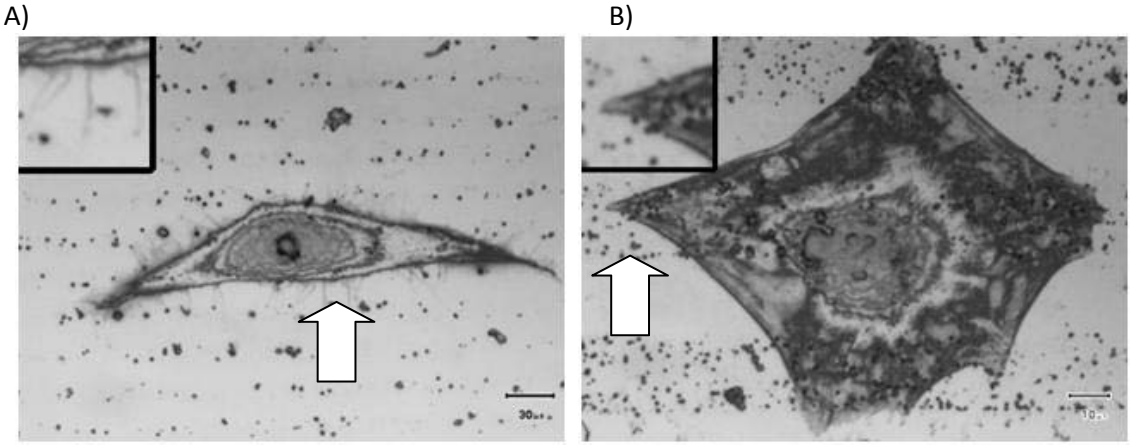

Figure 2.21 Optical microscopy images of 1BR3.G fibroblast cells growing on patterned substrates where cell's spreads A) filopodia and B) lamellipodia to reach the adhesive IBs can be observed. The upper left corner inserts show magnification images of the regions of interest indicated by arrows.

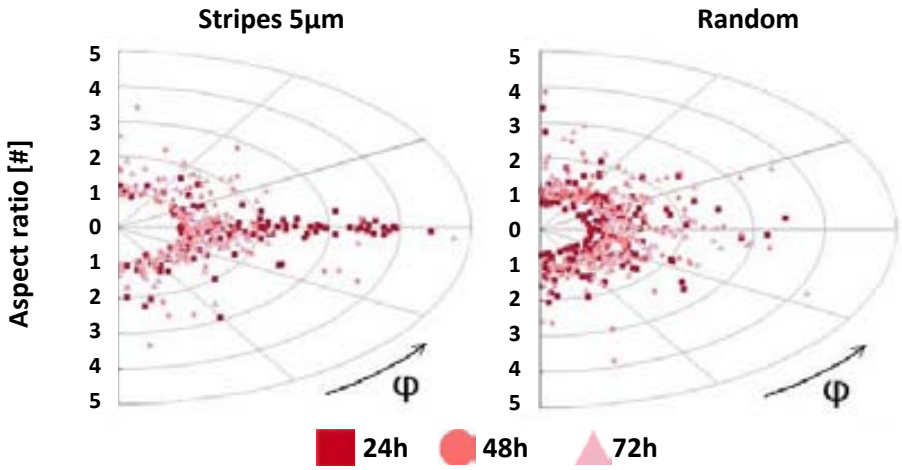

Figure 2.22 Influence of IBs pattern geometry on the cell morphology and orientation. Example plots of membrane aspect ratio versus orientation angles of cells cultivated on 5µm striped surfaces and on a surface with randomly distributed IBs and its evolution with time. Each dot´s distance from central point represents the cell's aspect ratio, and the angle from the horizontal line corresponds to the orientation of cells. Colours represent different times of cultivation.

2.3.5. Adding bio-functionality to structured surfaces with functional IBs

Finally, going one step forward, the structuring strategy with IBs was expanded by using biofunctional IBs to pattern substrates. The main idea was to conduct a proof of concept

experiment, where we applied the developed patterning methodology with one example of a biologically active IBs formed by the human basic fibroblast growth factor (FGF). This will enable to investigate the synergy between the IBs´ biological function and its topographical stimuli on cell´s behaviour.

The geometries we used were the same as we used in the previous experiments, stripes of 5µm and 20µm width (spaced with the same distances). Regarding the IBs concentration we used 244µg ml^{-1} and 9µg ml^{-1} for GFP and FGF IBs, respectively. 24 hours before seeding on substrates cultivation media was changed from one containing 10% fetal bovine serum (FBS) to the media with 1% of FBS. This procedure aimed to sensitize NIH-3T3 cells to FGF from IBs. NIH/3T3 fibroblast cells were seeded over samples at density 3×10^4 and cultured during 24, 48 and 72 hours, stained and fixed as described in Section A.8 ("Cell culture and dying for microscopy analysis").

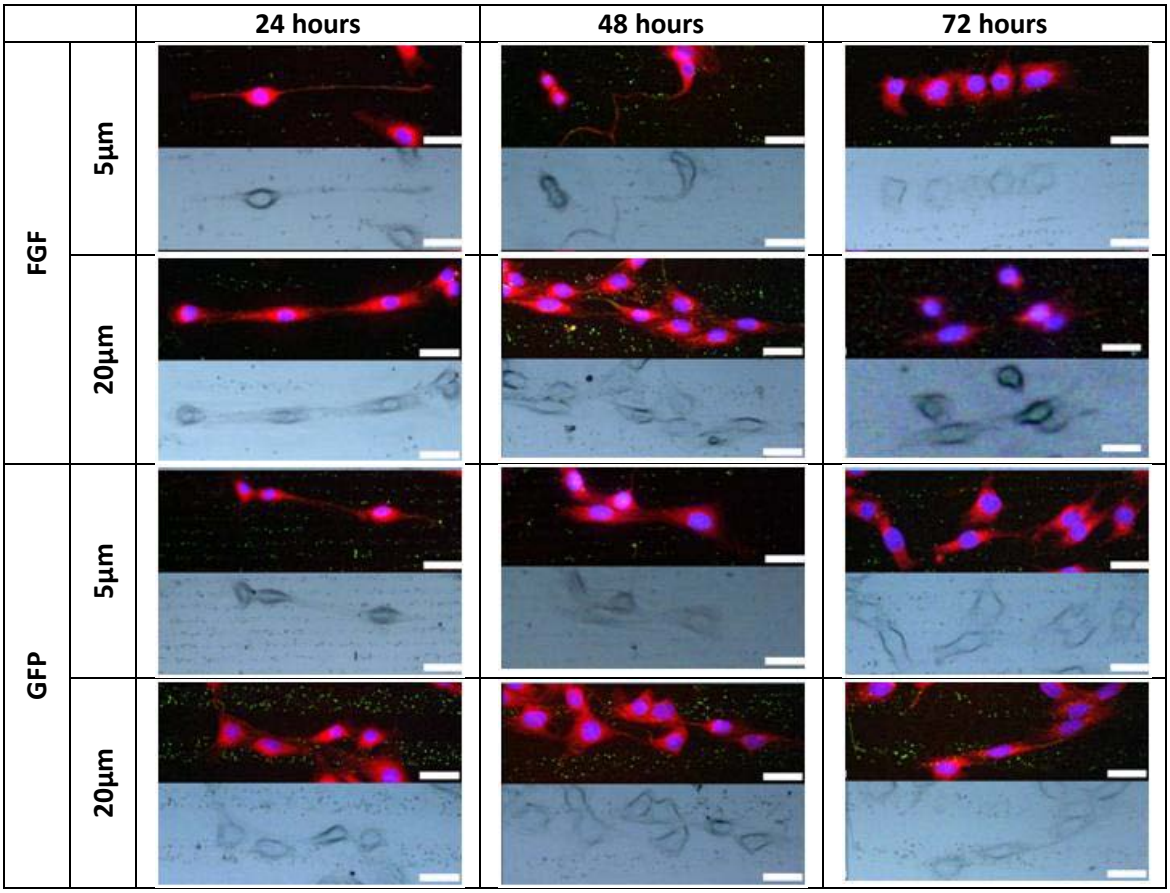

Figure 2.23 Bright field and merged fluorescence images of NIH/3T3 cells cultured over GFP and FGF derived IBs at different times. Colour code: red – membrane, blue-nuclei, green – GFP IBs. Scale bars indicate 30µm.

Figure 2.23 shows representative bright-field and merged fluorescence images of NIH/3T3 fibroblast cells cultured during 24, 48 and 72 hours on 5µm and 20µm striped patterns of FGF- and GFP-derived IBs printed with inks of 9 and 244µg ml^{-1} of the IBs, respectively. Figure 2.24 shows on the other hand the corresponding large field images captured after 48 hours of cell growth over the different substrates that were subsequently used to obtain statistical data.

It is a remarkable fact that NIH/3T3 cells are guided by the biofunctional FGF-derived IBs with a similar extension than with the GFP-IBs in spite of using a much more than one order of magnitude lower concentration of IBs. This result cannot only be due to surface topography and geometry of the pattern but also to the bioactivity of FGF derived IBs since it has been recently shown that FGF derived IBs retain the biologic activity of the protein,[66] and that the protein is released from IBs for a biological effect on the cells. This is due to a particular sponge-like architecture of these IBs [67] that permits a sustained delivery of the protein forming the IBs to the extracellular media or to target cell compartments [48,49,50].

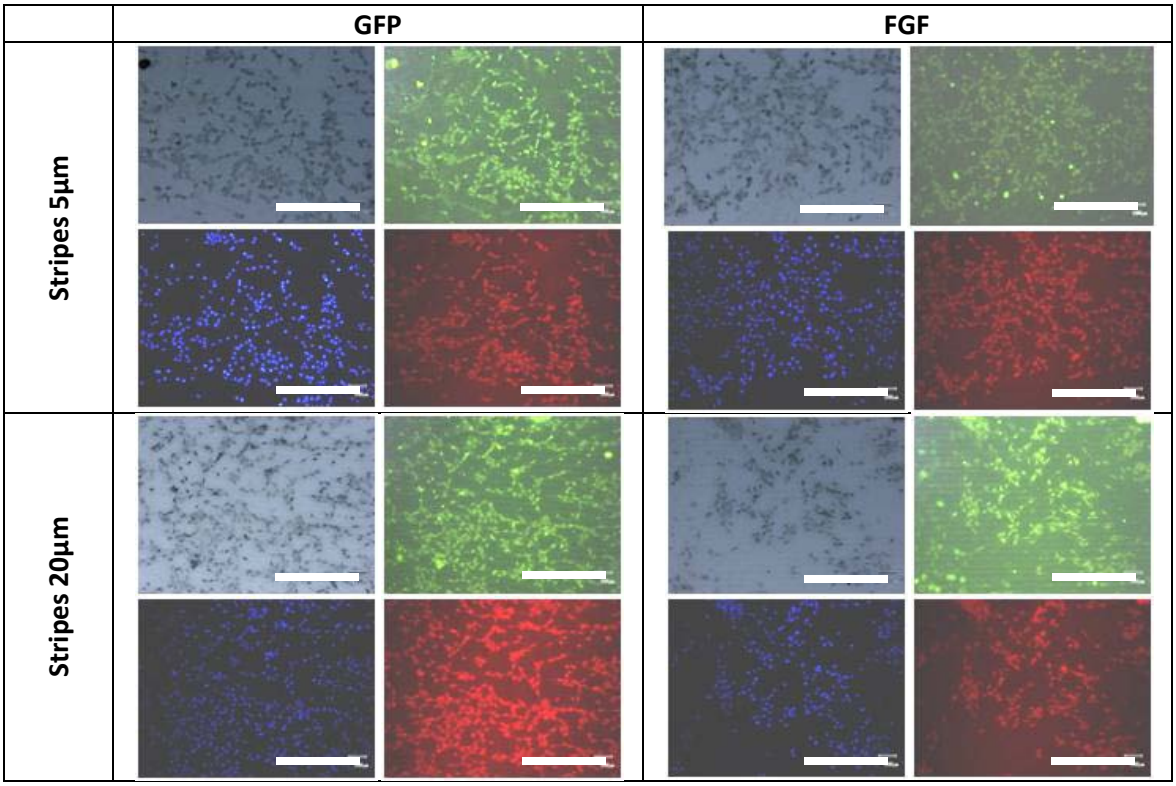

Figure 2.24 Example bright field and fluorescence (green – IBs, blue – nuclei and red – membrane) images of stained cells after 48 hours of cultivation on 5µm and 20µm patterned GFP- and FGF-derived IBs used for statistics. Scale bars indicate 500µm.

Detailed descriptions of all of the protocols used here can be found in Sections from A.7 ("Microcontact printing of IBs") to A.10 ("Image analysis").

2.3.5.1. *Cell positioning*

Cell positioning analysis was done in the same way as the one conducted for GFP-only patterns. There is practically no difference in the cells preference for inside or outside regions in the case of 5µm wide stripes, similarly to our findings in Section 2.3.4.1 ("Cell positioning"). However, as observed for GFP derived IBs the 20 µm wide stripes positioning analysis reveals that there is higher incidence for cells to grow over IBs rich zones instead of spaces between them (see Figure 2.25).

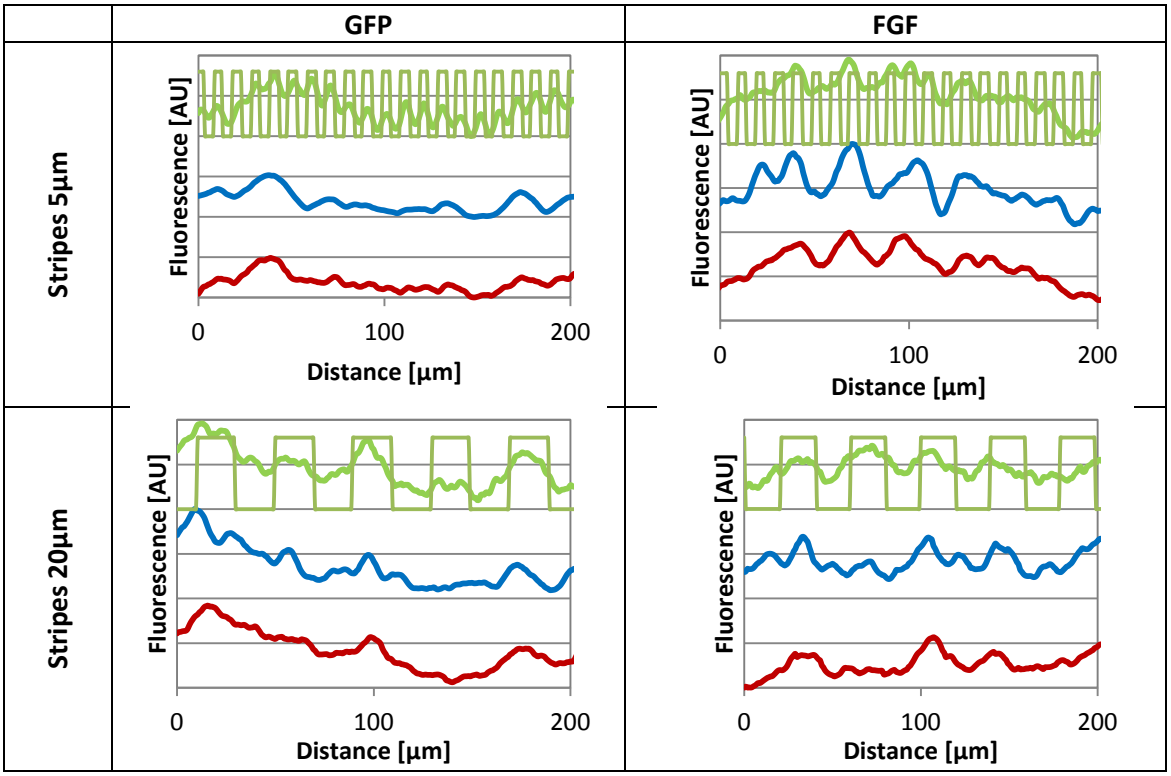

Figure 2.25 Positioning of cells after 48h of cultivation. Representative fluorescence profiles of IBs (in dark green), cell membrane (in red) and cell nuclei (in blue) after 48 of cultivation of NIH/3T3 cells on different substrates decorated with different IBs. Light green profile represents the "ideal" IB profile. Profiles are normalized so that maximal value is 1 and minimal is 0

As we have seen for the GFP patterns there is a clear correlation between the high IBs concentration in the pattern and the presence of cells for the 20µm stripes. Yet, cells can not accommodate on pattern that is smaller than itself (5µm stripes). However for bigger patterns non bound cells move and position themselves in the more suitable environment that happen to be IBs rich zones.

2.3.5.2. *Cell orientation*

Figure 2.26 shows in detail orientation distributions of cells growing on substrates patterned with GFP and FGF derived IBs. The spindle-like distribution observed for both GFP

and FGF patterned substrates. It is a clear indication of the cell membrane alignment to the horizontal direction following the patterned stripes and thus a strong guidance of the orientation. A coarse-grained analysis, that splits the cells´ orientations into three 30°-wide bins, highlights this effect even more. Figure 2.27 shows for both membrane and nuclei that cells growing on both GFP and FGF functionalized substrates are similarly oriented despite the much less proteic material deposited in case of FGF IB´s. The tendency that cells align better on 20µm wide stripes observed in previous experiments could also be clearly seen in this case.

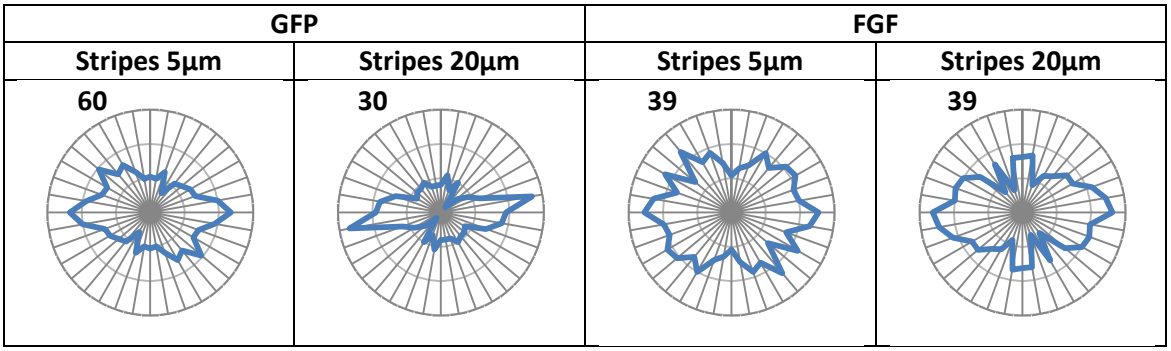

Figure 2.26 Impact of FGF biofunctional IBs pattern and culture time on NIH/3T3 cells orientation. Radial distribution plots of cell membranes' orientation versus frequency at 48 hours of cell culture for GFP and FGF patterned substrates. Data derived from patterns of 5 µm and 20µm stripes of IBs are shown. The spindle-like distribution for the pattern with stripes is an indication of the strong guidance of the orientation. Numbers indicate maximal value of the radial axis.

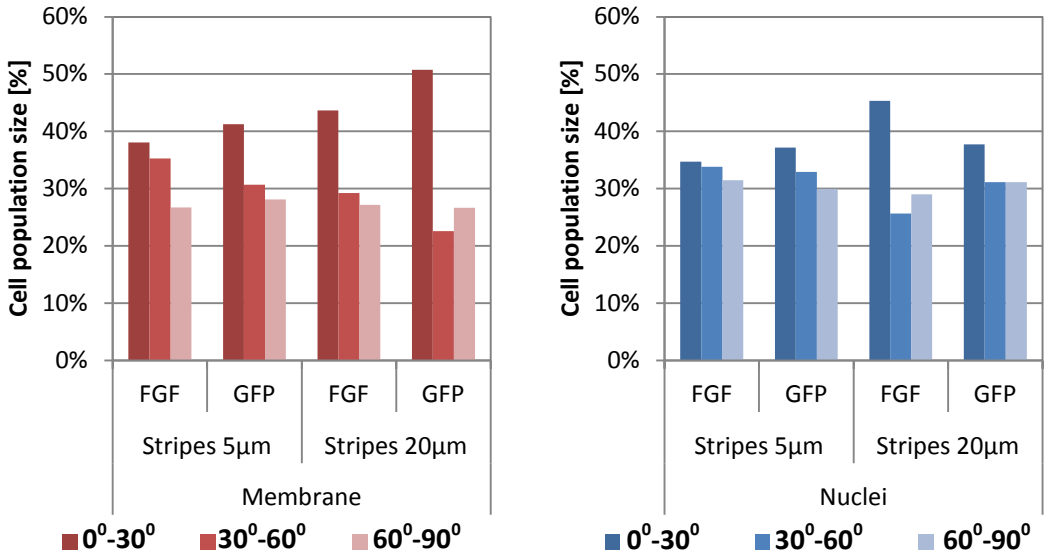

Figure 2.27 Coarse grained analysis of cell orientation. Cells were divided into three bins according to their aligning to the patterns: well oriented (0^0-30^0), moderately oriented (30^0-60^0) and misoriented (60^0-90^0). It appears that population of well-oriented cells is higher in every case, especially for the 20µm wide stripes.

2.3.5.3. Cell morphology

Morphology analysis also reveals that cells have similar morphology when cultivated on both types of substrates. A summary of aspect ratio average values is presented in Figure 2.28.

Geometry of pattern do not have much impact on cell morphology, as values of aspect ratio are very similar for both types of stripes used in this experiment. However one can observe an influence of the type of IBs on the cell shapes. Significant differences in morphology can be seen between cells cultured over functional (FGF) and non-functional (GFP) IBs after first 24 hours after seeding. Cells growing over GFP are characterized by elongated morphology that diminishes with time. Average aspect ratio of cells cultured over FGF is lower and it does not change as much during whole cultivation period. In the end, after 72 hours after seeding, all cells have similar shape of slightly elongated ovoids, indicating their correct and healthy development. This might be attributed to two factors. First, one can conclude, that cells growing over FGF-derived IBs acquire the final shape quicker, due to the functional properties of these nanoparticles. On the other hand, larger elongation of fibroblasts growing over GFP-derived IBs patterns might a result of higher IBs concentration. Higher IBs concentration in the "ink" suspension during µCP translates to more developed topography in patterned zones due to higher number of deposited IBs.

One way or another, this behaviour do not resemble our observations for 1BR3.G fibroblast cultivated on "Random" or "Blank" patterns (see Figure 2.20). Cell´s morphology is elongated from the very beginning, indicating, that both types of IBs have positive influence on cells morphology in this case. What is also worth of mentioning, is that the same morphology is achieved even if functional IBs concentration was over one order of magnitude lower, than in the case of GFP IBs. This evidences the impact of functional FGF IBs on the cell guidance.

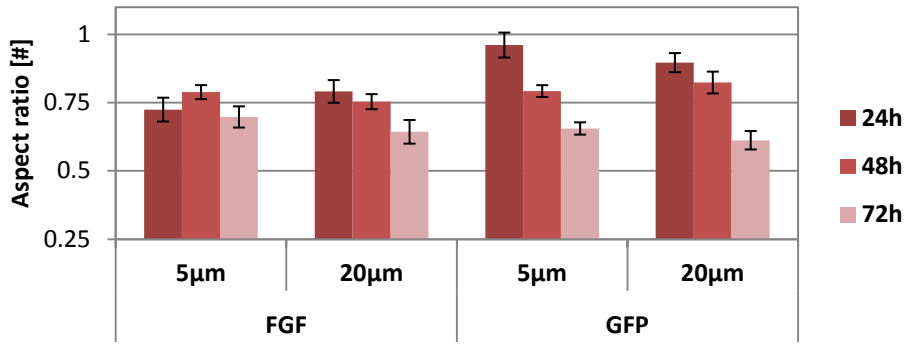

Figure 2.28 Influence of IBs types on the cell morphology. Average aspect ratio of cells membrane growing on the different IBs patterned substrates with error bars indicating +/- standard errors. The evolution of cell's membrane elongation with time can be traced for each pattern.

2.4. Conclusions

We have successfully engineered at the microscale planar supports by decorating them with a novel protein based nanomaterial, based on bacterial IBs, using a modification of the μCP technique that allows increasing the mass transfer of IBs from the stamps to the substrates. After a first optimization of the IBs density used for the patterning, we have cultured fibroblast cells over these supports and established a protocol to investigate IB-based regulation of cellular functions. One of the contributions of this study relies on the design of a novel methodology for the statistical analysis of images of cells cultured at different times over patterns of IBs, with various geometries and densities, to study the behaviour of cells. This method of analysis represents a new useful and generic tool for other researchers in the field. Specifically, in the present work, these analyses enabled the study of the influence of different structured of IBs on the orientation, morphology, and positioning of cells, demonstrating the importance of 2D microscale engineering and the usefulness of the IB nanoscale profiling for cell guidance. We have also shown that cells preferentially adhere to IB-rich areas, aligning and elongating according to the dimensions and shape of the IB pattern choosing the shortest way to reach new adhesion spots on the neighbouring IBs. FGF-derived IBs are proven to have some influence on cell growth especially on the cell morphology. Therefore synergy between biological activity and topographical stimuli of cells by IBs is confirmed.

This two dimensional engineering technique, based on IBs fills, the gap between the existing protocols which are based on the local modification of the chemical nature of the surface and those based on the modification of the topography at the nanoscale level by physical methods. This is due to the fact, that IBs combine at the same time biofunctionality as well as mechanical properties that are significant for topographical modification of the substrate. It has therefore been proved that IBs are interesting and useful nanomaterials in the control of cell culture as well as promising biomaterials for regenerative medicine.

2.5. Bibliography

[1] Hoffman-Kim D., Mitchel J. A., Bellamkonda R. V. “Topography, Cell Response, and Nerve Regeneration”; *Annu. Rev. Biomed. Eng.* **2010**, Vol. 12, 203–231

[2] Ito A., Hayashida M., Honda H., Hata K., Kagami H., Ueda M., Kobayashi T. “Construction and Harvest of Multilayered Keratinocyte Sheets Using Magnetite Nanoparticles and Magnetic Force”; *Tissue Eng.* **2004**, Vol. 10, 873–880

[3] Dalby M.J., McCloy D., Robertson M., Agheli H., Sutherland D., Affrossman S., Oreffo R.O.C. “Osteoprogenitor Response to Semi-ordered and Random Nanotopographies” *Biomaterials* **2006**, Vol. 27, 2980–2987

[4] Heydarkhan-Hagvall S., Choi C.H., Dunn J., Heydarkhan S., Schenke-Layland K., MacLellan W.R., Beygui R. “Influence of Systematically Varied Nano-scale Topography on Cell Morphology and Adhesion” *Cell Commun. Adhes.* **2007**, Vol. 14, 181–194

[5] Uttayarat P., Toworfe G.K., Dietrich F., Lelkes P.I., Composto R.J. “Topographic Guidance of Endothelial Cells on Silicone Surfaces with Micro- to Nanogrooves: Orientation of Actin Filaments and Focal Adhesions” *J. Biomed. Mater. Res.* **2005**, Vol. 75A, 668–680

[6] McKee C.T., Raghunathan V.K., Nealey P.F., Russell P., Murphy C.J. “Topographic Modulation of the Orientation and Shape of Cell Nuclei and Their Influence on the Measured Elastic Modulus of Epithelial Cells” *Biophys. J*. **2011**, Vol. 101, 2139–2146

[7] Peterbauer T., Yakunin S., Siegel J., Hering S., Fahrner M., Romanin C., Heitz J. “Dynamics of Spreading and Alignment of Cells Cultured in Vitro on a Grooved Polymer Surface” *J. Nanomater*. **2011**, 413079–413088

[8] Hu H., Ni Y., Montana V., Haddon R.C., Parpura V. "Chemically functionalized carbon nanotubes as substrates for neuronal growth"; Nano Letters 2004, Vol. 4(3), 507-511

[9] San Thian E., Ahmad Z., Huang J., Edirisinghe M.J., Jayasinghe S.N., Ireland D.C., Brooks R.A., Rushton N., Bonfield W., Best S.M. "The role of electrosprayed apatite nanocrystals in guiding osteoblast behaviour"; *Biomaterials* **2008**, Vol. 29(12), 1833-1843

[10] Ferreira L., Karp J.M., Nobre L., Langer R. "New Opportunities: The Use of Nanotechnologies to Manipulate and Track Stem Cells"; *Cell Stem Cell* **2008**, Vol. 3(2), 136-146

[11] Shi J., Votruba A.R., Farokhzad O.C., Langer R. "Nanotechnology in drug delivery and tissue engineering: From discovery to applications"; *Nano Letters* **2010**, Vol. 10(9), 3223-3230

[12] Roach P., Eglin D., Rohde K., Perry C.C. "Modern biomaterials: A review - Bulk properties and implications of surface modifications"; *Journal of Materials Science: Materials in Medicine* **2007**, Vol. 18(7), 1263-1277

[13] Philipsborn A.C., Lang S., Bernard A., Loeschinger J., David C., Lehnert D., Bastmeyer M., Bonhoeffer F. "Microcontact Printing of Axon Guidance Molecules for Generation of Graded Patterns" *Nature Protocols* **2006**, Vol. *1* (3), 1322-1328

[14] Falconnet D., Csucs G., Grandin H.M., Textor M. "Surface Engineering Approaches to Micropattern Surfaces for Cell-Based Assays" *Biomaterials* **2006**, Vol. 27, 3044-3063

[15] Ruiz S.A., Chen C.S. "Microcontact Printing: A Tool to Pattern" *Soft Matter* **2007**, Vol. 3, 168-177

[16] Mrksich M., Dike L.E., Tien J., Ingber D.E., Whitesides G.M. "Using Microcontact Printing to Pattern the Attachment of Mammalian Cells to Self-Assembled Monolayers of Alkanethiolates on Transparent Films of Gold And Silver" *Experimental Cell Research* **1997**, Vol. 235, 305-313

[17] Zhang S., Yan L., Altman M., LaKssle M., Nugent H., Frankel F., Lauenburger D.A., Whitesides G.M., Rich A. "Biological Surface Engineering: A Simple System for Cell Pattern Formation" *Biomaterials* **1999**, Vol. 20, 1213-1220

[18] Zhang J., Nie J., Mühlstädt M., Gallagher H., Pullig O., Jandt K.D. "Stable Extracellular Matrix Protein Patterns Guide the Orientation of Osteoblast-Like Cells" *Adv. Funct. Mater.* **2011**, Vol. 20, 1-9

[19] Lange S. A., Benes V., Kern D. P., Horber J.K.H., Bernard A. "Microcontact Printing of DNA Molecules" *Anal. Chem.* **2004**, Vol. 76, 1641-1647

[20] Yoo S.Y., Chung W.J., Kim T.H., Le M., Lee S.W. "Facile Patterning of Genetically Engineered M13 Bacteriophage for Directional Growth of Human Fibroblast Cells" *Soft Matter* **2011**, Vol. 7, 363-368

[21] Raghavan S., Desai R. A., Kwon Y., Mrksich M., Chen C. S. "Micropatterned Dynamically Adhesive Substrates for Cell Migration" *Langmuir* **2010**, Vol. 26(22), 17733-17738

[22] Yan X., Yao J., Lu G., Chen X., Zhang K., Yang B. "Microcontact Printing of Colloidal Crystals" *J. Am. Chem. Soc.* **2004**, Vol. 126, 10510-10511

[23] Weibel D.B., Lee A., Mayer M., Brady S.F., Bruzewicz D., Yang J., DiLuzio W.R., Clardy J., Whitesides G.M. “Bacterial Printing Press That Regenerates Its Ink: Contact-Printing Bacteria Using Hydrogel Stamps” *Langmuir* **2005**, Vol. 21, 6436-6442

[24] Liu W.F., Chen C.S “Engineering biomaterials to control cell function” *Materials Today* **2005**, Vol. 8, 28-35

[25] Martinez E., Engel E., Planell J.A., Samitier J. “Effects of Artificial Micro- And Nano-Structured Surfaces on Cell Behaviour” *Ann. Anat* **2009**, Vol. 191, 126-135

[26] Bettinger C.J., Langer R., Borenstein J.T. “Engineering Substrate Topography At the Micro- And Nanoscale to Control Cell Function” *Angew. Chem. Int. Ed.* **2009**, Vol. 48, 5406-5415

[27] Clark P., Connolly P., Curtis A.S.G., Dow J.A.T., Wilkinson C.D.W. “Cell Guidance By Ultrafine Topography In Vitro” *Journal of Cell Science* **1991**, Vol. 99, 73-77.

[28] Dalby M.J., Gadegaard N., Riehle M.O., Wilkinson C.D W., Curtis A.S.G. “Investigating Filopodia Sensing Using Arrays of Defined Nano-Pits Down to 35 nm Diameter in Size” *International Journal of Biochemistry & Cell Biology* **2004**, Vol. 36, 2005 2015

[29] Teixeira A.I., Abrams G.A., Bertics P.J., Murphy C.J., Nealey P.F. “Epithelial Contact Guidance on Well-Defined Micro- And Nanostructured Substrates” *Journal of Cell Science* **2003**, Vol. 116, 1881-1892

[30] Abdullah C.A.C., Asanithi P., Brunner E.W., Jurewicz I., Bo C., Azad C.L., Ovalle-Robles R., Fang S., Lima M.D., Lepro X., Collins S., Baughman R.H., Sear R.P., Dalton A.B. “Aligned, Isotropic And Patterned Carbon Nanotube Substrates That Control the Growth And Alignment of Chinese Hamster Ovary Cells” *Nanotechnology* **2011**, 22, 205102

[31] Kang K., Choi S.E., Jang H.S., Cho W.K., Nam Y., Choi I.S., Lee J.S. “In-Vitro Developmental Acceleration of Hippocampal Neurons on Nanostructures of Self-Assembled Silica Beads In Filopodium-Size Ranges” *Angew. Chem. Int. Ed.* **2011**, Vol. 50, 1-5

[32] Charest J.L., Eliason M.T., Garcia A.J., King W.P. “Combined Microscale Mechanical Topography And Chemical Patterns on Polymer Cell Culture Substrates” *Biomaterials* **2006**, Vol. 27, 2487-2494

[33] Feinberg A.W., Wilkerson W.R., Seegert C.A., Gibson A.L., Hoipkemeier-Wilson L., Brennan A.B. “Systematic Variation of Microtopography, Surface Chemistry And

Elastic Modulus And the State Dependent Effect on Endothelial Cell Alignment" *Journal of Biomedical Materials Research Part A* **2008**, Vol. 86 (2), 522-534

[34] Recknor J.B., Sakaguchi D.S., Mallapragada S.K. "Directed Growth And Selective Differentiation of Neural Progenitor Cells on Micropatterned Polymer Substrates" *Biomaterials* **2006**, Vol. 27, 4098-4108

[35] Villaverde A., Carrio M.M. "Protein aggregation in recombinant bacteria: Biological role of inclusion bodies" *Biotechnol. Lett.* **2003**, Vol. 25, 1385

[36] Carrió, M.M., Corchero, J.L., Villaverde, A. "Dynamics of in vivo protein aggregation: Building inclusion bodies in recombinant bacteria"; *FEMS Microbiology Letters* **1998**, Vol. 169, 9-15

[37] Bowden G.A., Paredes A.M., Georgiou G. "Structure and morphology of protein inclusion bodies in Escherichia coli" *Bio/Technology* **1991**, Vol. 9, 725-730

[38] Carrió M.M., Cubarsi R., Villaverde A. "Fine architecture of bacterial inclusion bodies"; *FEBS Letters* **2000**, Vol. 471, 7-11

[39] Bucciantini M., Giannoni E., Chiti F., Baroni F., Formigli L., Zurdo J., Taddei N., Ramponi G., Dobson C.M., Stefani M. "Inherent toxicity of aggregates implies a common mechanism for protein misfolding diseases"; *Nature* **2002**, Vol. 416, 507–511

[40] Baneyx F., Mujacic M. "Recombinant protein folding and misfolding in Escherichia coli"; *Nat. Biotechnol.* **2004**, Vol. 22, 1399–1408

[41] Ventura S., Villaverde A. "Protein quality in bacterial inclusion bodies"; *Trends Biotechnol.* **2006**, Vol. 24, 179-185

[42] Neubauer P., Fahnert B., Lilie H., Villaverde A. "Inclusions in Prokaryotes"; *Microbiology Monographs Vol. 1* **2006**, Ed: J.M. Shively, Springer, Berlin (Germany)

[43] Garcia-Fruitos E., Rodriguez-Carmona E., Diez-Gil C., Ferraz R.M., Vazquez E., Corchero J.L., Cano-Sarabia M., Ratera I., Ventosa N., Veciana J., Villaverde A. "Surface Cell Growth Engineering Assisted By A Novel Bacterial Nanomaterial"; *Adv. Mater.* **2009**, Vol. 21, 4249

[44] Rodríguez-Carmona E., Villaverde A. "Nanostructured Bacterial Materials for Innovative Medicines"; *Trends Microbiol*. **2010**, Vol. 18(9), 423-430

[45] García-Fruitós E., Vazquez E., Díez-Gil C., Corchero J.L.; Seras-Franzoso J., Ratera I., Veciana J., Villaverde A. "Bacterial Inclusion Bodies: Making Gold from Waste"; *Trends Biotechnol.* **2012**, Vol. 30, 65–70

[46] García-Fruitos E., Seras-Franzoso J., Vazquez E., Villaverde A. “Tunable Geometry of Bacterial Inclusion Bodies As Substrate Materials for Tissue Engineering”; *Nanotechnology* **2010**, Vol. 21, 205101

[47] Rodríguez-Carmona E., Cano-Garrido O., Seras-Franzoso J., Villaverde A., García-Fruitós E. “Isolation of Cell-Free Bacterial Inclus ion Bodies” *Microbial Cell Factories* **2010**, Vol. 9, 71

[48] Villaverde A. “Bacterial Inclusion Bodies: An Emerging Platform for Drug Delivery and Cell Therapy”; *Nanomedicine* **2012**, Vol. 7, 1277–1279

[49] Villaverde A., García-Fruitós E., Rinas U., Seras-Franzoso J., Kosoy A., Corchero J.L., Vazquez E. “Packaging Protein Drugs as Bacterial Inclusion Bodies for Therapeutic Applications”; *Microb. Cell Fact.* **2012**, Vol. 11, 76

[50] Vazquez E., Corchero J. L., Burgueno J.F., Seras-Franzoso J., Kosoy A., Bosser R., Mendoza R., Martínez-Láinez J.M., Rinas U., Fernandez E., Ruiz-Avila L., García-Fruitós E., Villaverde A. “Functional Inclusion Bodies Produced in Bacteria as Naturally Occurring Nanopills for Advanced Cell Therapies”; *Adv. Mater.* **2012**, Vol. 24, 1742–1747

[51] Nahalka J., Dib I., Nidetzky B.E. “Encapsulation of Trigonopsis variabilis D-amino acid oxidase and fast comparison of the operational stabilities of free and immobilized preparations of the enzyme”; *Biotechnol. Bioeng.* **2008**, Vol. 99, 251-260

[52] Nahalka J., Gemeiner P., Bucko M. Wang P.G. “Bioenergy beads: A tool for regeneration of ATP/NTP in biocatalytic synthesis”; *Artif. Cells Blood Substit. Immobil. Biotechnol.* **2006**, Vol. 34, 515-521

[53] Nahalka J., Vikartovska A., Hrabarova E. “A crosslinked inclusion body process for sialic acid synthesis”; *Biotechnol.* **2008**, Vol. 134, 146-153

[54] Nahalka J. „Physiological aggregation of maltodextrin phosphorylase from Pyrococcus furiosus and its application in a process of batch starch degradation to alpha-D-glucose-1-phosphate”; *Ind. Microbiol. Biotechnol.* **2008**, Vol. 35, 219-223.

[55] Díez-Gil C., Krabbenborg S., García-Fruitós E., Vazquez E., Rodríguez-Carmona E., Ratera I., Ventosa N., Seras-Franzoso J., Cano-Garrido O., Ferrer-Miralles N., Villaverde A., Veciana J. “The Nanoscale Properties of Bacterial Inclusion Bodies And their Effect on Mammalian Cell Proliferation”; *Biomaterials* **2010**, Vol. 31, 5805

[56] Seras-Franzoso J., Díez-Gil C., Vazquez E., García-Fruitós E., Cubarsi R., Ratera I., Veciana J., Villaverde A. “Bioadhesiveness And Efficient Mechanotransduction Stimuli Synergistically Provided By Bacterial Inclusion Bodies As Scaffolds for Tissue Engineering”; *Nanomedicine* **2012**, Vol. 7(1), 79

[57] Carrio M.M., Villaverde A. “Role of molecular chaperones in inclusion body formation”; *FEBS Lett.* **2003**, Vol. 537, 215-221

[58] Garcia-Fruitos E., Martinez-Alonso M., Gonzalez-Montalban N., Valli M., Mattanovich D., Villaverde A. “Divergent genetic control of protein solubility and conformational quality in Escherichia coli”; *J. Mol. Biol.* **2007**, Vol. 374, 195-205

[59] Chang J.C., Brewer G.J., Wheeler B.C. “Modified Microstamping Technique Enhances Polylysine Transfer And Neuronal Cell Patterning”; *Biomaterials* **2003**, Vol 24, 2863-2870

[60] Charest J.L., Garcia A.J., King W.P. “Myoblast alignment and differentiation on cell culture substrates with microscale topography and model chemistries”; *Biomaterials* **2007**, Vol 28, 2202–2210

[61] Rivera-Gil P., Yang F., Thomas H., Li L., Terfort A., Parak W.J. “Development of an Assay Based on Cell Counting with Quantum Dot Labels for Comparing Cell Adhesion within Cocultures”; *Nano Today* **2011**, Vol. 6, 20–27

[62] Wood M.A., Wilkinson C.D., Curtis A.S. “The Effects of Colloidal Nanotopography on Initial Fibroblast Adhesion and Morphology”; *IEEE Trans. Nanobiosci.* **2006**, Vol. 5, 20–31

[63] Ballo A., Agheli H., Lausmaa J., Thomsen P., Petronis S. “Nanostructured Model Implants for In Vivo Studies: Influence of Well-Defined Nanotopography on De Novo Bone Formation on Titanium Implants”; *Int. J. Nanomed.* **2011**, Vol. 6, 3415–3428

[64] Dalby M.J., McCloy D., Robertson M., Agheli H., Sutherland D., Affrossman S., Oreffo R.O.C. “Osteoprogenitor Response to Semi-ordered and Random Nanotopographies”; *Biomaterials* **2006**, Vol. 27, 2980–2987

[65] McNamara L.E., McMurray R.J., Biggs M.J., Kantawong F., Oreffo R.O., Dalby M.J. “Nanotopographical Control of Stem Cell Differentiation”; *J. Tissue Eng.* **2010**, 120623

[66] Seras-Franzoso J., Peebo K., Corchero J.L., Tsimbouri M.P., Unzueta U., Rinas U., Dalby M.J., Vazquez E., García-Fruitós E., Villaverde A. “Nanostructured Bacterial Bio-Scaffold for the Sustained Bottom-up Delivery of Protein Drugs”; *Nanomedicine* **2013**, Vol. 8, 1587-1599

[67] Cano-Garrido O., Rodríguez-Carmona E., Díez-Gil C., Vázquez E., Elizondo E., Cubarsi R., Seras-Franzoso J., Corchero J.L., Rinas U., Ratera I., Ventosa N., Veciana J., Villaverde A., García-Fruitós E. “Supramolecular Organization of Protein-Releasing Functional Amyloids Solved in Bacterial Inclusion Bodies”; *Acta Biomater.* **2013**, Vol. 9, 6134–6142

3.Two dimensional gradient deposition of protein nanoparticles from colloidal suspensions

3.1. Objectives

In the previous Chapter we have demonstrated that cells can be guided by the IBs patterns. We have deeply studied its influence on cells positioning, orientation and morphology at three instances of time (24, 48 and 72 hours). In order to go one step forward we would like here to further explore the opportunities that are given by the use of IBs patterning for studying cell´s motility.

Cell motility in living organisms is directed by a number of stimuli, among them spatial biomolecular concentration and topological gradients. Thus, the objective of this Chapter will be the development of a new platform for the two dimensional engineering of gradients of protein nanoparticles (NPs) from colloidal suspensions. Our objective will be divided in three parts:

- Selection of the appropriate deposition technique that enables the control of patterning and the formation of gradients of IBs on surfaces.
- Development of a device that enables the deposition of IBs patterns from IBs colloidal suspensions in a controlled way.
- Development of a robust protocol for the gradient deposition of IBs colloids in a reproducible way to study of cell motility.

3.2. Introduction

3.2.1. Gradients for cell motility

Cell motility plays an essential role in both physiological (e.g. embryogenesis, wound healing) and pathological processes (e.g. tumour invasion). Controlling cell movement is also in the focus of regenerative medicine as it is vital for an implant to be accepted by the host. Because of its prominent role, immense effort has been made in understanding cell motility over the past few decades.

The driving force for cell movement in the complex physiological environment is the need of cells to accommodate to various stimuli such as gradients of soluble biomolecules, topography or stiffness of the environment [1]. Reproducing these gradients *in vitro* has been one of the most popular and effective approaches to study cell motility in recent years. These artificial gradients can be a result of spatial modifications of the concentration of small biomolecules, changes of substrate hydrophobicity, alterations of the substrate topographical (geometrical) and mechanical (stiffness) properties, among many others [2,3]. There are many different methodologies that can be used to generate such gradients (see Figure 3.1). One of most popular approaches is based on the **controlled diffusion** – where a gradient of concentration is being obtained as an effect of mass transport in the medium (liquid or gas) and then immobilized on the substrate. Spatial concentration due to diffusion is higher towards the source of defunding molecules. In this case, the sample to be functionalized can be exposed in a stationary environment [4] as well as in a flowing media, as in the case of microfluidics [5,6]. Another possibility to generate gradients is the use of **external stimuli** to induce uneven distribution of particles, molecules (dipoles) or electric charges in space. Both electric and magnetic fields can be applied depending on the properties of the system [7,8]. Time-dependent phenomena can be also used to obtain surface-bound gradients. In this so-called **recording approach**, reaction kinetics, reaction rate constants and activation energies can be studied [9,10]. Gradients can be also deposited by **screening** i.e. by the shielding of the sample in a corona discharge chamber or using a moving aperture during UV (plasma) radiation, or by drawing the substrate from an oxidising media [11,12,13]. Finally, one can use predetermined geometry of stamps or masks in order to **imprint** well defined (often discrete) gradients [14,15]. An excellent example of the use of gradients in order to find optimal condition for cell growth and its influence on cell movement can be found in the

Reference [16] where also an impressive application of machine learning algorithms for image data treatment is reported.

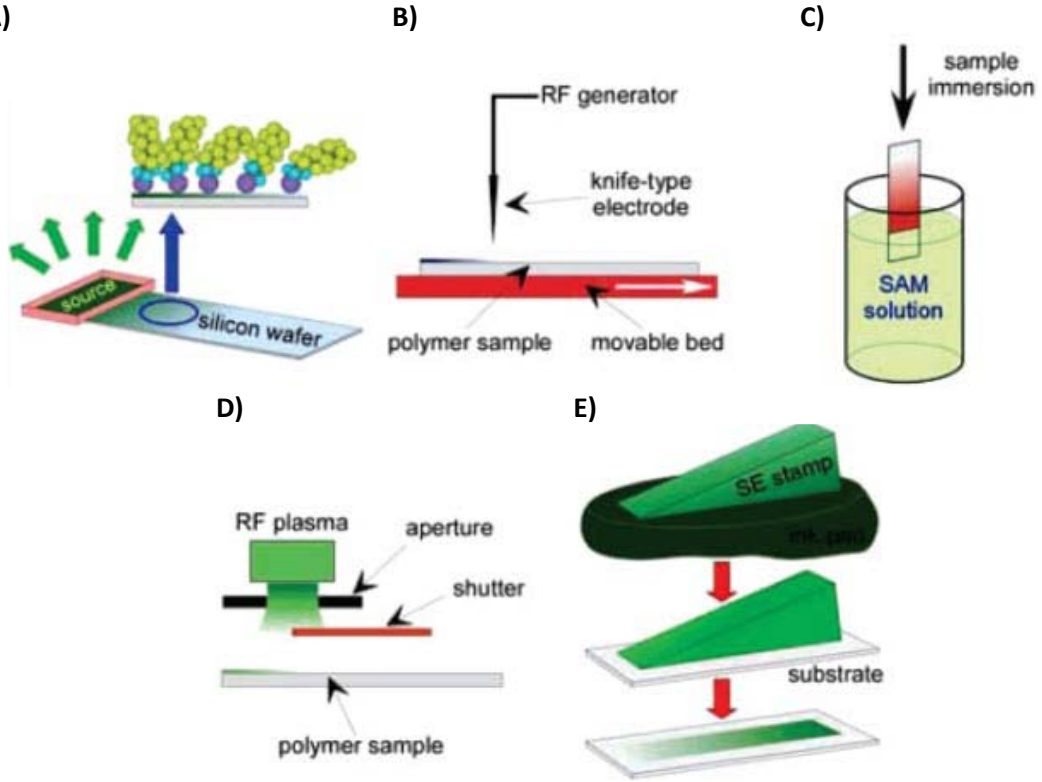

Figure 3.1 Examples of various methodologies used for gradient preparation. A) Controlled diffusion, B) External field application, C) Recording: time-dependent phenomena, D) Screening: shielding the sample from plasma discharge, E) Imprinting. Image adapted from Reference [3].

Using these techniques it is possible to obtain different kinds of surface-bound gradients each characterized by a unique set of properties such as directionality, dimensionality, length scale, or time dependency etc.

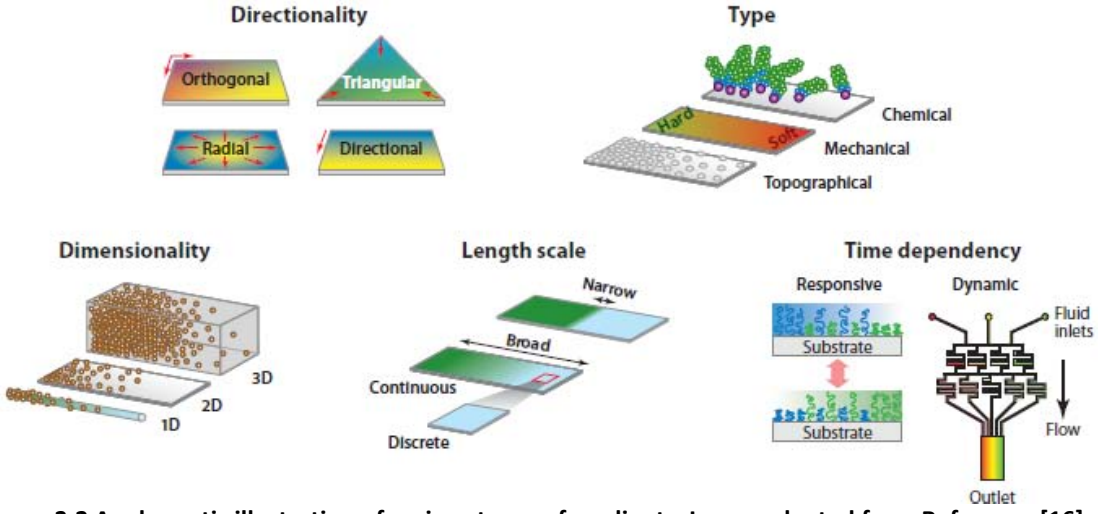

Figure 3.2 A schematic illustration of various types of gradients. Image adapted from Reference [16].

Moreover, gradients can be also of different nature i.e. chemical, topographical or mechanical (range of stiffness). Worth mentioning is the fact, that it is usually difficult to couple more than one nature of gradient, i.e. biochemical and topographic, in the same substrate. Examples of various types of gradients are presented in Figure 3.2

3.2.2. Controlled structuring of nanoparticles on surfaces

Fabrication structures out of nanoparticles is within industrial interest, as colloidal particles are fundamental building elements that can find many potential applications, such as transparent conductive electrodes [17,18] or plasmonic sensing materials [19], etc. Fabricating patterned structures including stripes, rings, grids and dot-arrays have been already reported [20]. Although general methodologies for the generation of surface-bound gradients from soluble factors has been already described, as far as we know there is no straightforward technique that allows obtaining surface-bound particle gradients from colloidal suspensions.

In order to address our objective we needed to find a technique to deposit gradients from colloidal suspensions, concretely from colloids of the previously introduced protein-based nanoparticles i.e. Inclusion Bodies. The use of protein nanoparticles will result in the simultaneous formation of both biochemical and topographical gradients on the surface which can be very interesting for cell motility studies since they will provide cells with two simultaneous inputs.

In order to determine which technique would be the best one for our purposes, we preformed a bibliographic search of the different methodologies that could be considered for this aim. These techniques can be classified as “bottom-up” or “top-down” approaches. The “bottom-up” approach refers to the formation of structures from basic nanoscale subunits. In this case the assembly is driven by chemical or physical forces present in the systems. The “top-down” approach refers to the processing of a macroscale bulk material to get nano sized features. In this case the structuration is governed by external stimuli, often using sophisticated appliances.

Below we have listed several techniques that were considered for this aim with a short description of their principles, advantages and disadvantages.

Bottom-up techniques:

- **Langmuir-Blodgett.** Methodically simple method that consist of drawing a substrate from a solution of surface-active molecules. Although it was originally developed for transferring monolayers of self-assembled amphiphiles from air-liquid interface onto substrate, its use have been broadened and experiments with nanoparticles and colloids have been reported. Good pattern resolutions can be obtained, however no gradient deposition of colloids has been reported to the authors best knowledge [21].
- **Layer-by-Layer.** This method consists of alternately depositing polyelectrolytes that self-assemble on the surface, leading to the formation of multilayer films. The driving forces behind deposition using this technique include electrostatic as well as non-electrostatic interactions such as hydrophobicity, hydrogen bonds, Van der Waals forces, charge transfer, halogen interactions and covalent bonds formed by click chemistry. To our best knowledge, no gradient formation has been reported with this technique so far, and poor spatial resolutions are obtained [22,23].
- **Electrophoretic deposition.** A processing technique that uses an external electric field to stimulate the movement of charged particles suspended in a colloidal suspension in order to deposit them on a substrate. Both thin and thick films, as well as free-standing bodies can be produced. It has been successfully used to manipulate biological materials, e.g. proteins, enzymes, cells, as well as colloids, polymers and solid inorganic particles. The main disadvantage of this technique for our purposes is that it is designed to cover large areas with homogenous layers [24,25].
- **Soft lithography.** This group of microfabrication techniques gathers many processes used for patterning surfaces used in chemistry and biology. Each of these processes use stamps or channels fabricated in an elastomeric ("soft") material to deposit patterns. Soft lithographic techniques are generally not expensive, procedurally simple and can be used to pattern a variety of different planar and non-planar substrates. Some examples are:
    - **Microcontact printing (μCP).** It is a widely known technique that uses the relief pattern on the surface of an elastomeric stamp (usually PDMS) to form patterns of SAMs on the surfaces of substrates. The stamp is "inked" with the desired solution/suspension, dried, and brought into conformal contact with a substrate. The material is transferred to the substrate only in the regions where the stamp contacts the substrate. This technique was adopted to a broad spectrum of deposited materials and surfaces. However it is usually used to generate homogenous deposits, not gradients [26]. It is also possible to use more than one stamp in order to transfer different types of materials onto the same substrate, which is called multicolour μCP [27,28].
    - **Robotic printing.** Robotic microspotters that are used to produce DNA or protein arrays for analytical and genomic assays. In theory, it could be used for production of well defined patterns of various proteins for cell cultivation study. However transition from soluble to colloidal material could be

cumbersome. Also, the high cost of the equipment is a rather limiting factor [29].

- **Microfluidics (μ-Fluidics).** In this approach a PDMS stamp with rows is in the conformational contact with sample and liquid pushed through these rows that serve as channels. Laminar conditions of flow enable fine control over time of interaction of fluid with surface, resulting in a straightforward approach for gradient fabrication out of soluble factors on prefunctionalized surfaces. A limiting factor is that colloidal particles used in working fluids can result in clogging of the tubing or PDMS canals [5,30].
- **Hybrid: μCP and μ-Fluidics.** Methods that combine microfluidics and microcontact printing have been recently reported. Stamps are being "multicolour inked" in μfluidics channels while laminar flow of two or more liquids is being pushed through. This pattern is being later on transferred onto the desired substrate. This technique has both advantages as well as disadvantages of both μCP and μfluidics [31,32].

- **Evaporation driven self-assembly (EDSA).** A general term to describe phenomena that occur during the evaporation of solutions and colloids leading to the formation of well-defined deposits. Some researchers regard dip, spin, spray, gravure, slot, roll and ink-jet coating as subclasses of EDSA [33]. Various phenomena that occur during evaporation are described in more detail in Section A.13 ("Evaporation-related phenomena"). Examples of evaporation driven self-assembly are:
  - **Coffee drop effect.** It is a well-known formation of a ring deposit in an evaporating sessile drop in which solids are dispersed, as it occurs in a drying coffee drop (hence the name). During evaporation dissolved material is being forwarded to the pinned rim (three-phase contact line). After evaporation, the ring-shaped deposit contains almost all solute and non uniform material distribution [34].
  - **Controlled Evaporative Self-Assembly (CESA).** It is a special case of "coffee-drop effect" when the contact line is periodically pinned to the surface during the evaporation. It results in stick-slip-like movement of the contact line and formation of deposit in form of periodical patterns [20,35].
  - **Dip coating.** In this process the substrate is being plunged into liquid with the solute and automatically dawned at low and constant speed in order to obtain homogenous layers. In contrast to Langmuir-Bodgett method, with this method: (i) is possible to deposit not only molecular monolayers, (ii) there is a speed/layer thickness dependence and (iii) not only amphiphilic molecules can be applied. Latest publications report also colloidal material depositions [36,37].
  - **Interfacial self-assembly.** Another, special case of coffee-effect in which highly ordered layers of nanoparticles are being formed during evaporation in precisely controlled conditions requiring organic solvents and geometries of the deposited particles [38,39].

Top-down techniques:

- **Dip-pen nanolithography.** It is a direct-write scanning probe-based lithography in which an atomic force microscopy (AFM) tip is used to deliver chemical reagents or solutions directly to nanoscopic regions of a target substrate. This technique is compatible with many inks, from small organic molecules to organic and biological polymers, and from colloidal particles to metal ions and sols. However, it requires expensive equipment [40,41,42,43].
- **Ink jet printing.** It is a group of techniques that are based on computerized machines that form, propel and deliver ink droplets onto the desired substrates. Recent advancements in this field consist of enhancement of resolution, droplet volume decrease or broadening the spectrum of materials, etc. Colloids can be printed by this methodology [44].
- **Photolitography.** It is a sophisticated technique of microfabrication developed for electronics. It uses light to transfer a geometrical pattern from the photomask to a light-sensitive layer of polymer (photoresist) on a substrate. Then a series of chemical treatment procedures are undertaken in order to create surface patterns [45].

An overall comparison of the mentioned techniques in the light of the requirements needed for our objective is presented in the Table 3.1. We have focused on four main requirements that need to be satisfied by an optimal technique: (i) control the pattern with enough resolution, (ii) the possibility to form gradients, (iii) the possibility to use nanoparticles (colloids) and (iv) the low cost. As far, as we know, there is no technique that up to now meets all these requirements.

Microcontact printing with IBs was proven to deliver good results when using simple patterns, as demonstrated in Chapter 2. However, the gained experience suggested that a complication of the protocol would not lead to expected results and repeatability.

Another promising technique is the CESA, as it allows to pattern colloids. However, a critical problem in controlling the surface pattern in this approach is its stochastic nature, leading to difficulties in predicting the periodicity of the structures [46]. Moreover, no gradient formation using CESA has been ever reported.

In general, there are only a few techniques that have been used to obtain gradients. If we focus our attention on the “gradient” column of Table 3.1, we found the techniques based on microfluidics could be considered. However they are difficult to work with particles (colloids). On the other hand, our attention was drawn to the “coffee drop” phenomena, which allows obtaining gradients of particles but little or no control over pattern can be achieved.

Taking all into account, in this Thesis we will develop a new methodology in order to fill the gap found for the evaporation driven self-assembly methods in order to obtain from colloids in a reproducible, simple and cheap way, gradients of nanoparticles on surfaces for cell guidance studies. In order to do so let us first have a closer look on the "coffee-drop effect".

Table 3.1. Summary of the surface modification techniques in the light of our objective of patterning gradients (or at least with resolution) of nanoparticles (colloids) at low cost. This table offers a snapshot view enabling efficient comparison between techniques and to identify potential techniques that satisfy our requirements. Symbol explanation: ☑-methods used for this purpose, ☒/☑-methods capable when optimized for specific use (not primary purpose of the method), ☒-not applicable or not reported.

Technique:			Patterning resolution	Gradients	Colloids	Low cost	References
Bottom-up	Langmuir-Bodgett		☒	☒	☑/☒	☑	[21]
	Layer-by-layer		☒	☒	☑	☑	[22,23]
	Electrophoretic deposition		☒	☒	☑	☑	[24,25]
	Soft litography	µCP	☑	☑/☒	☑/☒	☑	[26,27,28]
		Robotic printing	☑	☒	☑/☒	☒	[29]
		Microfluidics	☒	☑	☑/☒	☑	[5,30]
		Hybrid: µCP and Microfluidics	☑	☑	☒	☑	[31,32]
	Evaporation driven self assembly	Coffee-drop effect	☒	☑	☑	☑	[20,34]
		Controlled evaporative self assembly (CESA)	☑	☒	☑	☑	[35]
		Dip coating	☑	☒	☑/☒	☑	[36,37]
		Interfacial self assembly	☒	☒	☑	☑	[38,39]
Top-down	Dip-pen nanolitography		☑	☒	☑	☒	[40-43]
	Ink jet printing		☑	☒	☑	☒	[44]
	Photolitography		☑	☒	☑	☒	[45]

3.2.3. Evaporation of colloidal suspensions in confined conditions

The "coffee-drop effect" is named after the daily observation of stains left by coffee drops on plane surfaces. After drying, a characteristic deposit with a darker rim and a clear centre can be observed. This is opposed to homogenous deposition in which an even layer of material is formed. The rim of the drop defines the shape of the deposited pattern and in subject literature it is referred as "contact line", "pinning line" or the "three-phase line". The latter is to highlight the coexistence of a gas phase that enables evaporation, a liquid phase that evaporates and a solid substrate on which the particulate material is self-assembled (see Figure 3.3).

First scientific evidences of particle aggregation during evaporation date back to classic experiments of Perrin on determining the Avogadro number value, where he observed ordered patterns of gomme-gutte monodisperse particles [47]. The first direct observations were done by Denkov *et al*. while working with polystyrene latex particles [48]. As an effect of further work of the same group various parameters were recognised as critical for this phenomenon to occur, such as the meniscus shape and the liquid evaporation rate [49]. Early observations confirmed the occurrence of this phenomena on a variety of substrates (glass, metal, polyethylene, roughened Teflon, freshly cleaved mica, ceramic, and silicon), drop sizes (big drops, ø~15 cm^2 and in small drops, ø~1mm^2), solvents (water, acetone, methanol, toluene, and ethanol), solutes and their sizes (ranging from molecular sizes of sugar and dye compounds to the colloidal 10µm polystyrene microspheres) and volume fractions (from 10^{-6} to 10^{-1} v/v). Furthermore, the effect was observed in a range of environmental factors such as temperature, humidity and pressure.

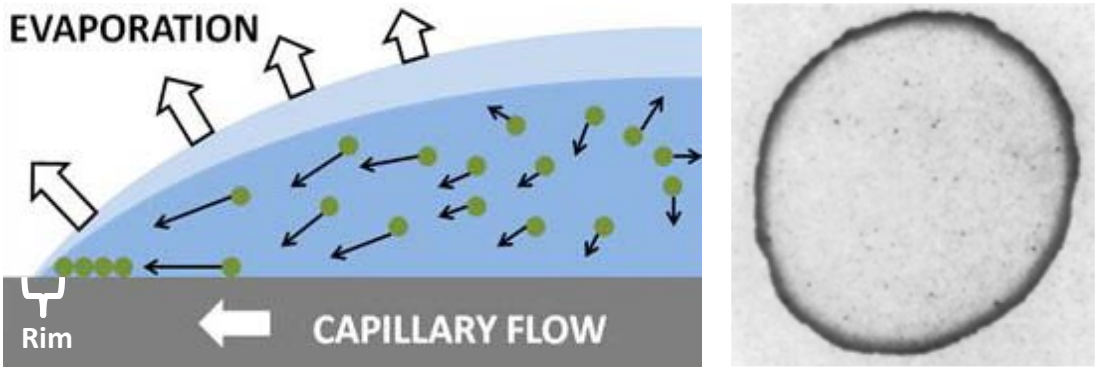

Figure 3.3 Scheme of coffee-drop effect. Left: the mechanism of outward flow during evaporation of a sessile colloidal drop left on a flat substrate. Internal flow of liquid caused by evaporation leads to deposition of particulate material in the rim of the droplet. Right: view of a "coffee ring" deposit with a radius of approximately 5 cm. Image reproduced from Ref. [20].

This phenomenon is due to a flow caused by the evaporation. When the "three-phase" line of the drying drop is pinned, the liquid evaporating from the edge must be replaced by the liquid from the bulk causing a flow that drags the suspended material to the drop rim. After evaporation a ring-like deposit is obtained (see Figure 3.3). The effect occurs as long as there is evaporation and resulting convective flow and the contact line can be pinned to the surface. This fact was confirmed by observations that no coffee rings are formed on hydrophobic and low friction Teflon surface or when evaporation is reduced at the drop perimeter [34a, 34b].

It has been found recently, that the particle-particle and particle-substrate interactions the gravity are parameters to be taken into account for the control of the "coffee ring" formation. A more complete description of particle kinetics based on experimental observations of drying

colloids by confocal microscopy has been given by Bodiguel *et al.* [50]. Numerical simulations of this phenomenon were used in order to confirm or reject possible requisites of deposit formation and to assess their impact on the final geometry of the ring stain. Monte-Carlo simulations showed that Marangoni flow and particle adsorption and interaction can even suppress the coffee-drop effect, leading to homogenous deposition. Factors such as the particle adsorption on the air-liquid interface, particle agglomeration and strong surface tension gradient, Derjaguin and Landau, Verwey and Overbeek theory (DLVO) forces between the particles, Brownian forces have a clear influence on the final shape of the ring deposit [34d,34e]. However, Rabani *et al.* have proved, that even coarse-grained square-lattice simulations of colloidal suspension evaporation result in patterns very similar to real case examples, as long as they include dynamics of the evaporating solvent [51].

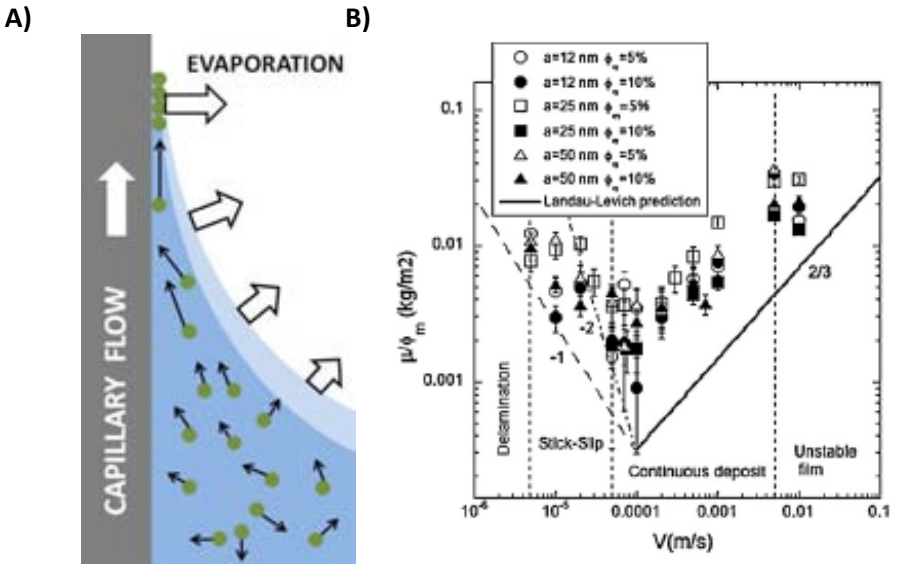

Figure 3.4 Mass deposition studied via dip coating of colloids. A) General scheme of liquid flow and meniscus configuration in a vertical orientation. B) Mass of silica colloids per unit surface deposed on a glass plate by dip coating versus deposition speeds, normalized by the initial particle mass concentration. Roughly, two regimes of deposition appear. The one on the right being linked to the entrainment of a Landau–Levich film at high plate velocity. The other on the left with deposition and evaporation directly at the contact line. The continuous line is the exact result expected from Landau–Levich, while the two discontinuous lines, of respective slope −1 and −2 are guides for the eyes. Image adapted from Ref. [36].

Apart from experimental and numerical approaches also theoretical physics were applied in order to reveal the mechanism of the phenomena occurring during evaporation of colloidal suspensions. Analytical models resulted in good agreement with spatial geometry [34f] and spatiotemporal evolution [34g] of deposit formation. It was also established that there can be two types of evaporation regimes in a sessile drying drop: one with outward circulation of solvent resulting in coffee-ring deposition (Figure 3.3) and another with an inward flow resulting in an homogenous deposition [34h]. In fact, many studies of the coffee drop effect

were motivated by the desire to avoid this phenomenon, as it is often regarded as a side effect or an artefact. It occurs especially in applications, where a homogenous deposition is required, such as in the printing industry or the polymer thin film deposition [52]. From these discoveries it has been found out that the addition of surfactants, namely sodium dodecyl sulfate (SDS), can be used to prevent the formation of coffee rings [53].

A recent study in this field was accomplished by Berteloot *et al.* [36] (see Figure 3.4). They examined the deposition thickness of a deposit as a function of contact line migration speed using the dip coating technique. Until this study, the speed of contact line movement over the substrate was not scrutinized as this parameter is rather difficult to control while working with sessile droplets. It was found that two regimes of deposition exist: one with increasing deposition material thickness with increasing speed corresponding to the Landau–Levich film at high plate velocity [54] and another with the opposite tendency corresponding to the direct evaporation at the contact line at low velocity resulting in the coffee-drop effect. In the second regime for a given range of concentrations of suspended particles the deposit thickness is inversely proportional to the speed of the contact line movement.

3.2.4. Applications of the evaporation driven self-assembly of nanoparticles

Exploration of the rich field of evaporation driven self-assembly has already resulted in a few ingenious applications, as for example a template-directed colloidal self-assembly technique. In this approach a colloidal suspension is let to evaporate on a substrate with a previously modified topography, where groves and pits guide the particles to the desired positions as drying front crosses these cues [55,56] (see Figure 3.5.A).

Other possibility proposed by Celio *et al.* [57] and Harris *et al.* [58], denominated as "confined dewetting lithography" or "evaporative lithography", uses microgrid masks as a template set above the substrate to control solvent evaporation. No topological or chemical pre-modification of the substrate is needed in order to deposit regular, geometrical patterns on flat substrates, (see Figure 3.5.B).

Another approach, is based on the introduction of a chemical pattern onto the surface. Predefined by microcontact printing, wettability patterns were reported to guide the deposition of colloids, as these zones govern the pinning and the dewetting phenomena [59,60,61] (see Figure 3.5.C). Very complex forms with single particle resolution using a similar method have been also reported [62].

However, as it was noticed by Watanabe and Miyahara [46] "(…) *those approaches still encounter a critical problem that any desired change in pattern periodicity or morphology requires another template mask that needs to be created by costly and complicated top-down lithography techniques. In that respect, a template-free or lithography- free self-assembly technique is strongly required to realize controlled fabrication of patterned structures of colloidal particles.*"

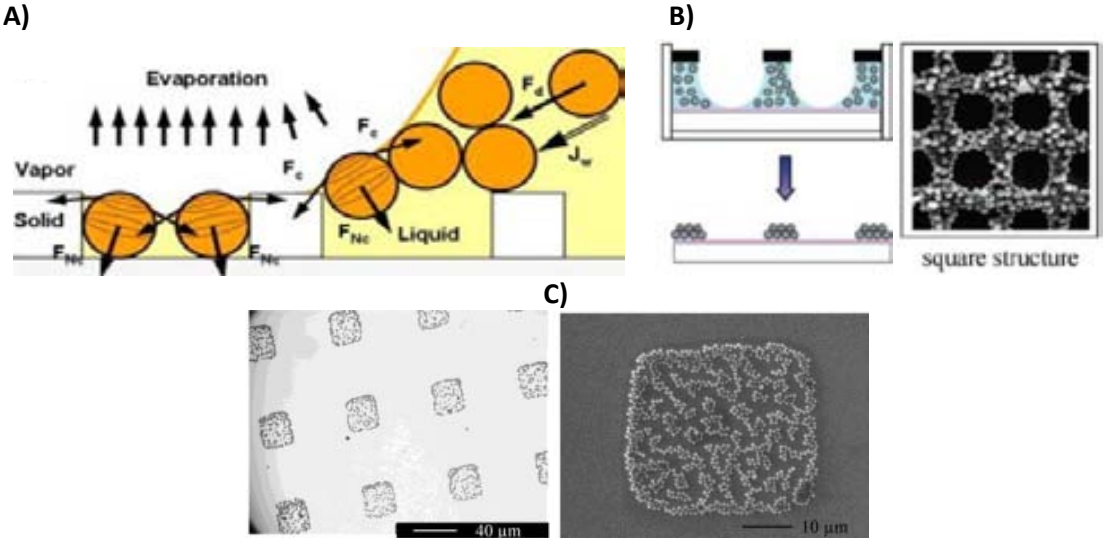

Figure 3.5 Examples of strategies used to pattern substrates using the coffee-drop effect. A) Sketch of the principle of capillary separation. Hydrodynamic (F_d) and capillary (F_c and F_{Nc}) forces exerted on colloids at the triple contact-line and the capillary forces responsible for colloids separation in a template. Image adapted from Reference [63]. B) A schematic view of "confined dewetting lithography" and an example of the resulting geometrical deposit. Evaporation of colloidal suspension is confined by the use of a mask. Image adopted from Reference [57].C) Colloidal particles assembled on 50nm carboxylic acid terminated square patterned SAMs surfaces on a continuous methyl-terminated surface. An optical micrograph (left) of 0.8µm microspheres deposited at 0.01% volume fraction and its corresponding SEM image (right) is presented. Images adopted from Reference [64].

A breakthrough in this field was recently made, when external control over the patterned stripe distances by an externally governed liquid level was demonstrated Miyahara *et al.* [65]. By using of computer-controlled syringe pump, fine tuning of the contact line velocity over the sample was achieved, having a direct impact on the geometry of deposited patterns. This technique, referred by the authors as convective self-assembly with liquid-level manipulation (CSA-LLM), enables governing the deposit geometry in a template-free manner as presented in Figure 3.6. It was successfully used to fabricate stripe, grid, and triangle patterns out of Au NPs colloids with controlled periodicity by a two- or three-step protocol by controlling macroscopic experimental parameters, such as particle concentration and temperature (Figure 3.7) [46,66]. Also hybrid grids using first silica and then silver NPs were obtained and studied [67]. Another

example consists of deposition of self-assembled “dotted lines” composed of gold NPs clusters [68]. To this point CSA-LLM was already applied to deposit stripes from aqueous suspensions of commercially available model nanoparticles (silica, Au, Ag) of range of sizes between 10 and 270nm on glass and polymer substrates (PS, PET) [46,66-69].

Recently, this technique has also been adapted to pattern thermoactive microgel stripes on substrates for spatially control of cell adhesion and detachment [69].

In spite of all of these advancements, to our best knowledge, there are no reported examples of using this approach to pattern surface-bound gradients of nanoparticles from colloidal suspensions. Thus, our objective was to develop a methodology based on the coffee-drop effect or CESA phenomena in order to pattern and form gradients of protein nanoparticles on surfaces for cell motility studies.

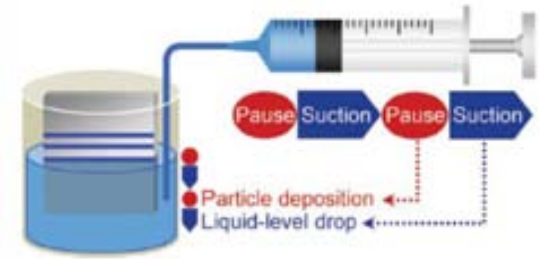

Figure 3.6 A schematic illustration of the convective self-assembly with liquid-level manipulation (CSA-LLM) technique. Stripes are deposited on a vertically oriented sample in a reservoir in which liquid level is governed by a syringe pump. Adopted from Reference [65].

As we wanted to apply this technique to deposition IBs, we aimed to take advantage of the fact, that interaction of this material with modified surfaces is well characterized [70]. In particular we aimed to chemically modify surface in order to incorporate an additional parameter to CSA-LLM method: control over substrate wettability. We aimed to enhance interactions between nanoparticles and the substrate and therefore enhance patterns formation. Ultimately two-dimensional surface-bound gradients of NPs could be obtained and applied to study cell motility.

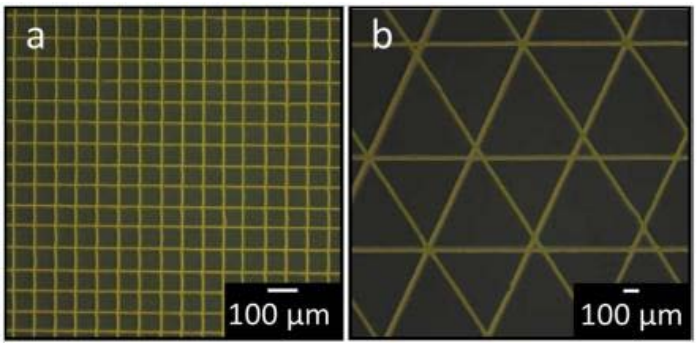

Figure 3.7 Optical images of a) rectangular grid pattern and b) triangle network from a 20nm gold particle suspension at 1.0×10^{-4} v/v by combining the convective self-assembly with liquid-level manipulation with the two/three-step convective self-assembly. Image reproduced from Reference [46].

3.3. Results and Discussion

Based on the bibliographic research presented in the Introduction to this Chapter, we have chosen the evaporation assisted methodology to pattern colloids of IBs on surfaces which up to now it has never been used to obtain gradients on surfaces of any NPs in a controlled way.

3.3.1. Evaporation of IBs suspensions

3.3.1.1. Preliminary studies

First of all, in order to evaluate whether or not IBs can be used for evaporation driven self-assembly, based on the coffee-drop effect, simple experiments with drying drops of their colloidal suspensions were preformed. IBs suspension at a concentration of approximately $4 \cdot 10^{11}$ particles/ml was prepared and small drops (1-3 µl) were deposited on clean glass slides and left to evaporate in the air at ambient temperature. A fluorescent microscopy video was used to study the flow of the particles towards the rims. Representative mosaic images of developing and final stains are presented in Figure 3.8. It can be seen that IBs float towards the rim, where they are pinned to the surface. Evolution of the fluorescence profile clearly indicates, that the deposition occurs firstly in the outer regions of the drop, i.e. on the three-phase contact line. This experiment confirmed that we have reproduced conditions, such as particle concentration, temperature, evaporation rate, etc., that enable the occurrence of the coffee-drop effect with IBs.

We have also checked for the occurrence of CESA. To obtain straight lines instead of the rings we used a cylinder-on-flat geometry as it has been already reported for other NPs [35]. A clean glass test tube was used as a cylinder and placed on a clean glass coverslip and a drop of aqueous suspension of IBs (1-5µl) was introduced into space between substrate and tube and left at room temperature for drying. In this configuration the liquid is confined between the substrate and the cylinder (cross-section presented in Figure 3.9 A). As drop is elongated along the cylinder and its rim is a straight line parallel to the tube. During evaporation this line moves towards tube and is periodically pinned to the substrate, leaving straight deposits due to CESA. Results are presented in Figure 3.9, where it is shown, that particles are forming clearly visible self-assembled lines due to stick-slip motion of the contact line of drying suspension. However, using this methodology, the striped pattern only occurs in a very narrow area of the whole deposition zone as indicated in Figure 3.9 B.

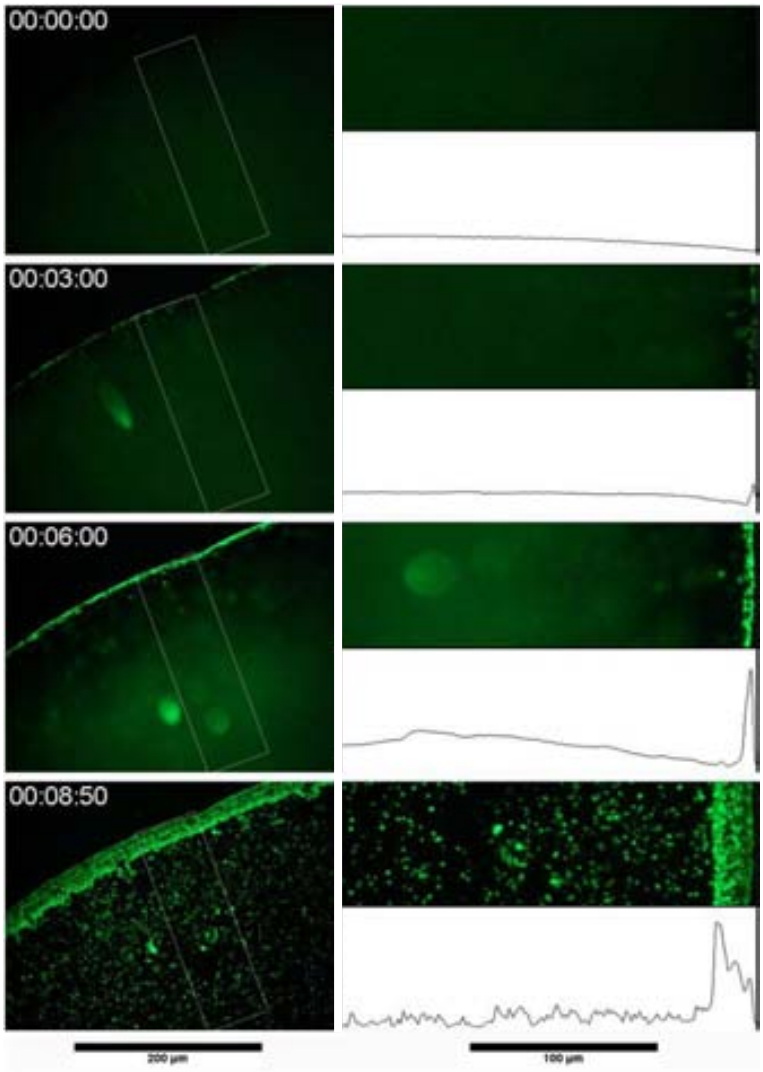

Figure 3.8 Mosaic of snapshots taken during in situ observation of drying drop of a GFP-derived IBs suspension. Left images shows the entire microscopic view of the drying drop. Right images shows an oriented zoom of the rim with its fluorescence profile (y-scale in arbitrary units). Time of snapshot is indicated in hh:mm:ss format.

Basing on these results, it was concluded, that although a IBs suspension can be processed using the CESA technique, the cylinder methodology is not a suitable, as only a small fraction of deposition area can be useful. Moreover, the precise control of the geometry of the pattern (separation between stripes, their width, etc…) depends on the parameters that are beyond control with this methodology.

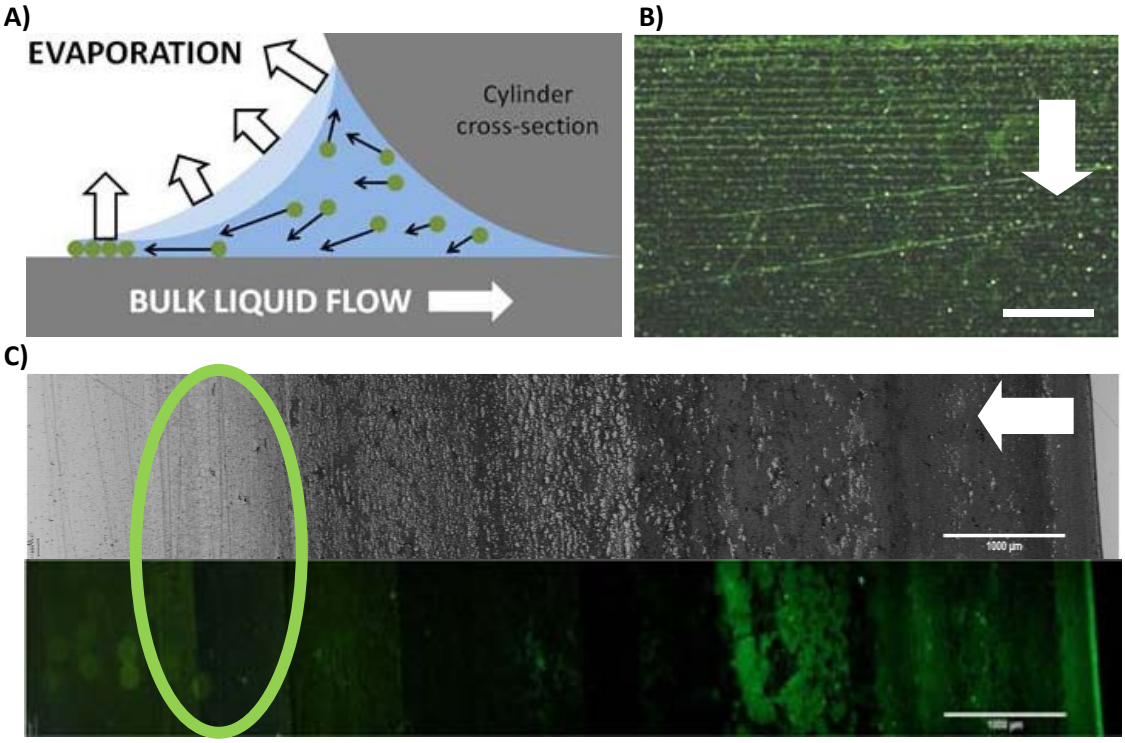

Figure 3.9 CESA patterns of evaporated IBs suspensions using a cylinder-on-flat geometry. A) Schematic view of the setup cross-section. B) Fluorescence image of zones where self-assembled lines of IBs were deposited (scale bar indicates 200 µm). White arrow indicates the direction of the contact line movement. C) Overall microscopic image of deposited IBs. CESA patterns occur only in a very narrow zone marked with an oval. Right-hand bright line corresponds to the initial pinning line of liquid. White arrow indicates direction of contact line movement.

Next, we explored the possibility of an external control of the pattern deposition. In order to externally control the liquid level to enable a template-free patterning, the glass coverslip substrate is introduced vertically into a 50 ml Falcon® tube with IBs suspension (at approximately $4 \cdot 10^{11}$ particles/ml), in which we have introduced a pump tubing. The pump was programmed to work in a step-wise manner removing precise amounts of the suspension in controlled periods of time. In this configuration the evaporation rate around the tip of the meniscus is larger than that of the bulk solvent due to the heat transfer from the substrate. The evaporation at the meniscus tip induces an upward convective flow to compensate the amount of the solvent evaporated (as in Figure 3.4). The convective flow carried particles into the meniscus tip, at which the particles assembled due to the laterally acting capillary force between the particles. This results in the deposition of IBs at the contact line while pump was stopped. Turning the pump on (removing some volume of liquid) provoked an abrupt change of the three-phase line position and introduce disruptions into otherwise continuous layer of IBs deposit being formed on the glass substrate. An example of deposited IBs pattern of lines is presented in Figure 3.10.

The final result consisted of a well defined pattern of lines, covering a big area of the surface. High concentration of IBs deposit was achieved in the lines and almost no IBs were deposited in between them while the pump was removing liquid. Accidental imperfections were caused by big impurities of the suspension that disturbed the contact line position resulting in curved patterns of the IBs deposit. It is worth noting that the kind of material that we are interested to structure is not conventional or commercially available monodisperse nanoparticles (Au, SiO_2, etc.). IBs are "soft" nanoparticles with a broad distribution of sizes and other physiochemical properties such as Z-potential, porosity, density, etc. They are made of a proteic material and obtained form a living bacteria. Thus, it must be taken into account that deposits obtained with this methodology are not as homogeneous and pure like the ones reported in the literature. Therefore handling with IBs is by far more challenging than with model nanoparticles that are routinely used in this field. Remarkable is also the interaction of IBs with surfaces with modified wettability. We have demonstrated that this parameter has clear impact on IBs adhesion, proving its importance in considered case [70].

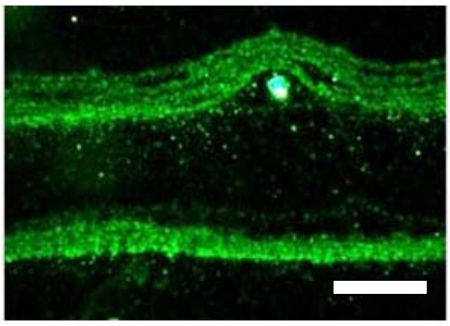

Figure 3.10 Example of fluorescence image of preliminary pump-induced patterns obtained from GFP-derived IBs suspensions. As it can be seen, deposited material follows the contact line geometry around impurities on the substrate, curvy deposits are formed. For production of straight lines it is vital to use suspensions free from big particles and impurities. Direction of contact line movement was from top to down. Scale bar indicates 200 µm.

3.3.1.2. Parameters optimisation for evaporation assisted pattern deposition of IBs

A) IBs colloidal suspension enhancing. In order to avoid formation of curved patterns due to impurities and to assure repeatability between IBs suspension batches, special care was devoted to IBs suspension preparation. In order to homogenize the IBs suspension we developed a protocol for the suspension preparation, consisting in resuspending IBs in water, sedimentation and decantation of the upper phase from above the precipitated impurities. This procedure is described in detail in the Section A.14 ("IBs suspension preparation for evaporation driven deposition").

B) Temperature control. As mentioned before, for the efficient deposition of particles a high evaporation rate is required. In case of aqueous media it can be done simply by rising the temperature. However, in our case too extreme temperatures would deteriorate the proteic material. On the other hand assembly at lower temperature results in disordered deposits due to insufficient liquid convection. As a compromise, during all depositions performed in this Thesis, a moderately high temperature of 60°C was used. We have confirmed that this temperature level can be withstood by IBs as its fluorescence is clearly visible even after the deposition process, so that the suspension can be reused more than once. In addition deposition at this temperature yielded well structured deposits of IBs on the surface.

C) Modification of surfaces. We have also optimized coverglass preparation protocol in order to enhance localized IBs deposition by increasing the interaction of IBs with the substrate. The protocol for coverglass cleaning consisted of 10 minutes sonication in EtOH, 10 minutes sonication in MiliQ water, 10 minutes sonication in EtOH and drying in a nitrogen flow. The resulting clean slides were used for deposition or additionally exposed to oxygen plasma or hexamethyldisilazane (HMDS, Sigma) in order to obtain hydrophobic surface. IN order to do so they were introduced into the dessicator and exposed to HMDS vapours overnight. A schematic of deposited SAM formation is presented in Figure 3.11.

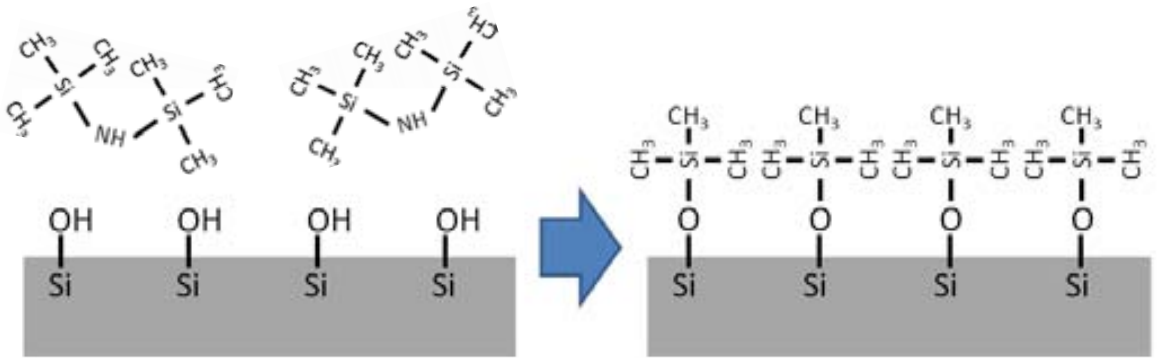

Figure 3.11 Schematic representation of HMDS chemisorption on a glass substrate. Dangling bonds of silicon atoms and native oxide are occupied with OH groups, leaving a hydrophilic surface. HMDS molecules leave their NH group and bind to the silicon atoms on the surface, leaving a hydrophobic surface. Adapted from Reference [71].

As presented in Figure 3.12, the best results of pattern deposition were obtained for glass functionalized with hydrophobic silane, since we have obtained more localized contact line and well pronounced patterns of IBs. We attribute This outcome to the nature of IBs, that are not regular, homogenous, monodisperse NPs. As this is proteic material, hydrophobic forces exists between proteic domains and may play important role in interactions between particle and substrate. In fact IBs are attracted to hydrophobic surfaces, as it was thoroughly studied in

Reference [70]. Moreover in the case of hydrophilic substrate, the deposition zone, that is the area close to the rim where particles are deposited, is broader. It results wider deposits but with less IBs concentration. In the case of hydrophobic surface, the contact line can be more precisely controlled and deposition occurs in narrower zone, as depicted schematically in Figure 3.12.

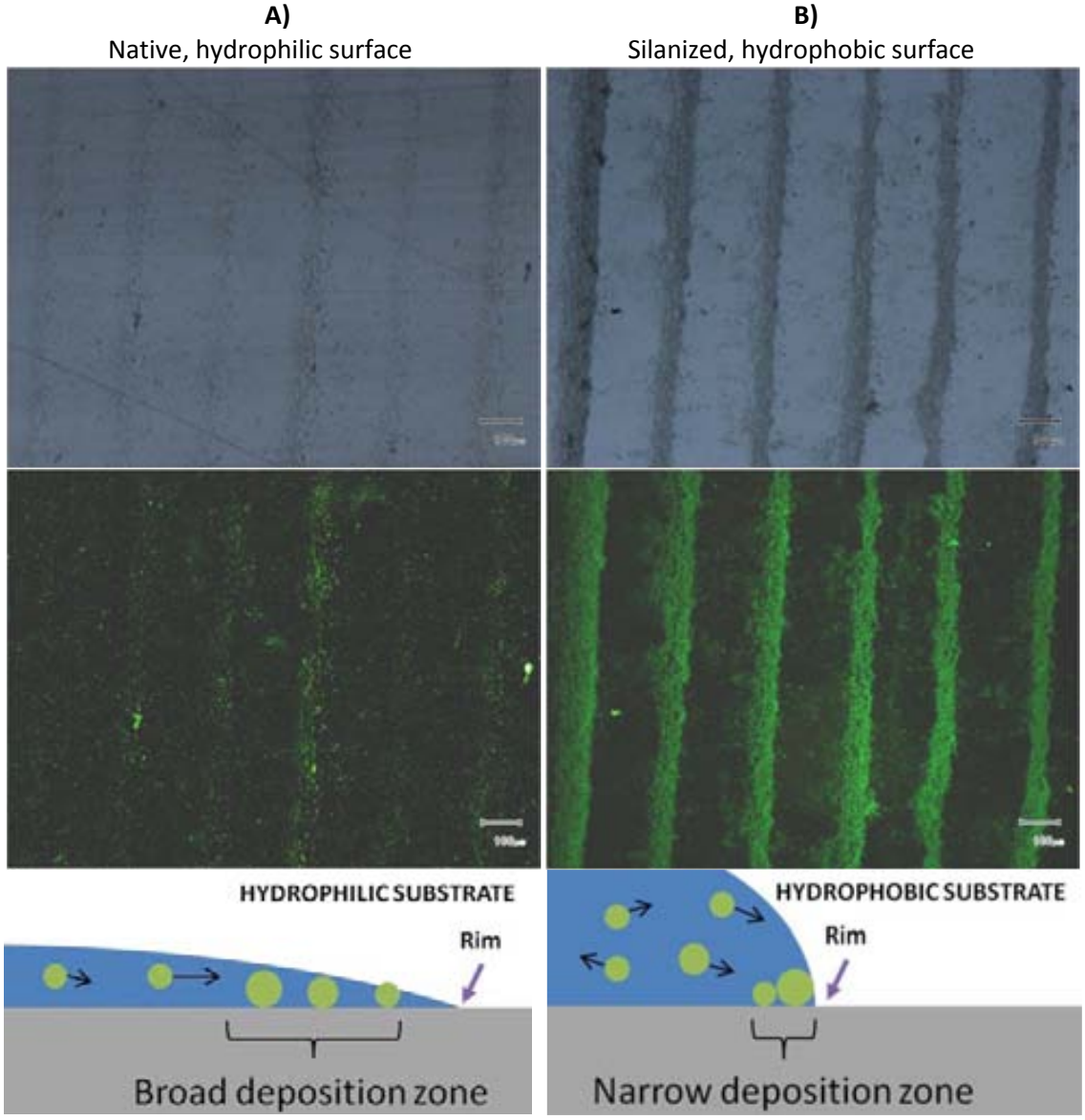

Figure 3.12 Comparison of IBs deposit formed on native and silanized glass substrates. Bright field microscopic images are presented in top row and corresponding fluorescence images in bottom row. Both depositions were performed at the same temperature, IBs concentration and pump protocol. Deposits on hydrophobic surfaces are better pronounced and higher IBs concentration is deposited.

Taking it all into account, the silanisation of clean glass coverslips were incorporated into optimised protocol of substrate preparation for all the experiments. When not in use, cleaned

and modified substrates were kept in dust-tight, dry containers. They were blown with nitrogen immediately before using in order to avoid any dust particles.

3.3.2. Development of a device for evaporation assisted pattern deposition

In order to perform pattern depositions of colloidal IBs over large areas in a controlled geometry and under temperature conditions a custom device was designed and constructed. A picture of the assembled device is presented in Figure 3.13. A cartoon of the cross-section and separate parts with their dimensions are presented in Figure 3.14.

We have designed this device taking into account two basic aims: to maximize the patterned area and to minimize the volume of the used suspension (ca. 10ml) as IBs is a limited and expensive material. To fulfil both requirements a rectangular deposition cuvette with a very narrow cross-section was used. The device consists of two planar polystyrene plates separated by a custom U-shaped PDMS seal and attached to rectangular metal reservoir by elastic rubber bands. When compressed, polystyrene plates and PDMS seal together forming a water-tight vessel that is large enough for introducing a 50mm x 25mm coverglass.

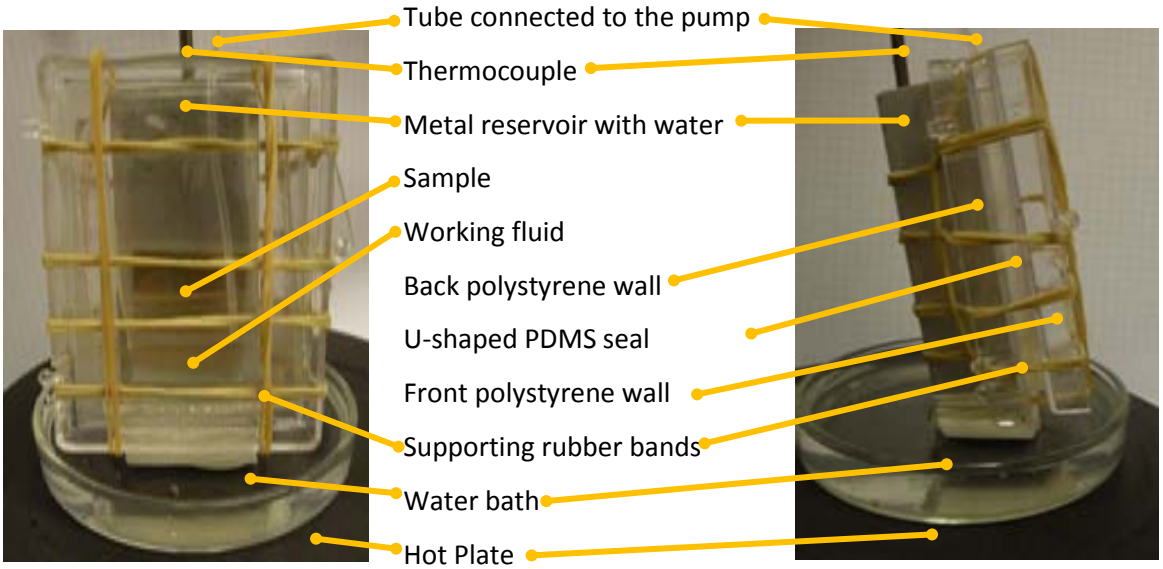

Figure 3.13 Assembled device for evaporation assisted patterning with liquid level control. Left: front view, right: side view.

Further advantages of the designed device are following: (i) the suspension in the reservoir has homogenous, controllable and constant temperature, which is very important for the reproducibility, and (ii) the movement of the contact line due to the evaporation is relatively slow when compared to the speed of the pump suction. The main disadvantage of this design

is that with a low cross-section of the cuvette the deposition accuracy is lower, and thus, small differences in liquid volume result in big differences in the three-phase line level.

Before mounting, all the internal parts of the cuvette were wiped with EtOH soaked paper in order to keep it clean and sterile. The open top of the cuvette enables the evaporation of the suspension and gives access to a tube leading to the peristaltic pump that allows the control over liquid level. During the deposition, the device is put on a hot plate in a water-filled Petri dish. Device rests firmly on the lower part of reservoir with a stable position, but slightly tilted in the direction of sample. The temperature is controlled with a thermocouple put into the metal reservoir filled with water for getting a better thermal inertia. In this way stable and homogenous temperature (60±3°C) during deposition is maintained.

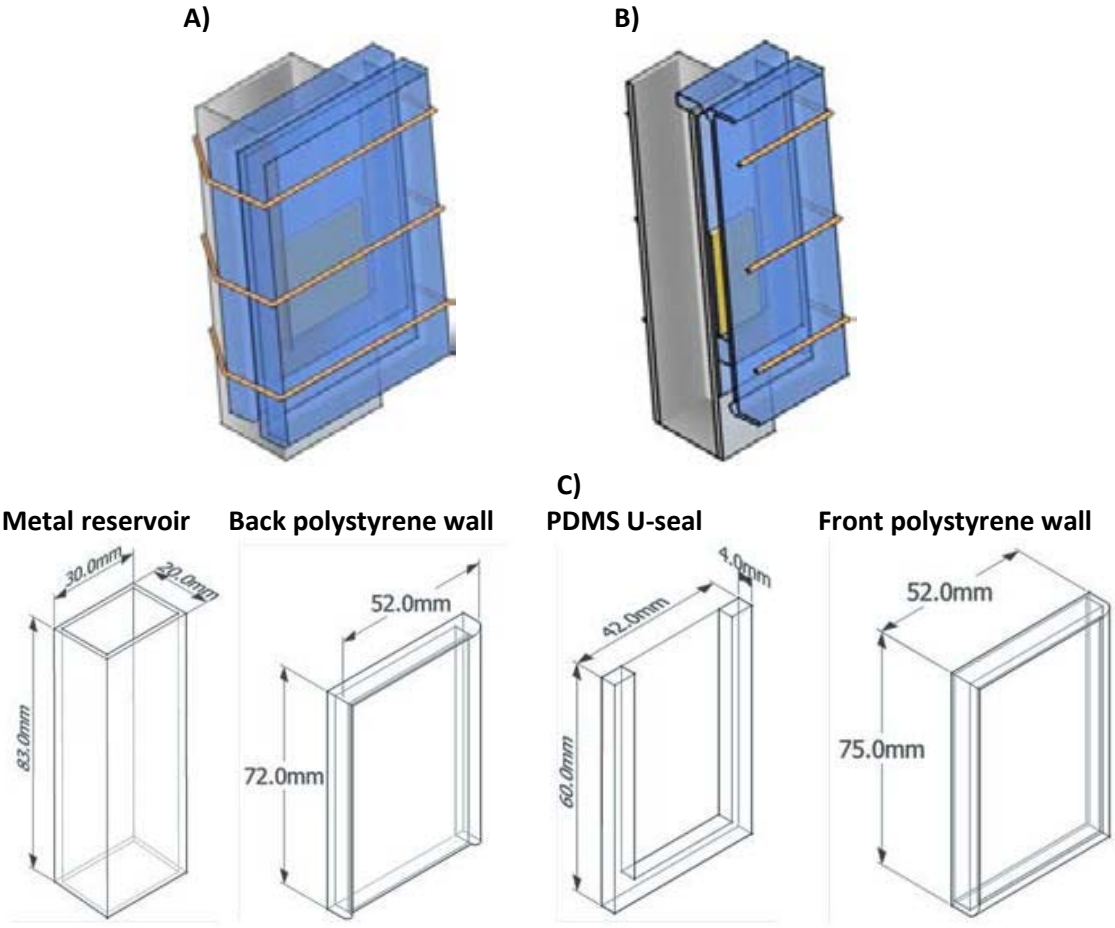

Figure 3.14 Schematic view of the device for an evaporation assisted pattern deposition. A) Assembled device (the glass coverslip is marked in yellow), B) cross-section, C) separate parts of the device with dimensions.

The formation of patterns is governed by a programmable Watson Marlow 403U/VM2 peristaltic pump (see Figure 3.15) which is governed by the FIALab software (FIALab Instruments).

In contrast with other gradient forming approaches in which the extent of surface modification is determined by the time of contact of the solution with the substrate, in this technique the substrate is modified by particle deposition only in a narrow area close to the contact line. The control of the speed of the contact line migration over the substrate gives us the opportunity to locally adjust the particle concentration of deposits. We expected that that the gradient of contact line speed resulted in a gradient of deposited particle concentration. Therefore, we can classify this type of patterning as "recording approach", as explained in Section 3.2.1 ("Gradients for cell motility") or in Figure 3.1.

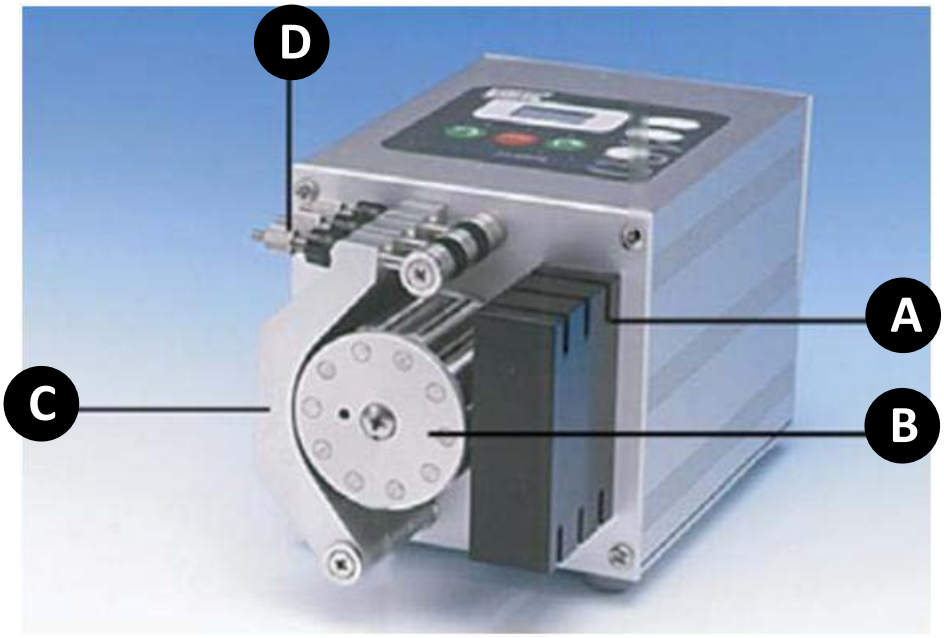

Figure 3.15 Watson Marlow 403U/VM2 peristaltic pump used to remove IBs suspension from the cuvette. A) Tube clamping block, B) rotor, C) track, D) track occlusion arm. Image adapted from Watson-Marlow's promotional materials available on-line.

3.3.3. Input and output parameters for a simple pattern deposition

To pattern NPs on the substrate we used a peristaltic pump, in which, the desired speed can be programmed (in our setup this speed is expressed as % of maximal pump speed and V_{MAX}≈3.5ml/min). This results in a removal of the colloidal suspension from the cuvette in a controlled manner (expressed in units of volume over time) where the substrate that we want to functionalise is placed. As a result, a controlled movement of the three-phase contact line across the deposition surface is achieved (it can be expressed in units of length over time). This approach is similar to the one presented in Figure 3.6.

As it was highlighted in the introduction to this Chapter, the deposition is driven by evaporation, and therefore, occurs only on the three-phase line. We keep constant all the intrinsic variables that govern the coffee-drop effect and therefore the evaporation driven deposition rate (number of deposited particles per unit of time) on that line is constant. Thus, by governing externally (with the pump) the rate of movement of the contact line (unit of length over time) over the substrate, it is possible to control the concentration of deposited material (number of deposited particles per unit of area). The lower the speed of contact line over the sample, the higher number of particles is deposited. In consequence, low speeds are used to deposit high concentrations of IBs, moderate speeds to deposit lower concentration of particles and extremely high speeds to obtain areas with practically no particle deposition, separating the areas of deposited IBs.

Table 3.2 defines the input parameters used for the description of the protocols used for the device performance, as well as the output parameters that describe the geometry and characteristics of deposited patterns. The width (*W*) of a zone with a homogenous or gradient deposit depends on the total displacement of a contact line at given speed. This is governed by two parameters: speed (V_{CL}, V_V, or V_P) and time of deposition (*t*). The product of these two parameters defines the total amount of liquid removed by the pump. The speed can be expressed with different units depending whether it is considered the distance travelled by the contact line in a given time (V_{CL} in µm/s), the rate of liquid removal (V_V in ml/s) or the percentage of maximal pump speed (V_P in %). In fact, these values can be used interchangeably.

The third variable that can be externally governed is the IBs concentration in the suspension (C_S) expressed as number of particles in unit volume. We assume, that this parameter is constant during deposition, as the amount of the deposited material (number of particles removed from the suspension) is negligible (~10^7) compared with material in the bulk suspension (~10^{11}/ml) and the volume of evaporated liquid per deposition (~0.1 ml) is much smaller than the total volume of liquid in the reservoir (~10 ml).

In this way, for a given IBs concentration in the suspension (C_S), by controlling the velocity (*V*) and the time (*t*) of suspension removal it is possible to control the width (*W*) and deposited concentration (C_D) of the pattern. In our case, since we deposit fluorescent GFP-derived IBs, the concentration of the deposited material has a direct impact on the total fluorescence from each zone, and that can be studied with fluorescence microscopy and quantified as average pixel brightness intensity from given area (*I*). The concentration of IBs on the surface has also

an impact on the average height of deposited material over the substrate that can be measured by AFM and expressed in units of length (*H*). Thus, the quantification of deposited material can be described using the following parameters: C_D, *H* or *I*. In this Thesis, as we are working with high fluorescent material it is more straightforward to use *I*. Gradient shape descriptor, *G*, will be used in the case of gradient pattern deposition, in order to quantitatively compare their quality. Value of this parameter is defined as quadratic sum of errors between actual fluorescence profile of pattern and best fitting idealized triangular envelope, divided by pattern width, *W*. Therefore broad, gradients well fitting to the envelope are characterized by a low value of *W*.

Table 3.2 Description of the input parameters of the deposition protocol and output parameters describing the geometry and characteristics of deposited patterns. General relationships existing between these parameters are summarized at the bottom. Subindices "1" and "2" correspond to two hypothetical deposition protocols and are shared by all parameters (C_{D1} corresponds to V_1, etc.).

	Symbol	Unit	Description
Input parameters:	V_{CL}	[µm/s]	Deposition speed expressed as distance travelled by contact line per unit of time
	V_V	[ml/s]	Deposition speed expressed as volume of liquid pumped per unit of time
	V_P	[%]	Deposition speed expressed as percentage of maximal pump speed (used as input for pump protocol)
	t	[s]	Time of deposition
	C_S	[#/ml]	Concentration of IBs in suspension expressed as number of particles per unit of volume
Output parameters:	*W*	[µm]	Width of deposited stripe
	C_D	[#/mm^2]	Concentration of deposited particles expressed as number of particles per unit of surface
	H	[µm]	Height of deposited material according to AFM measurements
	I	[AU]	Intensity of green fluorescence of deposited material expressed as pixel brightness per unit surface
	G	[#]	Gradient shape descriptor – the lower the value, the better fit between deposit´s fluorescence profile and an idealised, linear gradient envelope.

General relationships between input and output variables:

For a given C_S:			**For given V and t:**		
$V_1 > V_2$	→	$C_{D1} < C_{D2}$	$C_{S1} > C_{S2}$	→	$C_{D1} > C_{D2}$
$V_1 \cdot t_1 > V_2 \cdot t_2$	→	$W_1 > W_2$	$C_{S1} > C_{S2}$	→	$W_1 > W_2$

As described in Table 3.2, there are intuitive relationships between the described parameters. For example, for a given concentration of NPs in the colloidal suspension, C_S, high speeds *V* results in low concentrations of deposited material C_D. For a given speed *V* and

deposition time *t* a higher concentration of IBs suspension, C_S, gives place to a higher concentration of deposited material, C_D, and wider patterned areas, W, etc.

Figure 3.16 shows an example of a general protocol for a pump for patterning deposition (input) and the resulting deposited pattern characteristics (output). In this example three stripes are being deposited (denoted with subscripts "1", "2" and "3") in three consecutive protocol steps. Various representations of speed are complementary, and therefore, they are presented on the same axis. Similarly, deposit characteristics (IBs density, IBs fluorescence and height) are presented on the same axis in the resulting IBs deposit profile, as they are proportional. Stripes "1" and "3" are deposited with the same speed and therefore their resulting intensities will be equal. Speed for stripe no. "2" is higher, and therefore, its intensity is lower. Stripes "2" and "3" have bigger product of speed and time of deposition when compared with stripe "1" and therefore their widths are also bigger.

A) Input protocol.

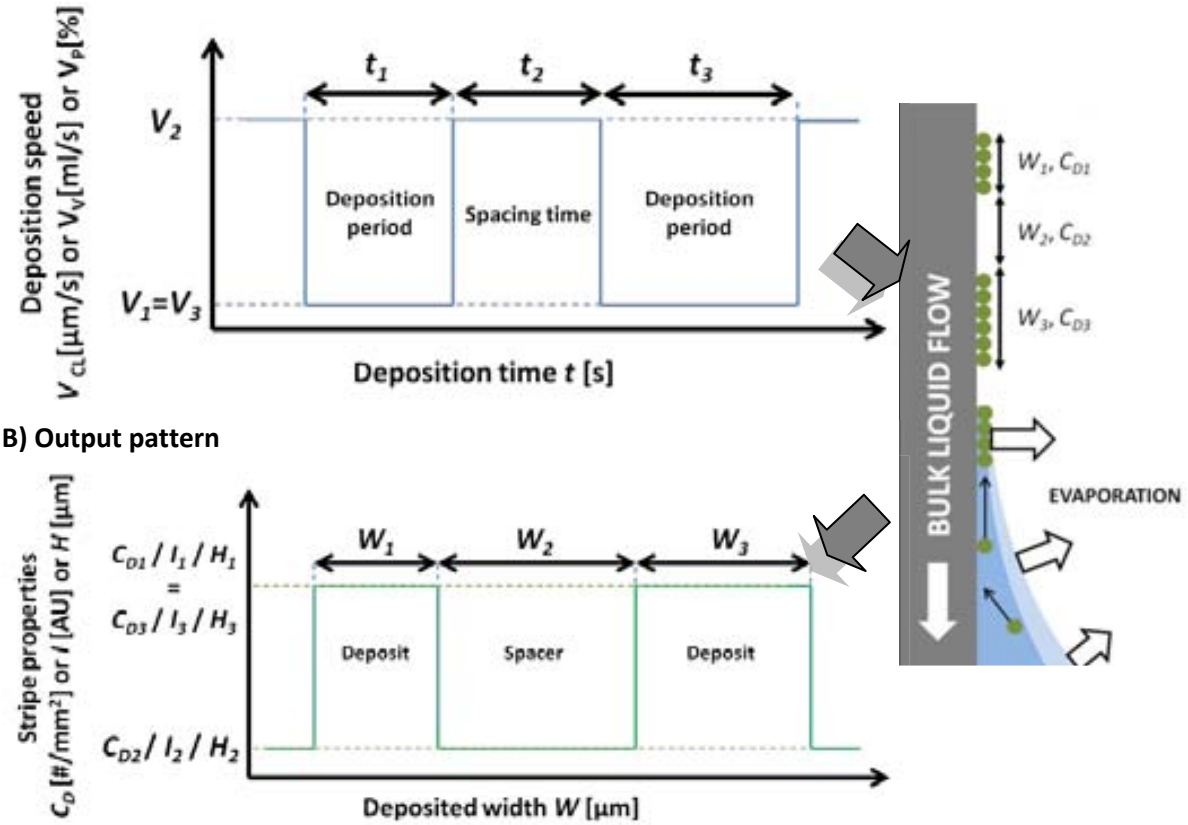

B) Output pattern

Figure 3.16 Schematic cartoon of protocol consisting of three consecutive steps with deposition input and output parameters presented on separate plots. Constant IBs suspension concentration C_S is assumed during the whole process. A protocol resulting with the deposition of three stripes is presented. For a detailed description see the main text.

In practice three regimes can be distinguished for the purpose of pattern depositions:

- Contact line stopped: resulting in extremely high concentration of deposited IBs
- Low speeds: resulting in considerably high concentration of deposited material
- High speeds: resulting in low concentration or almost no IBs deposition that can serve as spacers between IBs patterned areas

Therefore low speeds and their corresponding times will be often referred as “deposition” parameters, and high speeds and their corresponding times as “separation” parameters. Thus, these parameters will be denoted with subscripts “D” and “S”, respectively.

3.3.4. Device calibrations

In order to conduct experiments in a reproducible manner, the device needs to be calibrated. Thus, we investigated how externally governed parameters (“input”: deposition speed V, deposition time t, suspension concentration C_S) influenced the deposited patterns (“output”: stripe width W, deposition concentrations C_D and intensity I).

Here we will describe the deposition protocols using aforementioned input parameters (Table 3.2). Example of actual pump protocol that was applied for calibration experiments is presented in Section A.16 (“A general pump protocol for simple patterns”).

3.3.4.1. Calibration of pump speed

Before any experiment is conducted a calibration of the pump was performed. To do so we measured the time needed by the pump to remove 1ml of liquid from the reservoir. Repeating the experiment at different speeds (expressed in % in the pump software) a calibration curve can be obtained (Figure 3.17). A linear fit to the experimental data points gives the conversion equation to translate units of the pump speed (%) to liquid removal rate (ml/min).

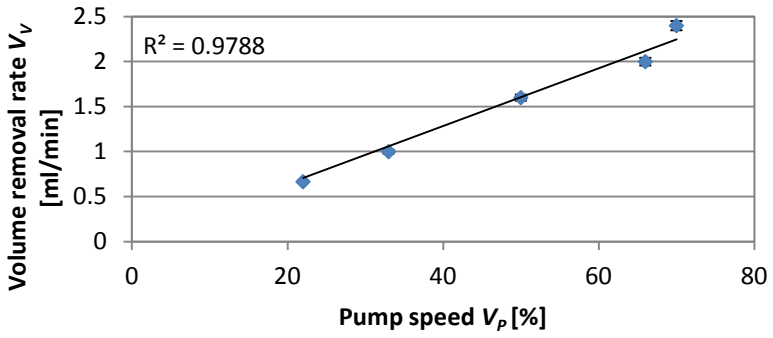

Equation 1. $V_V = 0.0321 \cdot V_P$

Figure 3.17 Calibration curve for conversion of the pump speed units (%) into volume removal rate (ml/min).

3.3.4.2. Calibration of deposit geometry

To perform the geometrical calibration we deposited a IBs suspension in MiliQ water at a concentration of $4 \cdot 10^{11}$ particles/ml (unless stated otherwise) on glass substrates functionalized with an hydrophobic SAM at a temperature of 60°C. Detailed protocols of the suspension preparation can be found in Section A.14 ("IBs suspension preparation for evaporation driven deposition").

Series of stripes of protein NPs were deposited at various conditions in order to investigate the influence of deposition parameters on the resulting geometry of the patterns. Symbols are explained in detail in Table 3.2, additional subscripts for time and speed parameters "D" and "S" denote deposition and separation parameters, respectively. Four experiments were designed in order to test the following input parameters: A) deposition time, t_D; B) deposition speed, V_{CLD}; C) particle concentration, C_S and D) separation speed, V_{PS}. A complete list of parameters used in these experiments is presented in Table 3.3.

Table 3.3 Experiments with the corresponding parameters. *Investigated*, denotes parameter that was changed during the experiment. *N/I* are the parameters that have no impact on the results of the experiment.

Experiment	Deposition speed V_{CLD} [ml/min]	Deposition time t_D [s]	Separation speed V_{PS} [ml/min]	Separation time t_S [s]	Particle concentration C_S [#/ml]
A)	0	*Investigated*	*N/I*	*N/I*	$4 \cdot 10^{11}$
B)	*Investigated*	30	*N/I*	*N/I*	$4 \cdot 10^{11}$
C)	0	30	*N/I*	*N/I*	*Investigated*
D)	*N/I*	*N/I*	*Investigated*	1	$4 \cdot 10^{11}$

The resulting patterns of these calibrating experiments were observed by optical microscopy in bright field mode as well as in fluorescence mode, as described in Section A.9 ("Optical microscopy") and are presented in Figure 3.18. Widths of IBs deposited stripes and widths of the spacing gaps were extracted from the obtained images and used to prepare the calibration curves and the conversion equations given in Figure 3.19. In all cases good linear fits were obtained with regression coefficients, R^2, superior to 0.85.

In experiment A (see Figure 3.18) we can see deposits of IBs formed for stopped pump flow (V_{VD}=0ml/min) for a range of deposition times. Deposits are formed for periods of times as short as 7 seconds, but those tend to be very thin, discontinuous, and prone to imperfections caused by impurities in the suspension or on the substrate surface. In this particular case the three-phase line movement across the substrate is caused directly by the liquid evaporation, not by liquid removal with the pump. This is the reason why longer deposition times cause broader stripes. It can also be seen, that wider stripes, formed with

deposition time exceeding 30 seconds, have uneven distribution of IBs across their width. Deposits tend to have higher concentrations in the outer regions from the bulk of suspension. We attribute it as a result of the flow induced by evaporation. Despite we have managed to produce some number of patterns it is very to repeat this results.

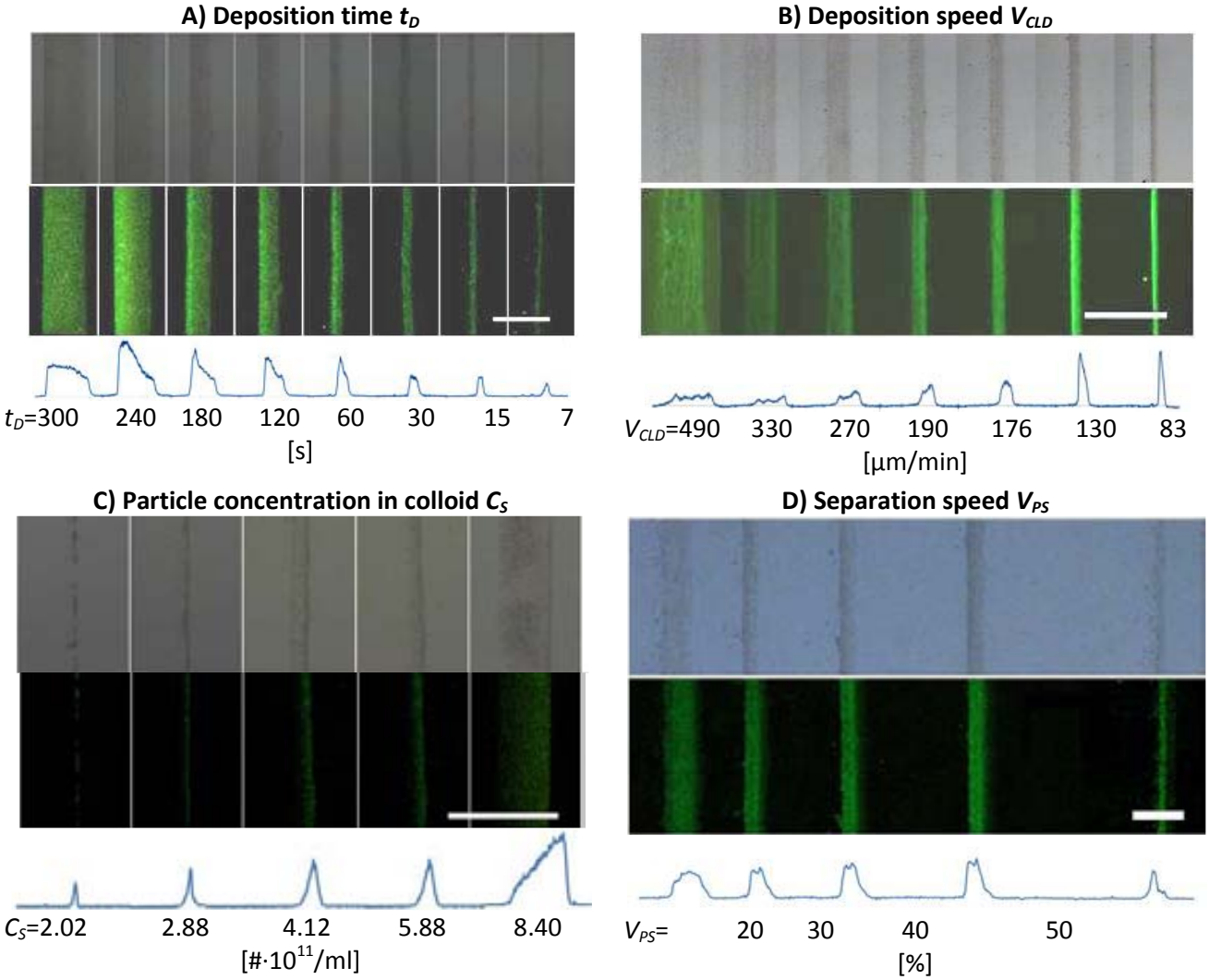

Figure 3.18 Bright field and fluorescence images used to study the influence of input parameters (deposition factors) on the resulting stripes. A series of IBs pattern depositions changing one factor at a time were preformed (see Table 3.3). GFP IBs fluorescence intensity profiles of the resulting patterns with description of the used conditions are presented above. Scale bar in indicates 100 µm.

Experiment B proves that for a constant time of deposition, t_D=30s, higher deposition speed results in wider stripes with lower fluorescence intensity. However, for high deposition speeds (>300µm/min) stripes are non homogenous as local maxima are clearly visible in the fluorescence intensity profile plots. These artefact are attributed to pulsations that occur during the peristaltic pump's rotor movement. These pulsations are always present during pumping, yet they have more impact for high speeds than for low speeds being thereby more

relevant in the wider stripes. Speeds greater than ~600µm/min result in almost no IBs deposits ($C_D \approx 0$), so they can be used for producing separations between patterned stripes. In this case gradients are not formed: for low deposition speeds IBs are deposited very at high concentration over narrow zone and in the case of high deposition speeds intensity is low and homogenous all over broad stripe.

A Deposition time -> stripe width

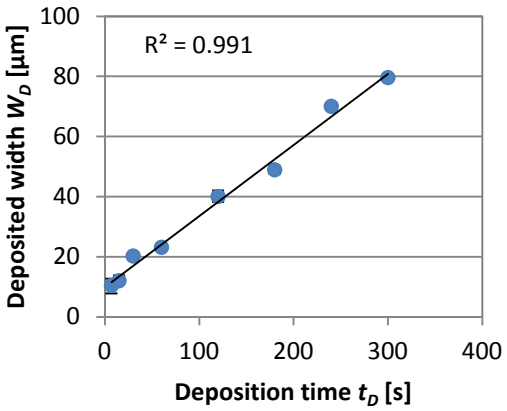

Equation 2. $W = 0.237 \cdot t_D + 9.89$

[for V_{VD}=0ml/min and C_S=4·10^{11} #/ml]

B) Deposition speed -> stripe width

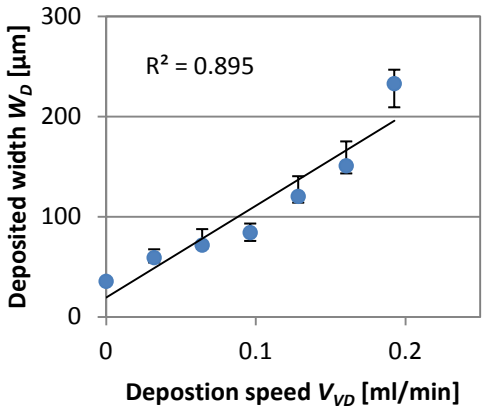

Equation 3. $W = 916.4 \cdot V_{VD} + 19.4$

[for t_D=30s and C_S=4·10^{11} #/ml]

C) Particle concentration -> deposition width

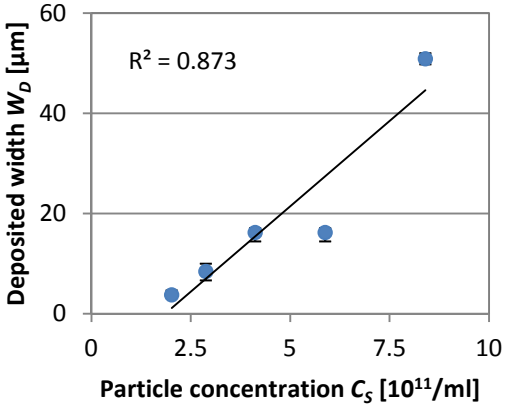

Equation 5. $W = 6.81 \cdot C_S - 12.6$

[for V_{VD}=0 ml/min and t_D=30s]

D) Separation speed -> separation distance

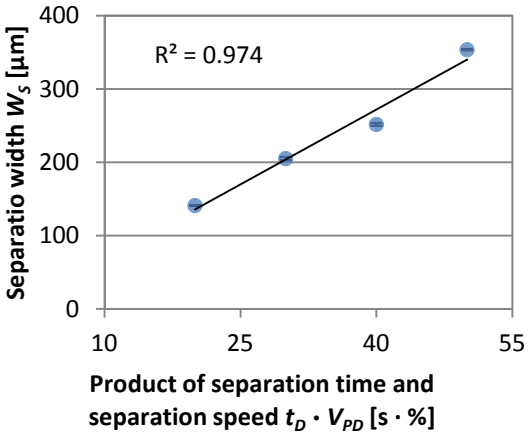

Equation 4. $W = 6.80 \cdot (t_D \cdot V_{PD})$

[for t_S=1s and C_S=4·10^{11} #/ml]

Figure 3.19 Calibration curves showing the influence of deposition and separation factors on the resulting patterns. A series of depositions with change of only one factor at a time was preformed. Fluorescence images of the resulting patterns with description of conditions are presented in the previous figure. Numbering corresponds to one in Figure 3.18.

Experiment C exemplifies that a pattern deposition is possible for a wide range of particle concentrations. Depositions in this experiment were performed with constant deposition time of t_D=30s and a stopped pump, V_{VD}=0ml/min. The resulting stripes' intensity *I* varies depending

on particle concentration, as expected. The more material is present in the suspension, the more particles are deposited during evaporation. Also the width of the deposited stripes, *W*, is broader for high IBs concentration. As a consequence for higher concentrations gradient shape of deposits can be clearly distinguished. This is not observed in the case of low concentrations (low with and intensity). It is worth to recall at this point, that particle concentration also has impact on the evaporation conditions at the contact line. However, we are not going to focus on the details here.

Finally, experiment D shows the impact of the separation speed on the actual separation width between the patterned stripes. Even though, in this experiment, only separation speed was changed, it is the product of deposition speed and time that determines the actual width of stripes. This is why this value is represented on horizontal axis instead deposition speed, although the value does not change numerically values as in this case the separation time was equal to 1 second. Because these are separation parameters, they do not have impact on the morphology of deposited stripes – eventual gradients are due to the specific deposition parameters. For the deposition of wide stripes the resolution is around 100µm which means that the stripes will be merged in one stripe if the separation time is too small. In general, the smaller and less intense stripe the better deposition resolution. Narrow stripes can be clearly distinguished using separations as low as 20µm (see Figure 3.20).

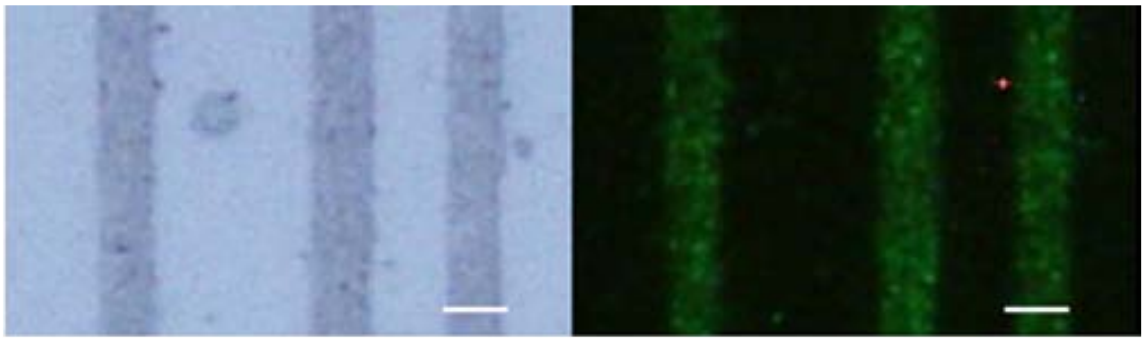

Figure 3.20 Detailed views of stripes deposited with a high spatial resolution. Left: bright field image, right – UV fluorescence. Lower IBs concentrations (C_S=2.4·10^{11}#/ml) and deposition times (t_D=10s) than in the main series of experiments described in main text were used to obtain this result. Scale bar indicates 20µm.

As it can be seen from the previous experiments both deposition time and deposition speed have influence on the stripe width. The product of these two parameters determines the volume pumped out from the cuvette during a certain time. To investigate this more in detail, focusing on speed ranges relevant for IBs deposition, an additional experiment was carried out with deposition speeds below 0.1ml/min (3% in pump's software notation). A mosaic of obtained bright field and fluorescence images with their corresponding fluorescence

profiles is presented in Figure 3.21. As we can see, the broad stripes are non homogenous. This is attributed to be caused by a pump artefact: low pump speeds are burdened with relatively big rotor speed variations. These variations are insignificant for narrow stripes, but relevant in the case of broad ones. Moreover, stripes tend to have more material on the leftmost extreme that corresponds to the starting line of deposition of each stripe (whole series of stripes was deposited from left to right). We assume that the three-phase line was more time in contact with the sample at the beginning of stripe´s deposition due to pump artefact, and this resulted in this outcome. This may also explain deposition of gradients stripes, as observed in Figure 3.18.

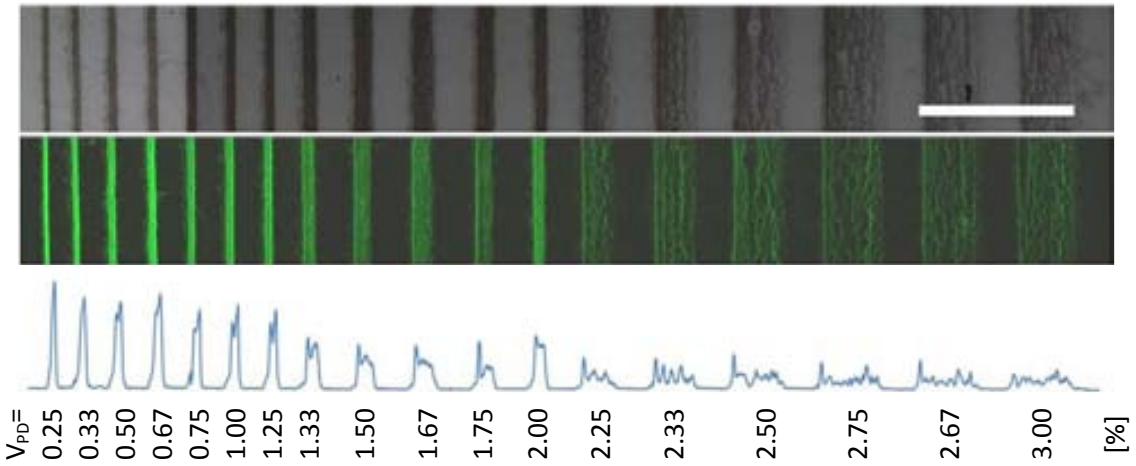

Figure 3.21 Mosaic of bright field and fluorescence images of IBs stripes used to study the influence of the low deposition speed on resulting stripe width. Scale bar indicates 1mm.

The resulting experimental stripes width data and calibration line are presented in Figure 3.22. As it can be seen, different ranges manifest slight differences in the relation between time-speed product and stripe width. Especially for very low speeds variation of width is considerable, as very low R^2 value is obtained for linear fit. However, an overall calibration line fits well with the data from whole range. Corresponding conversion equation is given below the plot.

Knowing the volume of liquid removed in a unit of time (V_V [ml/s]) and the width between stripes (W [μm]), which is the distance that the contact line travels in that period of time, it is possible to calculate the cross-section of the reservoir which is approximately ~100.6mm^2. The nominal value, calculated from the dimensions of the cuvette, is 120mm^2 (see Figure 3.14). The error can be attributed to the following facts: (i) the PDMS seal is deformed (compressed) during the deposition, (ii) the U-seal was cut by hand, and (iii) the cuvette is slightly tilted. All

three facts together could explain why the experimental value is smaller than the nominal one, obtained by means of geometrical calculations.

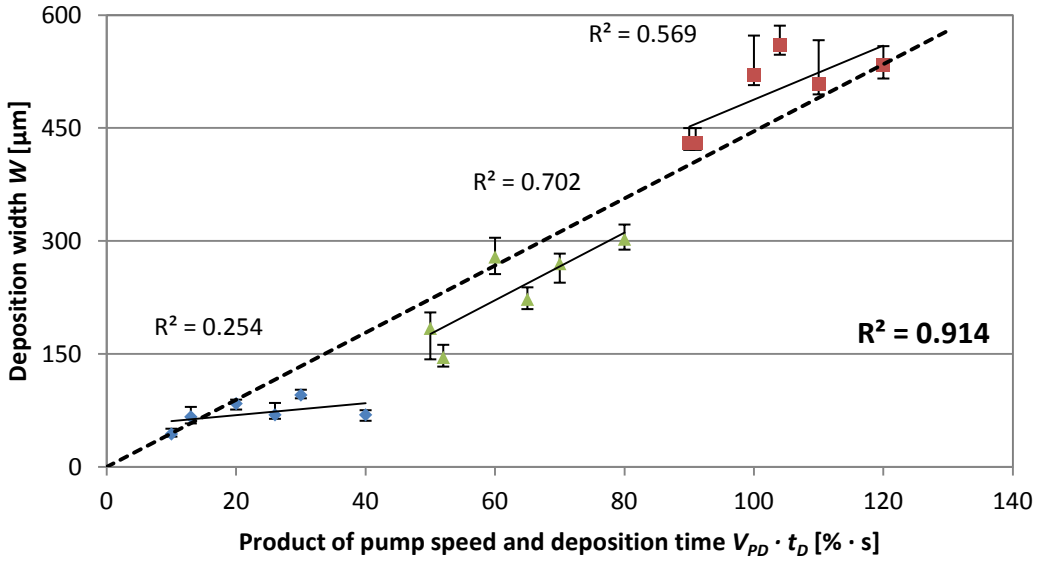

Equation 6. $$W = 4.46 \cdot (t_D \cdot V_{PD})$$

[for V_{PD}<3%, C_S=4·10^{11} #/ml t_D≈40s]

Figure 3.22 Calibration curve for deposited IBs stripe width as function of product of deposition speed and time. In colours, different speed ranges are marked: blue 0-1% (0-33µl/min), green 1-2% (33-66µl/min), red 2-3% (66-100µl/min). For each range the linear fit is presented. Dashed line and bolded equation correspond to the overall conversion equation presented below the plot.

3.3.4.3. Calibration of deposited IBs concentration

As it can be seen in Figure 3.18 the investigated input parameters have also a big impact on the IBs fluorescence intensity (*I*) of the stripes. The corresponding experimental plots of fluorescence intensity and the calibration curves are presented in Figure 3.23. Arbitrary units in this context correspond to medium fluorescence on 8-bit gray scale images, where a zero value (black, no fluorescence) corresponds to no IBs while a value of 255 (white, every pixel has maximal fluorescence) to a full IBs coverage.

As it can be seen in experiment A (Figure 3.23 A), the deposition time t_D is the parameter that has the less impact on the fluorescence intensity (the lowest slope value). Also, a very low regression coefficient indicates, that governing the concentration of deposited IBs, C_D, by different deposition times would be burdened with a substantial error. On the other hand, by changing the deposition speed, V_{VD} (experiment B), or the IBs concentration in the suspension, C_S (experiment C), one can obtain a fair range of deposited IBs concentrations, as depicted in Figure 3.23 B and C. In accordance with these plots the IBs concentration in deposits, C_D, can

be reliably adjusted by changes of IBs concentration in used suspension, C_S. However governing IBs deposition density, C_D, by the deposition speed, V_{VD}, is more practical, as it can be freely and easily changed during the experiment.

A) Deposition time -> stripe intensity

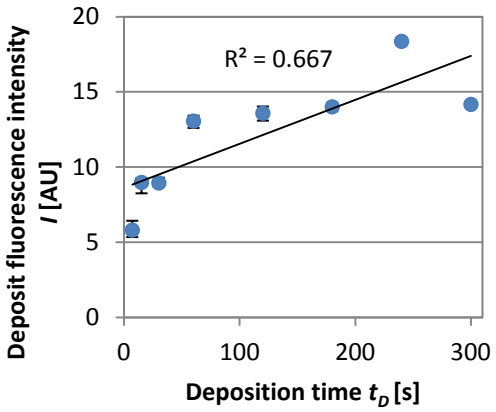

B) Deposition speed -> Stripe intensity

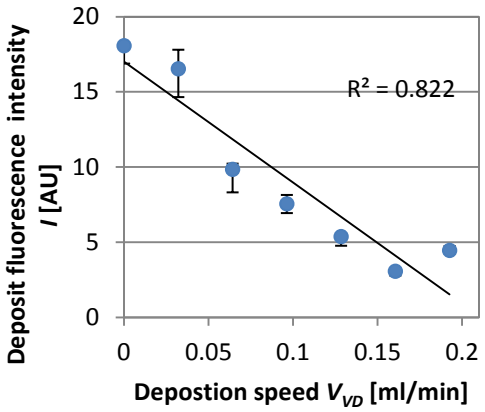

Equation 7. $I = 0.0292 \cdot t_D + 8.64$
[for V_{VD}=0ml/min and C_S=4·10^{11} #/ml]

Equation 8. $I = -2.1 \cdot V_{VD} + 16.8$
[for t_D=30s and C_S=4·10^{11} #/ml]

C) Particle concentration -> deposit intensity

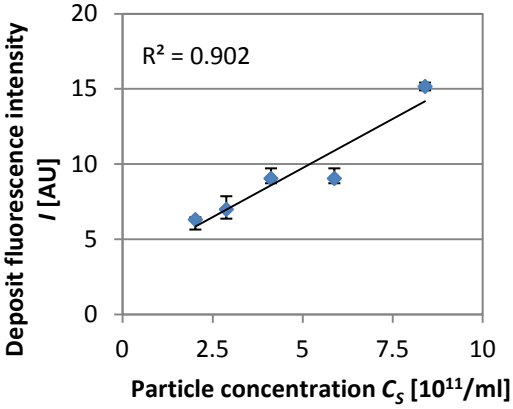

Equation 9. $W = 1.30 \cdot C_S + 3.23$
[for V_{VD}=0 ml/min and t_D=30s]

Figure 3.23 Calibration curves for the fluorescence intensity as a function of A) deposition time, B) deposition speed and C) particle concentration in the IBs suspension. Arbitrary units in this context correspond to medium fluorescence on 8-bit gray scale images where value 0 (black) corresponds to no IBs and 255 (white) to full IBs coverage.

Since the use of arbitrary units to quantify the amount of deposited material on the stripes is cumbersome and counterintuitive, efforts were taken in order to quantify this value in units of IBs concentration on the surface. In order to perform such quantification we played with the deposition speed, V_V, patterning parallel stripes on the surface in two perpendicular orientations. This rendered in a rectangular lattice of stripes with different concentrations of IBs on each rectangle as shown in Figure 3.25. This array was prepared by deposition of four

broad stripes with various IBs concentrations separated by narrow stripes of very high IBs concentration in the vertical and horizontal direction prepared one over another. In total 16 areas with 10 different combinations of IBs concentrations were deposited leading to a symmetric pattern with respect to the diagonal. The reference notation for each zone corresponds to the number of row and column from the lowest (1) to the highest (4) IBs concentration. The average fluorescence intensities as well as profiles of rows and columns are also presented in Figure 3.25 where it can be clearly seen, that the IBs deposition was accomplished successfully. The areas formed by the intersection of a column and a line with lower indices have lower intensities than areas with higher indices as $V_1>V_2>V_3>V_4$. This fact can also be seen in the profiles of both rows and columns (Figure 3.25).

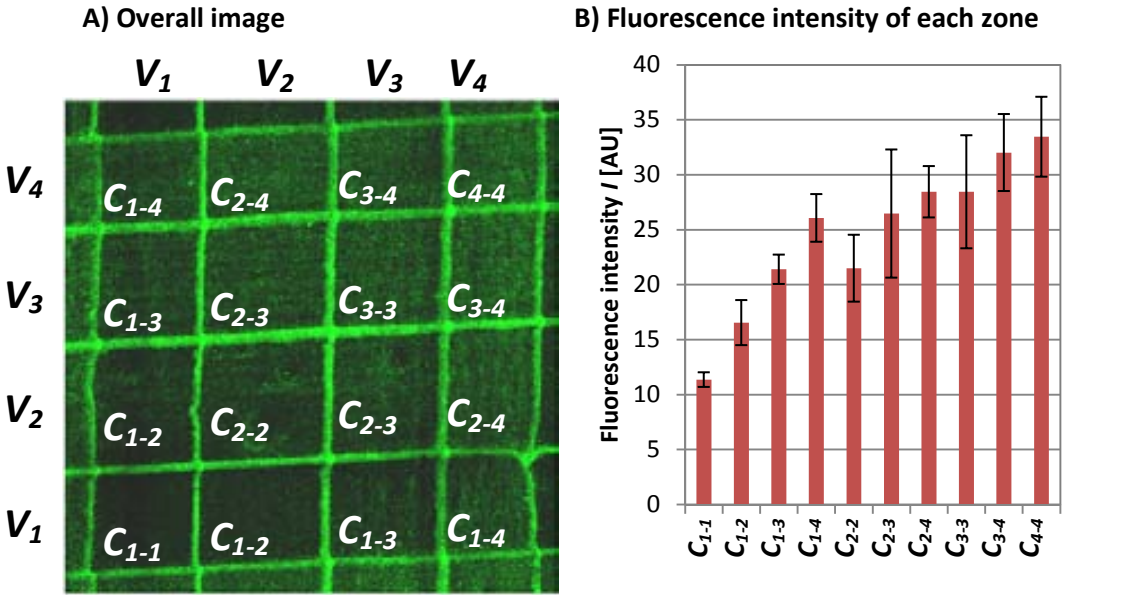

Figure 3.24 Calibration of the deposited number of IBs by a fluorescence intensity calibration. A) Confocal microscope image with areas labelled according to the speed of deposition ($V_1>V_2>V_3>V_4$). Subscripts of each area corresponds to subscripts of speeds used to deposit horizontal and vertical stripes. B) Average intensities of fluorescence in each area.

In order to prepare the calibration curve, the number of IBs from each area was calculated based on the fluorescence images. The ImageJ freeware was used to extract bright spots (groups of pixels), that were identified as separate IB's particles. Counting their number and dividing the resulting value by the total area of the corresponding zone, one can obtain the averaged IBs surface densities, expressed in number of particles per unit area. The histogram of IBs densities and its calibration curve is presented in Figure 3.26.

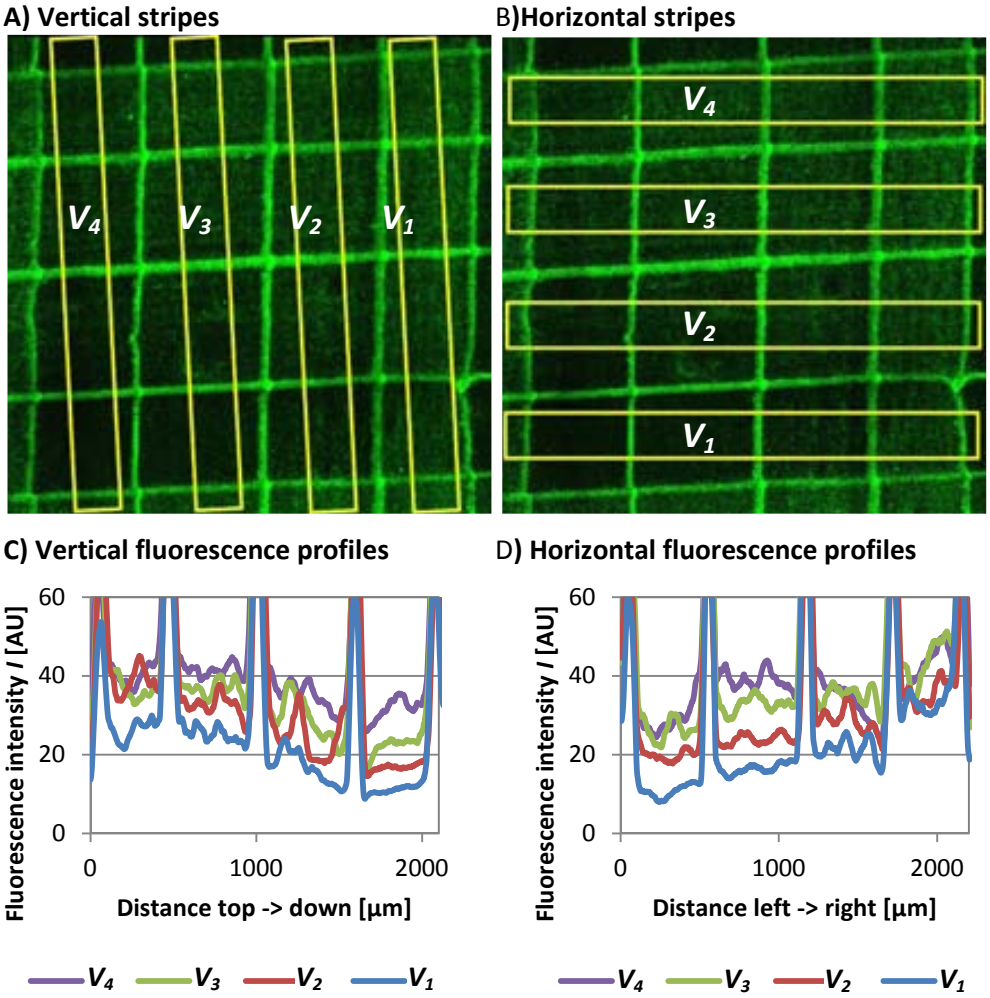

Figure 3.25 Fluorescence profiles of the resulting grid pattern. Parts A) and B) shows vertical and horizontal ranges used to calculate the fluorescence profiles presented in C) and D), respectively.

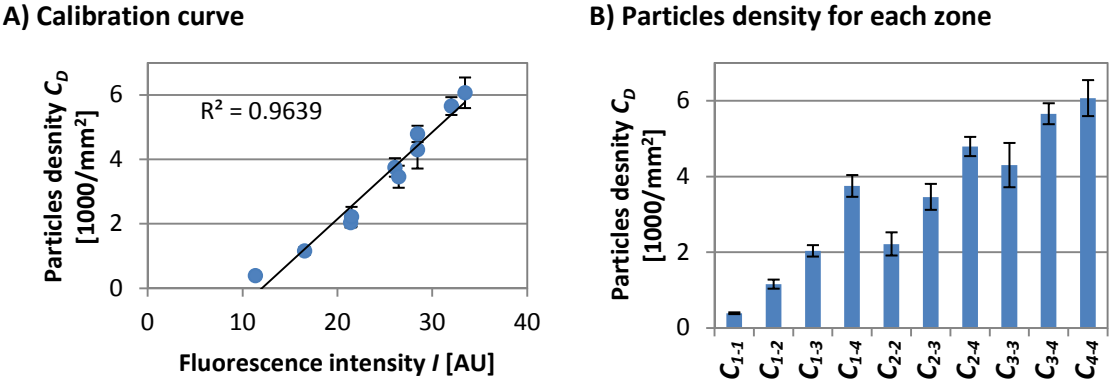

Equation 10. $C_D = 0.27 \cdot I - 3.25$

[for V_{PD}<10% and C_S=4·10^{11} #/ml]

Figure 3.26 Quantification of IBs on deposited substrates. A) Calibration curve to calculate the number of IBs as a function of fluorescence intensity. B) Total density of IBs in each area.

3.3.5. Evolutionary algorithm for gradients deposition

With all the calibrations done for the developed device, series of stripes can be easily prepared using simple protocols and the resulting final patterns can be predicted with high precision. Although in some cases, we have examples of gradient deposits, they are only occasional and very difficult to reproduce. Moreover, simple protocols based on only two deposition parameters do not permit to deposit gradients with desired width and slope, which are the main objective of this Chapter. The very steep gradients could not be obtained because long deposition time (required for high IBs concentration) would imply high width of deposit. Therefore it would be desired to develop protocol for deposition gradients as a series of consecutive stripes with controlled width and concentrations. However, deposition of such complex patterns is a more complicated task. Although, in principle, we have all the resources needed to generate the patterns, in reality, we have not enough knowledge about the system, to properly calculate the optimal protocol for achieving a desired gradient deposition. Indeed, to produce gradients, there are numerous factors that influence the final profile of the deposited pattern and that are difficult to control.

This situation represents a typical “black-box” problem. In order to overcome this inconvenience, we decided to develop and implement an “evolutionary algorithm” for the optimisation of pump protocol for gradient deposition.

Evolutionary algorithms (EA) are iterative and nature inspired techniques used to search the space of alternative solutions in order to find the best ones [72,73]. They are often used in cases of high computational complexity, where the initial conditions set (genotype) influence the final outcome (phenotype). An algorithm consists of an **initial step** (1), where a number (population) of genotypes (individuals) are generated (first generation). It is followed by an **evaluation step** (2) consisting of calculation of the fitness function for each individual phenotype. Next step is the **selection** (3) in which the best-fitting individuals are chosen (parents). It is followed by **proliferation step** (4) where the next generation of genotypes are generated through: breeding (mixing of parental genes), mutation (random parameter generation) or a combination of both. The newly obtained population is sent to the evaluation step and the algorithm is let to iterate. The algorithm is repeated until a limit of time or until a certain iteration number or a sufficient fitness function value is achieved. A schematic flow chart of a generic evolutionary algorithm is presented in Figure 3.27.

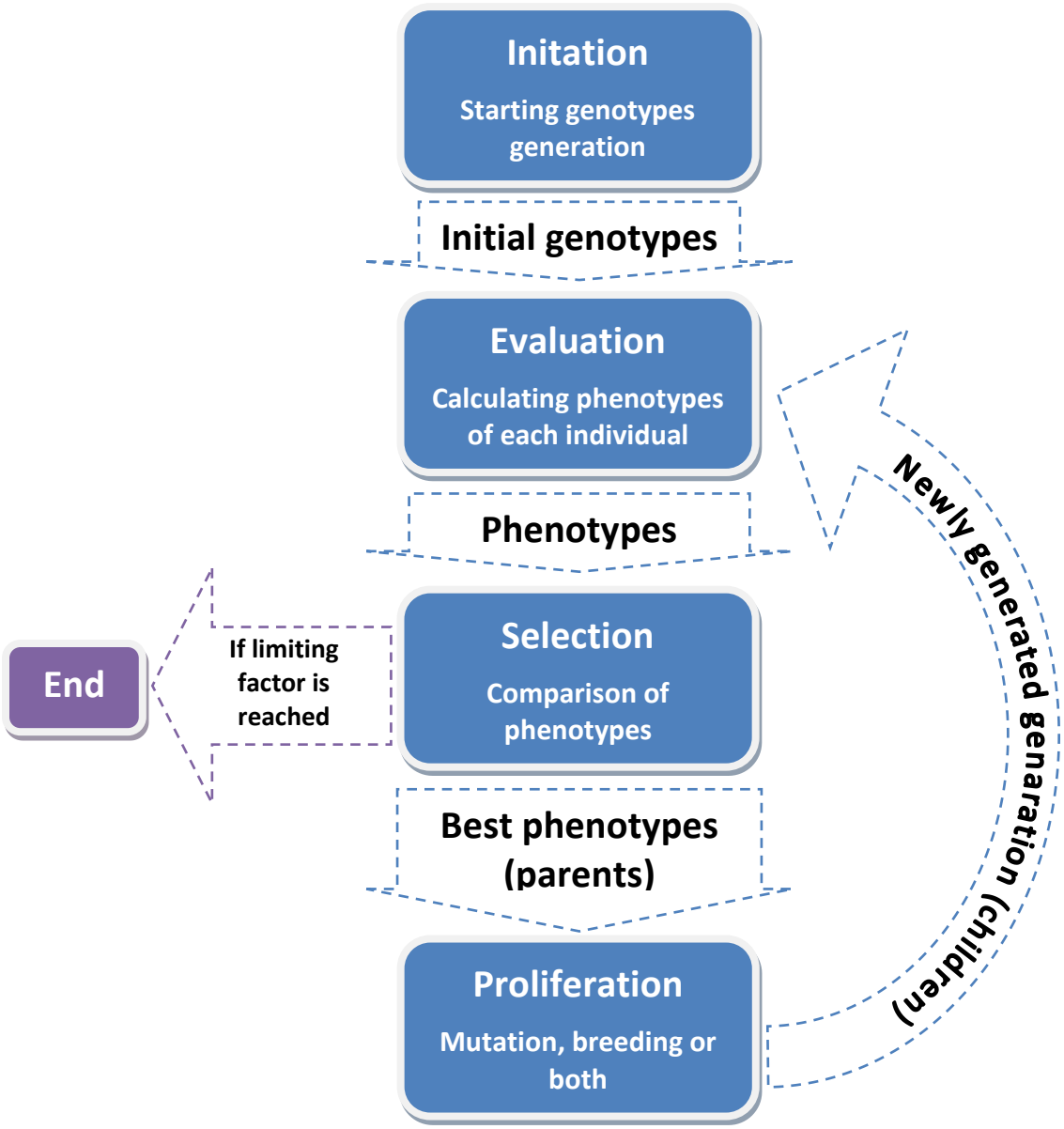

Figure 3.27 Flow chart of a genetic evolutionary algorithm. Boxes contain the name of each step and a brief description. Texts on arrows denote which information passed to the next step.

In our case, the genotypes are the pump protocols and the phenotypes are the deposits that resulted from each protocol. Following this evolutionary algorithm a schematic pipeline of the gradient protocol optimization is presented in Figure 3.28.

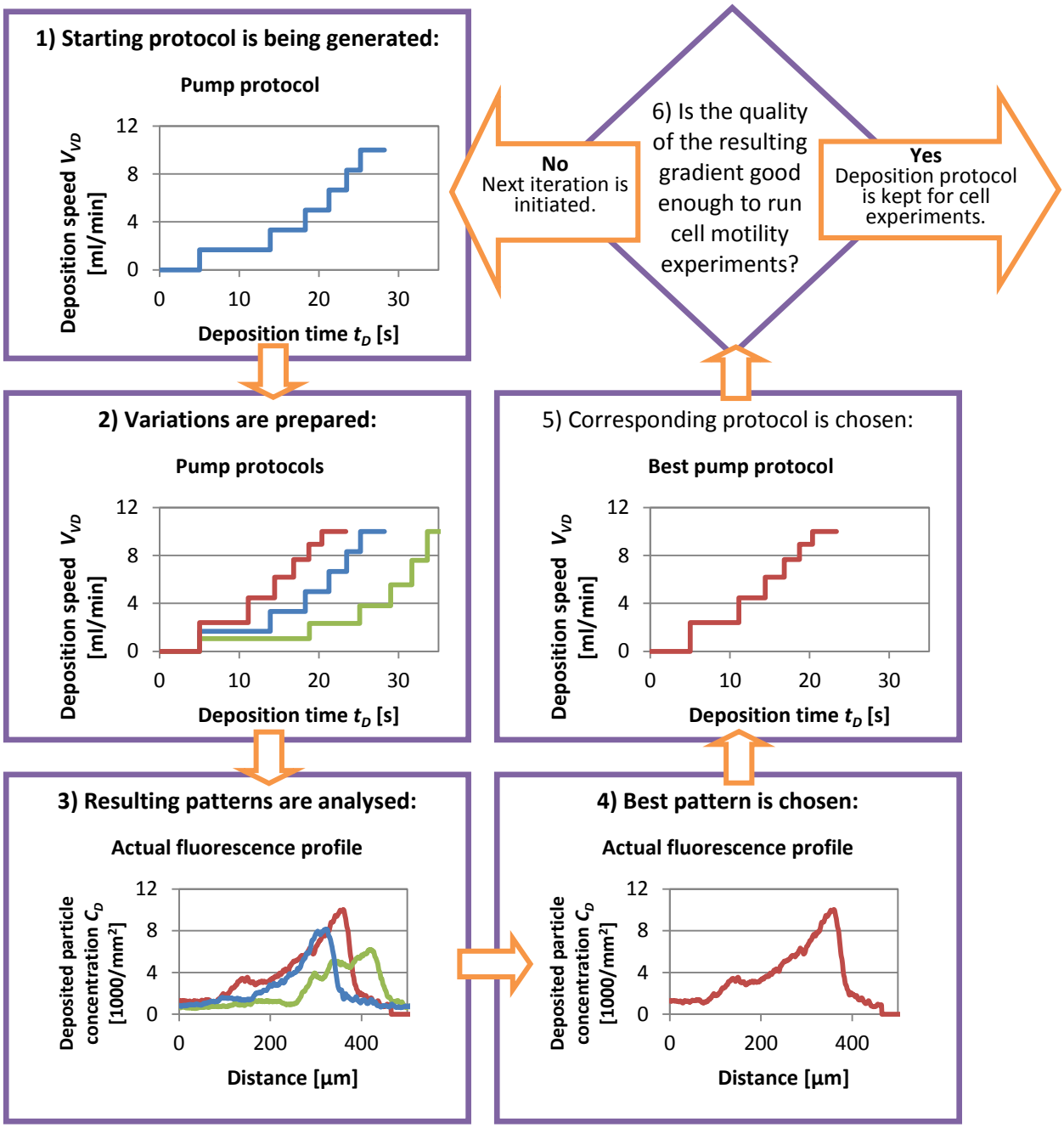

Figure 3.28 Schematic cartoon of evolutionary algorithm used to develop a protocol for IBs gradient deposition.

In this implementation the starting input is one pump operating protocol (genotype) that consists of deposition steps using different pump speeds and deposition times. From this starting point, variations of the initial protocol are calculated, changing slightly each step (time span and/or pump speed). These variations are introduced in a well defined and controlled manner (mutation approach is applied within a given threshold). Such set of protocols defines the first generation. Subsequently, all protocols are executed and the resulting IBs deposition

patterns (phenotypes) are assessed. From all the resulting deposits we choose the best result. If this gradient is satisfactory, its protocol is used for preparing samples for cell cultivation and cell motility study, which is the object of the final Chapter of this Thesis. However, if the best result in a generation is not satisfactory, its protocol is treated as an input to the next iteration of algorithm (next generation).

If some imperfections are localized in one part of the resulting deposit, the corresponding part of the protocol is manually substituted by part of another protocol that is correct in this particular zone (breeding).

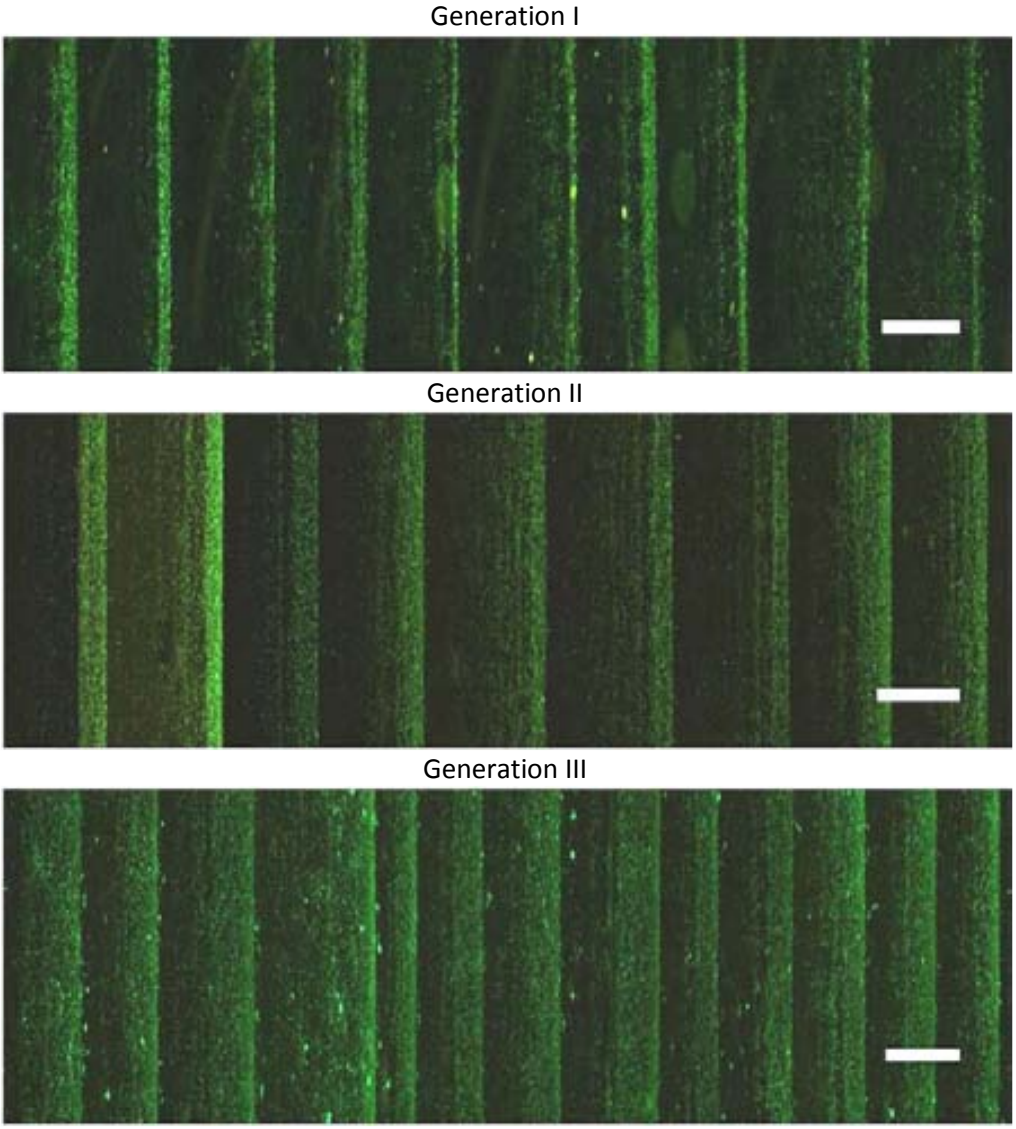

Figure 3.29 Mosaic of fluorescence microscopy images of the ~10 different resulting patterns (phenotypes) used to obtain the satisfactory gradient. Scale bar indicates 500µm.

Using the above described evolutionary algorithm we have successfully optimised protocol for deposition of surface-bound IBs gradients. Only three generations, that is three algorithm

iterations (~10 protocols each), were needed in order to obtain a satisfactory gradient as a result. Fluorescence images of these generations are presented in Figure 3.29. Profiles of particle density, measured basing on the fluorescence intensity of these generations are presented in Figure 3.30. The specific pump protocols used are given in Section A.17 ("Pump protocols for gradient development").

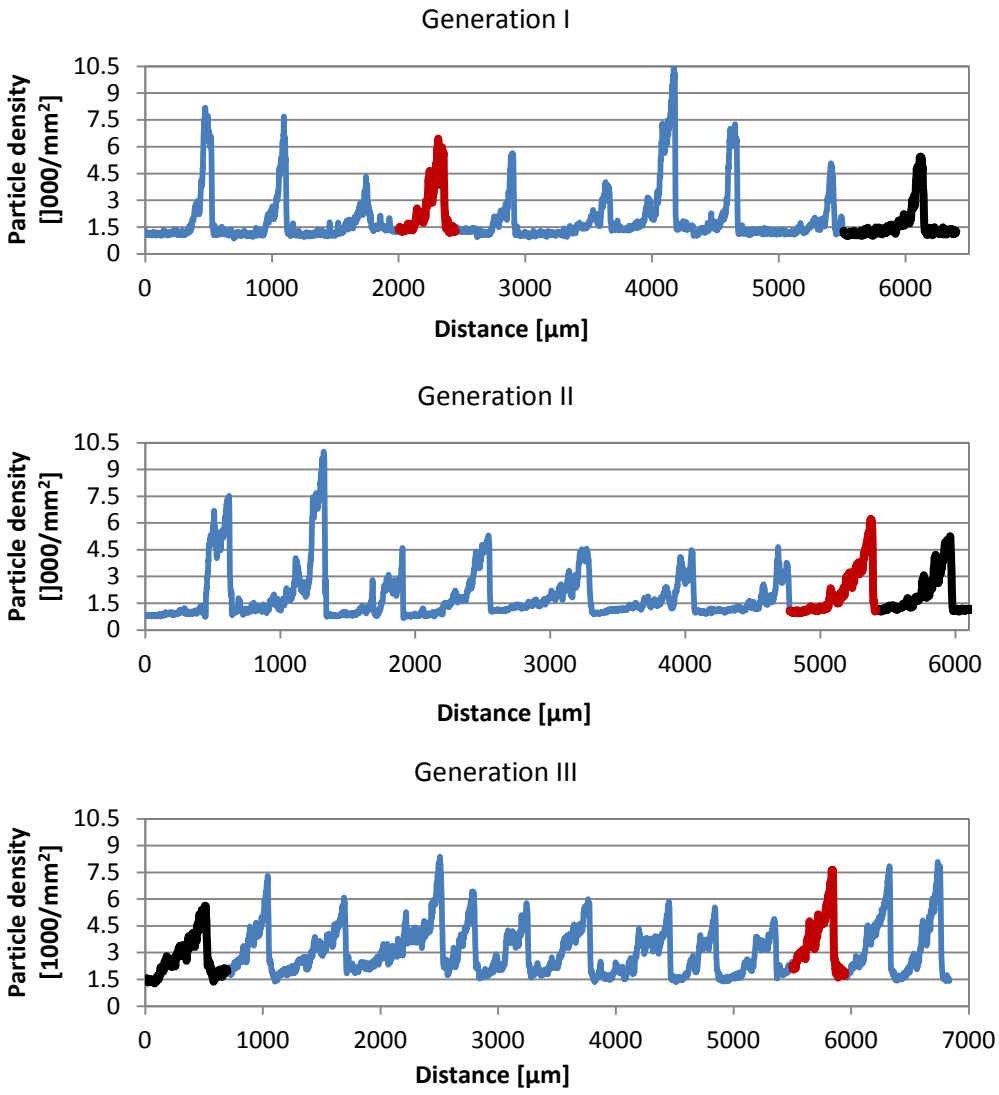

Figure 3.30 Profiles of gradients of generations I, II and III. Protocols corresponding to black profiles were used as "initiator" pump protocols for each generation. In red are marked profiles with lowest value of shape descriptor *G* in the series, in another words, the best profiles of each generation. Protocols corresponding to red profiles become "initiator" protocols of the next generation (black profiles).

The evaluation step was performed as depicted in the example of Figure 3.31. Each gradient was plotted separately and fitted with a simple linear gradient envelope. Parameters such as the start of slope, the end of slope, the gradient height and the base level, were the fitting parameters. The sum of squares of the residuals (SSR, sum of squared differences

between the experimental data and the estimated values) was minimized in order to obtain parameter values of the best fit. The final value of SSR for the best fit divided by the gradient's width was considered as the score function and shape descriptor *G*. The profile with the lowest value of this parameter was considered the best one and was used to initiate the next generation. The whole protocol was stopped as soon as any gradient reached a score $G<0.85$, the threshold value that we have fixed arbitrarily in order to consider gradient satisfactory for our purposes.

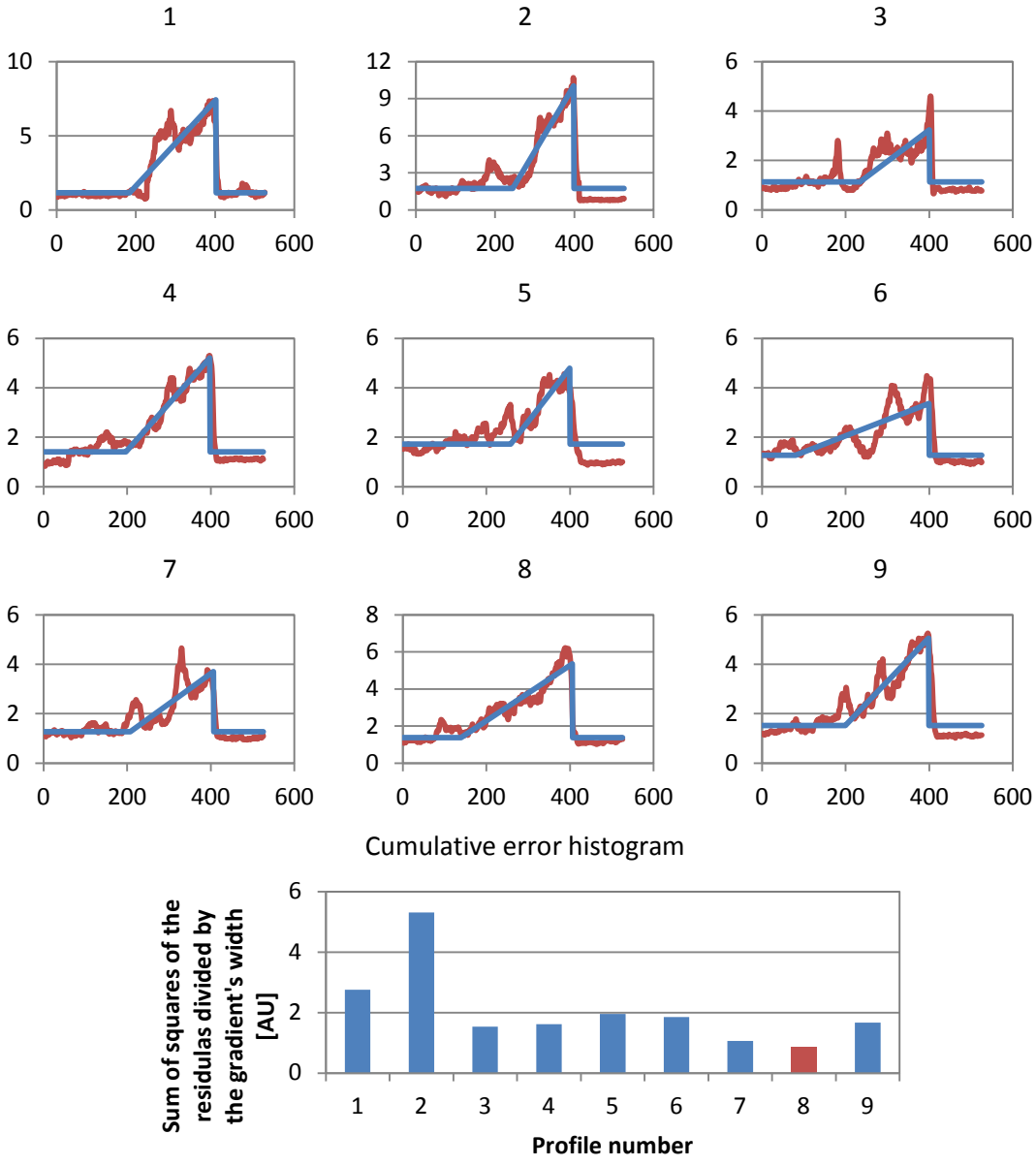

Figure 3.31 Example of a profile validation. Each profile from generation II was fitted with a simple linear gradient function. Horizontal axis – width *W* [µm], vertical axis – deposited particle density C_D [1000 particles per mm^2]. The profile with less value of sum of squares of the residuals divided by the gradient's width was used for further proceedings. In this example it was the profile No. 8.

3.3.6. *Fabrication and characterization of IBs gradients*

Using the previously described device we have been able to optimize a protocol for IBs gradient deposition by implementing an evolutionary algorithm. The obtained protocol was used to form an array of two dimensional gradients by depositing series of gradients in two perpendicular directions. The resulting patterns are presented in Figure 3.32.

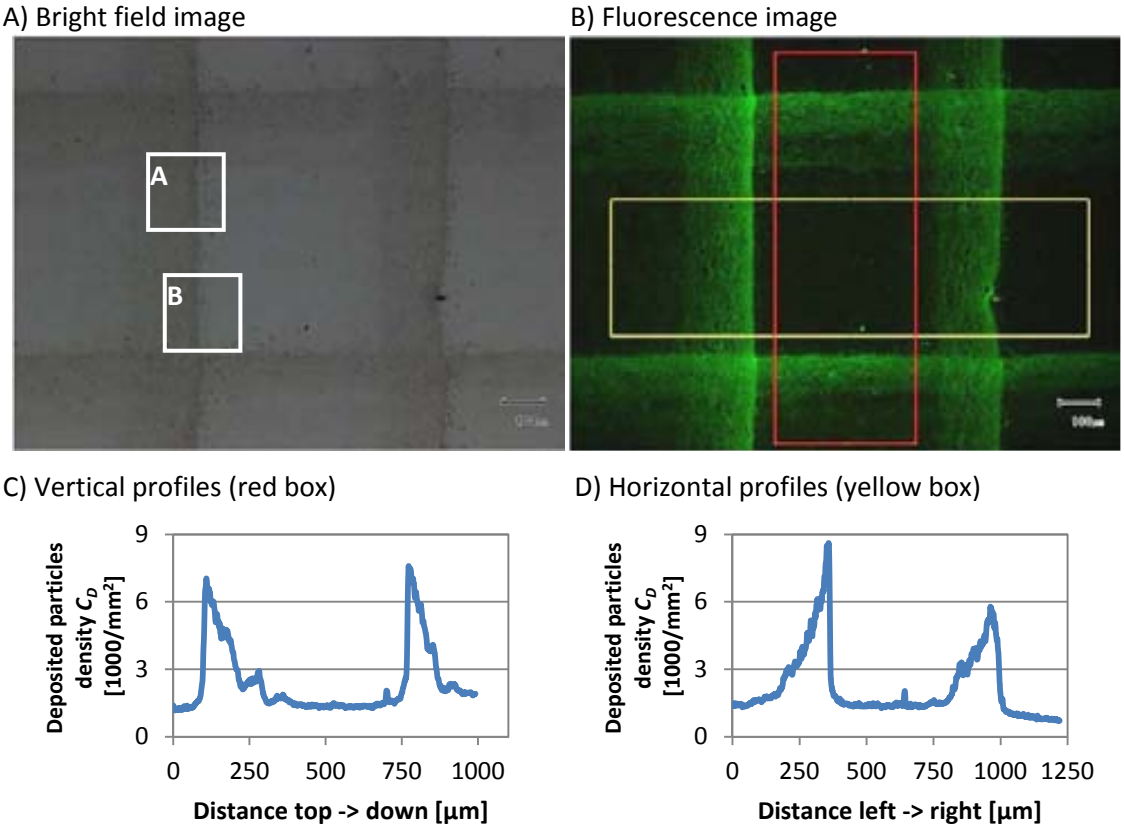

Figure 3.32 Array of two dimensional gradients of GFP-derived IBs deposited on a modified cover glass. A) Bright field image. White boxes depict the areas that were characterized by AFM (see Figure 3.33). B) Green fluorescence image. Red and yellow boxes are depicting areas used to prepare vertical and horizontal fluorescence profiles presented in C) and D), respectively.

The resulting patterns were characterized by AFM as described in the Section A.15 ("Atomic Force Microscopy"). The AFM topography, phase contrast maps and topography profiles are presented in Figure 3.33. As it can be clearly seen, deposits are easily distinguishable from the underlying glass substrates in both topography and phase contrast modes. It indicates that the layer of IBs have different morphology as well as mechanical properties than the substrate material. This is a promising indication, as we can expect that cells will react to these differences by changing their motility patterns.

In Figure 3.33A two profiles of gradient topography are presented: the green one is the profile of the marked line, and the blue one is an averaged profile of the whole image. The green profile is jagged, it contains high (200nm) and narrow peaks that can be assigned to the presence of individual IBs particles that appear all over the deposited area. However, as expected, their concentrations closer to the high fluorescence rim of the gradient, are higher. The blue profile is smoother, as it averages height along a broad area. Another important conclusion is that even in areas with very densely packed IBs these particles do not form a multilayer as heights are within the range of a single IBs diameter.

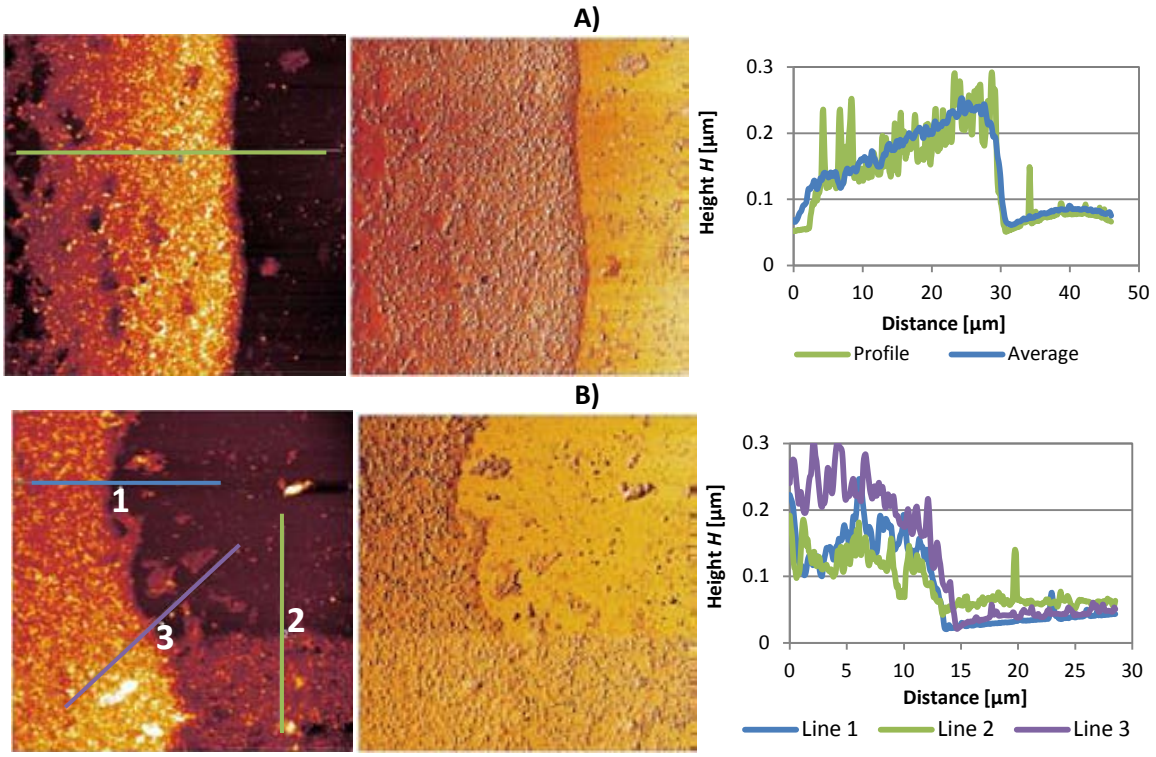

Figure 3.33 AFM images of gradient surfaces corresponding to the boxes A and B of Figure 3.32. Left: topography contrast, right: phase contrast. Next to each set of images its corresponding height profiles are presented.

Horizontal (dark blue), vertical (light green) and diagonal (purple) profiles derived from the perpendicular intersection of two gradient patterns are shown in Figure 3.33B. It can be clearly seen, that horizontal and vertical patterns are very similar, as they are produced by the same protocol. Purple profile, however, shows higher topography, because is the superposition of both protocols and therefore it contains more proteic material.

3.4. Conclusions

This Chapter describes how is possible to engineer a new device able to process colloids allowing their deposition on surfaces in patterns and even as gradients. The evaporation-assisted technique applied in the device is based on this widely known coffee drop effect. A deposit forming tool enabling a control of the liquid level (position of contact line with vertical substrate) was constructed and successfully used to prepare samples with desired striped patterns. This technique does not require preparation of stamps, scaffolds or replicas nor any type of labelling. Fully customizable patterns covering large areas (~10cm^2), that are easy to modify, can be obtained in a fast (up to 1 mm per 1 min) and cost-effective manner.

Finally, a robust procedure allowing the optimization of pump protocols for deposition of complex IBs surface-bound gradients was proposed and implemented. The obtained gradients were characterized, confirming the presence of linear changes of IBs concentration over broad areas of approximately 500 µm.

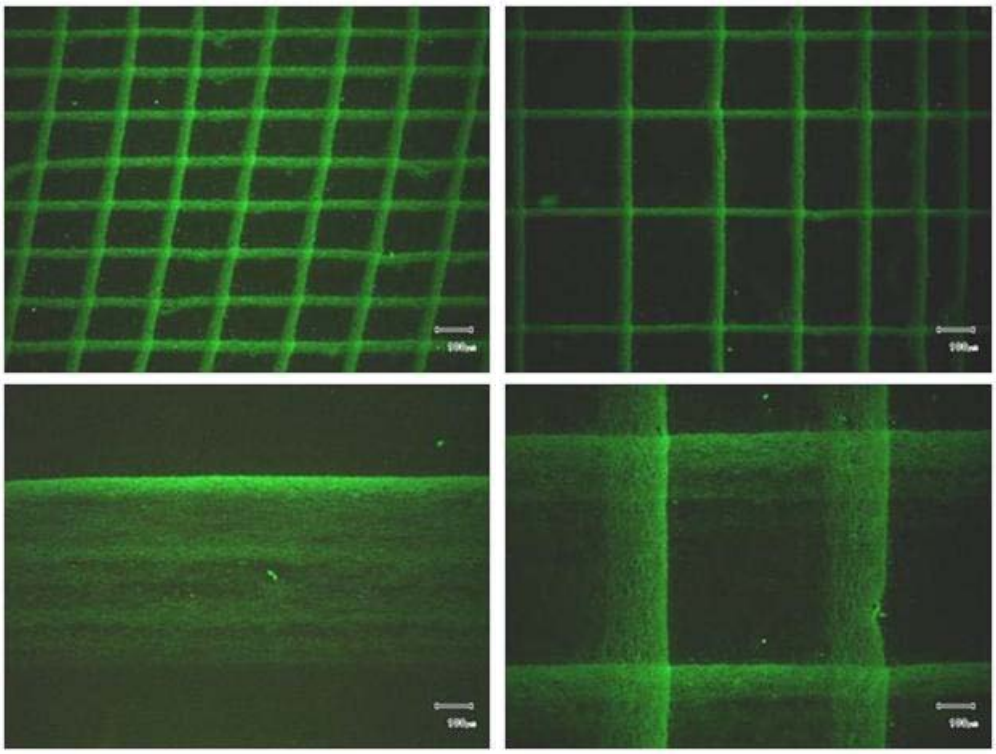

Figure 3.34 Examples of complex patterns and gradients obtained with the designed evaporation-assisted pattern deposition device. Resulting lines are parallel, cover big areas and their spacing can be freely and easily modified, by changing the protocol input Obtained gradients are broad (500µm width) and smooth, from very low to very high IBs concentrations. Superposition of a gradient pattern over another one rotated 90° results in two-directional gradients.

Examples of complex patterns produced by the evaporation assisted pattern deposition are presented in Figure 3.34. In this figure are depicted regular lattices of lines crossing at a controllable angle, with fully customizable distances in both directions. Also, the width of the deposited stripes can be modified at will (not shown). By applying an evolutionary algorithm for the optimisation of the IBs gradient protocol, we can obtain good quality one- and two-directional gradients. Such optimized IBs gradients will be used in the next Chapter for cell motility studies.

The prospective use of this technique by far surpasses the particular goal it was developed for. Even though its main aim was to deposit gradients of proteic NPs from aqueous suspensions, its prospective technological applications can involve other types of NPs (polymeric particles, quantum dots etc.), solvents (e.g. ethanol, hexane, halogenated solvents, their mixtures etc.) and substrates (Si, Au, glass etc.) if mutual interactions between particle, substrate and solvent are properly controlled. In general, all systems that are susceptible to the coffee-drop effect can be used to produce patterns in a controllable way using the methodology described in this Chapter.

3.5. Bibliography

[1] Petrie R.J., Doyle A.D., Yamada K.M. "Random versus directionally persistent cell migration"; *Nature Reviews: Molecular cell Biology* **2009**, Vol. 10, 538-549

[2] Wu J., Mao Z., Tan H., Han L., Ren T., Gao C. "Gradient biomaterials and their influences on cell migration"; *Interface Focus* **2012**, Vol. 2, 337–355

[3] Genzer J. "Surface-Bound Gradients for Studies of Soft Materials Behavior"; *Annu. Rev. Mater. Res.* **2012**, Vol. 42, 435–68

[4] (a) Liedberg B., Wirde M., Tao Y., Tengvall P., Gelius U. "Molecular gradients of ω-substituted alkanethiols on gold studied by X-ray photoelectron spectroscopy"; *Langmuir* **1997**, Vol. 13(20), 5329-5334; (b) Bhat R.R., Fischer D.A., Genzer J. "Fabricating planar nanoparticle assemblies with number density gradients"; *Langmuir* **2002**, Vol. 18(15), 5640-5643; (c) Genzer J., Bhat R.R. "Surface-bound soft matter gradients"; *Langmuir* **2008**, Vol. 24(6), 2294-2317

[5] Caelen I., Bernard A., Juncker D., Michel B., Heinzelmann H., Delamarche E. "Formation of gradients of proteins on surfaces with microfluidic networks"; *Langmuir* **2000**, Vol. 16(24), 9125-9130

[6] Jeon N.L., Dertinger S.K.W., Chiu D.T., Choi I.S., Stroock A.D., Whitesides G.M. "Generation of solution and surface gradients using microfluidic systems" *Langmuir* **2000**, Vol. 16(22), 8311-8316

[7] Jayaraman S., Hillier A.C. "Construction and reactivity mapping of a platinum catalyst gradient using the scanning electrochemical microscope"; *Langmuir* **2001**, Vol. 17(25), 7857-7864

[8] Terrill R.H., Balss K.M., Zhang Y., Bohn P.W. "Dynamic monolayer gradients: Active spatiotemporal control of alkanethiol coatings on thin gold films"; *Journal of the American Chemical Society* **2000**, Vol. 122(5), 988-989

[9] Xu C., Barnes S.E., Wu T., Fischer D.A., Delongchamp D.M., Batteas J.D., Beers K.L. "Solution and surface composition gradients via microfluidic confinement: Fabrication of a statistical-copolymer-brush composition gradient"; *Advanced Materials* **2006**, Vol. 18(11), 1427-1430

[10] Baker B.E., Kline N.J., Treado P.J., Natan M.J. "Solution-based assembly of metal surfaces by combinatorial methods"; *Journal of the American Chemical Society* **1996**, Vol. 118(36), 8721-8722

[11] Pitt W.G. "Fabrication of a continuous wettability gradient by radio frequency plasma discharge"; *Journal of Colloid And Interface Science* **1989**, Vol. 133(1), 223-227

[12] Lee J.H., Kim H.G., Khang G.S., Lee H.B., Jhon M.S. "Characterization of wettability gradient surfaces prepared by corona discharge treatment"; *Journal of Colloid And Interface Science* **1992**, Vol. 151(2), 563-570

[13] Kim M.S., Seo K.S., Khang G.b, Lee H.B. "First preparation of biotinylated gradient polyethylene surface to bind photoactive caged streptavidin"; *Langmuir* **2005**, Vol. 21(9), 4066-4070

[14] Venkateswar R.A., Branch D.W., Wheeler B.C. "An electrophoretic method for microstamping biomolecule gradients"; *Biomedical Microdevices* **2000**, Vol. 2(4), 255-264

[15] Choi S.H., Newby B.M.Z. "Micrometer-scaled gradient surfaces generated using contact printing of octadecyltrichlorosilane"; *Langmuir* **2003**, Vol. 19(18), 7427-7435

[16] Reynolds P.M., Pedersen R.H., Stormonth-Darling J., Dalby M.J., Riehle M.O., Gadegaard N. "Label-Free Segmentation of Co-cultured Cells on a Nanotopographical Gradient"; *Nano Lett.* **2013**, Vol. 13, 570−576

[17] Layani M., Gruchko M., Milo O., Balberg I., Azulay D., Magdassi S. “Transparent conductive coatings by printing coffee ring arrays obtained at room temperature”; *ACS Nano* **2009**, Vol. 3, 3537–3542

[18] Higashitani K., McNamee C.E., Nakayama M. “Formation of large-scale flexible transparent conductive films using evaporative migration characteristics of Au nanoparticles”; *Langmuir* **2011**, Vol. 27, 2080–2083

[19] Fan J.A., Bao K., Sun L., Bao J., Manoharan V.N., Nordlander P., Capasso F. “Plasmonic mode engineering with templated self-assembled nanoclusters”; *Nano Lett.* **2012**, Vol. 20, 5318-5324

[20] Han W., Lin Z. "Learning from “Coffee Rings: Ordered Structures Enabled by Controlled Evaporative Self-Assembly"; *Angew. Chem. Int. Ed.* **2012**, Vol. 51, 1534 –1546;

[21] (a) Zasadzinski J.A., Viswanthan R., Madsen L., Garnaes J., Schwartz D.K. "Langmuir-Blodgett Films"; *Science* **1994**, Vol. 263(5154), 1726-1733; (b) Chen X., Lenhert S., Hirtz M., Lu N., Fuchs H., Chi L. "Langmuir–Blodgett Patterning: A Bottom–Up Way To Build Mesostructures over Large Areas"; *Acc. Chem. Res.* **2007**, Vol. 40, 393–401; (c) Clemente-Leon M., Coronado E., Lopez-Munoz A.,

Repetto D., Catala L., Mallah T. "Patterning of Magnetic Bimetallic Coordination Nanoparticles of Prussian Blue Derivatives by the Langmuir−Blodgett Technique"; *Langmuir* **2012**, Vol. 28, 4525−4533; (d) Bardosova M., Pemble M.E., Povey I.M., Tredgold R.H. "The Langmuir-Blodgett Approach to Making Colloidal Photonic Crystals from Silica Spheres"; *Adv. Mater.* **2010**, Vol. 22, 3104–3124; (e) Reculusa S., Perrier-Cornet R., Agricole B., Héroguez V., Buffeteauc T., Ravainea S. "Langmuir–Blodgett films of micron-sized organic and inorganic colloids"; *Phys. Chem. Chem. Phys.* **2007**, Vol. 9, 6385-6390; (f) Ariga K., Yamauchi Y., Mori T., Hill J.P. "25th Anniversary article: What can be done with the langmuir-blodgett method? Recent developments and its critical role in materials science"; *Advanced Materials* **2013**, Vol. 25(45), 6477-6512

[22] Ai H., Jones S.A., Lvov Y.M. "Biomedical Applications of Electrostatic Layer-by-Layer Nano-Assembly of Polymers, Enzymes, and Nanoparticles"; *Cell Biochemistry and Biophysics* **2003**, Vol. 39, 23-43

[23] Boudou T., Crouzier T., Ren K., Blin G., Picart C. "Multiple Functionalities of Polyelectrolyte Multilayer Films: New Biomedical Applications"; *Advanced Materials* **2010**; Vol. 22, 441–467

[24] Bailey R.C., Stevenson K.J., Hupp J.T. "Assembly of Micropatterned Colloidal Gold Thin Films via Microtransfer Molding and Electrophoretic Deposition"; *Adv. Mater.* **2000**, Vol. 12, 1930-1934

[25] Boccaccini A.R., Keim S., Ma R., Li Y., Zhitomirsky I. "Electrophoretic deposition of biomaterials"; *J. R. Soc. Interface* **2010**, Vol. 7, 581–613

[26] Kane R.S., Takayama S., Ostuni E., Ingber D.E., Whitesides G.M. "Patterning proteins and cells using soft lithography"; *Biomaterials* **1999**, Vol. 20, 2363-2376

[27] Ng E., Gopal A., Hoshino K., Zhang X. "Multicolor microcontact printing of proteins on nanoporous surface for patterned immunoassay"; *Appl Nanosci.* **2011**, Vol. 1, 79–85

[28] Park H., Jeong H., Lee W.E., Yoon K., Oh C.J., Kwak G. "Positive-/Negative-, Erasable-/Immobilized-, Mono-/Multi-Color Fluorescence Image Patterning of Molecular-Scale Porous Polymer Film via a Microcontact Printing Method Using Various Chemical Inks"; *Macromol. Rapid Commun.* **2011**, Vol. 32, 360–365

[29] Bertone P., Snyder M. “Advances in functional protein microarray technology”; *FEBS Journal* **2005**, Vol. 272, 5400–5411

[30] (a) Yeo L.Y., Chang H.C., Chan P.P.Y., Friend J.R. "Microfluidic Devices for Bioapplications"; *Small* **2011**, Vol. 7, 12–48; (b) Kim S., Kim H.J., Jeon N.L.

"Biological applications of microfluidic gradient devices"; *Integrative Biology* **2010**, Vol. 2(11-12), 584-603

[31] Crozatier C., LeBerre M., Chen Y. "Multi-colour micro-contact printing based on microfluidic network inking"; *Microelectronic Engineering* **2006**, Vol. 83, 910–913

[32] Khademhosseini A., Suh K.Y., Jon S., Eng G., Yeh J., Chen G.J., Langer R. "A Soft Lithographic Approach To Fabricate Patterned Microfluidic Channels"; *Anal. Chem.* **2004**, Vol. 76, 3675-3681

[33] Maenosono S., Okubo T. Yamaguchi Y. "Overview of nanoparticle array formation by wet coating"; *Journal of Nanoparticle Research* **2003**, Vol. 5, 5–15

[34] (a) Deegan R.D., Bakajin O., Dupont T.F., Huber G., Nagel S.R., Witten T.A."Contact line deposits in an evaporating drop"; *Physical review E* **2000**, Vol. 62, 756-765; (b) Deegan R.D., Bakajin O., Dupont T. F., Huber G., Nagel S.R., Witten T A. "Capillary flow as the cause of ring stains fromdried liquid drops"; *Nature* **1997**, Vol. 389, 827-829; (c) Sommer A.P., Rozlosnik N. "Formation of Crystalline Ring Patterns on Extremely Hydrophobic Supersmooth Substrates: Extension of Ring Formation Paradigms"; *Crystal Growth & Design* **2005**, Vol. 5(2), 551-557; (d) Crivoi A., Duan F. "Elimination of the Coffee-Ring Effect by Promoting Particle Adsorption and Long-Range Interaction"; *Langmuir* **2013**, Vol. 29, 12067–12074 ; (e) Lebedev-Stepanov P., Vlasov K. "Simulation of self-assembly in an evaporating droplet of colloidal solution by dissipative particle dynamics"; *Colloids and Surfaces A: Physicochem. Eng. Aspects* **2013**, Vol. 432, 132– 138; (f) Popov Y.O. "Evaporative deposition patterns: Spatial dimensions of the deposit" *Physical Review E* **2005**, Vol. 71, 036313; (g) Tarasevich Y.Y., Vodolazskaya I.V., Bondarenko O.P. "Modeling of spatial–temporal distribution of the components in the drying sessile droplet of biological fluid"; *Colloids and Surfaces A: Physicochem. Eng. Aspects* **2013**, Vol. 432, 99– 103; (h) Fischer B.J. "Particle Convection in an Evaporating Colloidal Droplet"; *Langmuir* **2002**, Vol. 18, 60-67

[35] (a) Han W., Byun M., Li B., Pang X., Lin Z. "A Simple Route to Hierarchically Assembled Micelles and Inorganic Nanoparticles" *Angew. Chem. Int. Ed.* **2012**, Vol. 51, 12588 –12592; (b) Frastia L., Archer A.J., Thiele U. “Dynamical Model for the Formation of Patterned Deposits at Receding Contact Lines”; *Phys. Rev. Lett.* **2011**, Vol. 106, 077801; (c) Adachi E., Dimitrov A.S., Nagayama K. “Stripe Patterns Formed on a Glass Surface during Droplet Evaporation”; *Langmuir* **1995**, Vol. 11, 1057 – 1060; (d) Kim H.S., Lee C.H., Sudeep P.K., Emrick T., Crosby A.J. "Nanoparticle Stripes, Grids, and Ribbons Produced by Flow Coating"; *Adv. Mater.* **2010**, Vol. 22, 4600–4604; (e) Byun. M., Han W., Li B., Xin X., Lin Z. "An

Unconventional Route to Hierarchically Ordered Block Copolymers on a Gradient Patterned Surface through Controlled Evaporative Self-Assembly"; *Angew. Chem. Int. Ed.* **2013**, Vol. 52, 1122 –1127

[36] Berteloot G., Daerr A., Lequeux F., Limat L. "Dip coating with colloids and evaporation"; *Chemical Engineering and Processing: Process Intensification* **2013**, Vol. 68, 69–73

[37] Grosso D. "How to exploit the full potential of the dip-coating process to better control film formation"; *J. Mater. Chem.* **2011**, Vol. 21, 17033-17038

[38] Xiong S., Dunphy D.R., Wilkinson D.C., Jiang Z., Strzalka J., Wang J., Su Y., dePablo J.J., Brinker C.J. "Revealing the Interfacial Self-Assembly Pathway of Large-Scale, Highly-Ordered, Nanoparticle/Polymer Monolayer Arrays at an Air/Water Interface"; *Nano Lett.* **2013**, Vol. 13(3), 1041–1046

[39] Bigioni T.P., Lin X.M., Nguyen T.T., Corwin E.I., Witten T.A., Jaeger H.M. "Kinetically driven self assembly of highly ordered nanoparticle monolayers"; *Nature Materials* 2006, Vol. 5(4), 265-270

[40] Ginger D.S., Zhang H., Mirkin C.A. "The Evolution of Dip-Pen Nanolithography"; *Angew. Chem. Int. Ed.* **2004**, Vol. 43, 30– 45

[41] Salaita K., Wang Y., Mirkin C.A. "Applications of dip-pen nanolithography"; *Nature Nanotechnology* **2007**, Vol. 2, 145-155

[42] Sniadecki N.J., Desai R.A., Ruiz S.A., Chen C.S. "Nanotechnology for Cell–Substrate Interactions"; *Annals of Biomedical Engineering* **2006**, Vol. 34, 59–74

[43] Lee K.B., Lim J.H., Mirkin C.A. "Protein Nanostructures Formed via Direct-Write Dip-Pen Nanolithography"; *J. Am. Chem. Soc.* **2003**, Vol. 125, 5588-5589

[44] Calvert P. "Inkjet Printing for Materials and Devices"; *Chem. Mater.* **2001**, Vol. 13, 3299-3305

[45] Wilkinson C.D.W. "Making Structures for Cell Engineering"; *Materials* **2004**, Vol. 8, 21-26

[46] Watanabe S., Miyahara, M.T. "Particulate pattern formation and its morphology control by convective self-assembly"; *Advanced Powder Technology* **2013**, Vol. 24(6), 897-907

[47] Perrin J. "Mouvement brownien et réalité moléculaire"; *Annales de Chimie et de Physique* **1909**, Vol. 18, 1–114.

[48] Denkov N.D., Velev O.D., Kralchevsky P.A., Ivanov I.B., Yoshimura H., Nagayama K. "Two-dimensional crystallization"; *Nature* **1993**, Vol. 361, 26

[49] Denkov N.D., Velev O.D., Kralchevsky P.A., Ivanov I.B., Yoshimura H., Nagayama K. “Mechanism of formation of two-dimensional crystals from latex particles on substrates”; *Langmuir* **1992**, Vol. 8(12), 3183-3190

[50] Bodiguel H., Leng J. "Imaging the drying of a colloidal suspension"; *Soft Matter* **2010**, Vol. 6, 5451–5460

[51] Rabani E., Reichman D.R., Geissler P.L., Brus L.E. "Drying-mediated self-assembly of nanoparticles"; *Nature* **2003**, Vol. 426(6964), 271-274

[52] Tekin E., deGans B.J., Schubert U.S. "Ink-jet printing of polymers – from single dots to thin film libraries"; *J. Mater. Chem.* **2004**, Vol. 14 ,2627–2632

[53] Nquyen V.X., Stebe K.J. “Patterning of small particles by a surfactant-enhanced Marangoni–Benard instability”; *Phys. Rev. Lett.* **2002**, Vol. 88(16), 164501

[54] Maleki M., Reyssat M., Restagno F., Quéré D., Clanet C. "Landau–Levich menisci"; *Journal of Colloid and Interface Science* **2011**, Vol. 354, 359–363

[55] Yin Y., Lu Y., Gates B., Xia Y. “Template-assisted self-assembly: a practical route to complex aggregates of monodispersed colloids with well-defined sizes, shapes, and structures”; *J. Am. Chem. Soc.* **2001**, Vol. 123, 8718–8729

[56] Xia D., Biswas A., Li D., Brueck S.R.J. “Directed self-assembly of silica nanoparticles into nanometer-scale patterned surfaces using spin-coating”; *Adv. Mater.* **2004**, Vol. 16, 1427–1432

[57] Celio H., Barton E., Stevenson K.J. “Patterned Assembly of Colloidal Particles by Confined Dewetting Lithography”; *Langmuir* **2006**, Vol. 22, 11426-11435

[58] Harris D.J., Hu H., Conrad J.C., Lewis J.A. “Patterning colloidal films via evaporative lithography”; *Phys. Rev. Lett.* **2007**, Vol. 98, 148301

[59] Masuda Y., Itoh T., Koumoto K. “Self-assembly patterning of silica colloidal crystals”; *Langmuir* **2005**, Vol. 21, 4478–4481

[60] Choi Y.J., Luo T.J.M. “Self-assembly of silver–aminosilica nanocomposites through silver nanoparticle fusion on hydrophobic surfaces”; *ACS Appl. Mater. Interfaces* **2009**, Vol. 1, 2778–2784

[61] Fan F. "Assembly of Colloidal Particles by Evaporation on Surfaces with Patterned Hydrophobicity"; *Langmuir* **2004**, Vol. 20, 3062-3067

[62] Kraus T., Malaquin L., Schmid H., Riess W., Spencer N.D., Wolf H. "Nanoparticle printing with single-particle resolution"; *Nature Nanotechnology* **2007**, Vol. 2, 570-576

[63] Rivera T.P., Lecarme O., Hartmann J., Inglebert R.L., Peyrade, D. "Spectroscopic studies of plasmonic interactions in colloidal dimers fabricated by convective-capillary force assembly"; *Microelectronic Engineering* **2009**, Vol. 86(4-6), 1089-1092

[64] Fan F., Stebe K.J. "Assembly of Colloidal Particles by Evaporation on Surfaces with Patterned Hydrophobicity"; *Langmuir* **2004**, Vol. 20, 3062-3067

[65] Mino Y., Watanabe S., Miyahara M.T. "Colloidal Stripe Pattern with Controlled Periodicity by Convective Self-Assembly with Liquid-Level Manipulation"; *ACS Appl. Mater. Interfaces* **2012**, Vol. 4, 3184−3190

[66] Hanafusa T., Mino Y., Watanabe S., Miyahara M.T. "Controlling self-assembled structure of Au nanoparticles by convective self-assembly with liquid-level manipulation"; *Advanced Powder Technology* **2014**, Vol. 25, 811-815

[67] Mino Y., Watanabe S., Miyahara M.T. "Fabrication of Colloidal Grid Network by Two-Step Convective Self-Assembly"; *Langmuir* **2011**, Vol. 27, 5290-5295

[68] Watanabe S., Mino Y., Ichikawa Y., Miyahara M.T. „Spontaneous Formation of Cluster Array of Gold Particles by Convective Self-Assembly"; *Langmuir* **2012**; Vol. 28, 12982−12988

[69] Tsai H.Y., Vats k., Yates M.Z., Benoit D.S.W. "Two-Dimensional Patterns of Poly(N-isopropylacrylamide) microgels to spatially control Fibroblast Adhesion and Temperature-Responsive Detachment"; *Langmuir* **2013**, Vol. 29, 12183−12193

[70] Díez-Gil C., Krabbenborg S., García-Fruitós E., Vazquez E., Rodríguez-Carmona E., Ratera I., Ventosa N., Seras-Franzoso J., Cano-Garrido O., Ferrer-Miralles N., Villaverde A., Veciana J. "The Nanoscale Properties of Bacterial Inclusion Bodies And their Effect on Mammalian Cell Proliferation"; *Biomaterials* **2010**, Vol. 31, 5805

[71] Arjmandi N. "Resist Homogeneity, Updates in Advanced Lithography"; *InTech* **2013**, Ed. Prof. Sumio Hosaka, ISBN: 978-953-51-1175-7, DOI: 10.5772/56618. Available from: http://www.intechopen.com/books/updates-in-advanced-lithography/resist-homogeneity

[72] Whitley D. "An overview of evolutionary algorithms: practical issues and common pitfalls"; *Information and Software Technology* **2001**, Vol. 43, 817-831

[73] Hibbert D.B. "Genetic algorithms in chemistry"; *Chemometrics and Intelligent Laboratory Systems* **1993**, Vol. 19, 277-293

4. Cell motility on two-dimensional proteic nanoparticles gradients

4.1. Objectives

In previous Chapters we have studied the influence of two-dimensional patterns of proteic NPs on the cell positioning, orientation and morphology (Chapter 2) and developed of a new tool for the preparation of gradients of nanoparticles on surfaces (Chapter 3).

In this Chapter we aim to move one step forward and study how different IB´s gradient environments can stimulate the cell motility. The main objective of this Chapter was to compare cell responses to substrates decorated with various IBs patterns. In particular, we compare: A) Constant vs. gradient concentrations of IBs, B) Different steepness of IB´s concentration gradients, C) Different absolute IB´s concentrations, and D) Broad vs. narrow paths to study the influence of constraining cell´s paths. Illustrations of each case are shown in Figure 4.1.

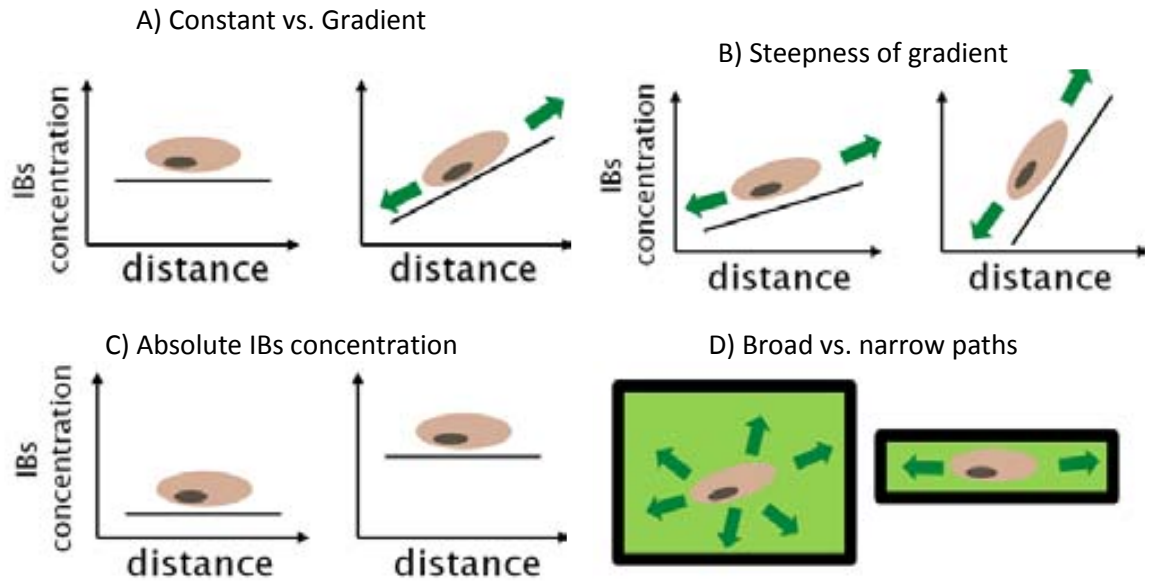

Figure 4.1 Cartoons depicting comparisons that will be made within the framework of this Chapter.

To reach this objective the work was divided into the following stages: 1) Substrate engineering and its production, 2) Cell seeding and data acquisition, 3) Development of a protocol for statistical data treatment and 4) Discussion of the results and conclusions.

4.2. Introduction

As mentioned in the introduction of the previous Chapter, cell migration is important for embryogenesis [1,2], immune surveillance and wound healing [3]. Although it is a universal ability and can be performed by all nucleated types of cells at a given point of their development, it is executed in various manners and, very often, specific conditions are required [4].

Most of the cells, including epithelial, stromal, and neuronal cells, are motile only during their morphogenesis and lose this ability after differentiation. It can be regained, to some extent, during healing (regenerative process) or neoplastic processes. In some cases, however, migration is an inherent property, needed by the cell, to fulfil its function during its all life cycle. Whereas some cell types are motile only in well defined conditions (like epithelial cells, moving only along basement membrane), others are versatile and can interact with almost any environment found within the body (for example leukocytes). Therefore, although the same basic function is preformed, in many cases, there are no universal cues that trigger the cell motility. Indeed, each cell operates within a distinct context and responds to environments in a distinct manner [4].

Because of the prominent role of cell motility in a large number of biological processes, immense effort has been made in understanding cell migration over the past few decades. Nowadays, some basic mechanisms of this complex phenomenon are already fairly well known.

4.2.1. Cell movement in physiological conditions

In general, cell migration can be usefully described as a cyclic process. The initial response of a cell to an agent promoting the migration is to polarize adopting an asymmetric morphology with well differentiated “front” and “rear” parts [5], as presented in Figure 4.2. This symmetry breaking polarizes intracellular signalling machinery that makes a cell moves. The position change is achieved by forming a protrusion at the cell front and the subsequent retraction at the rear. This protrusion can have a form of a rod-like spike (filopodia), broad, sheet-like projection (lamellipodia), or bulbous “blebs” [4]. The formation of these protrusions is based on remodelling the cytoskeleton by actin polymerization and is stabilized by integrin-mediated adhesion to the extracellular matrix (ECM) or adjacent cells [3].

The cyclic repetition of protrusion, interaction with the extracellular environment and retraction of the cell rear results in cell movement. For each cell type various migratory modes result in different migration speeds: it can be a fast “scanning” of leukocytes, moderately slow migration of fibroblast into a wounded area or a collective migration of tissue during organ formation. All these modes can experimentally be observed in 2D environments [3,4,6].

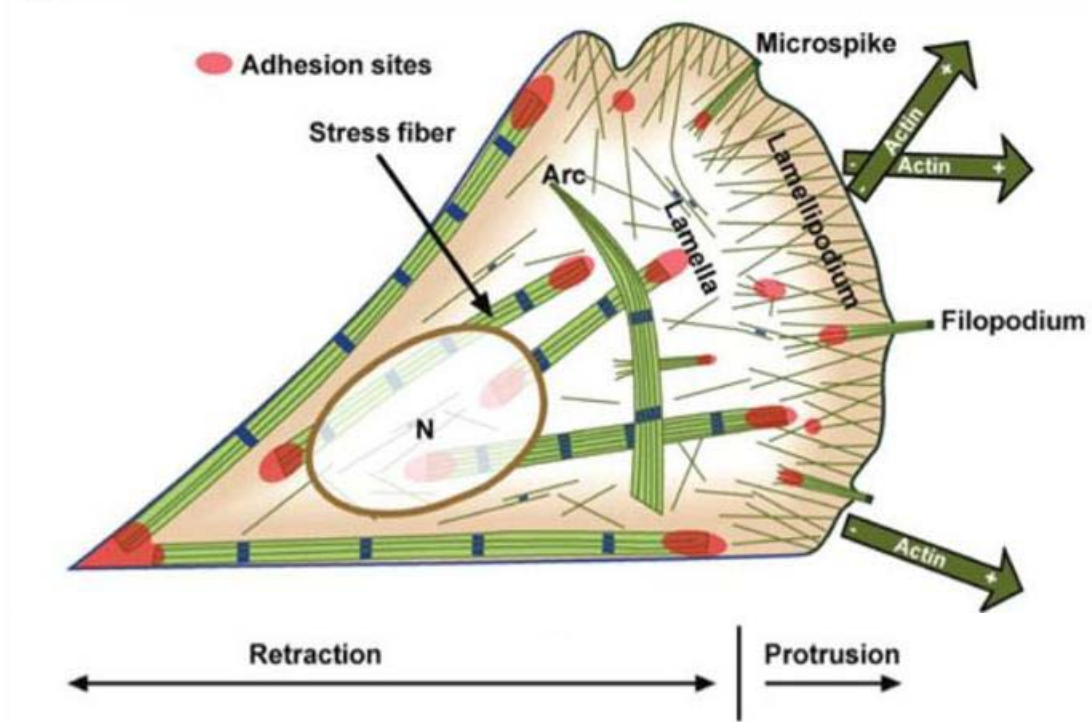

Figure 4.2 Schematic representation of the actin cytoskeleton in a polarised fibroblast moving to the right. The different organisational forms of actin filaments are depicted: diagonal actin filament meshwork in the lamellipodium, with associated radial bundles (filopodium and microspike); contractile bundles of actin (stress fiber) in the cell body and at the cell edge; and a loose actin network throughout the cell. The diagram shows an idealized cell; in reality, the actin arrays are interconnected in various combinations and geometries. Sites of adhesion of the cell with the substrate are also indicated (red). The letter N indicates nucleus. Image adapted from Reference [3].

Intrinsic movement is obtained when cells respond to stimuli that activate the cell movement machinery without providing directional information, as for example when the spatial distribution of chemokines is isotropic. Directionality occur when apart from establishing cell polarity, it is also maintained in response to an external asymmetric extracellular stimulus. These can be presented as a gradient of chemical attractors or repellents or other external cues. A good example of combination of these intrinsic and external stimuli can be observed during the elongation of an amniote embryo [7]. In this case, although single cells move randomly, the whole tissue elongates due to gradients of growth factors that have length scales larger than the size of a single cell.

In vivo cell mode of movement depends on both external and cell´s intrinsic properties. External factors, provided by the ECM, operate at every stage of the movement cycle stabilizing protrusions and maintaining the direction of migration [8]. In general, it is the number, availability and distribution of ECM binding sites, which dictate the shape of a cell and determine its mobility which are governed by the following factors:

- Dimensionality: 2D, 3D, or 1D in case of a single fibre of collagen
- Density and gap size: nanoscale or microscale structure of the ECM
- Stiffness: mechanical properties of the substrate
- Orientation: whether the ECM texture is random and loose or aligned

All these factors form a multimodal context which is integrated by cells and impacts strongly on the cells type of movement. Any modification of these conditions can lead to a different pattern of cell movement [4,9,10].

As mentioned before, not only the movement *per se,* but also, its organization in space and time is needed for cells to perform their roles. Actually, agents that increase random intrinsic migration will often diminish directed migration [3]. Directionality is achieved by a steering mechanism that forms part of the basic motility apparatus. It responds to motogenic stimuli such as external guidance cues or an asymmetric environmental factors (gradient) [3]. Gradients that influence direct cell migration have to operate at a scale perceived by the cell and can be of different nature provoking various responses:

- Haptotaxis – gradient of adhesion sites density influenced by topography
- Durotaxis – gradient of stiffness
- Chemotaxis – gradients of soluble factors
- Others, such as thermotaxis, phototaxis, magnetotaxis, galvanotaxis, mechanotaxis or gravitaxis

Also geometrical distribution (patterns) of binding sites have an impact on cell behaviour, as cells have been proven to react by cell shape, speed and orientation changes to local substrate anisotropy [11].

In complex environments it is often very difficult to predict which of these factors, or their combination, may have a predominant impact on cell movement. For example information from cell-cell contacts, soluble factor gradients, matrix bounded cues, and overall matrix properties contribute together to govern axonal growth cones [3]. Indeed, physiological conditions are extremely rich in cues that influence cell behaviour with a multitude of gradient generation mechanisms [12]. Many efforts have been done in order to reproduce *in vitro* the complex aspects of physiological conditions [13].

In summary cell motility is an important phenomenon and its mechanism has been thoroughly studied and generally is well known. However, tools to precisely control the cell movement and guidance at a large scale have not been developed yet due to the complexity of factors that influence the cell behaviour.

4.2.2. In vitro studies of cell motility

Control over cell motility can have many practical applications in the field of medical implants, supports for tissue regeneration and tissue engineering are among the most obvious ones [14]. Indeed, first publications in the field were welcomed with a great deal of excitement by the implant industry. It quickly become clear that using an appropriate material, that for example favours osteoblasts to osteoclasts movement, could be a major breakthrough in alleviating aseptic loosening and subsequent failure of implants. Furthermore, the possibility of generating 3D materials that can provide appropriate context maps of biological and mechanical information for cells and using them as scaffolds would greatly enhance the production of tissues or even entire organs for regenerative medicine. However, to accomplish that, further advancements in fundamental matrix biology, nanofabrication, synthetic self assembly, recombinant DNA technology etc. are needed [14].

4.2.2.1. Gradients production mimicking physiological conditions

The first achievement in this field was the establishment of protocols to generate *in vitro* gradients of soluble factors on surfaces. There have emerged a few distinct techniques to produce gradients in controlled laboratory conditions on model substrates [15], however the most popular are microfluidics devices [16,17]. The use of microfluidics has become a successful approach that enabled a combinatorial approach for gradient generation [18] and production of surface bound gradients [19]. In this way various types of molecules have been used to form gradients for studying cell motility. Chemokines are the most often used candidates, but also antigens [20], drugs [21], or calcium ions [22] have been proven to influence cell motility.

Apart from reacting to soluble gradients, cells react also to mechanical properties of the ECM. Two main modes of movement govern this process: haptotaxis – where cell react to gradients of binding sites on the substrate and durotaxis – where stiffness gradient of the substrate determines the cell´s behaviour [23]. Thus, topography and chemical patterning have both important influence on the stem cells behaviour, as reviewed in Reference [24].

Topography gradients have been also used for high throughput screening of biomaterials to control osteoblasts stem cells (see Figure 4.3) [25].

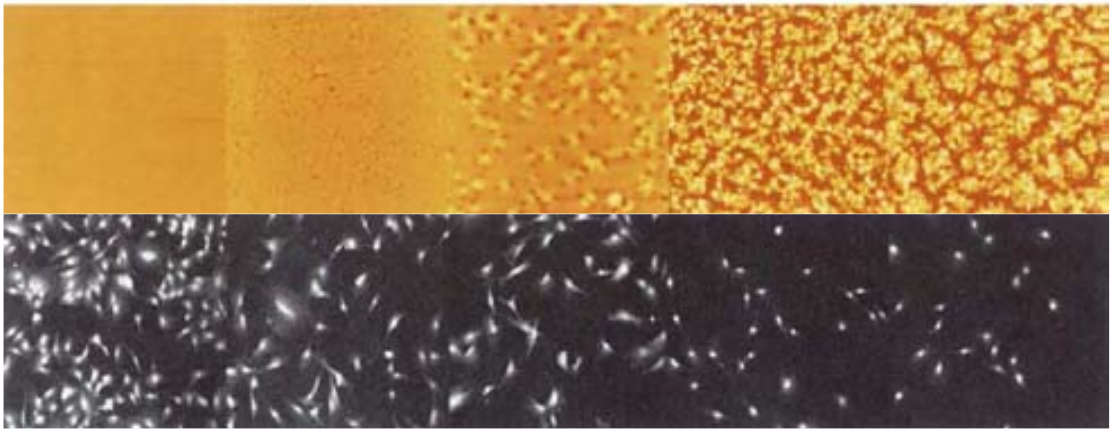

Figure 4.3 Influence of substrate roughness on cell morphology. Top: Representative AFM images of surface with different morphology made with poly-l-lactic acid (field of view in each image is 20μm). Bottom: Corresponding cell images from fluorescent microscopy (field of view in each image is 1500 μm). On flat substrates (leftmost panel) cells are elongated, whereas on rough substrates (rightmost panel) cells are round and smaller. Adapted from Ref. [25].

The sensitivity of cells to these parameters is very high. For example in one study the concentration gradients of surface-bound gold NP functionalised with RGD peptides were used to investigate cell sensitivity to binding sites [26]. Results suggested that cells react by elongation and migration to gradients as weak as resulting a difference of ~1nm in average ligand patch spacing between the front and rear of the cell. The remarkable sensitivity to such subtle variations is assumed to be achieved by signal time integration [27]. No wonder, that there are experiments demonstrating that multi-cue environment topography may have a predominant role over chemical gradients in cell guidance [28].

In contrast to those experiments indicating that cells can navigate in shallow chemical gradients, it was established that fibroblasts require a very steep stiffness gradient to perform durotaxis [29]. Although there are clear differences between mechanotaxis and durotaxis, they have many similarities [23] as very rarely such modes of motility occur separately. In fact, cells can interact with more than one type of cues at a time; e.g. integrating sets of chemical and topographical parameters [3,30].

4.2.2.2. Individual cell motility studies

The conventional methods for study cell motility are based on Boyden chamber [31]. This experimental setup consist of cell culture well with polycarbonate membrane bottom nested in other, bigger culture well. Cells are seeded into inner well while compound of interest is added to the outer well. Cells move from one well to another through membrane. Overall

migration can be quantified with standard plate reader after cell staining. This approach enabled significant advances in biological understanding of cell motility and become standard in the field of smooth muscle cell study [32].

Recently, individual cell studies based on time-lapse exposition become a very popular tool to quantify *in vitro* cell motility. Several, home-made, simple, cost-effective, yet robust tools dedicated to such observations have emerged recently [33,34,35]. Also custom designs that enable *in situ* gradient formation have already been reported. For example, Caserta *et al.* reported a device that enabled t perform a chemoattractant concentration gradient in a collagen gel sample produced by diffusion through a porous membrane. It was used subsequently to study the behaviour of three distinct cell lineages [36]. More complex platforms with incorporated image treatment units are delivered by big players in laboratory equipment companies. For instance GE Healthcare distributes the EZ-TAXIScan: microchannel device for *in situ* gradient formation which is readily combined with a microscopy and PC unit enabling image data treatment for cell motility studies [37]. As a result, cell motility studies are no longer reserved to study model cells and environments. More and more researches are focusing on specific cell lineages and environmental contexts. As examples we can mention experiments on leukocytes migration in the light of immunodeficiencies [38], research on mechanisms of smooth muscle cells movement [32], hemocyte movement quantification by time-lapse acquisition [39], *ex vivo* study of how chemokine gradients influence on interstitial dendritic cells [40], or *in vivo* studies of zebra fish embryo development [41]. Moreover, cell motility study has become also a tool for genetic studies. Effects of expression/silencing of genes can be quantified based on time-lapse individual cell assays [42,43], as well as in the presence of gradients [44].

4.2.2.3. Cell movement quantification

Time-lapse confocal images deliver large quantities of data. They can be used to assess the morphology of cells and how it changes upon stimuli in time [45]. However, its potential lies in the possibility to record precise data on cell´s position. Based on these data cell movement can be quantitatively characterized by calculating distances, velocities and orientation (angles) of cell movement [35,39,40].

Based on cell position data over time one can calculate parameters that enable the distinction between random and directional cell movement. The calculation of these parameters is not straightforward in the case of cell motility as cells movement is persistent in short periods of time but random in long periods of time. These parameters are [36,46]:

- Directional persistence time, *P*: the time in which the cell movement persists in the same direction
- Random motility coefficient, μ:– as an analogy to a molecular diffusion coefficient
- Chemotaxis index, *cI*: a weighted ratio between the distance along gradient and the total travelled distance (where 1 is only towards gradient and -1 in the opposite direction)

These parameters have been used for example in order to quantify the movement of ameboid stage of *Dictyostelium discoideum* cells on PDMS substrates covered with various patterns of micropillars [47], to develop a standard assay to test a drug efficiency [48], or to characterize cell movements in complex environments with both chemical and topographical cues [28].

4.2.3. Inclusion bodies and cell movement

Development of new biomaterials is also recognised as one of the most vital challenges of tissue engineering [49]. As mentioned before, the ideal biomaterial for a scaffold must transmit various signals, thus creating an artificial ECM, or scaffold, for cells in order to allow them to behave in a desired way. By that means, scaffolds should [49]: (i) guide migration of target cells into the injury site, stimulate their growth and/or differentiation and (ii) degrade in response to matrix remodelling enzymes released by the cells during the progress of tissue repair.

Design principles of biomaterials usually emerge based on biomimetic approaches derived from *in vivo* studies of the interactions of cells with growth factors. In normal tissues many growth factors, such as angiogenic Fibroblast Growth Factors (FGFs) and Vascular Endothelial Growth Factors (VEGFs) are an integral part of ECM. The FGFs family is especially interesting within this area, as some of its members have been proven to be responsible for the behaviour of a very wide range of cells (e.g NIH-3T3 fibroblasts [50]) and also for cell activities like motility [51]. Positive impact of FGF present in the form of IBs on cell proliferation also has been already confirmed [52,53].

Biomaterial implants could interact with specific adhesion and growth factor receptors expressed by target cells surrounding damaged tissues. Therefore, one of the strategies adopted for the fabrication of new biomaterials for tissue engineering is the integration of growth factor proteins into the scaffold itself which has been proven to be much more effective than releasing such proteins into a liquid medium as soluble proteins [49].

Encouraged by our previous findings demonstrating that Inclusion Bodies can be a useful tool to govern cell´s positioning, orientation and morphology (see Chapter 2), we aimed to explore its applicability in the research of cell motility. In order to do so, we have engineered a new technique that allows the functionalisation of two-dimensional substrates with complex patterns of such proteic nanoparticles (see Chapter 3).

As we have previously mentioned, *in vitro* studies suggest that not only physical structures (topography) but a combination of topography and biological cues (growth factors) induce responses and signalling mechanisms that promote cell migration. Thus, in order to include biological activity to the topographic factors already brought by the use of fluorescent GFP-derived IBs, we will also use FGF-based IBs giving a real biological activity to the substrate. In this way, cells will be stimulated not only by the topographical alteration of the substrate, but also by the biological activity of proteic nanoparticles.

In this Chapter we study the cell motility in response to substrates decorated with patterns and gradient concentrations of biologically active FGF IBs. We embark this journey, in hope of revealing secrets of the cell motility, as well as in an attempt to prove IBs usefulness in tissues engineering.

4.3. Results and Discussion

4.3.1. Preliminary experiments

4.3.1.1. Cell sensing IBs gradient's slopes

Before designing more complex patterns containing gradients of IBs we were interested to know whether the range of concentrations we can obtain is actually perceived by cells. If the gradient's slope is to gentle, a cell will not perceive it as a gradient and will not react by polarisation of its body with the subsequent directional movement. Thus, we have calculated the IBs concentration of deposits produced by the evaporation-assisted deposition technique (Chapter 3) using high resolution confocal images comparing them with the values obtained using the µCP technique that we have previously used to pattern IBs on surfaces (Chapter 2).

To put the obtained values in an adequate perspective, let us consider the typical geometry and dimensions of a fibroblast cell like the one, presented in the inset of Figure 4.4. In this image we have defined as "sensing areas" two areas of c.a. 150 µm^2 if 12 µm radius at both extremes of the 60 µm long cell. These values, although chosen arbitrarily, are reasonable assumptions, consistent with the actual cell's dimensions.

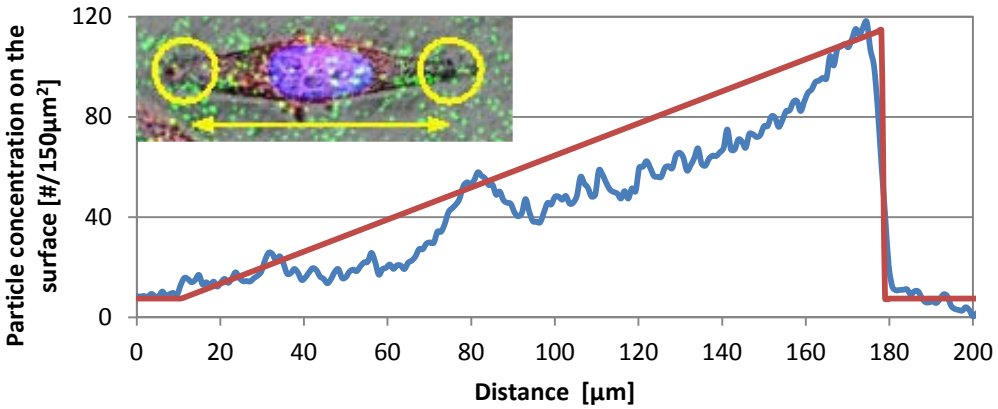

Figure 4.4 Representative IBs gradient obtained by evaporation assisted deposition. Blue –particle concentration (number of IBs per "sensing area") calculated based on GFP-based IBs fluorescence profile. Red – simple gradient fit. Inset shows a confocal microscopy image of a typical NIH-3T3 fibroblast scaled to dimensions of the plot (arrow denotes 60 µm). Each of the marked circles has an area of 150 µm^2. Red, blue and green denote cell membrane, cell nucleus and GFP IBs, respectively.

Assuming such values we have obtained IBs density values of 0.041 and 0.77 particles per µm^2 for most densely deposited IBs using the µCP and the evaporation assisted deposition technique, respectively. These values scale up to 6.1 and 118 particles per "sensing area" for both patterning methods, respectively. This means, that all the changes in orientation,

morphology and positioning presented in Chapter 2 were triggered by cells distinguishing unpatterned areas (0 particles per “sensing area”) from areas where the IBs density was at a level of 6.1 particles per “sensing area”.

Next, knowing that 118 particles per “sensing area” is the maximal IBs concentration obtained for the gradient that is approximately 170 µm wide (as example in Figure 4.4), we obtain a slope that changes 42 particles per “sensing area” at the distance of 60µm. In other words, the difference of IBs concentration between two “sensing areas” at the opposite ends of a cell along the gradient´s slope is 42 particles per “sensing area”. This value is much higher than the value required to be noticed by cells and therefore we can assume, that the gradient’s slope that we will use has an adequate steepness in order to be relevant for the cell movement.

4.3.1.2. Cell interactions with high concentrations of IBs

For cell motility experiments we used NIH-3T3 fibroblasts, which are commonly used for motility research due to its high movement rate.

Before performing the motility study, we have checked how cells react to undecorated substrate (coverglass functionalised with hydrophobic CH_3 terminated SAMs) as well as to substrate decorated with IBs at various concentrations. Fibroblasts cultivated at densities of 5000 cell/cm^2 over samples with no IBs as well as with low (0-6·10^4 particles/mm^2) and moderate (6·10^4-1.2·10^5 particles/mm^2) IBs concentrations had correct morphologies compared to cells cultivated in standard conditions in cell culture flasks. However, we have discovered, that very high IBs concentrations (5·10^5-8·10^5 particles/mm^2) limit cell movement. When cells encounter high IBs concentration zones, they cease to move randomly over the sample and “stuck” to the areas where they are confined, named as “corrals”, and interact with them. In some cases the cells detached IBs from the substrate and lifted them in order to cross the barrier as can be seen in a snapshot from confocal microscopy presented in Figure 4.5. It turns out, that “corrals” or areas surrounded by such high IBs concentration can be used as an effective way to limit the cell movement to a precise area. Similar observations have been made for cells interacting with simple GFP-derived IBs gradient pattern at high cell concentration (40 000 cell/cm^2). Snapshots from this experiment are presented in Figure 4.6.

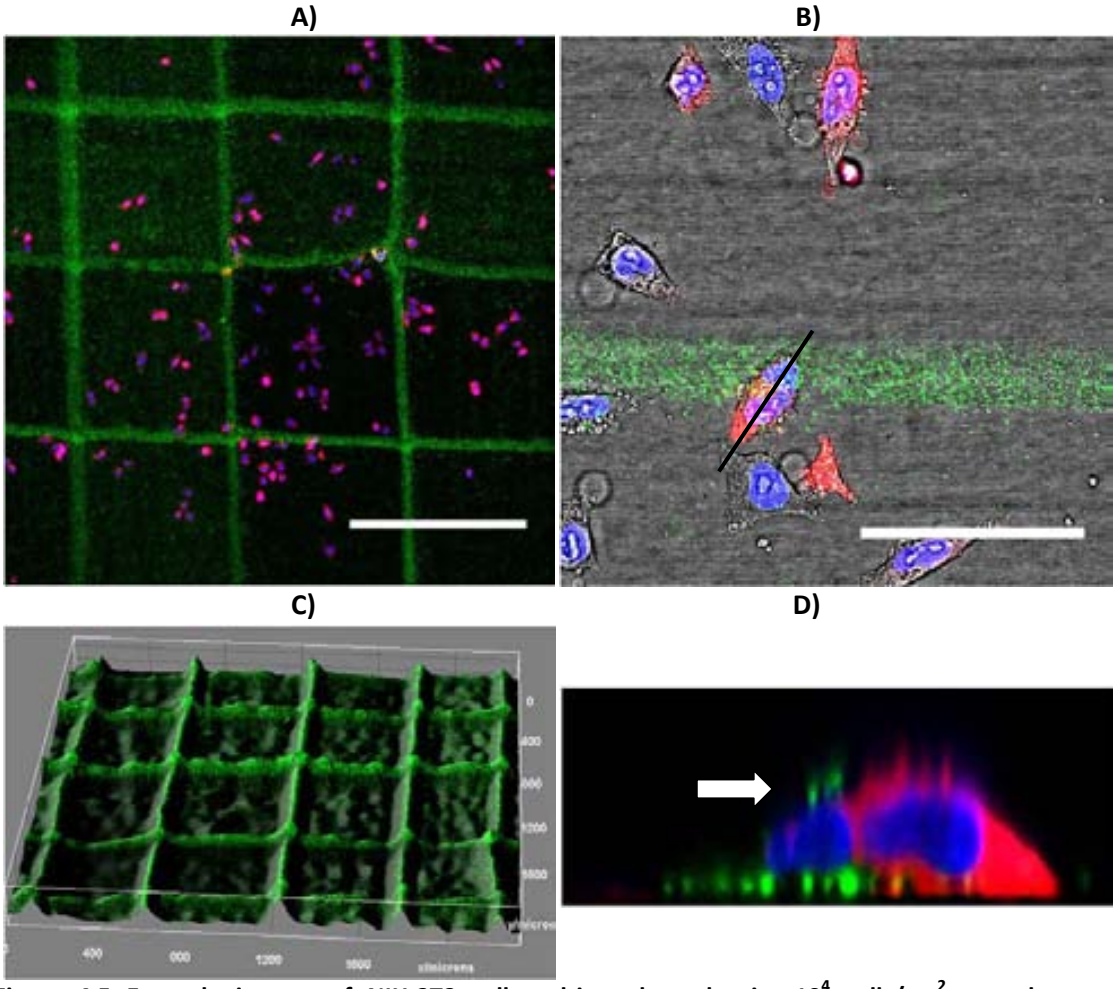

Figure 4.5 Example images of NIH-3T3 cells cultivated at density 10^4 cells/cm^2 on substrates decorated with GFP-derived IBs by the evaporation assisted deposition technique. A) Confocal microscopy image of cells in areas limited by corrals. Scale bar denotes 500µm. B) Detailed view of a cell crossing the corral (phase contrast image merged with fluorescence channels) Scale bars corresponds to 100µm. C) 3D visualization of deposited corrals. Z-axis corresponds to GFP fluorescence, not to actual topography. D) Cross-section of black line indicated in (B) obtained from 3D stack images indicating a cell detaching IBs from a IBs-rich stripe (arrow). Actual relation between cell and IBs sizes can be seen. Colour coding: green – IBs, blue – nuclei, red – cell membrane.

Cells moving from the "cliff" side of a gradient – the side where the maximum IBs concentration drops abruptly to virtually zero – were strongly attracted to IBs. We have observed that with time, cells disintegrate the pattern by removing IBs from the supporting material. On the other hand, we have observed that cells approaching from the side of gradient´s slope do not climb in the direction along the gradient (towards IBs higher concentrations), but they prefer to move along the pattern (perpendicular to the gradient) within a zone of moderate IBs concentrations, without approaching high IBs concentrations. At present we have any solid explanation to their behaviour.

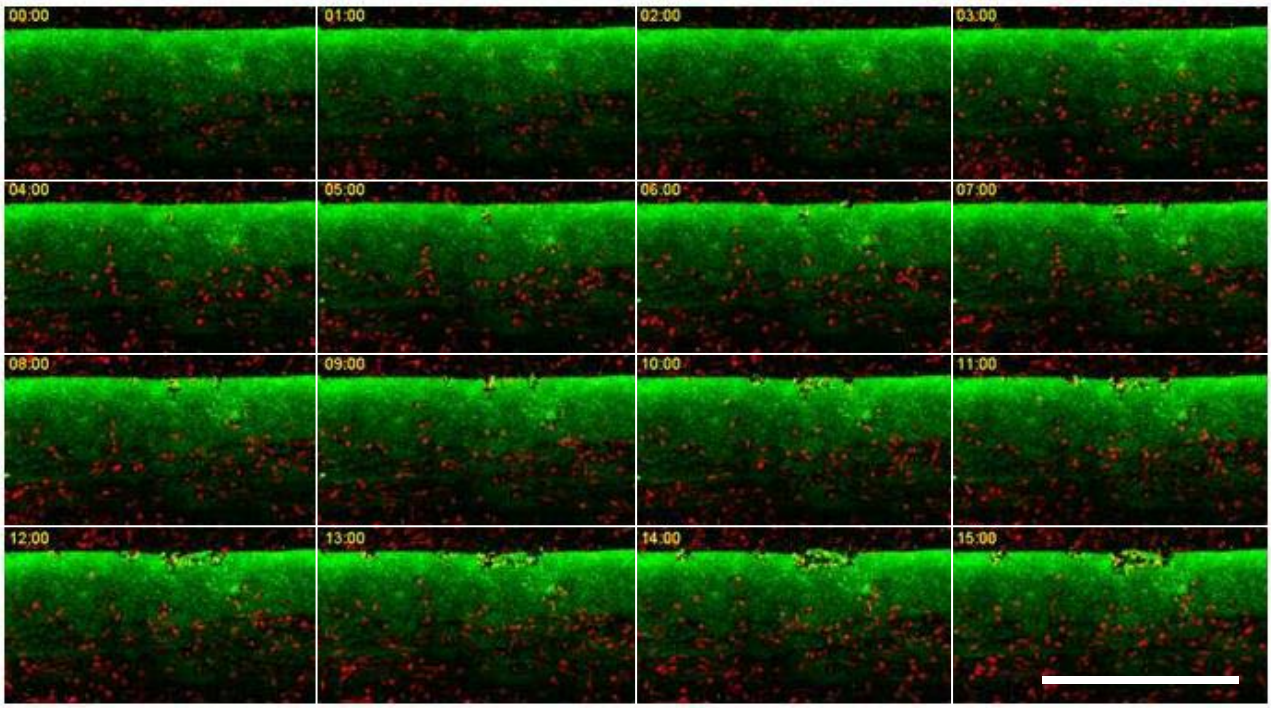

Figure 4.6 Snapshots from confocal microscopy time-lapse observation of cells seeded over a GFP simple gradient. It can be seen, that IBs are gradually detached from the support, by the cells approaching "from top" where the gradient is extremely steep, whereas cells approaching "from bottom" do not damage the pattern. Timestamps in hh:mm format are given in the top left corner of each snapshot. Colour coding: green IBs and red – cell membrane. Scale bar indicates 500µm.

4.3.1.3. Optimizing the ratio of FGF- to GFP-based IBs on surface

Despite that we are interested in stimulating cell movement by FGF-derived IBs, we have decided to keep at least some portion of fluorescent GFP-derived IBs in the colloidal mixture. There are two main reasons for such a decision: (i) to facilitate the pattern characterization by means of fluorescence microscopy and (ii) to facilitate the orientation of the substrate during confocal microscopy acquisition. Thus, we have made preliminary experiments in order to see if the presence of FGF IBs in the colloidal mixture has any influence on the deposited pattern.

Colloids with the same overall IBs concentration ($2 \cdot 10^{11}$ and $4.5 \cdot 10^{11}$ particles/ml) but different FGF to GFP IBs ratio were prepared and used for pattern deposition. Profiles of patterns obtained for colloids containing 5%, 50% and 95% of GFP IBs are presented in Figure 4.7. From these profiles, we can see that the number of deposited GFP-IBs depends on the total IBs concentration used in colloidal suspension (Figure 4.7. left). However, the normalised profiles (Figure 4.7. right) of deposits of various GFP/FGF-IBs mixtures align quite well. Thus, we can conclude that the final form (shape) of deposits depends on the pump protocol during deposition, not on the colloid composition or particle concentration. It is remarkable, that the

presence of as little as only 5% of GFP-IBs in the colloidal suspension is enough to obtain patterns that can be characterized with fluorescence analysis.

In summary, in this Chapter we used GFP-IBs as a fluorescent marker for an easy localization of IBs rich zones and the biologically active FGF-IBs used in order to stimulate the cell movement, as this material have been proved to have a positive impact on cell proliferation [52,53]. Therefore, the deposited pattern is expected to influence cell behaviour in a twofold manner: (i) by the presence of topological cues and (ii) by the presence of biological cues from the functional IBs patterned at various concentrations.

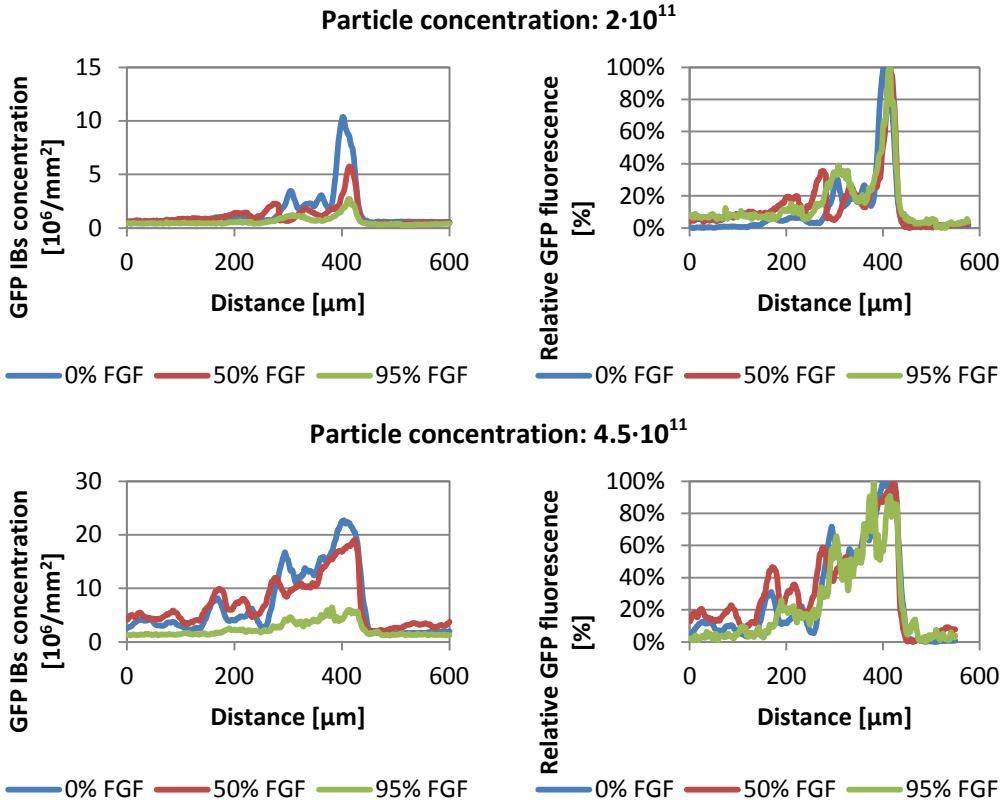

Figure 4.7 Examples of fluorescence profiles of IBs patterns deposited with different total particle concentration using various FGF- to GFP-IBs ratios. Left: absolute concentration of GFP-IBs calculated based on fluorescence profiles. Right: normalized concentration of GFP IBs (minimal concentration: 0%, maximal concentration: 100%). It can be seen that even though absolute GFP IBs concentration varies (as calculated based on fluorescence intensity), profile shapes are indifferent, as depicted on normalized plots.

4.3.2. Engineering a substrate for high throughput cell motility studies

A complex architecture for the two dimensional substrate was proposed in order to explore cell responses in many different contexts in the same experiment. The design of the

final pattern was based on our previous experiments indicating, that areas surrounded by high concentrations of IBs deposits act as corrals for cell movement. Using them as fences limiting cell movement we designed two IBs concentration profiles that were used to deposit IBs consecutively in perpendicular directions on the same substrate. Idealized designed profiles are presented in Figure 4.8.

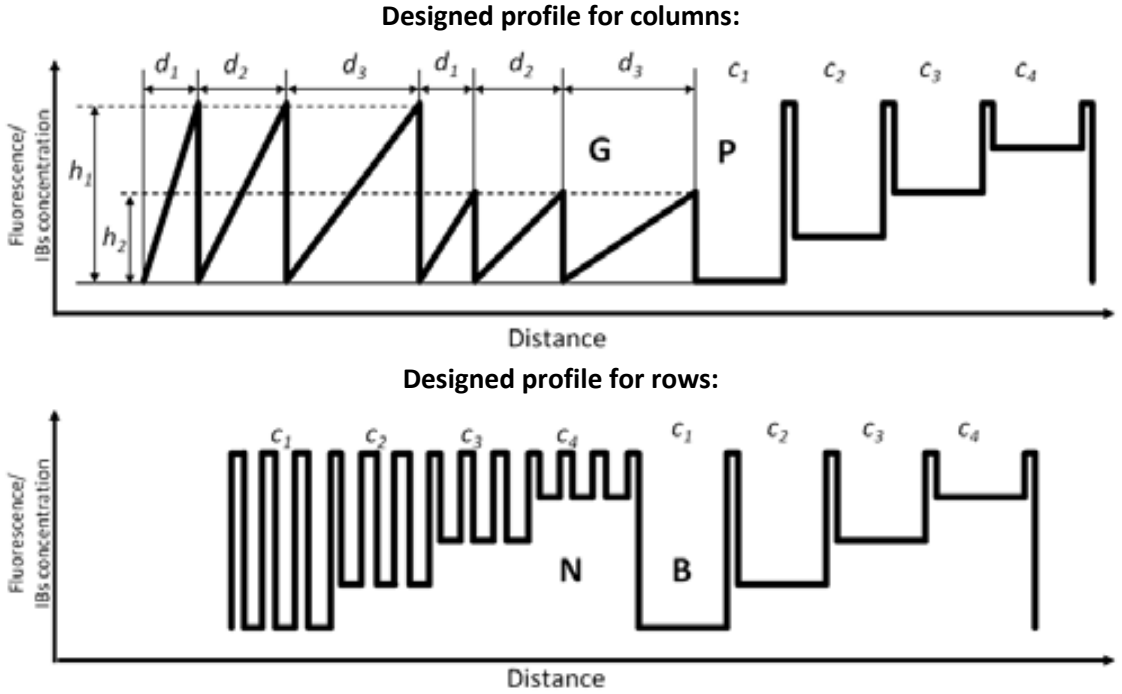

Figure 4.8 Designed profiles used to deposit IBs on a surface. The "column" profile consisted of 10 zones, each one with a different pattern: 6 distinct gradients and 4 plain zones. Gradients are denoted with "G" and are characterized by their heights (*h*) and widths (*d*). Plain zones marked with "P" have various IBs concentrations. The "row" profile consisted of 8 zones: 4 with narrow tracks "N" and 4 with broad zones "B". Each non-gradient subzone is characterized by four different IBs concentration ($c_1 > c_2 > c_3 > c_4$).

The intersection of columns and rows results in a final pattern that consisted of 80 well-defined zones with 80 different IBs profiles. Thus, each zone is characterized by a unique combination of parameters, as presented in Table 4.1.

The final pattern was deposited using a mixture containing 95% of FGF-IBs and 5% GFP-IBs at a total concentration of $4.5 \cdot 10^{11}$ particles/ml. Measurements of particle concentrations are summarized in Section A.14.3 ("Nanoparticle Tracking Analysis"). Overall image from confocal microscopy of the green fluorescence of the deposited patterns of IBs is presented in Figure 4.9. Numeration of zones corresponds to the one presented in Table 4.1. The differences in ordering between Table 4.1 and Figure 4.9 are a result of the last row being out of visible range of the microscope. However, as the pattern repeats itself over the surface it was substituted with a row "above" the first one.

Table 4.1 Parameters of the 80 zones from the designed pattern. Symbol meaning: G – column with a gradient, P-column with a plain zone, N – row with a narrow tracks, B – row with a broad zone, *h* – gradient height, *d* – gradients width, *c* - IBs concentrations (c_1<c_2<c_3<c_4). Each of 80 zones has its unique number (in black) and is characterized by a combination of parameters inherited from columns (blue), and rows (red).

	G, d_1, h_1	G, d_2, h_1	G, d_3, h_1	G, d_1, h_2	G, d_2, h_2	G, d_3, h_2	P, c_1	P, c_2	P, c_3	P, c_4
N, c_1	1 G, d_1, h_1 N, c_1	2 G, d_2, h_1 N, c_1	3 G, d_3, h_1 N, c_1	4 G, d_1, h_2 N, c_1	5 G, d_2, h_2 N, c_1	6 G, d_3, h_2 N, c_1	7 P, c_1 N, c_1	8 P, c_2 N, c_1	9 P, c_3 N, c_1	10 P, c_4 N, c_1
N, c_2	11 G, d_1, h_1 N, c_2	12 G, d_2, h_1 N, c_2	13 G, d_3, h_1 N, c_2	14 G, d_1, h_2 N, c_2	15 G, d_2, h_2 N, c_2	16 G, d_3, h_2 N, c_2	17 P, c_1 N, c_2	18 P, c_2 N, c_2	19 P, c_3 N, c_2	20 P, c_4 N, c_2
N, c_3	21 G, d_1, h_1 N, c_3	22 G, d_2, h_1 N, c_3	23 G, d_3, h_1 N, c_3	24 G, d_1, h_2 N, c_3	25 G, d_2, h_2 N, c_3	26 G, d_3, h_2 N, c_3	27 P, c_1 N, c_3	28 P, c_2 N, c_3	29 P, c_3 N, c_3	30 P, c_4 N, c_3
N, c_4	31 G, d_1, h_1 N, c_4	32 G, d_2, h_1 N, c_4	33 G, d_3, h_1 N, c_4	34 G, d_1, h_2 N, c_4	35 G, d_2, h_2 N, c_4	36 G, d_3, h_2 N, c_4	37 P, c_1 N, c_4	38 P, c_2 N, c_4	39 P, c_3 N, c_4	40 P, c_4 N, c_4
B, c_1	41 G, d_1, h_1 B, c_1	42 G, d_2, h_1 B, c_1	43 G, d_3, h_1 B, c_1	44 G, d_1, h_2 B, c_1	45 G, d_2, h_2 B, c_1	46 G, d_3, h_2 B, c_1	47 P, c_1 B, c_1	48 P, c_2 B, c_1	49 P, c_3 B, c_1	50 P, c_4 B, c_1
B, c_2	51 G, d_1, h_1 B, c_2	52 G, d_2, h_1 B, c_2	53 G, d_3, h_1 B, c_2	54 G, d_1, h_2 B, c_2	55 G, d_2, h_2 B, c_2	56 G, d_3, h_2 B, c_2	57 P, c_1 B, c_2	58 P, c_2 B, c_2	59 P, c_3 B, c_2	60 P, c_4 B, c_2
B, c_3	61 G, d_1, h_1 B, c_3	62 G, d_2, h_1 B, c_3	63 G, d_3, h_1 B, c_3	64 G, d_1, h_2 B, c_3	65 G, d_2, h_2 B, c_3	66 G, d_3, h_2 B, c_3	67 P, c_1 B, c_3	68 P, c_2 B, c_3	69 P, c_3 B, c_3	70 P, c_4 B, c_3
B, c_4	71 G, d_1, h_1 B, c_4	72 G, d_2, h_1 B, c_4	73 G, d_3, h_1 B, c_4	74 G, d_1, h_2 B, c_4	75 G, d_2, h_2 B, c_4	76 G, d_3, h_2 B, c_4	77 P, c_1 B, c_4	78 P, c_2 B, c_4	79 P, c_3 B, c_4	80 P, c_4 B, c_4

Actual fluorescence intensity profiles of the gradients with their nominal descriptors are presented in Figure 4.10. As it can be seen in part A) the profile follows our initial design, with the exception of the third gradient (*G*, h_1, d_3) which is characterized by the right nominal width, but with resulting intensity higher than expected.

Experimental particle density per "sensing zone" of an area of 150 µm^2 (which is a good approximation for typical cell's adhesion site area) is calculated in the maximal point of each gradient and presented in the part B) of Figure 4.10. Widths of gradients follow the assumed order: narrow, medium and broad, as presented in part C).

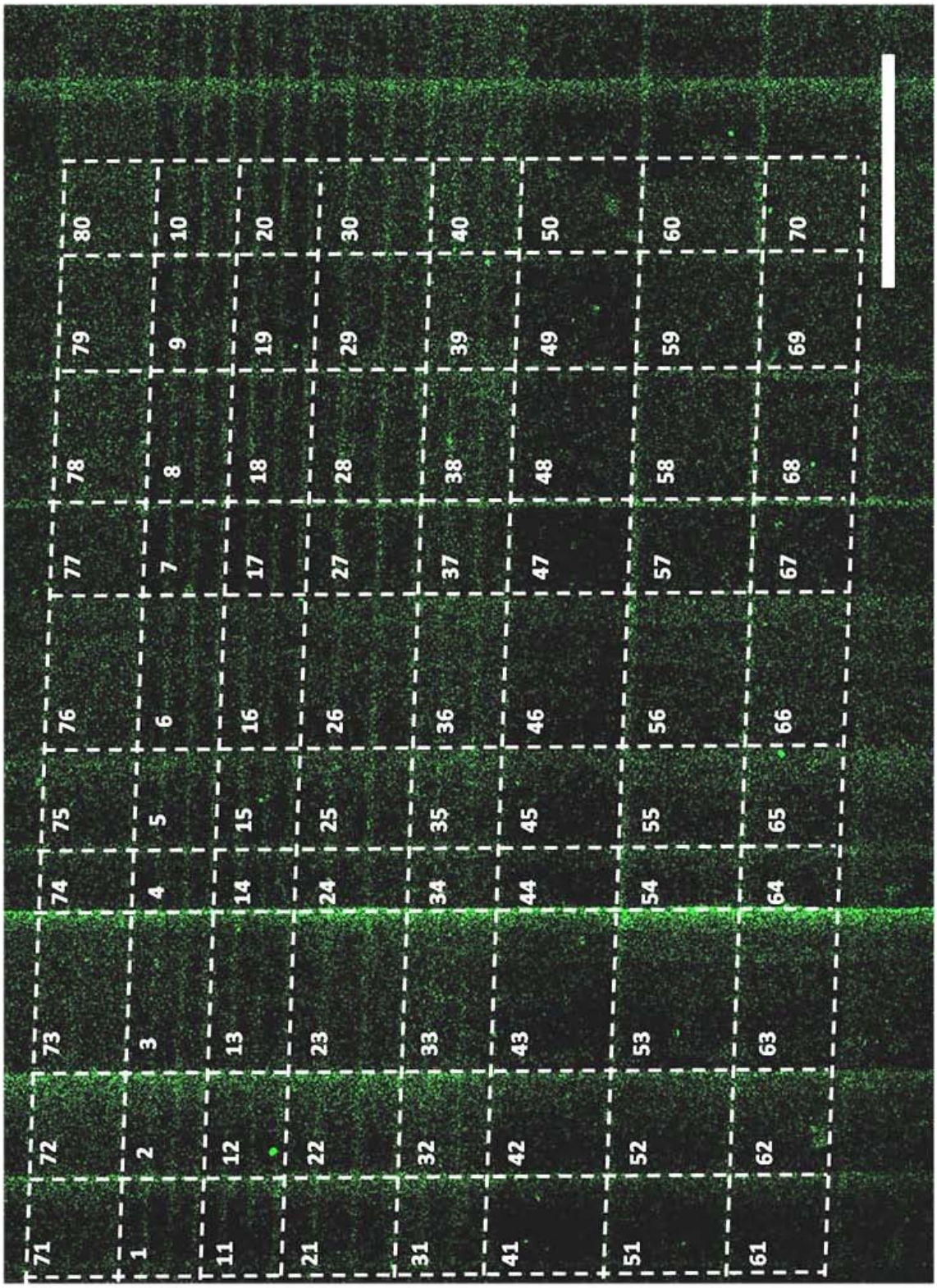

Figure 4.9 Confocal microscopy image of the substrate engineered with IBs for cell motility studies. 80 different zones are marked. Scale bar indicates 1mm.

Slopes are quantified as a difference of number of IBs particles between two "sensing zones" separated by of 60μm (the typical cell length) along the gradient and are presented in

part D) of Figure 4.10. Narrow gradients (d_1) have the highest slope compared with the medium (d_2) and broad (d_3) ones (with the exception of the misshaped G_3 gradient). Another way to quantify the gradient's slope is to express absolute value calculated in part D) to the maximal IBs concentration in each gradient resulting a percentage ratio as presented in E). In both representations we can see that we have obtained a different steepness of slopes, as intended. Moreover, absolute values given in part D) of Figure 4.10 are within the range of steepness that can be perceived by fibroblast cells, as considered in Section 4.3.1.1 ("Cell sensing IBs gradient's slope").

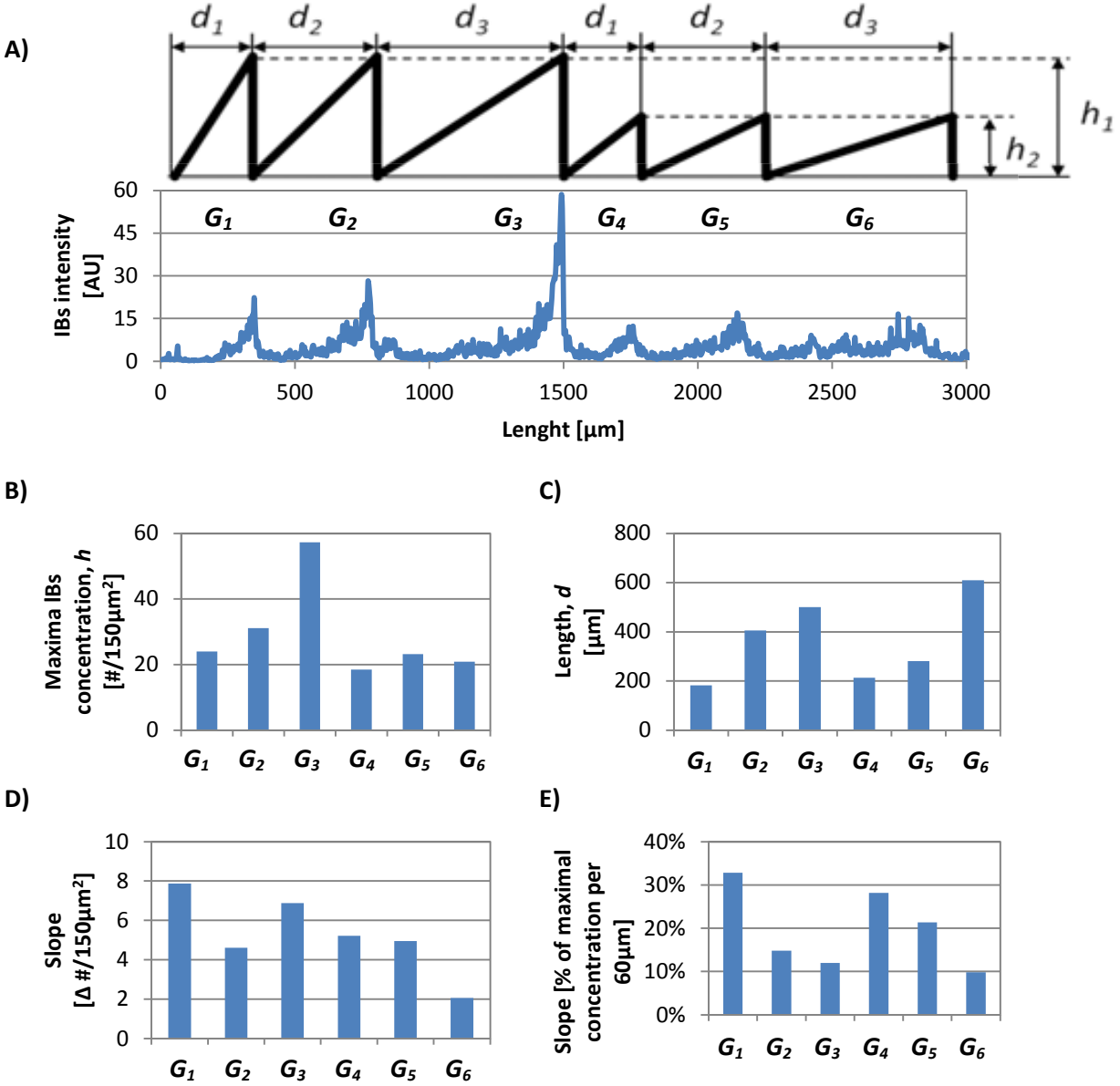

Figure 4.10 Characterization of resulting gradients. A) Actual fluorescence intensity profiles with nominal designed profiles (above). B) Quantification of the maximal IBs concentration per "sensing zone". C) Gradient lengths. D) Gradient slopes expressed in absolute values. E) Gradients slopes expressed in percentage of the maximal IBs concentrations per 60µm. Indexes follow notation give in Table 4.1.

Although special care was taken during the two-step orthogonal pattern deposition, due to the manual manipulation of sample, zones are not rectangles, but rather a parallelograms. Figure 4.9 will serve as an orientation reference for all data and plots discussed further in this Chapter.

In an ideal case each zone would have the same size. However in our case each zone has a unique surface due to various widths of profiles. Despite that, the range of surfaces is rather narrow ranging from 0.09 to 0.25mm^2 and therefore enabling their comparison. This factor influenced the number of cells that were seeded to each zone (bigger zones tend to have more cells). To take into account such a factor, values of cell movement descriptors will be always given as averages for all cells in each zone.

4.3.3. Evaluation of cell movements

Once the design and the preparation of the patterned substrate with IBs was completed we have proceed with confocal microscopy time-lapse acquisition of NIH-3T3 fibroblast cells cultivated over the prepared substrate. The complete cell medium in a cultivation flask was changed to a cell medium with a 1% of serum 24 hours prior to cell seeding over the sample in order to sensitize cells to the FGF content. Cells were then seeded at a concentration of 10 000 cells/cm^2. Confocal microscopy observations were carried out as described in Section A.18 (“Time-lapse confocal microscopy”). All the data that characterise cell positions originate from series of raw phase-contrast images captured during 22 hours, every 30 minutes.

Image treatment was carried out using the ImageJ 1.48g software coupled with the FIJI image processing package (GPL licence) and the MTrackJ plugin (http://www.imagescience.org/meijering/software/mtrackj/). First, images were enhanced and then cell positions were extracted from the time series. The average value of GFP fluorescence intensity was calculated for a circular zone of ~2500 µm^2 around cell´s position. This value enabled us the calculation of average IBs concentration beneath the cells and in their close neighbourhood. Data treatment pipeline is schematized in Figure 4.11.

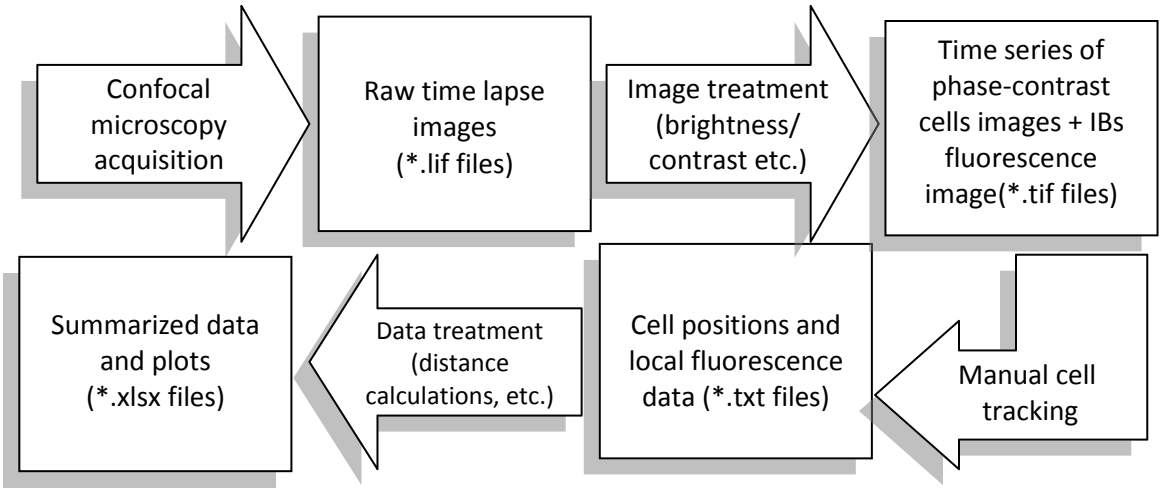

Figure 4.11 Scheme of the data treatment pipeline. Raw time-lapse confocal microscopy images were treated in order to obtain the background fluorescence image and a time series of high contrast images of moving cells. For each image in the time series the cell position was tracked (x and y coordinates) and local average IBs intensity was calculated. Knowing cell positioning at each instance, as well as distances and orientations, time resolved profiles for each cell could be calculated. For every cell in each zone such data was averaged in order to obtain statistically relevant descriptors of the cell motility in each of the 80 distinct environments of the high-throughput substrate.

Only cells that could be followed for at least 30 instants of time within one particular zone (that corresponds to a period of 14,5 hours) and cells that moved a total distance over 100 µm were taken into account to perform the statistical analysis. In this way we exclude cells that migrate from one zone to another and other possible artefacts like dead cells, impurities, etc. Example images of a single cell movement are presented in Figure 4.12.

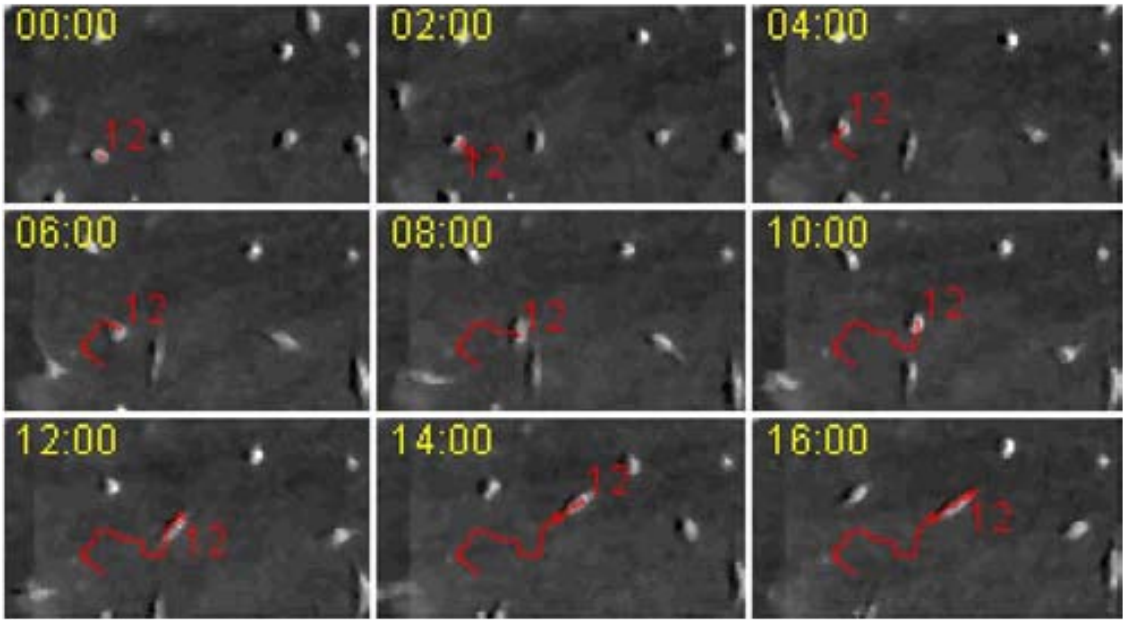

Figure 4.12 Example images of a moving cell. Each frame presents a snapsot image of confocal microscopy observation. Time label is given in hh:mm format. The track of cell no. 12 in this zone is marked in red.

4.3.3.1. Analysis of number of cells in each zone

Table 4.2 summarizes the number of cells that were taken into account to perform the statistical analysis for each zone. The different cell number obtained in each zone is the effect of a random distribution of cells during seeding (although media with cells was thoroughly pipetted during transfer and agitated after the seeding). Distribution of cell number is presented in Figure 4.13. To take that factor into account, cell movement descriptor values are given as averages for all cells in each zone.

Table 4.2 Number of cells studied in each zone. Red, orange, yellow and green colours indicate zones with low (>9), moderate (9-21), medium (21-41) and high (<41) number of cells, respectively. The position of values in this table corresponds to the layout of the zones shown in Table 4.1.

Cell number N [#]		Gradient						Plain			
		High h_1			Low h_2						
		Narrow d_1	Moderate d_2	Broad d_3	Narrow d_1	Moderate d_2	Broad d_3	c_1	c_2	c_3	c_4
Narrow	c_1	14	13	14	5	9	11	8	5	6	5
	c_2	16	16	27	5	9	15	7	8	3	3
	c_3	18	28	57	30	27	19	12	7	12	8
	c_4	19	29	47	28	27	27	6	7	10	7
Broad	c_1	31	39	56	35	28	30	10	15	5	4
	c_2	27	30	30	25	43	48	21	10	12	6
	c_3	26	26	37	8	19	50	40	19	17	10
	c_4	4	5	13	9	13	14	6	4	7	6

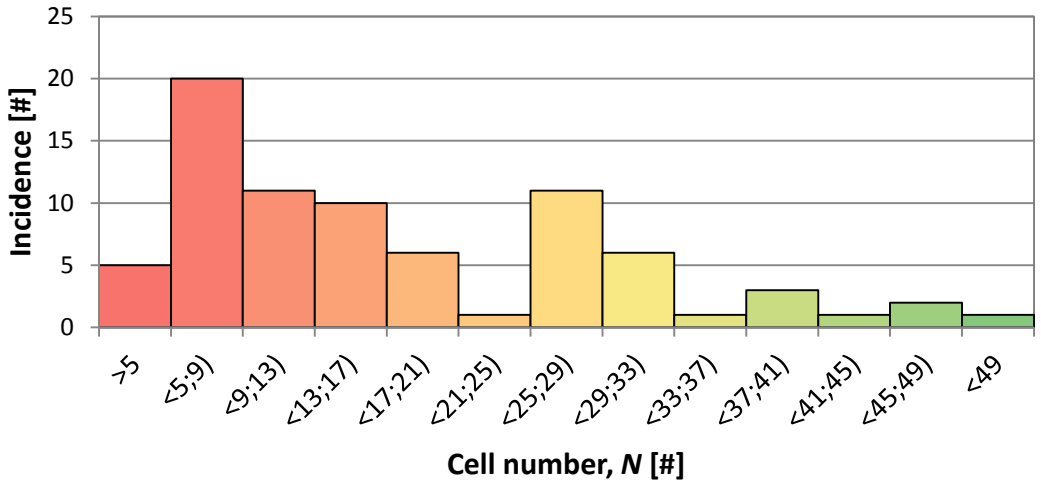

Figure 4.13 Distribution of cell number in zones. Zones with very few cells as well as zones with many cells were analysed. On average there are 18.3 cells in each zone (1462 cells in total).

From now on, in order to represent data for all the 80 different zones, to keep clarity and avoid ambiguity, we will use colour-coded tables where green, yellow and red represent areas

where the values are high, medium and low, respectively. The position of each zone is in accordance with the position presented in Table 4.1.

4.3.3.2. Analysis of cell distances travelled by cells

In order to have a complete picture of cell movements we have calculated different parameters describing distance travelled by the cells. For each zone we calculated:

- Averaged total distance travelled by the all cells, $\overline{D}_{total}$: sum of total distances travelled by all cells over a period of 22 hours of image acquisition divided by the total number of cells, N, in this zone
- Averaged total effective distance travelled by all cells, $\overline{D}_{effective}$: averaged distance between the last and the initial cell position for all cells in each zone

These descriptors are figuratively represented in Figure 4.14.

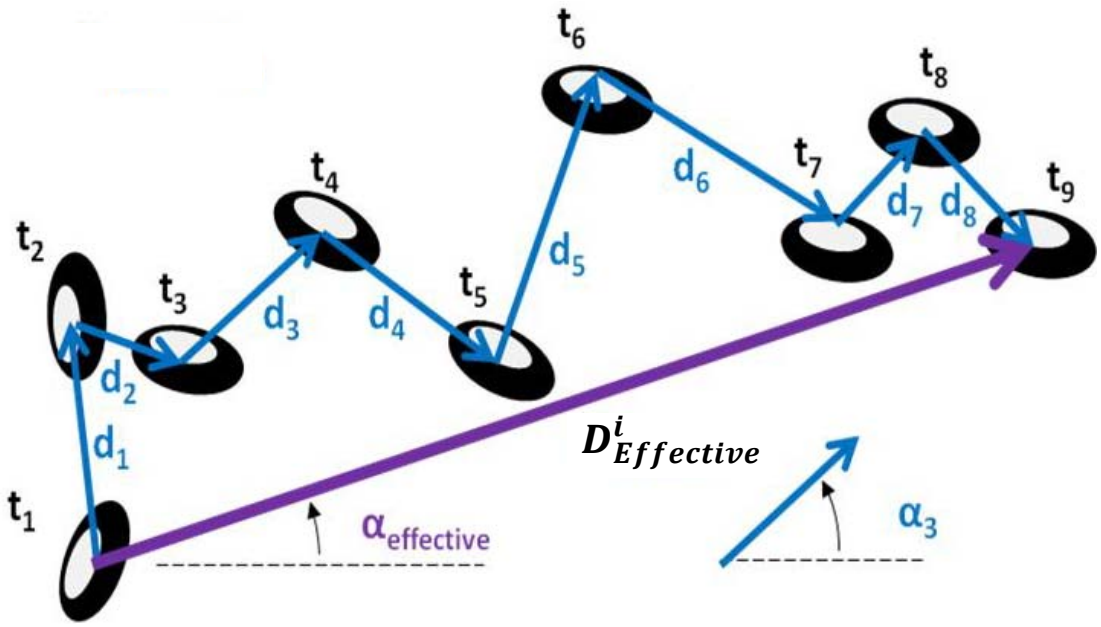

For i-th cell, n instants of time and N cells in zone:

$$D^i_{Total} = \sum_{t=1}^{n} d^i_t \qquad \overline{D}_{Total} = \frac{1}{N}\sum_{i=1}^{N} D^i_{Total} \qquad \overline{D}_{Effective} = \frac{1}{N}\sum_{i=1}^{N} D^i_{Effective}$$

Figure 4.14 Representation of cell movement descriptors. In this scheme the superposition of position of the cell *i* over *t*=9 periods of time, from t_1 to t_9, is presented. Partial distance between cell positions in *t*-th and *t*+1-th instances of time is denoted as d_n. The sum of distance moduli is the total distance D^i_{total}. The effective cell distance $D^i_{effective}$ is the distance between the last and the first cell´s position and is determined by the modulus of vector sum of all displacements. Averages of D_{total} and $D_{effective}$ for each zone were calculated ($\overline{D}_{total}$ and $\overline{D}_{effective}$ respectively). Also partial (α_i) and effective angles ($\alpha_{effective}$) of motions are presented at the bottom part of this image, which are defined as the angle between partial distance vector d_i or effective vector $D^i_{effective}$ with respect to the reference (horizontal) line, respectively.

Averaged total distance values for each zone are presented in Table 4.3. Distribution of this parameter is presented in Figure 4.15. From this data we can conclude that the different

IBs patterns of each region have a clear effect on the cell motility. Specially, we can say that cells translate more when seeded over areas with steeper gradients of IBs. The presence of "lower" IBs gradients also stimulates cells to move, although to a less extent. The shortest distances are travelled by cells seeded over "plain" zones with constant IBs concentrations. Moreover, it is also observed, that limiting the cell movement in narrow areas also stimulates cell movement more than in broader areas as total distances of cells in narrow zones are higher than those seeded over broader zones. However, this tendency is more pronounced for the IBs gradient areas than in the "plain" ones.

Table 4.3 Average total distance travelled by cells of each zone calculated for translations over a period of 22 hours of image acquisition. Colours are added for clarity: red, yellow and green corresponds to low (>270 µm), moderate (270-315 µm) and high (<315 µm) average total distance, respectively. Position of values in this table corresponds to layout of zones in Table 4.1.

Average total distance $\bar{D}_{total}$ [µm]		Gradient						Plain			
		High h_1			Low h_2						
		Narrow d_1	Moderate d_2	Broad d_3	Narrow d_1	Moderate d_2	Broad d_3	c_1	c_2	c_3	c_4
Narrow	c_1	256	304	364	306	294	243	233	295	231	246
	c_2	367	343	386	344	308	286	237	256	266	269
	c_3	304	361	361	318	282	312	260	236	336	280
	c_4	372	366	372	367	343	316	243	340	342	322
Broad	c_1	309	295	319	299	282	298	229	273	182	241
	c_2	309	334	322	280	310	302	250	241	247	250
	c_3	287	345	304	292	292	323	299	296	269	352
	c_4	307	323	252	256	320	268	297	280	328	272

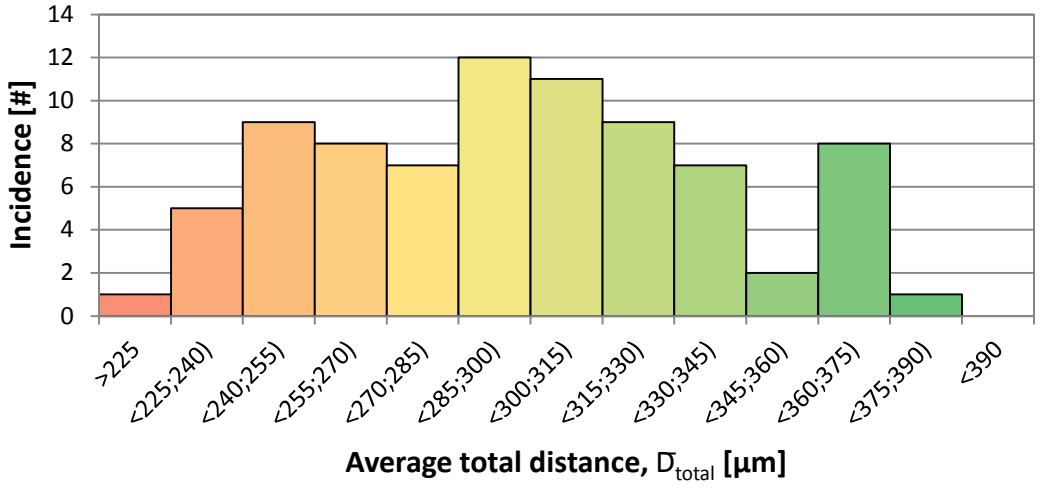

Figure 4.15 Distribution of average total distances, $\bar{D}_{total}$, travelled by cells. A multimodal distribution can be observed with three distinct population of cells with low (>270 µm, red), medium (270-315 µm, yellow) and high (<315 µm, green) average total distances. This population corresponds roughly to zones where cells were seeded: cells characterized by low distances were seeded over plain zones, and cells with high distances were seeded on zones with narrow tracks and high gradients.

This comparison becomes more visible when the average values for each column or row are all juxtaposed, as presented in Figure 4.16, where it can be clearly seen, that the bars obtained for gradients and for narrower zones are higher than for other areas. Thus, the steepness of the gradient and the higher density of IBs of plain zones stimulate the cell movement.

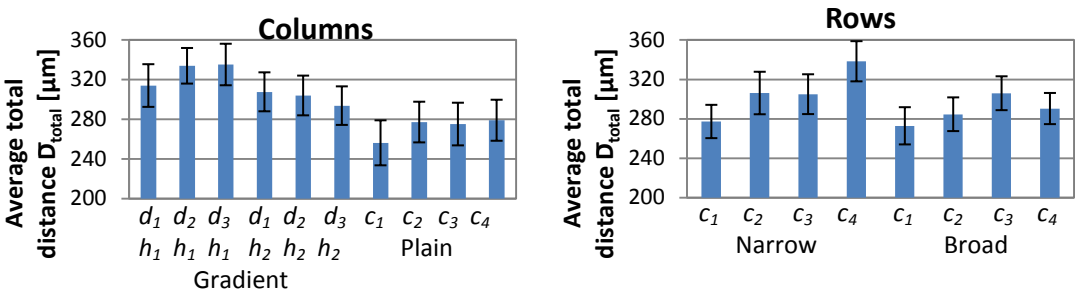

Figure 4.16 Summary of the averaged total cell distances calculated for all columns and rows of Table 4.3. Error bars indicate standard errors which we calculated for each column or row.

Averaged effective distance values for each zone are presented in Table 4.4. This analysis shows that there is no clear influence of the different biological and topographic profiles of each zone on this parameter. Contrary to what we have previously seen for the averaged total distance, the total effective distance is very similar in all areas. This result suggests, that the tested biological and topographic profiles stimulated movement but only on short distances. Cells do move more vigorously when seeded on gradients, however these conditions do not bring any long distance stimuli for cells and the total net distance remains the same. Thus, result seem quite reasonable since cell have no memory to remember.

Table 4.4 Values of average effective distance travelled by cells for each zone. Effective distance is the distance between the last and the initial cell position during the time-lapse deposition. The position of values in this table corresponds to the layout of zones presented in Table 4.1. Colour coding is according to colour scale used in Figure 4.15 assuming the same variation of both populations. Therefore all values are relatively close to the middle range of colours, resulting yellow shades of all the zones.

Average effective distance $\bar{D}_{effective}$ [µm]		Gradient						Plain			
		Narrow d_1	High h_1 Narrow d_1	Narrow d_1	Narrow d_1	High h_1 Narrow d_1	Narrow d_1	c_1	c_1	c_1	c_1
Narrow	c_1	67.3	66.8	85.9	71.8	73.9	59.0	61.5	105.5	44.3	70.3
	c_2	90.7	99.1	72.3	76.2	77.3	63.4	71.3	52.3	90.4	68.4
	c_3	58.9	80.3	72.8	61.0	56.2	56.5	50.0	66.3	89.0	51.7
	c_4	89.5	81.5	81.1	91.2	77.3	63.2	57.3	63.1	87.6	96.6
Broad	c_1	75.2	64.2	72.6	69.7	72.2	77.8	70.7	78.0	64.7	1001.1
	c_2	67.5	72.3	81.1	80.3	62.3	60.9	62.2	35.7	59.3	71.5
	c_3	68.0	83.6	73.6	65.8	87.7	74.2	65.6	75.3	56.2	72.6
	c_4	105.5	46.2	51.5	47.3	60.3	38.1	93.4	80.7	59.7	61.0

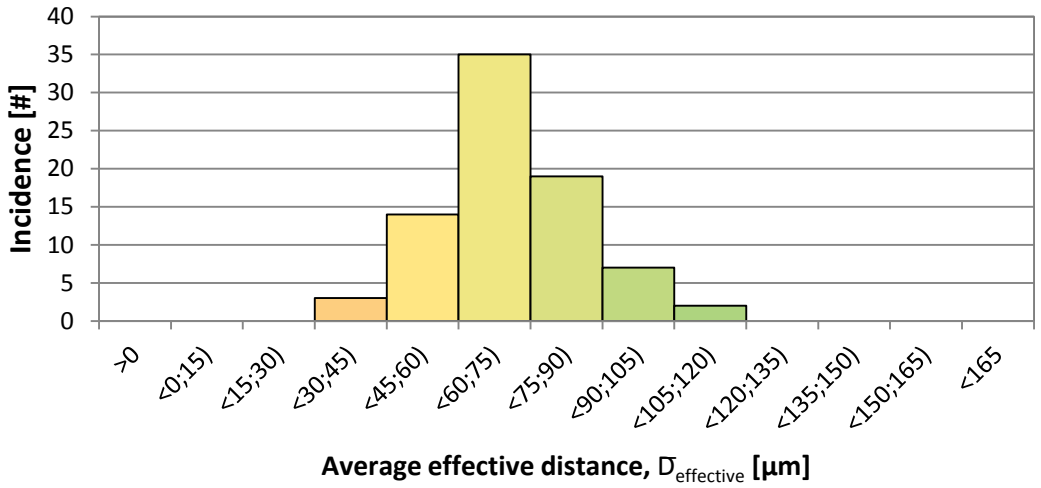

Figure 4.17 Distribution of average effective distances, $\bar{D}_{effective}$, travelled by cells. A unimodal distribution of low variance can be observed. Colour coding is according to colour scale used in Figure 4.15 assuming the same variation of both populations. Therefore all values are relatively close to the middle range of colours, resulting yellow shades of all the bars.

4.3.3.3. Analysis of movement directionality of cells

Preferences in directionality of cell movement were also analysed on the different patterned areas. The angle of cell movement, α_i, was defined as the angle between a reference horizontal line and the line passing through the cell positions at two different times. Similarly the effective angle, $\alpha_{effective}$, is given by the angle formed between reference line and line defined by initial and final cell position (see Figure 4.14).

Although special care was taken during the two-step pattern deposition, due to the manual manipulation of the sample, zones are not exact rectangles, but rather parallelograms. The shape and orientation of each zone presented in Figure 4.9 will serve as reference to obtain the angles α_i and $\alpha_{effective}$ and their corresponding plots for each zone.

In Figure 4.18 the effective cell direction distributions are shown for each of the 80 areas (in blue). Due to the fact, that some zones have a very low number of cells, data from different areas have been pooled and partial averages of column and row were obtained (in red). The overall averages of columns and rows have been also calculated (in purple). In this radial plots the distance from the centre of the plot indicates the number of cells that were moving in the due direction.

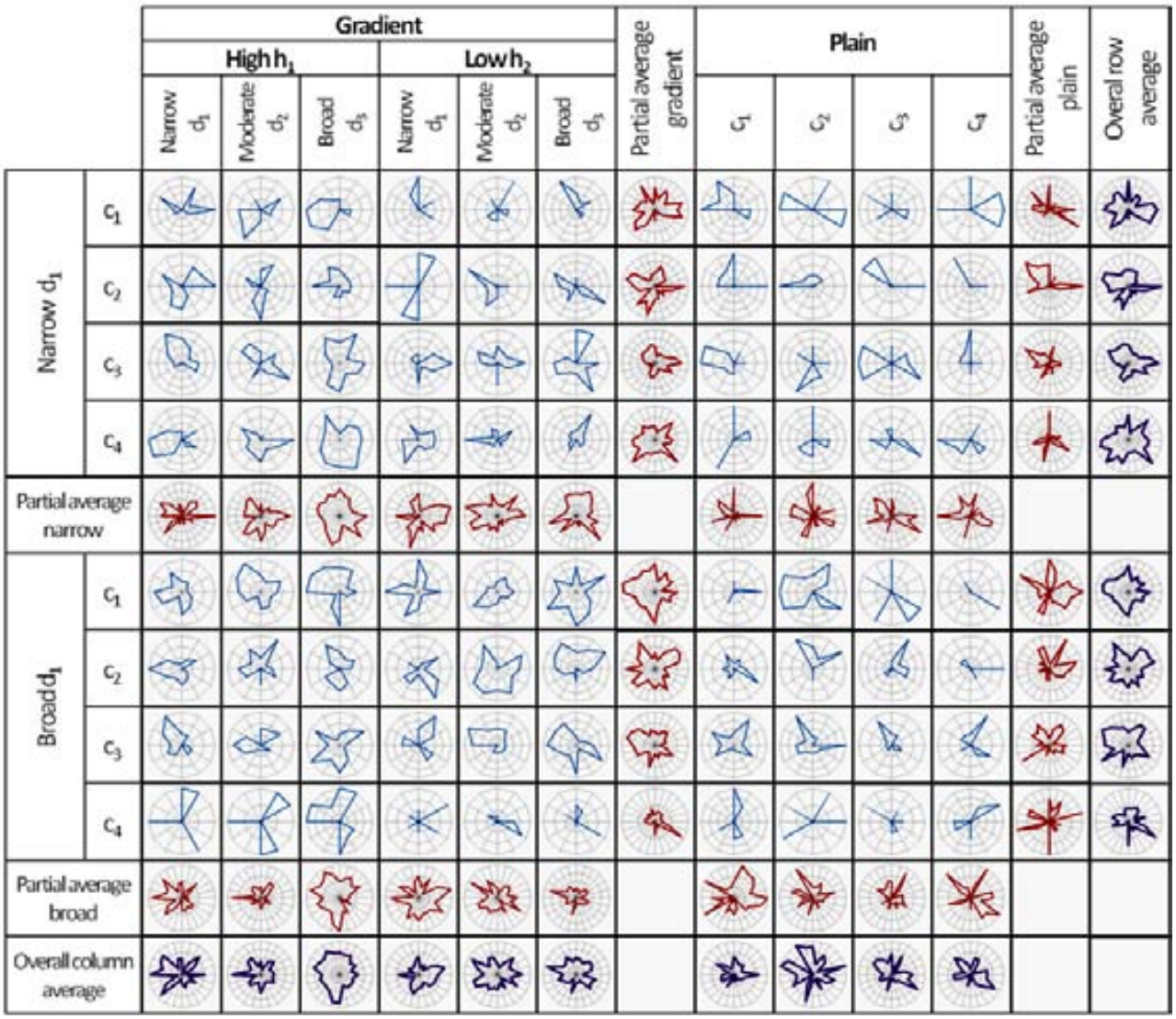

Figure 4.18 Radial plots of effective cell movement directionality. Angles between the reference (horizontal) line and a straight line passing through the initial and final position of cell after 22 hours of movement are represented in each radial plot. In blue – orientation distributions from each one of the 80 zones. In red – data pooled from partial columns/rows. In purple – data pooled from all columns/rows.

Although some conclusions can be drawn, from the Figure 4.18, better insights into cell directionality preferences can be accomplished when partial averages of cell movement directions are taken into account. For this purpose cell position data was divided into 4 equally long (5 hours) non-overlapping periods of time, and effective directions were calculated for each period separately, according to Reference [46]. Directionality data for each cell and each period was pooled for every zone. In this way the number of data points increased 4-fold. Obtained data are visualized with the radial plots given in Figure 4.19.

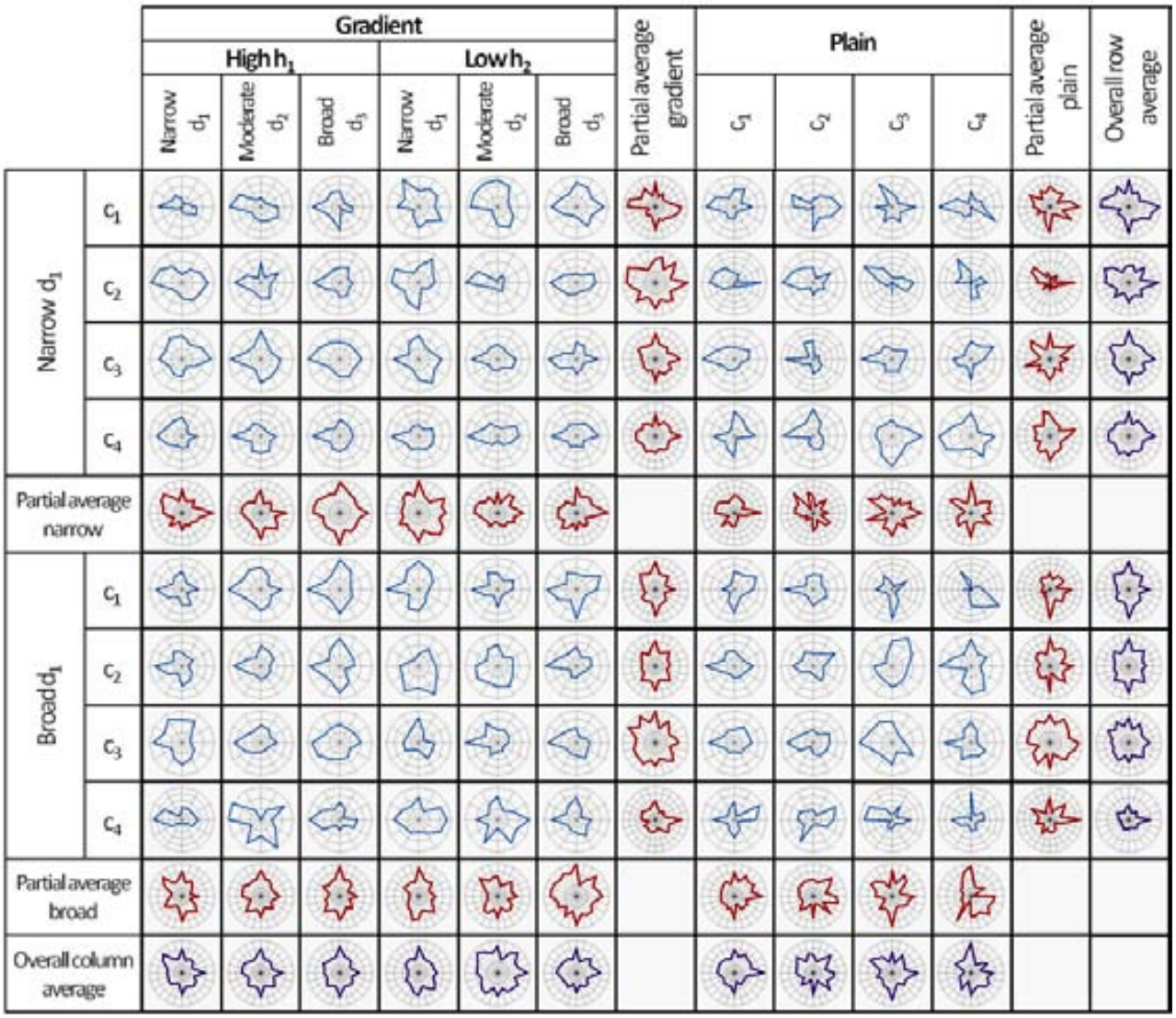

Figure 4.19 Momentary angle distributions obtained from data derived from cell´s positions separated by 5 hours. Angles between the reference line and straight line passing through the cell initial position and the position after 5h (4 events per cell) are shown. In blue – orientation distributions from each zone. In red – data pooled from partial columns/rows. In purple – data pooled from all columns/rows.

In this representation it can be clearly seen, that movement direction of cell have a more "spindle-like" shape with high horizontal component of the angular distributions when cells are moving on narrow areas than in broader ones. This fact is a consequence of the use of high concentrations of IBs as cell borders to separate different patterned areas in order to limit cell movement. From this analysis it can be easily concluded, that such use of high IBs concentration barriers act indeed as cells "corrals", as already mentioned in Section 4.3.1.2 ("Cell interactions with high concentrations of IBs"). In this way cells are kept within the same area they have been seeded. Superposition of plots of partially pooled data from rows illustrates the preference of cells to move along the direction of narrow areas even better, as presented in Figure 4.20.

However, from this representation we cannot conclude, whether or not, gradients have any influence on cell directionality. Average distributions for columns are very alike in case of high and low slope gradients, as well as in the case of plain zones.

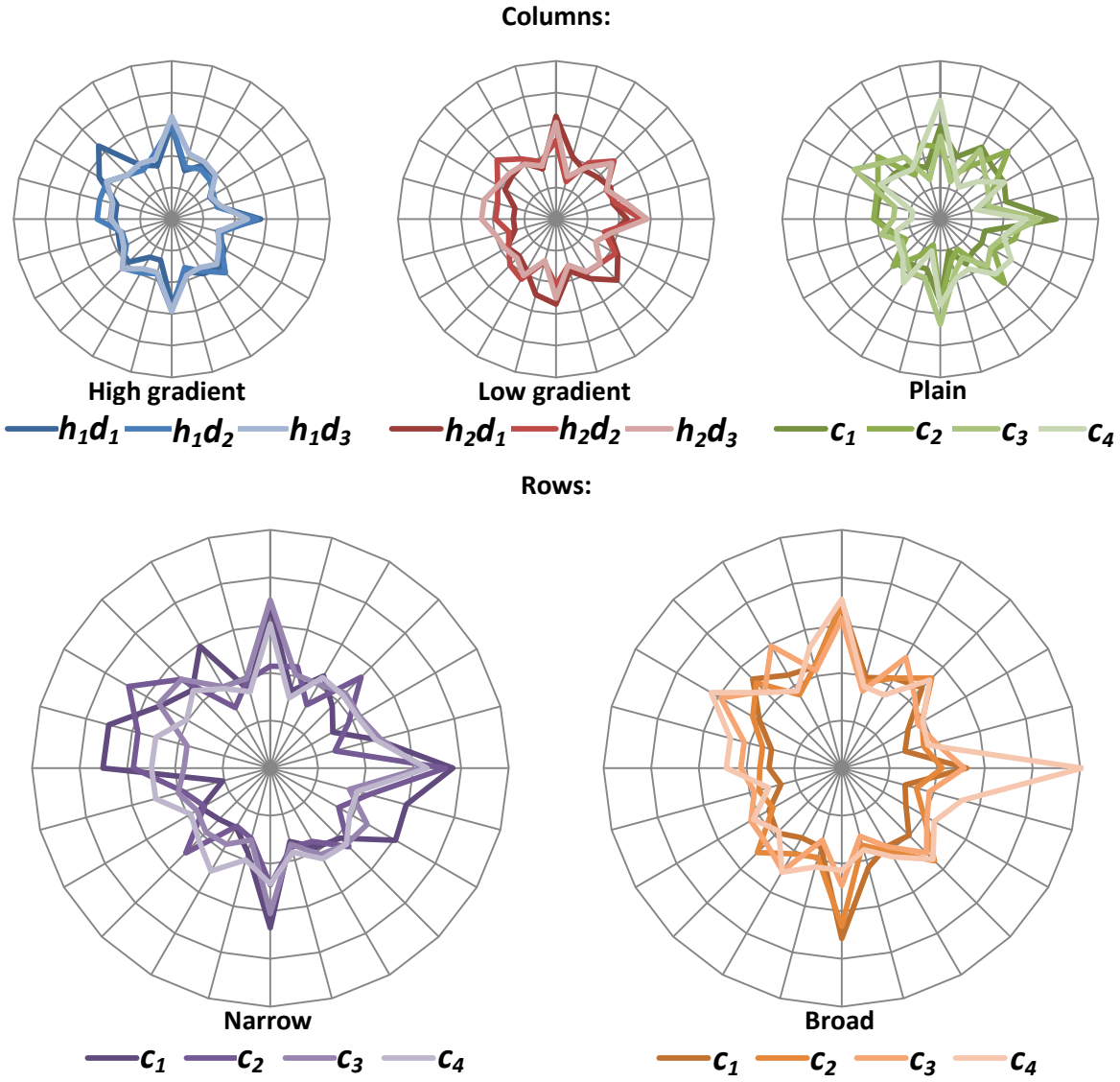

Figure 4.20 Momentary angular distributions calculated basing on positions separated by 5h of cell movement directions pooled for columns and rows normalized with respect to cell number in each zone. A spindle-like distribution is visible for cells growing on narrow tracks as opposed to random distributiona of cells growing on broader zones. The presence or absence of gradient does not seem to have any influence on the momentary cell directionality.

4.3.3.4. Analysis of cell motility dependence on IBs concentration

The averaged local IBs concentration around the cells can be calculated basing on the cell positions and the overall IB´s concentration distribution in the substrate. The cell positions are provided by cell tracking and the IBs local concentration by an overall fluorescence image of sample (Figure 4.9). A scheme of this procedure is presented in Figure 4.21.

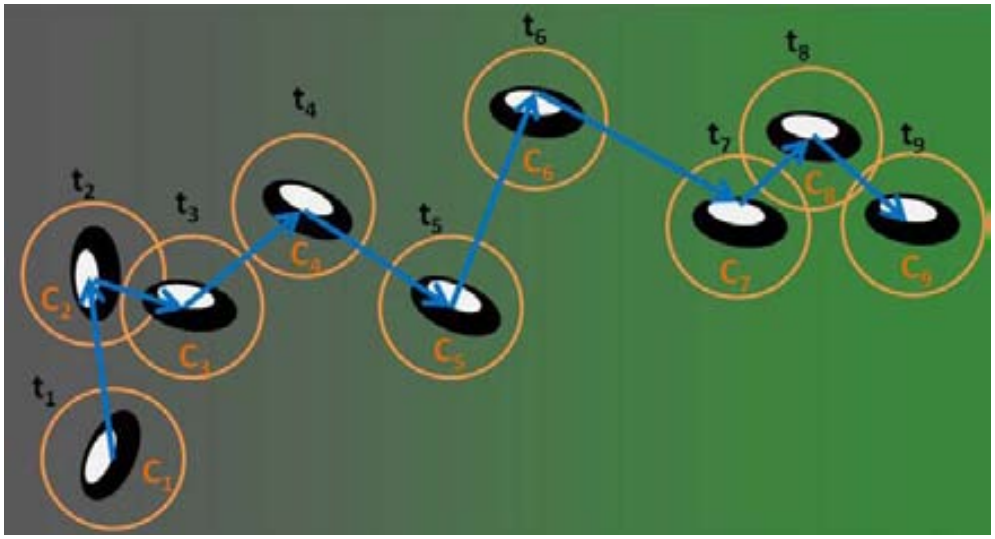

Figure 4.21 Schematic illustration of retrieving average fluorescence value from around cell positions at each time t_n. IBs distribution pattern is represented by a shaded background with a colour gradient. For each position of the cell, an average fluorescence intensity from a circular area around the cell was calculated (I_n). The circular area 2500µm^2 corresponding to a circle diameter of approximately 57µm – bigger than cell to take into account cells proximity. Based on c_n value the number of IBs in cell´s immediate neighbourhood (x_n) was calculated for each cell position.

The average IBs concentration at cell´s proximity, averaged both for all cells and times in each zone, is presented in Table 4.5. Although this "snapshot" does not reveal how the cell preferences change with the time, it shows that the patterning methodology was carried out correctly. Indeed, in zones intended to have higher concentrations of IBs the experimental concentration values are higher. This tendency is especially well depicted in the "Plain" areas where IBs concentration is constant.

Table 4.5. Average IBs concentration in cells nearest proximity during the whole period of time-lapse image capture. The layout of this table corresponds to the layout of zones shown in Table 4.1. The low (>1.6·10^5 #/mm^2), medium (1.6-2.4·10^5 #/mm^2) and high (<2.4·10^5 #/mm^2) average IBs concentrations are colour coded with red, yellow and green, respectively.

Average IBs concentration [1000/mm^2]		Gradient						Plain			
		High h_1			Low h_2						
		Narrow d_1	Moderate d_2	Broad d_3	Narrow d_1	Moderate d_2	Broad d_3	c_1	c_2	c_3	c_4
Narrow	c_1	115.7	245.9	218.9	217.1	206.1	205.6	182.3	231.4	208.3	242
	c_2	169.6	222.3	199.1	248.3	188.2	166	173.8	201.7	213.9	213.2
	c_3	182.3	261.3	216.9	232.3	221.2	214.1	238	241	215.9	223.2
	c_4	175.1	245.3	271.6	286.2	266.4	252.5	248.2	262.9	256.4	307.5
Broad	c_1	109.8	164.4	164	172.2	141.3	151.1	131.3	145.7	148.4	230.3
	c_2	124.1	186.5	229.5	216.1	208.3	169	168.8	177.5	172	245.5
	c_3	146.1	186.7	187.6	159	191.7	219.4	153.4	186.3	202.9	250.6
	c_4	257.3	214	238.4	232.6	226.6	252.4	231.4	273.1	241.2	267.9

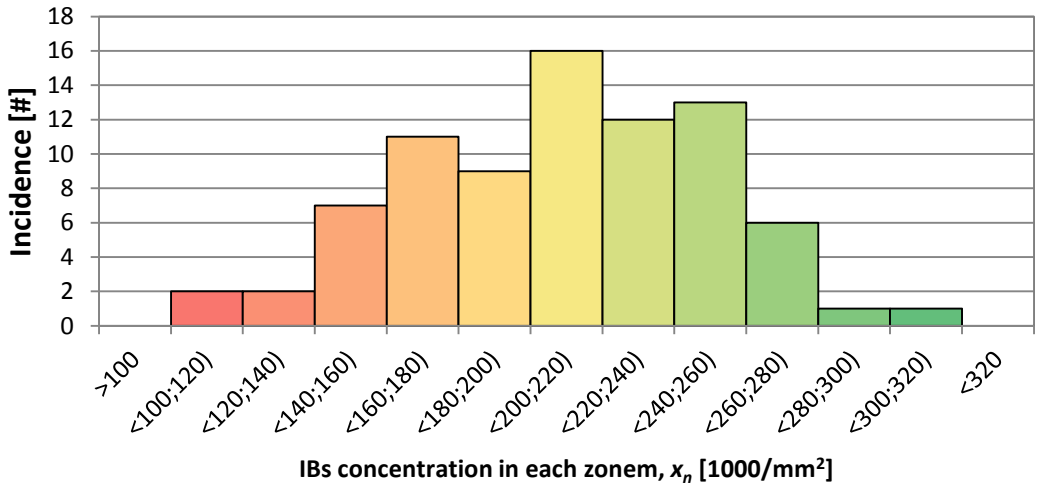

Figure 4.22 Distribution of average IBs concentration in zones. In our experiment a range of concentration was obtained ranging from low (>1.6·10^5 #/mm^2, red), through medium (1.6-2.4·10^5 #/mm^2, yellow) to high (<2.4·10^5 #/mm^2, green) IBs concentrations.

However, since these data were collected for each instant, it is possible to plot the IBs concentration in cell´s proximity versus time that represents cell´s "movement profiles", describing how cell´s local environment changed with time. This data-set describes the nearest neighbourhood of a cell in terms of IBs content, not taking into account the type of zone (gradient or plane etc.). Therefore, this analysis intended to answer whether or not cells are attracted to zones of high concentration of IBs. At first glance at these "movement profiles", exemplified in Figure 4.23, do not show any clear tendency.

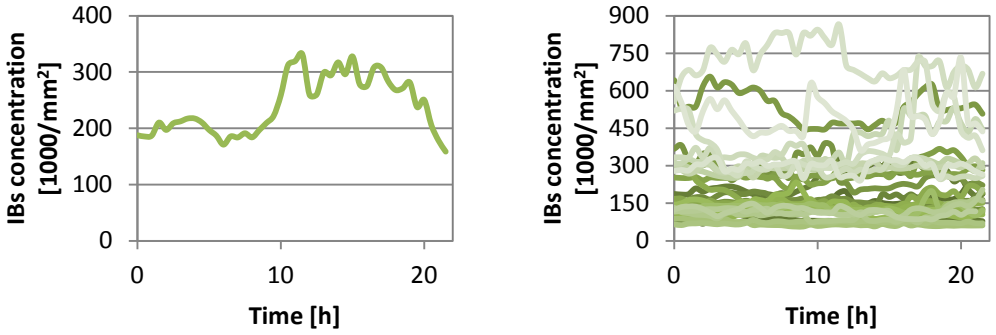

Figure 4.23 Example profiles of cells moving over the IBs pattern. Left – an example of one profile of cell that was initially occupying moderately low IBs concentration zones until the 8th hour of movement when it leaped to a more concentrated zone where it stayed until the last hour of image acquisition. Right – example of superposition of cell´s profiles from one zone, indicating that various behaviours are present in a population of cells and no clear pattern can be extracted in a straightforward manner.

Such a big amount of data represented in this way is very cumbersome to analyse and therefore useless. Thus, a more synthetic and generalized analysis of data based on heat maps

has been used. A step-by-step explanation for the construction of the heat maps is provided in Figure 4.24. This method was developed in order to highlight the preferences of cells moving within the patterned areas with different IBs concentrations. It aims to distinguish, whether or not, cells tend to go from low IBs concentrations to high IBs concentrations or vice versa.

Let us define the symbols that will be used in this analysis. Subindices *i* and *j* will correspond to the initial and final states for a cell movement, respectively. N_i will indicate the number of cells with a fixed initial IBs concentration x_i. The concentration of IBs around cell in the next instance will be denoted as x_j and can be calculated from experimental data. The number of cells that moved from x_i to x_j will be denoted as $n_{i,j}$ (see Figure 4.24 A). This value divided by the total number of cells $n_{i,j}/N_i$ will describe the probability that a cell move from a position with IBs concentration of x_i to another with x_j. Thus, a plot of $n_{i,j}/N_i$ for every final concentration x_j represent "the probability of cell destinations" as presented in Figure 4.24 B, which is a representation of where cell prefer to move starting from initial point *i* with given IBs concentration of x_i.

From this data a "matrix heat map" can be constructed. The horizontal position of the pixels in the matrix represents the initial IBs concentration around the cells (x_i), while the vertical position of pixels represents the final IBs concentration (x_j). The colour of each pixel corresponds to the percentage of cells that move from the initial concentration x_i to a final concentration x_j. An example of a "matrix heat map" is presented in Figure 4.24 C). Each column of pixels represent therefore a colour-coded "probability of cell destinations" for a given initial concentration x_i.

Heat maps for each area with different patterns are presented in Figure 4.25 as well as their partial and total averages obtained for columns and rows. Interestingly, in this representation the movement of all analysed cells at all times can be assimilated at one glance.

The highest probability is signalised by the pixels located at the diagonal of each heat-map. This indicates that in most of cases cells move between points of very similar IBs concentrations, without exploring other IBs concentrations. However, every pixel outside the diagonal evidences that there are cells that changed their position between points of different IBs concentration. The farther the pixel from the diagonal, the bigger is the absolute difference between the IBs concentration around the cell in the initial and the final point.

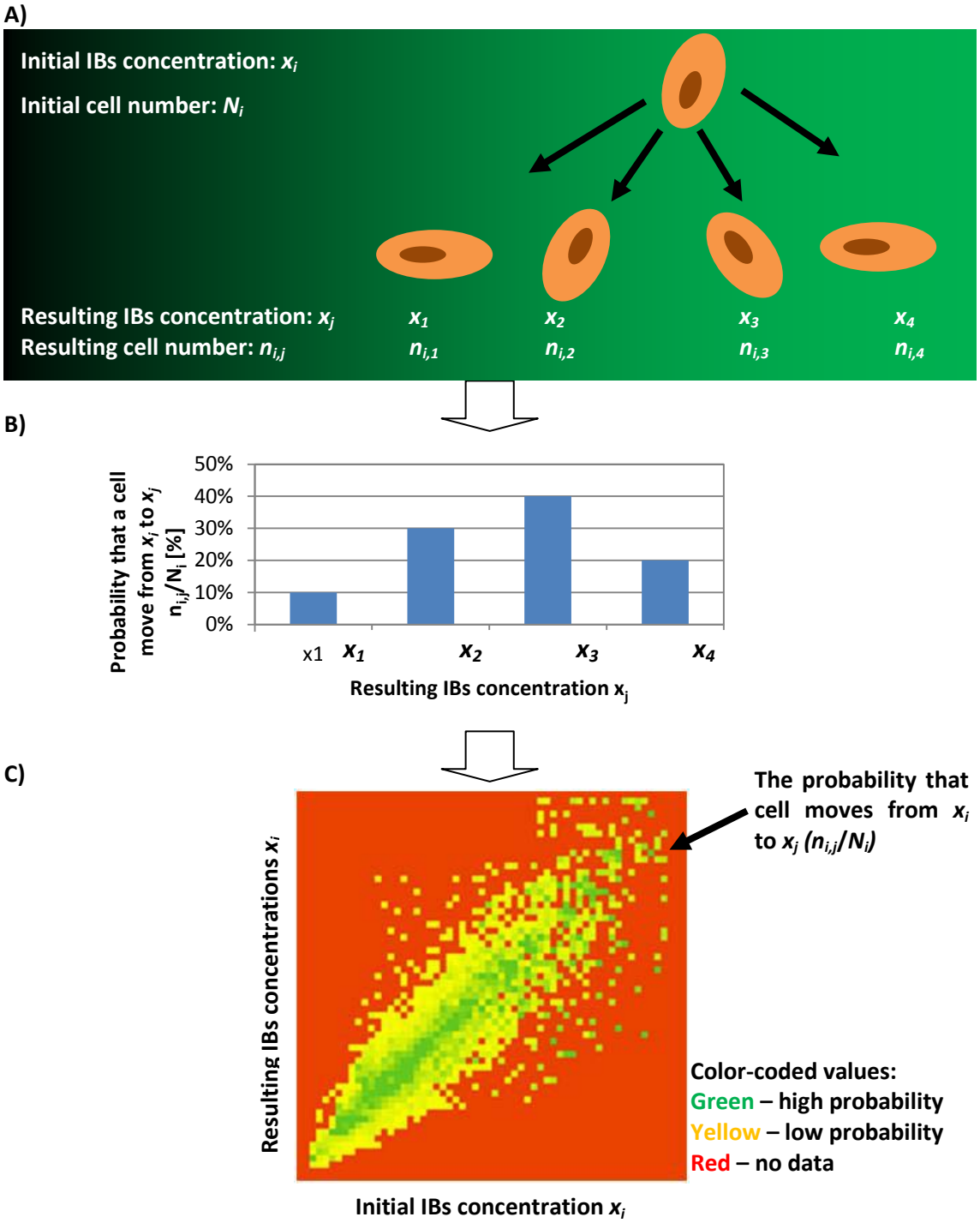

Figure 4.24 Cartoon describing the construction of the matrix heat map. A) Definition of initial and resulting states with symbol explanations. B) Simplified "distribution of cell destinations" histogram for only one starting IBs concentration x_i. C) Example of a resulting heat map with colour coded values of probability (see legend for explanation).

As a result, we obtained patterns of hat map resembling tilted ovals. The length of these ovals (long axis along the diagonal) corresponds to the range of IBs concentrations present in each patterned zone. If a gradient is present, the cells have an opportunity to move within zones with both high and low IBs concentrations and therefore the oval will be elongated

along the diagonal. Indeed, the spots obtained for the “plain” zones are very small, and are a clear indication that all concentrations are found within a very narrow range. The width of an oval (short axis perpendicular to the diagonal) corresponds to the steepness of the gradients presented in the different zones. There is a higher probability that cells move between points with bigger difference of IBs concentrations in the zones, where such difference is closer. That is, on steep gradients, because they have bigger IBs concentration difference per unit of length. In this representation such zones have more pixels indicating cell movements that are distant from the diagonal.

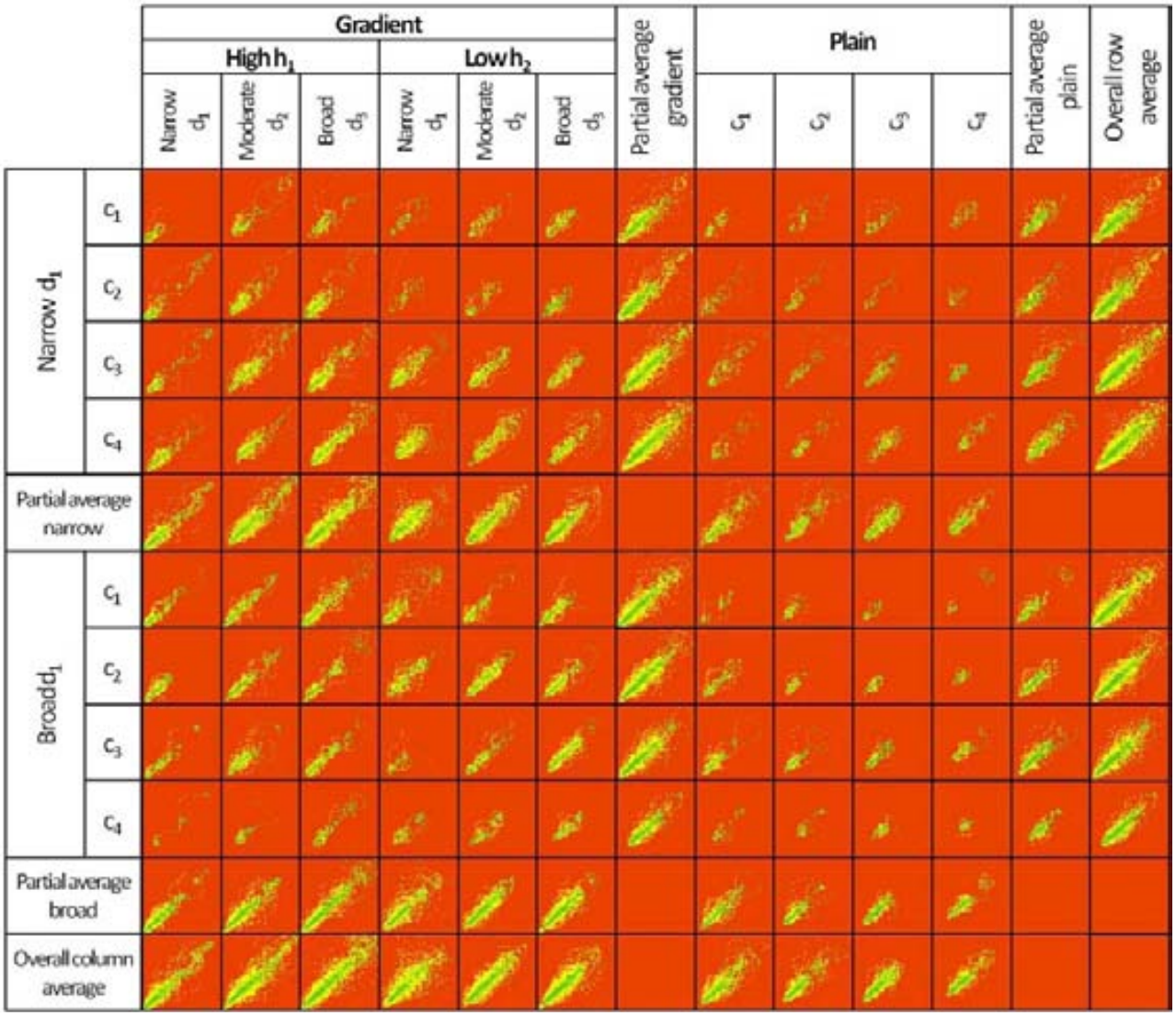

Figure 4.25 Probability heat maps for every zone as well as partial and total averages for columns and rows. The position of heat maps is similar to the one presented in Figure 4.18.

Matrix heat map plots appear to be symmetric with respect to the diagonal. This would indicate, that the probability of a cell to move from high to low IBs concentration area are the same as in the opposite case. To visualise this assumption we have prepared another type of

heat map plot, named a preference heat map. In the new approach, as before, horizontal and vertical axis represents initial x_i and resulting x_j concentrations, respectively. However pixels hold values of $(n_{i,j}/N_i)$-$(n_{j,i}/N_j)$ in order to compare the probability of cell shifting its position from a concentration of x_i to x_j to the probability of change in the opposite direction i.e.: from x_j to x_i. Both situations occur in nearly the same place in the sample, so that if there is a possibility to perform this operation in one way, it can also be reversed. A diagram explaining this operation and an example of such a plot are presented in Figure 4.26.

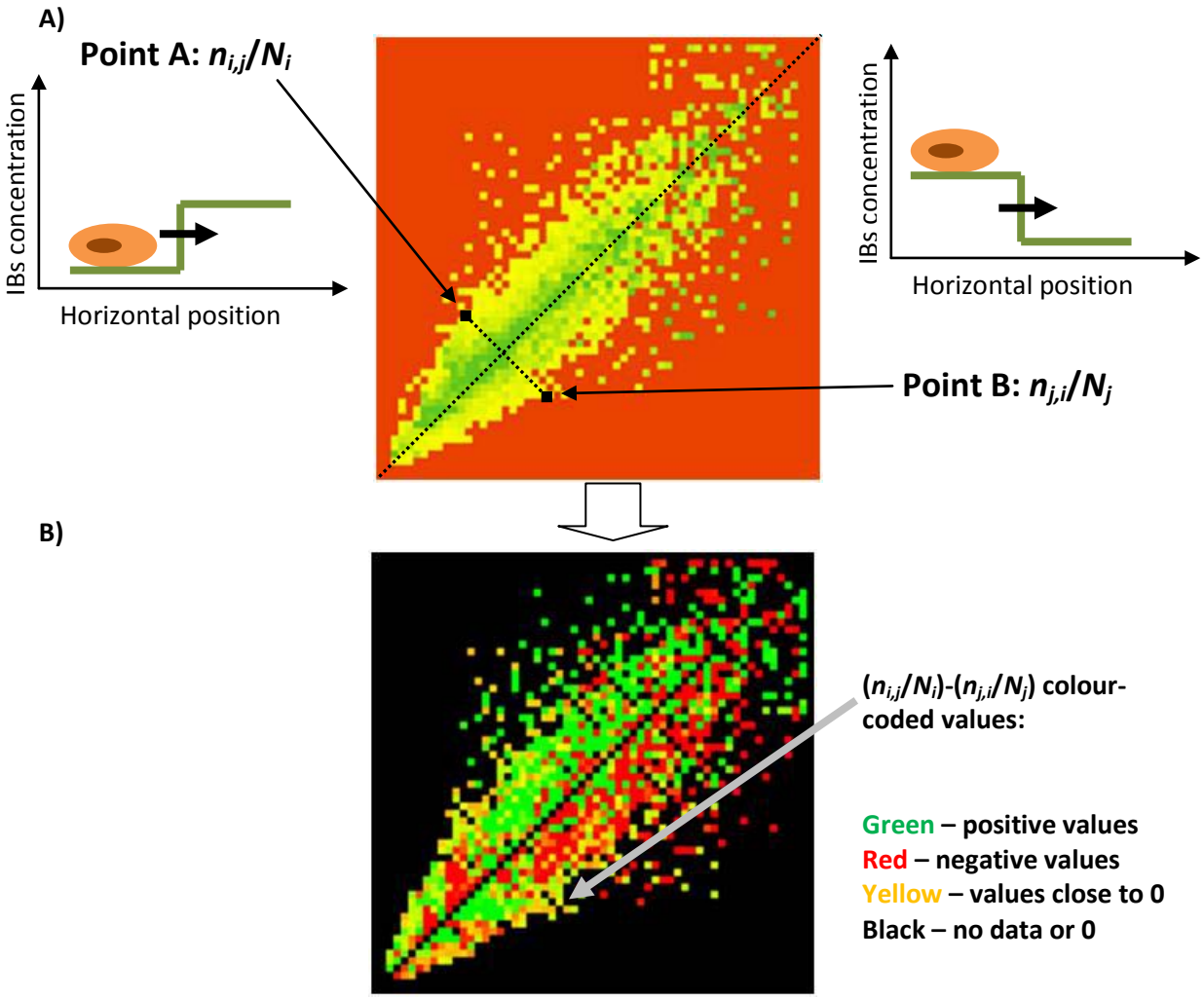

Figure 4.26 Construction of a "preference heat maps". A) Example of seemingly symmetric heat map. Two diagonally symmetric points are marked representing initial and final position of a cell. The values represented by colours denote probabilities of opposite situations. B) Resulting anti-symmetric preference matrix. Presented colour coding for pixels below the diagonal has following significance: green – preference to move towards higher IBs concentrations, red – preference of to move towards lower IBs concentrations, yellow – very low preference, black – no preference or no data. Colours of pixels above the diagonal have the opposite meaning.

The final "preference heat maps" obtained for all the areas are presented in Figure 4.27. The interpretation of the "oval" shape sizes remains the same as in the previous probability

heat map. However, in this case colouring casts light on cells´ preferences. In this representation every plot is diagonally anti-symmetric, therefore the data represented above the diagonal is just a "mirror reflection" of the data below the diagonal with reversed colours. Therefore, from now on the following analysis will be carried out using only one of the oval´s sides. We have chosen pixels below the diagonal. Thus, the colour interpretation is, as mentioned in the caption of Figure 4.26, as follows:

- Green – preference of cells to move towards higher IBs concentrations
- Red – preference of cells to move towards lower IBs concentrations
- Yellow – cells do not present strong preferences
- Black – no preference or no data

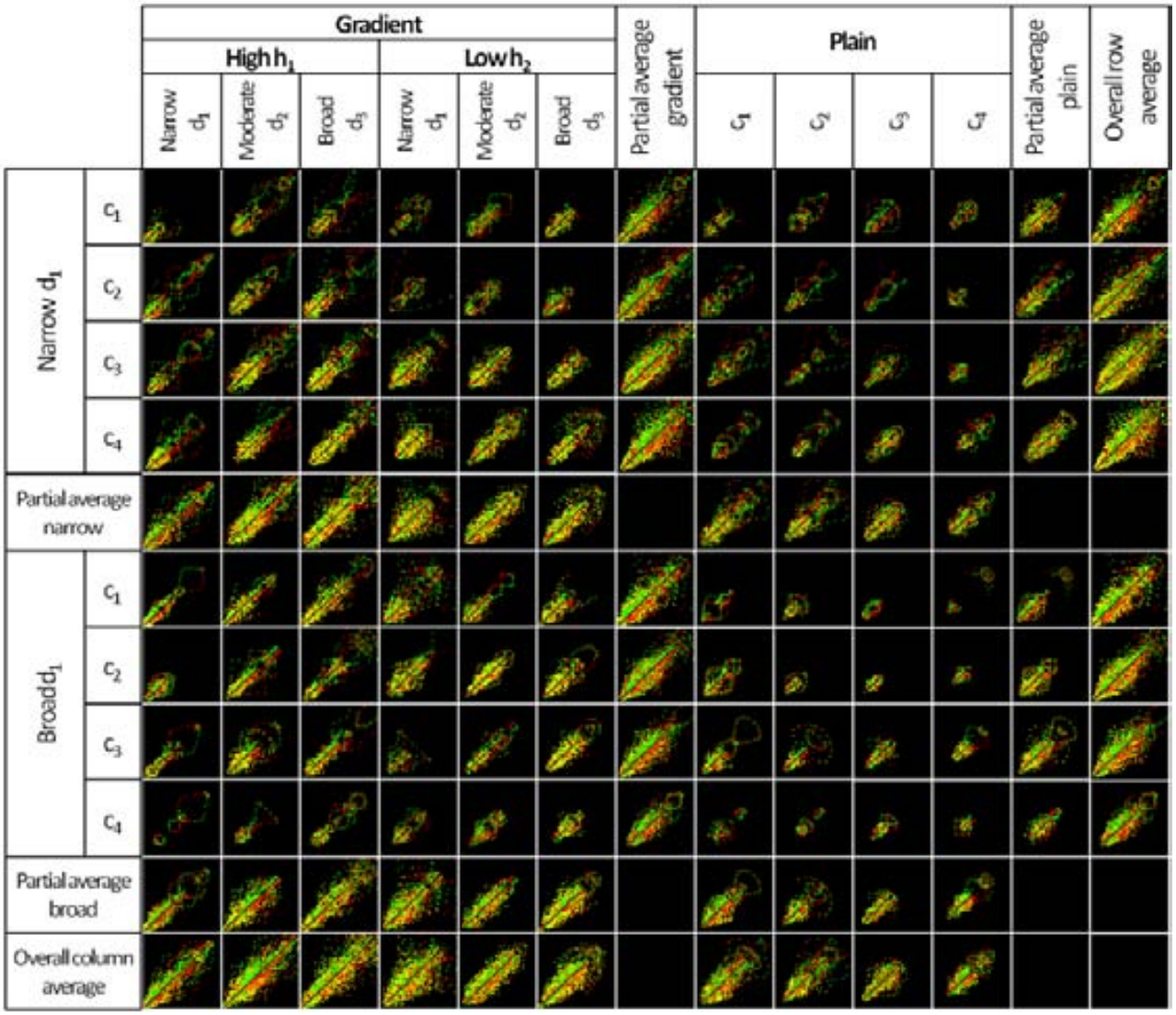

Figure 4.27 Preference matrices for every zone as well as partial and total averages for columns and rows. The layout of the image is similar to the one presented in Figure 4.18.

Close examination of the preference heat maps reveals, that the colouring of ovals follows the certain general pattern schematised in Figure 4.28. First of all, for low initial IBs concentrations, there is a clear spot of green pixels indicating that cells prefer to move towards higher concentrations: they “climb” when they find themselves in points with low IBs concentration. It is tempting, however, to treat this outcome as an artefact due to the methodology of the sample preparation saying that cells cannot “descend” in case of low IBs concentrations, because there are no points with lower IBs concentration that are accessible. On the other hand, in that case cells should always stay at the same IBs concentration, leaving traces only on the diagonal pixels. The fact that the colouring of pixels is not in the diagonal means that cells do have a choice and choose to move towards higher IB´s concentrations.

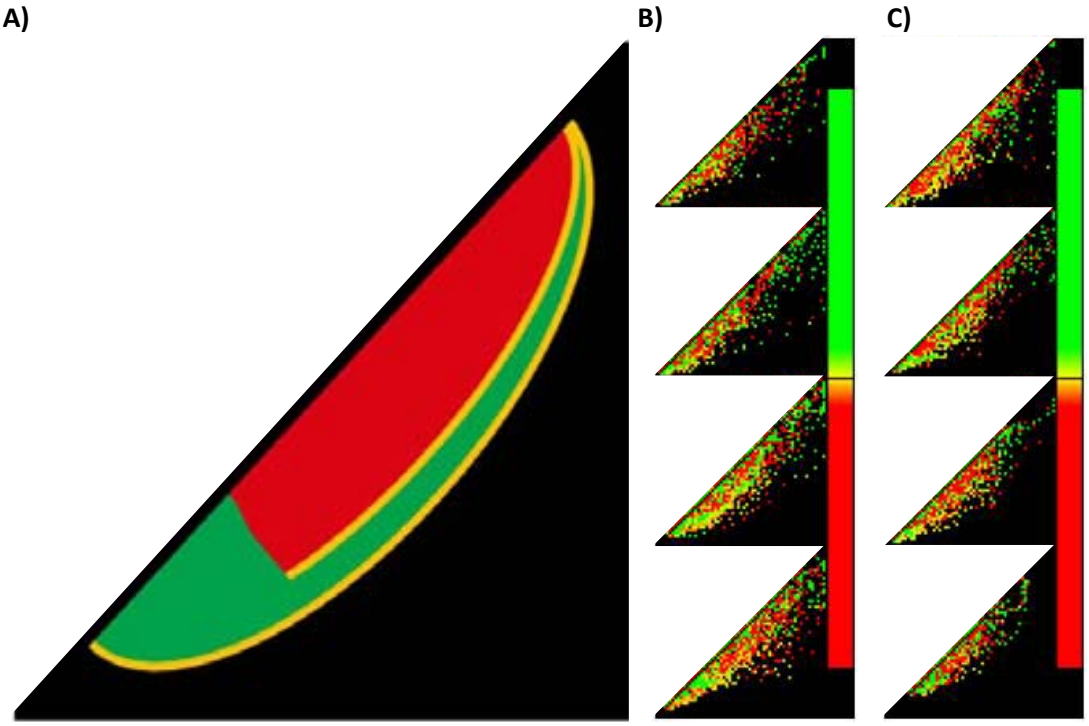

Figure 4.28 Scheme of pattern emerging from preference matrices. A) A general pattern. B) Preference matrices generated for data pooled from narrow track lines with gradients. C) Preference matrices generated for data pooled from broad zones lines with gradients. For panels (B) and (C) top-down order of plots corresponds to concentrations varying from the lowest to the highest (c_1 to c_4).

In case of high initial IBs concentrations cell behave differently. Pixels close to diagonal are painted red, indicating, that cells prefer to “descend”, but the farther from the diagonal, the bigger the probability of finding yellow or green pixels, indicating equilibrium of preferences (yellow) or a tendency to “climb” (green). In other words, for high IBs concentrations and mild slopes cells tend to descend, but in steep slopes they tend to climb. This situation is schematically presented in Figure 4.29.

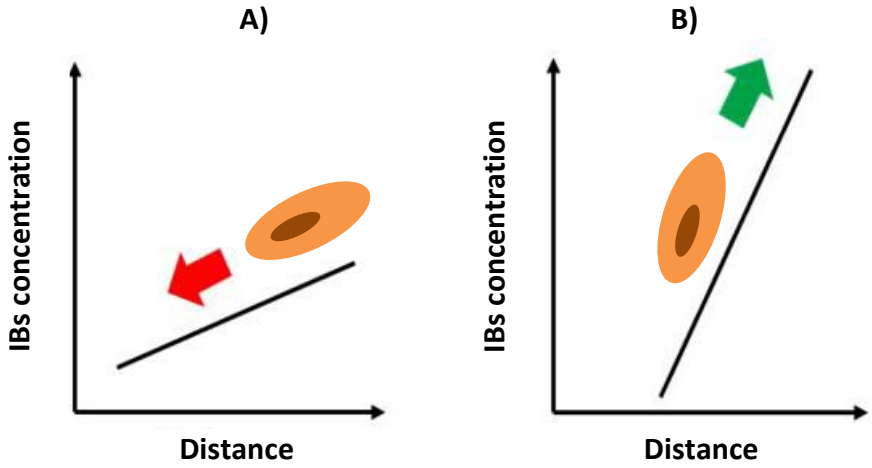

Figure 4.29 Scheme of the findings on the dependence of cell´s motility on steepness of IBs concentration gradients. A) Cells on mild slopes tend to descend and B) cells on steep slopes tend to climb.

Taking into account evidences from the subject literature data we could provide an explanation to this behaviour. As we have mentioned before, FGF IBs were proven to have a dose dependent and positive influence on the NIH-3T3 fibroblast proliferation [52]. However, the concentration used to perform this experiment was low: 1 µg in one millilitre of bulk cultivation medium. Assuming, that all the proteic material settled down on the bottom of 96-well plate used in the experiment, the concentration on the surface would be 6.7 ng/mm^2. We can reasonably estimate that the concentration of IBs deposited by the evaporation assisted protocol is much higher. In that case, the topography would have the predominant influence on the cell motility, and steep slopes or abrupt concentration changes would be the places where such impact is the strongest. This interpretation would also apply to the observations that we have mentioned in Section 4.3.1.2 (“Cell interactions with high concentrations of IBs”) when studying interaction of cells with only GFP-IBs patterns (without biological activity). In that configuration abrupt changes were also more attractive to cells (as they interacted with IBs) than the slope. This observation, that in the multi-cue environment the topography have a predominant impact on cell guidance over the chemical gradient are in agreement with previously reported observations from Reference [28]. The verification of this hypothesis, although tempting, would require further investigation, including a research on mechanisms at the cellular level, that is beyond the scope of this work.

4.4. Conclusions

Based on the presented data, we can conclude, that the deposition method developed in Chapter 3 is adequate for the preparation of substrates containing zones with different structural and compositional characteristics (up to 80 different zones). That enables us to perform high-throughput cell motility studies.

We have gathered data on cell motility by capturing confocal time-lapse images of fibroblasts cultured for 22 hours on the developed complex substrate. Data was thoroughly analysed using various approaches in order to extract meaningful and statistically relevant conclusions. Based on these analyses we have been able to explain how the following factors influence cell movement:

- Cell movement is promoted by the presence of a gradient in contrast with plain zones where cells have no preference to move. Gradient of concentrations of surface-bound IBs and therefore diversified topology of the substrate stimulates the total cell movement. However net distances that the cells are travelling are indifferent to this factor.
- Different slopes of gradients have a complex influence on cell movement, that can be summarised as follows:
    - on mild slopes cells prefer to move towards low concentrations
    - on steep slopes cells tend to move towards high concentrations
    - extremely high concentrations of IBs prevent cells from moving towards them acting like a barrier
- Absolute IBs concentrations have also an influence on the cell behaviour: the richer in IBs is the zone, the more motile are the cells seeded on it.
- The presence of corrals, defined by borders of high concentration IBs deposits, limits the cell movements and induces preferential orientation of cell movement. Moreover, cells tend to move more when growing on narrower zones.

To summarize, we can state that a proper surface decoration with proteic NPs, such as IBs, can be used to enhance and guide cell motility confirming, therefore, that IBs is a promising biomaterial for regenerative medicine as well as for tissue engineering.

4.5. Bibliography

[1] Reig G., Pulgar E., Concha M.L. "Cell migration: from tissue culture to embryos"; *Development* **2014**, Vol. 141, 1999-2013

[2] Solnica-Krezel L., Sepich D.S. "Gastrulation: Making and Shaping Germ Layers"; *Annu. Rev. Cell Dev. Biol.* **2012**, Vol. 28, 687–717

[3] Carlier M.F. "Actin-based Motility"; *Springer* **2010**, Pag. 4, DOI: 10.1007/978-90-481-9301-1

[4] Friedl P., Wolf K. "Plasticity of cell migration: a multiscale tuning model"; *J. Cell Biol.* 2010, Vol. 188(1), 11–19

[5] Ananthakrishnan R., Ehrlicher A. "The Forces Behind Cell Movement"; *Int J Biol Sci.* **2007**; Vol. 3, 303-317

[6] Mitchison T.J., Cramer L.P. "Actin-Based Cell Motility and Cell Locomotion"; *Cell* **1996**, Vol. 84, 371–379

[7] Benazeraf B., Francois P., Baker R.E., Denans N., Little C.D., Pourquie O. "A random cell motility gradient downstream of FGF controls elongation of an amniote embryo"; *Nature* **2010**; Vol. 466, 248–252

[8] Petrie R.J., Doyle A.D., Yamada K.M. "Random versus directionally persistent cell migration"; *Nature Reviews Molecular cell Biology* **2009**, Vol. 10, 538-549

[9] Friedl P. Wolf K. "Plasticity of cell migration: a multiscale tuning model"; *J. Cell Biol.* **2009**, Vol. 188(1), 11–19

[10] Petrie R.J., Doyle A.D., Yamada K.M. "Random versus directionally persistent cell migration"; *Nature Reviews Molecular Cell Biology* **2009**, Vol.10, 538-549

[11] Kim D.H., Seo C.H., Han K., Kwon K.W., Levchenko A., Suh K.Y. "Guided cell migration on microtextured substrates with variable local density and anisotropy"; *Adv. Funct. Mater.* **2009**, Vol. 19, 1579–1586

[12] Majumdar R., Sixt M. Parent C.A. "New paradigms in the establishment and maintenance of gradients during directed cell migration"; *Current Opinion in Cell Biology* **2014**, Vol. 30, 33–40

[13] Griffith L.G., Swartz M.A. "Capturing complex 3D tissue physiology in vitro"; *Nature Reviews Molecular Cell Biology* **2006**, Vol. 7(3), 211-224

[14] Stevens M.M., George J.H. "Exploring and engineering the cell surface interface"; *Science* **2005**, Vol. 310, 1135

[15] Li S., Guan J.L., Chien S. "Biochemistry and biomechanics of cell motility"; *Annu. Rev. Biomed. Eng.* **2005**, Vol. 7, 105–150

[16] Chung B.G., Manbachi A., Saadi W., Lin F., Jeon N.L., Khademhosseini A. "A Gradient-generating Microfluidic Device for Cell Biology"; *J. Vis. Exp.* **2007**, Vol. 7, e271, doi:10.3791/271

[17] Kim S., Kimz H,J, Jeon N.L. "Biological applications of microfluidic gradient devices"; *Integr. Biol.* **2010**, Vol. 2, 584–603

[18] Cho H., Hamza B., Wong E.A., Irimia D. "On-demand, competing gradient arrays for neutrophil chemotaxis"; *Lab on a Chip - Miniaturisation for Chemistry and Biology* **2014**, Vol. 14(5), 972-978

[19] Comelles J., Hortigüela V., Samitier J., Martinez E. "Versatile gradients of covalently bound proteins on microstructured substrates"; *Langmuir* **2012**; Vol. 28(38) 13688-13697

[20] Kawahara M., Hitomi A., Nagamune T. "Antigen-responsive regulation of Cell motility and migration via the signalobodies based on c-Fms and c-Mpl"; *Biotechnology Progress* **2014**, Vol. 30(2), 411-417

[21] Wu A., Loutherback K., Lambert G., Estévez-Salmerón L., Tlsty T.D., Austin R.H., Sturma J.C. "Cell motility and drug gradients in the emergence of resistance to chemotherapy"; *PNAS* **2013**, Vol. 110(40), 16103–16108

[22] Wei C., Wang X., Zheng M., Cheng H. "Calcium gradients underlying cell migration"; *Current Opinion in Cell Biology* **2012**, Vol. 24, 254–261

[23] Roca-Cusachs P., Sunyer R., Trepat X. "Mechanical guidance of cell migration: lessons from chemotaxis"; *Current Opinion in Cell Biology* **2013**, Vol. 25, 543–549

[24] Kolind K., Leong K.W., Besenbacher F., Foss M. "Guidance of stem cell fate on 2D patterned surfaces"; *Biomaterials* **2012**, Vol. 33, 6626-6633

[25] Washburn N.R., Yamada K.M., Simon Jr. C.G., Kennedy S.B., Amis E.J. "High-throughput investigation of osteoblast response to polymer crystallinity: Influence of nanometer-scale roughness on proliferation"; *Biomaterials* **2004**, Vol. 25(7-8), 1215-1224

[26] Arnold M., Hirschfeld-Warneken V.C., Lohmüller T., Heil P., Blümmel J., Cavalcanti-Adam E.A., López-García M., Walther P., Kessler H., Geiger B., Spatz J.P. “Induction of cell polarization and migration by a gradient of nanoscale variations in adhesive ligand spacing”; *Nano Lett.* **2008**, Vol. 8, 2063–2069

[27] Geiger B., Spatz J.P., Bershadsky A.D. "Environmental sensing through focal adhesions"; *Nature Reviews Molecular Cell Biology* **2009**, Vol. 10(1), 21-33

[28] Sundararaghavan H.G., Saunders R.L., Hammer D.A., Burdick J.A. "Fiber Alignment Directs Cell Motility Over Chemotactic Gradients"; *Biotechnology and Bioengineering* **2013**, Vol. 110(4), 1249-1254

[29] Kawano T., Kidoaki S., "Elasticity boundary conditions required for cell mechanotaxis on microelastically-patterned gels"; *Biomaterials* **2011**, Vol. 32, 2725-2733

[30] Britland S., Morgan H., Wojiak-Stodart B., Riehle M., Curtis A., Wilkinson C. "Synergistic and hierarchical adhesive and topographic guidance of BHK cells"; *Experimental Cell Research* **1996**, Vol. 228(2), 313-325

[31] Boyden S. "The chemotactic effect of mixtures of antibody and antigen on polymorphonuclear leucocytes"; *J. Exp. Med.* **1962**, Vol. 115, 453–466

[32] Gerthoffer W.T. "Mechanisms of Vascular Smooth Muscle Cell Migration"; *Circ. Res.* **2007**, Vol. 100(5), 607-621

[33] Lynch A.E. , Triajianto J., Routledge, E. "Low-Cost Motility Tracking System (LOCOMOTIS) for time-lapse microscopy applications and cell visualisation"; *PLoS ONE* **2014**, Vol. 9(8), e103547

[34] Pushkarsky I., Lyb Y., Weaver W., Su T.W., Mudanyali O., Ozcan A., Di Carlo D. "Automated single-cell motility analysis on a chip using lensfree microscopy"; *Scientific Reports* **2014**; Vol. 4, 4717

[35] Ascione F., Caserta S., Perris R., Guido S. "Investigation of cell dynamics in vitro by time lapse microscopy and image analysis"; *Chemical Engineering Transactions* **2014**, Vol. 38, 517-522

[36] Caserta S., Campello S., Tomaiuolo G., Sabetta L., Guido. S. "A Methodology to Study Chemotaxis in 3-D Collagen Gels"; *AIChE Journal* **2013**, Vol. 59(11), 4025-4035

[37] http://www.gelifesciences.co.jp/catalog/1204.html

[38] Lämmermann T., Germain R.N., "The multiple faces of leukocyte interstitial migration"; *Seminars in Immunopathology* **2014**, Vol. 36(2), 227-251

[39] Rioult D., Lebel J.M., Le Foll F. "Cell tracking and velocimetric parameters analysis as an approach to assess activity of mussel (Mytilus edulis) hemocytes in vitro"; *Cytotechnology* **2013**, Vol. 65, 749–758

[40] Weber M., Hauschild R., Schwarz J., Moussion C., de Vries I., Legler D.F., Luther S.A., Bollenbach T., Sixt M. "Interstitial Dendritic Cell Guidance by Haptotactic Chemokine Gradients"; *Science* **2013**, Vol. 339, 328-332

[41] Concha M.L., Adams R.J. "Oriented cell divisions and cellular morphogenesis in the zebrafish gastrula and neurula: a time-lapse analysis"; *Development* **1998**, Vol. 125, 983-994

[42] Nishio M., Watanabe K., Sasaki J., Taya C., Takasuga S., Iizuka R., Balla I., Yamazaki M., Watanabe H., Itoh R., Kuroda S., Horie Y., Forster I., Mak T.W., Yonekawa H., Penninger J.M., Kanaho Y., Suzuki A., Sasaki T. "Control of cell polarity and motility by the PtdIns(3,4,5)P3 phosphatase SHIP1"; *Nature Cell Biology* **2007**, Vol. 9(1), 36-44

[43] Nitta H., Wada Y., Kawano Y., Murakami Y., Irie A., Taniguchi K., Kikuchi K., Yamada G., Suzuki K., Honda J., Wilson-Morifuji M, Araki N., Eto M., Baba H., Imamura T. "Enhancement of Human Cancer Cell Motility and Invasiveness by Anaphylatoxin C5a via Aberrantly Expressed C5a Receptor (CD88)"; *Clin. Cancer Res.* **2013**, Vol. 19, 2004-2013

[44] Kamakura S., Nomura M., Hayase J., Iwakiri Y., Nishikimi A., Takayanagi R., Fukui Y., Sumimoto H. "The Cell Polarity Protein mInsc Regulates Neutrophil Chemotaxis via a Noncanonical G Protein Signaling Pathway"; *Developmental Cell* **2013**, Vol. 26, 292–302

[45] Wang Y, Teng H.L, Huang Z. “Intrinsic Migratory Properties of Cultured Schwann Cells Based on Single-Cell Migration Assay” *PLoS ONE* **2012**, Vol. 7(12), e51824

[46] Dickinson R.B., Tranquillo R.T. "Optimal Estimation of Cell Movement Indices from the Statistical Analysis of Cell Tracking Data"; *AIChE Journal* **1993**, Vol. 39(12), 1995-2010

[47] Gorelashvili M., Emmert M., Hodeck K.F., Heinrich D. "Amoeboid migration mode adaption in quasi-3D spatial density gradients of varying lattice geometry"; *New J. Phys.* **2014**, Vol. 16, 075012

[48] Ascione F., Caserta S., Perris R., Guido S. “Investigation of cell dynamics in vitro by time lapse microscopy and image analysis”; *Chemical Engineering Transactions* **2014**, Vol. 38, 517-522

[49] Griffith L.G., Naughton G. "Tissue engineering - current challenges and expanding opportunities"; *Science* **2002**, Vol. 295, 1009-1016

[50] Taylor W.R., Greenberg A.H., Turley E.A., Wright J.A. "Cell motility, invasion and malignancy induced by overexpression of K-FGF ro bFGF"; *Experimental Cell Research* **1993**, Vol 204, 295-301

[51] Szebenyi G., Fallon J.F. "Fibroblast growth factors as multifunctional signaling factors"; *International Review of Cytology* **1998**, Vol. 185, 45-106

[52] Seras-Franzoso J., Peebo K., García-Fruitós E., Vázquez E., Rinas U., Villaverde A. "Improving protein delivery of fibroblast growth factor-2 from bacterial inclusion bodies used as cell culture substrates"; *Acta Biomaterialia* **2014**, Vol. 10, 1354–1359

[53] Seras-Franzoso J., Peebo K.,Corchero J.L., Tsimbouri P.M., Unzueta U., Rinas U., Dalby M.J., Vazquez E., García-Fruitós E., Villaverde A. "A nanostructured bacterial bioscaffold for the sustained bottom-up delivery of protein drugs"; *Nanomedicine* **2013**, Vol. 8(10), 1587-1599

General conclusions

In this work we have characterized two promising supramolecular systems in the light of their prospective application in medical applications and tissue engineering.

In the first part of the thesis (Chapter 1) we have compared the mechanical properties of vesicular systems formed by two different amphiphilic systems (anionic surfactant and phospholipids) and prepared using three different preparation routes. We have concluded that regarding their mechanical properties, the prepared vesicles using different routes of preparation are much alike. On the other hand, we have found that from the structural standpoint, depending on the amphiphilic unit used the rigidity properties are different. This fact is indicative that their internal architecture, once achieved, is the one determining the mechanical properties of such supramolecular entities.

The second part of the research work (Chapters 2, 3 and 4), has been centered on the use of IBs for cell guidance. Cell positioning, orientation and morphology have been studied using different geometries of IB's patterns deposited by a modified μCP protocol (Chapter 2). In the next chapter (Chapter 3) we have developed a deposition method based on the coffee-drop effect that enables the deposition of surface-bound IBs gradients. Finally, using this technique we have prepared a substrate with an array of different gradients of biologically active protein nanoparticles and examined cell motility behavior on them (Chapter 4). In all of the aforementioned studies we have confirmed, that IBs can be successfully used for pattern formation and substrate decoration. Moreover, we can conclude that their presence, geometrical distribution, concentration and biological activity have a vast impact on different aspects of model cell´s behavior.

Apart from achieving all the proposed goals, an added value of this work lays in the development of numerous protocols, methodologies of data treatment and visualization. Especially, the evaporation assisted colloidal gradient deposition technique has a clear prospective use in other applications concerning surface decoration with colloidal nanoparticles. Moreover, the original protocol described for the construction of "preference cell distribution" heat maps might be successfully applied in other contexts.

As a general conclusion of this work we can state that with this thesis different aspects of the proposed systems have been explored in order to get one step closer to their potential opportunities in medical applications and tissue engineering.

A. Appendices

A.1. Vesicle preparation

A.1.1. Materials

5-Cholesten-3β-ol (Chol, purity 95%) was obtained from Panreac (Barcelona, Spain). Cetyltrimethylammonium bromide (CTAB, ultra pure for molecular biology) was purchased from Fluka-Aldrich. DOPC was supplied by Avanti Polar Lipids (Alabaster, AL, USA). Ethanol (ROMIL SpS^{TM}, purity > 99.8%) was obtained from Teknokroma (Sant Cugat del Vallès, Spain) and carbon dioxide (purity 99.9%) was supplied by Carburos Metálicos S.A. (Barcelona, Spain). All chemicals were used without any further purification. PBS buffer (pH=7.4) was prepared using 0.096M NaCl, 0.0031M Na_2HPO_4 and 0.0009M NaH_2PO_4 (all purchased from Sigma-Aldrich). All the water used was pretreated with the Milli-Q Advantage A10 water purification system (Millipore Ibérica, Madrid, Spain).

Care was taken to prepare all samples at the same liquid composition and surfactant concentration. As an result, we have been using 10.8% v/v EtOH solution in water as dispersing media, as presence of this quantity of ethanol is necessary in DELOS-susp procedure. Final concentration of surfactants depended on their maximal solubility in ethanol during DELOS-susp and was 5.4 mg/ml and 2.1mg/ml for CTAB-Chol and DOPC-Chol vesicles, respectively. Lower concentration of surfactents in DOPC-Chol vesicles is due to the fact, that both used surfactants (DOPC and cholesterol) have to be solubilised in an organic fraction.

A.1.2. Preparation of quatsomes by Tip Sonication (US)

Desired amounts of cholesterol and CTAB were weighted in glass bottles and suspended in 10ml of PBS containing 10.8% of ethanol to obtain the same PBS/ethanol proportion in all preparation routes. The resulting dispersion was sonicated at 298K, using a Vibracell Sonifier titanium probe working at 20kHz (Sonic and Materials Corporation) for 4 minutes until homogeneous dispersions were achieved. Before analysis, all mixtures were left to stabilize at 298K for 1 week.

A.1.3. Preparation of quatsomes by Thin Film Hydration (TFH)

Aliquots of cholesterol and CTAB dissolved in chloroform were mixed in a 2ml glass vial for a total lipid mass of 5.4mg and the desired molar ratio of the membrane constituents. The

solvent was slowly evaporated under a gentle N_2 flow for 15 minutes to create a thin lipid film. To ensure that all the solvent was removed, the glass vial was placed in vacuum for at least 4 hours. The lipid film was then hydrated over night at room temperature using 1ml of PBS containing 10.8% of ethanol. Next, the sample was taken through 10 rounds of freeze/thawing by transferring it between liquid nitrogen and a water bath (at 313K). Finally, the vesicles were extruded 21 times through a polycarbonate filter with a pore size of 50nm using a hand-operated Mini-Extruder (Avanti Polar lipids, Alabaster, AL, USA).

A.1.4. Preparation of quatsomes and liposomes by DELOS-susp.

Vesicle preparation was performed according to Reference [1]. In short, an ethanol solution containing all vesicular membrane components (but CTAB in the case of quatsomes) is loaded into a high-pressure vessel at atmospheric pressure and at a working temperature of 308K. After 20 minutes of thermal equilibration the autoclave was pressurized with compressed CO_2 to reach level of 10MPa producing a volumetric expanded liquid ethanol solution with a desired molar fraction of the compressed fluid. The system is left at 10MPa and 308K for 60 minutes to achieve a complete homogenization. In order to form vesicles, the CO_2-expanded solution is depressurized from working to atmospheric pressure through a non-return valve over an aqueous solution (containing CTAB in the case of quatsomes). A flow of N_2 at 10MPa was used as embolus to push down the alcoholic solution in order to maintain a constant pressure in the vessel during depressurization.

CTAB-Chol quatsomes: 76mg of cholesterol in 2.9ml of ethanol were pressurized with CO_2 at partial pressure of 0.62 and depressurized over a solution of 68mg of CTAB in 24ml of PBS.

DOPC-Chol liposomes*:* 4.28mg of cholesterol and 35.61mg of DOPC in 1.9ml of ethanol were pressurized with CO_2 at partial pressure of 0.84 and depressurized over 17ml of PBS.

A.2. Cryogenic Transmission Electron Microscopy

The morphology of the prepared vesicular systems was studied by cryo-TEM using a JEOL JEM-2011 transmission electron microscope (JEOL Ltd., Tokyo, Japan) operating at 120kV. The samples were frozen by plunge freezing in liquid ethane and stored in liquid nitrogen before being loaded onto a cryogenic sample holder (Gatan 626 CTH). The working temperature was kept below 98K. Images were recorded by a Gatan 724 CCD camera under low-dose conditions using Digital Micrograph 3.9.2. (Gatan Inc.).

A.3. Quartz Crystal Microbalance with Dissipation (QCM-D)

All QCM-D measurements were performed in the Laboratory of Biosurfaces at the Centre for Cooperative Research in Biomaterials-CIC biomaGUNE, located in San Sebastian (Spain) under the supervision of Dr Ralf Richter.

A QSense E4 device was used. Flow rate was maintained at 20µl/min at room temperature. Prior to experiment sensors were conditioned in an ozone chamber for 30 minutes and subsequently rinsed with copious amounts of EtOH, MiliQ water, again with EtOH and dried in a nitrogen stream. Between experiments each sensor's surface was recovered by the injection of 4% SDS aqueous solution, MiliQ water, EtOH, MiliQ water and again EtOH. The sensors were kept overnight in 4% SDS solution. The running buffer used to establish the base line and during the desorption was 10.8% v/v EtOH in PBS.

A.4. Surface Plasmon Resonance

Riechert SR7000DC dual channel SPR instrument (Reichert Analytical Instruments, NY, USA) was used to capture the SPR signals. The setup is based on the configuration introduced by Kretschmann and Reather [2]. On top of the sample, the standard flow cell with two reaction channels was used. Injections were conducted with a syringe pump with a flow rate of 20µl/min at 25ºC. Vesicles were run over a boron glass sensor covered with approximately 50nm of gold with 1.5nm of Ti adhesion layer (SSENS, Netherlands). The gold surface was recovered by two 5 minute-long flushes of HPLC grade EtOH. The running buffer used to establish the base line and desorption was 10.8% v/v EtOH in PBS.

A.5. Origin of values used for iterative protocol for coupling SPR and QCM-D data

The values of refractive index, density and viscosity for aqueous solution with 10.8% EtOH v/v were calculated basing on tabularised data as presented in Figure A.1.

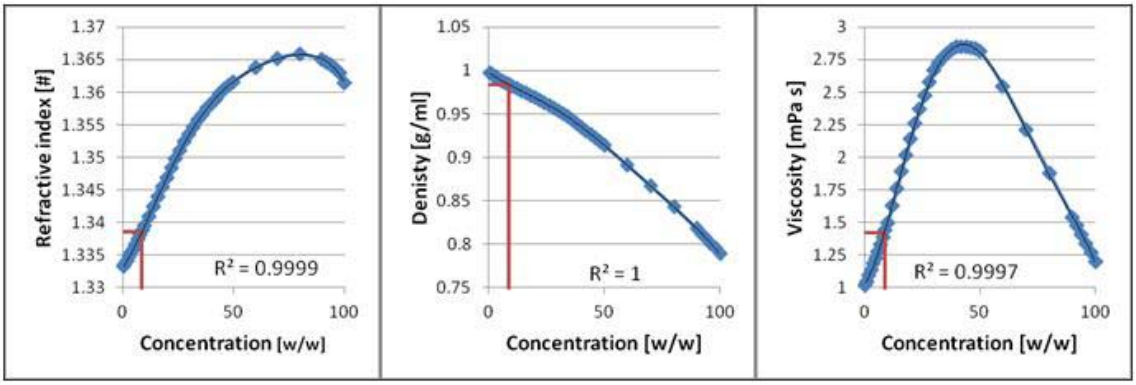

Figure A.1 Calculations of refractive index, density and viscosity of buffer based on tabularised data. Data from Reference [3] (blue diamonds) were approximated with 5th grade polynomial (thin black line). Values of each parameter were calculated for 8.72% w/w EtOh in MiliQ water (corresponding to 10.8% v/v) from fitting function (red lines) and used in further proceedings. Obtained values are: refractive index *n* 1.3386, density ρ_S 0.983.kg/ml, viscosity η_S 1.4192 mPa·s. We assume that these values are equal in our case of 10.8% v/v EtOH in PBS with vesicles.

In order to calculate the sensitivity factor κ of the SPR instrument we have measured it´s response to various concentrations of EtOH in water. In Figure A.2 the experimental SPR signal is presented (A) with the corresponding calibration line (B). The slope of this line is κ, and obtained value was 970250µRU.

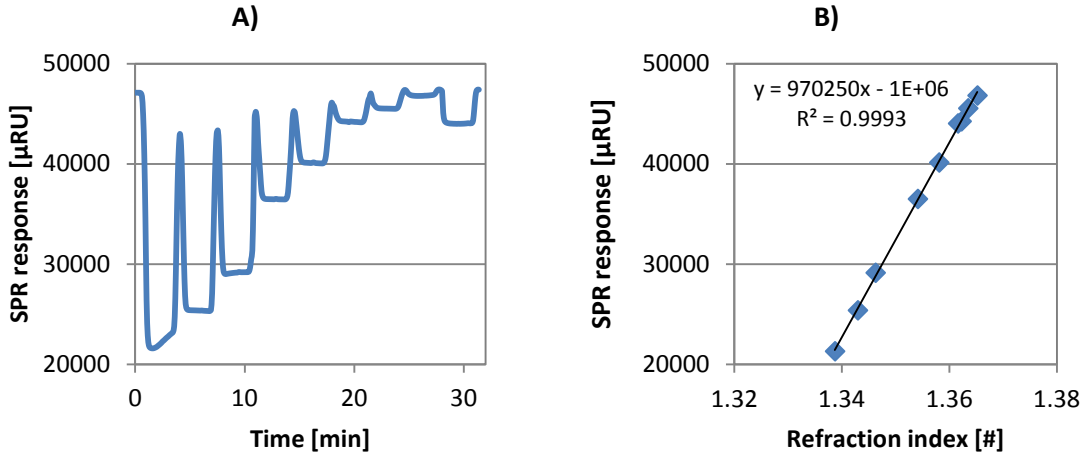

Figure A.2 Estimation of *κ*. A) sensogram of injections of EtOH:H_2O solutions of increasing EtOH concentration and known refractive index. B) Calibration curve with a linear equation.

Extraction of values of $\epsilon_{r,Au}$ based on tabularized data from literature [4] is presented in Figure A.3

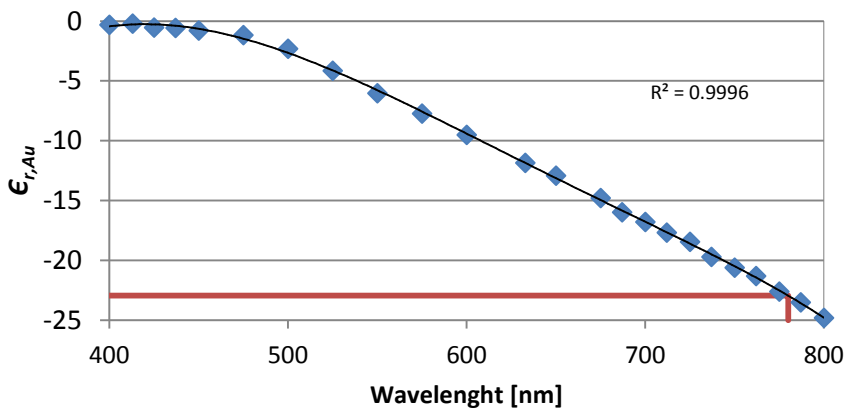

Figure A.3 Calculation of $\epsilon_{r,Au}$ basing on values reported in Reference [4] (blue diamonds). We have extrapolated this data with the 5th-order polynomial (black line) and found a value of -22.95 corresponding to a wavelength of the instrument of 780nm.

The specific refractivity of the bilayer *r* was calculated as a weighted average value of specific refractivity of the surfactants. Specific refractivity of CTAB is 0.300g/ml according to Reference [5]. To calculate these values for other compounds (Cholesterol and DOPC) we have used the following equation:

$$r_{Surf.} = \frac{MW_{Surf.}}{MR_{Surf.}}$$

Where $MW_{Surf.}$ is the surfactant´s molecular weight (386.66g/mol and 786.11g/mol for cholesterol and DOPC, respectively) and $MR_{Surf.}$ is its molar refractivity. $MR_{Surf.}$ of cholesterol is assumed to be equal to the molar refractivity of Cholesterol-3-D1: 119.97ml/mol according to Reference [6]. $MR_{Surf.}$ of DOPC was calculated to be 219.57ml/mol basing on molar refractivities of the atoms or atom groups given in Reference [7]. For these values retroactivities of bilayers *r* used for the calculations were 0.304ml/g and 0.285 ml/g for CTAB-Chol and DOPC-Chol bilayers, respectively.

Table A.1 summarizes other experimental values that were used to perform the calculations with the corresponding equations or references.

Table A.1 Calculation of CTAB-Chol and DOPC-Chol vesicle properties basing on geometrical considerations end experimental measurements.

Quantity	Symbol	Unit	Value CTAB-Chol	Value DOPC-Chol	Reference
Size of vesicle	d_V	nm	120	91	DLS
Bilayer thickness	d_B	nm	4.4	4.8	cryoTEM
Surfactant density	ρ_V	mg/ml	5.4	2.1	Experimental value
Vesicle volume	V_V	nm^3	904778	394569	$V_V = \frac{4}{3}\pi(\frac{d_V}{2})^3$
Bilayer volume per vesicle	V_B	nm^3	184811	112164	$V_B = V_V - \frac{4}{3}\pi(\frac{d_V}{2} - d_B)^3$
$N_{Avogadro}$	N_A	#/mol	$6.02 \cdot 10^{23}$		constant
Molar mass of lipids in vesicle	M_V	g/mol	$1.3 \cdot 10^8$	$1.0 \cdot 10^8$	Geometric calculations
# of vesicles	N_V	mol/ml	$4.15 \cdot 10^{-11}$	$2.05 \cdot 10^{-11}$	$N_V = \frac{\rho_V}{M_V}$
# of vesicles	N'_V	#/ml	$2.50 \cdot 10^{13}$	$1.23 \cdot 10^{13}$	$N'_V = N_V N_A$
Total bilayer volume per unit volume	V'_B	nm^3/ml	$4.62 \cdot 10^{18}$	$1.38 \cdot 10^{18}$	$V'_B = N'_V V_B$
		ml/ml	0.0046	0.0014	
		%	0.46	0.14	
Bilayer density	ρ_B	g/ml	1.17	1.48	$\rho_B = \rho_V / V'_B$
1/Bilayer density	v	ml/g	0.85	0.66	$V = 1/\rho_B$

A.6. IBs production and purification

IBs production and purification was performed by the group of Prof. Villaverde at the IBB (Institut de Biotecnologia i Biomedicina, Universidad Autónoma de Barcelona).

A.6.1. IBs production

IBs were produced in *E. coli* MC4100 strain (araD139 Δ[argF-lac] U169 rpsL150 relA1 flbB5301 deoC1 ptsF25 rbsR) and its derivative *E. coli* strain JGT20 (dnak756 thr::Tn10) [8]. These strains were transformed with the expression vector pTVP1GFP (ApR), encoding for a Green Fluorescent Protein (GFP) fused at the amino terminus to VP1, an hydrophobic capsid protein from foot-and-mouth disease virus [9], which promotes deposition as IBs [10]. IBs of FGF-2 (155 amino acid isoform, 18 kDa) were produced in *E. coli* BL21(DE3), transformed with the vector pET29c-(+)-hFGF-2 [11]. FGF-2 protein did not contain any additional pulldown protein to induce IB formation. Recombinant genes were expressed under the control of an IPTG inducible-trc promoter for VP1GFP expression and T7 RNA polymerase promoter for the FGF-2 expression. Bacterial cells were cultured in shake flasks using LB rich medium supplemented with the required antibiotics. When cultures reached an OD_{550} of 0.5 protein expression and therefore IB formation was induced by adding 1 mM IPTG at 37°C (GFP) and 25°C (FGF-2). Samples were taken 3 hours post-induction.

A.6.2. IBs Purification

Bacterial cell cultures were treated by adding, lysozyme and PMSF at 1 mg/ml and 0.4 mM respectively, and incubating them for 2 hours at 37°C. Lysozyme treatment attacked bacterial cell wall facilitating subsequent cell disruption by mechanical procedures. Samples were frozen at -80°C to release the IBs and washed in Triton X-100 1% (v/v) for 1 hour at room temperature (RT). After that, samples were frozen again at -80°C. An additional washing step was carried out by adding Nonidet P-40 detergent 0.03% (v/v) and incubating IBs 1 hour at 4°C. Mild detergents washings were used for removing cell membranes from the IB. Next, samples were treated with DNAse 1 µg/ml in presence of $MgSO_4$ 1mM during 1 hour at 37°C in order to get rid of contaminant DNA. Finally the absence of alive bacteria in the IB preparations was tested by plating 100 µL of sample on LB plates incubated overnight at 37°C. Samples were frozen/thawed until no viable bacteria were observed. Finally, IBs samples were centrifuged for 15 minutes at 15000 g and pellets were stored at -80°C till further use. Purified IBs were quantified by western blot using Quantity One software (Bio-Rad) to analyze band intensity and infer protein concentration from a GFP standard curve or BSA standard curve in the case of FGF-2 IBs.

Note that due to the looser structure of FGF-2 IBs the purification process was slightly modified with respect to the one employed for VP1GFP IBs. 500 ml cell cultures containing FGF-2 IBs were centrifuged and resupended in 30 ml PBS and frozen at -80 °C. Lysozyme and PMSF at 0.5 mg/ml and 0.4 mM respectively, were added and incubated for 2 hours at 37°C. Next, 3 rounds of French Press at 1300 PSI were performed and samples were frozen once more. The rest of the purification protocol was performed as described above but reducing Triton-X 100 concentration to 0.04 % (v/v) and removing NP-40 detergent washing step.

A.7. Microcontact printing of IBs

A.7.1. PBS preparation

Store solution of concentrated PBS was obtained by dissolving NaCl (5.494g), Na_2HPO_4 (0.44g) and NaH_2PO (0.108g) in MiliQ water (1000ml). Sodium hydroxide was used to reach 7.4 pH. Solution was diluted with MiliQ water 10 times before use.

A.7.2. Inclusion Bodies suspension preparation

IBs stored as received at -20°C in 1.5ml eppendorfs were brought to room temperature and resuspended in 1ml of PBS and then diluted to the desired concentration (for high

concentrations IBs from various eppendorfs were joined) to obtain approximately 10ml of suspension. This quantity was enough to cover the PDMS stamps during the soaking step. The suspension was sonicated for 10 minutes immediately before PDMS stamp soaking.

A.7.3. Stamp preparation

PDMS stamps were fabricated by casting a 10:1 (w/w) mixture of PDMS and curing agent (Sylgard 184, Dow Corning) against a photolithographically patterned silicon master. Next, uncured PDMS was degassed by repeated lowering and rising pressure in a desiccator, cured for 18 hours at 60°C, and finally peeled from the master. In order to overcome problems with IBs transfer from solution to the substrate we have used a procedure previously described in Reference [12]. Thus, before soaking stamps in the IB's suspension, they were sonicated for 5 minutes in acetone, exposed to vacuum for 10 minutes, sonicated in a sodium dodecyl sulfate (SDS) (Sigma) solution (10% w/w in MiliQ water) for 5 minutes, conditioned in the same media for 5 minutes, dried with a N_2 flow, dipped in MiliQ water to remove the excess of SDS and dried again with a N_2 stream.

A.7.4. Substrates preparation

Silicon <100> wafers (SiMat, Germany) covered with native SiO_2 where hand-cut into small pieces of approximately $1cm^2$. Substrates were placed in piranha solution for 15 minutes (mixture of concentrated sulphuric acid, (Panreac, Spain) and 33% aqueous hydrogen peroxide (Aldrich) in ratio 7 to 3 – **handle with caution**), copiously rinsed with ultrapure water (Advantage A10 water purification system, Millipore) and HPLC grade ethanol (Tecnokroma, Spain), and dried under a stream of nitrogen. After an eye inspection in order to eliminate any visible surface imperfections or impurities substrates were introduced into a desiccator with a 0,1 mL drop of N-[3-(trimethoxysilyl)propyl]ethylenediamine (Aldrich) on a clean Petri glass. The system was left under vacuum overnight at 36°C to obtain a complete and ordered amino-terminated SAM covering the SiO_2 surface. Substrates were stored in dust-tight containers, before being used within no longer than 7 days from production.

A.7.5. Printing

After the pretreatement stamps were soaked in a suspension of IBs in PBS buffer (pH 7.5) of desired density for 20 minutes. Next, stamps were gently rinsed with MiliQ water, dried under low nitrogen flow and placed on the clean silicon substrate on the amine-terminated SAM side. A 10g weight was placed on the stamp to provide repeatability and homogenous pressure. After 1 minute of contact the stamp was carefully peeled off. Each stamp was used no more

than 4 times and within one week from production. Random IBs patterns were produced using the flat side of a stamp. When not in use stamps were stored in MiliQ water.

A.8. Cell culture and dying for microscopy analysis

Prior to the cell seeding substrates were gently rinsed with DPBS, blocked with BSA (3% w/w in PBS), rinsed again with DPBS and introduced into the 24-wells plate (Nunclon^{TM}), one substrate per well. 1BR3.G human skin fibroblasts or NIH/3T3 fibroblasts were seeded per well and incubated in (2ml) DMEM (Dulbecco's Modified Eagle Medium) supplemented with 2 mM of L-glutamine and gentamicine (50 µg ml^{-1}). Additionaly medium was enriched with 10% or 1% of fetal bovine serum (FBS) for 1BR3.G and NIH/3T3 cells, respectively. Plates were incubated at 37°C in a 10% CO_2 humidified incubator for the desired time.

After the cultivation the substrates were rinsed with DPBS, cells were fixed with 4% of paraformaldehyde for 30 minutes with gentle agitation and rinsed again with DPBS. Then DPBS with fluorescent dyes: red CellMask (Invitrogen) for membrane and blue Hoescht (Invitrogen) for nuclei (1 µl ml^{-1} and 0.2 µl ml^{-1}, respectively) were added and the plate was incubated for 10 minutes at room temperature with gentle agitation. Finally supports were rinsed with DPBS and with MiliQ water to get rid of salt deposits of DPBS.

A.9. Optical microscopy

Substrates were observed under an Olympus BX51 microscope equipped with a CCD camera Olympus DP20. Fluorescence images were obtained with the help of Olympus U-LH100HG UV lamp and adequate filters. Magnification of 50x was used to obtain images for the statistical data treatment. Images were taken randomly from at least three different regions from different substrates. Greater magnifications (e.g. 200x) were used to depict details.

The time of exposure differed and was in a range between 0.2s for the nuclei and 8s for the membrane and GFP-derived IBs. For experiments where IB´s concentration was relevant special care was taken to always acquire images in the same exposure conditions.

A.10. Image analysis

Cells localization orientation and morphology data was extracted from images using ImageJ freeware software. Data was analyzed and visualized with MS Excel and Gnuplot software. The minimal number of data points used to make the statistical analysis was 120 in all cases.

A.10.1. Cell localization

Care was taken to assure that images are taken from the same area and that any operation of cropping and rotating is the same. Images were numerically rotated to align stripes (or rows of dots) horizontally. Then, the "plot profile" command of ImageJ was performed over a rectangular selection to calculate the average intensity of luminescence per pixel line. The results describe the average occurrence of membrane (red luminescence), nuclei (blue luminescence) or IB´s (green luminescence) versus the distance. Profile plots were normalized so that the minimum value was 0 and the maximum 1 and subsequently juxtaposed.

We approximated the actual profile of IB´s fluorescence with the "ideal" patterning assuming value 0 between stripes and 1 for stripes (or circular distribution for dotted pattern). These values were normalized taking into account the overall surface of patterned and unpatterned stripes within the inspected area. Dotted pattern was analyzed in two directions: parallel to dot´s rows and columns (horizontal and vertical). It is important to note that in the case of dotted pattern only 19 % of the surface was printed with IBs.

A.10.2. Cell orientation

Aligned images were turned into black and white with threshold tools. Then geometrical parameters of each cell were automatically calculated with ImageJ "Analyze particles" procedure. Each region corresponding to the investigated feature (cell membrane or nuclei) was approximated to an ellipse. The angle between the long axis of the ellipse and the x axis of the image (direction of stripes or dots´ line) was calculated. Moreover, the area of each region was calculated and only areas with surface greater than 100 μm^2 were considered for further analysis.

Data from different images but corresponding to the same growth conditions was pooled. The frequencies of angle orientation were separated into 10° wide bins from 0° to 180° and represented as radial plots. Values between 180° to 360° are a symmetric repetition of data added for convenience.

A.10.3. Cell morphology

Each cell was approximated to an ellipse and the elongation was calculated as a ratio between the long axis to the short one minus 1. Average values and standard errors were calculated for each condition. For morphology-orientation plots (e.g. Figure 2.22) values between 180° and 360° are a symmetric repetition of data from 0° to 180° and they are presented for clarity.

A.11. Confocal microscopy

In order to obtain confocal images samples were mounted on 35mm dishes (IBIDI, Germany) with Fluoprep (Bio-Merieux, France). A spectral confocal microscope Leica TCS SP5 AOBS (Leica Microsystems, Mannheim, Germany) with a Plan-Apochromat 63x1.4 NA lens was applied. Nuclei, membrane and IB´s were excited with 405nm diode laser beam, 633nm helium neon laser beam and 488 nm argon laser beam respectively and detected at 414–461nm, 656–789nm and 500–537nm, respectively.

A.12. Quality control of µCP

A.12.1. Pattern validation:

The methodology used to study the cell´s positioning described in Section A.10.1 ("Cell localization") can be also used to perform a pattern validation.

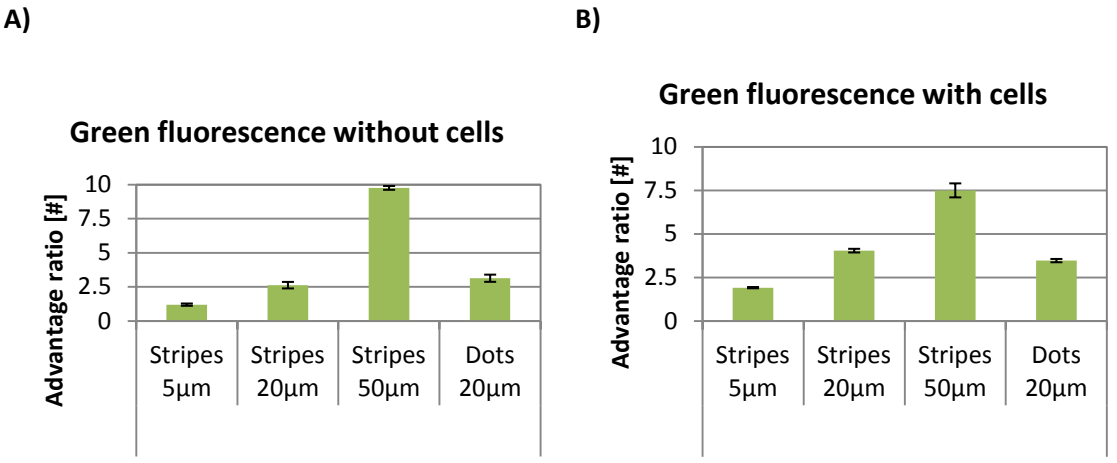

Figure A.4 Pattern validation: advantage ratio of the green fluorescence after 24 hours of cultivation. A) Only IBs and B) IBs with cells. Analysis reveals that despite all advantage ratios are bigger than 1, the different patterned substrates differ substantially in terms of IB´s content which may be explained by their geometrical differences.

We have calculated advantage ratio of the green fluorescence with and without. Obtained values show, that there is at least two-fold more green fluorescence inside than outside of the ideal pattern (see Figure A.4.A). Moreover, the very high values obtained for wider patterns, suggest, that they are much better defined than the smaller ones. This could be explained by the fact that bigger patterns facilitate IB adhesion to the stamp and better transferring to the silica support.

A.12.2. Analysis of cells´ internal green fluorescence

As a quality check we have also considered the cells´ internal green fluorescence, which could influence our findings. We analyzed control samples that underwent the same treatment but without the presence of IB's. Example images are presented in Figure A.5.

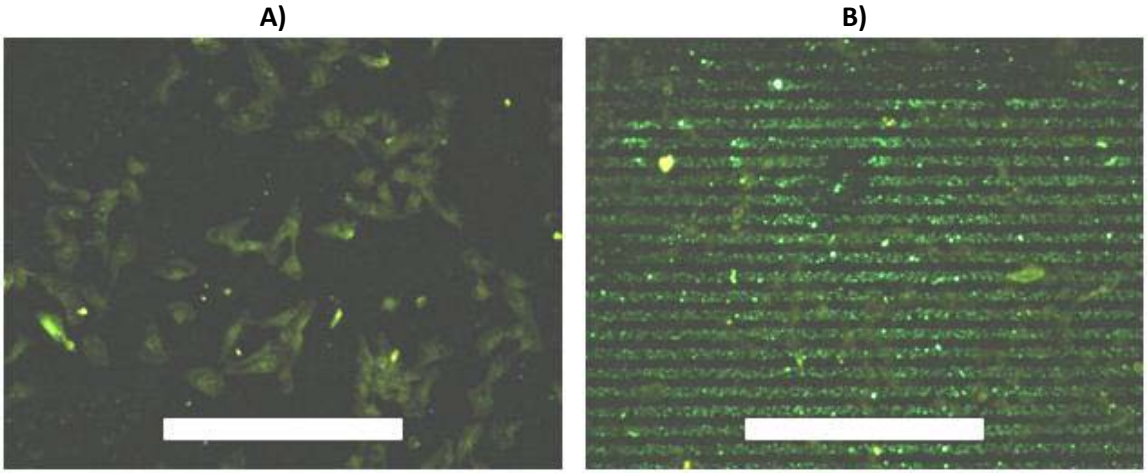

Figure A.5 Comparison of internal cell´s fluorescence and fluorescence of GFP-derived IBs. A) Green fluorescence image of cells cultivated without IBs. Green fluorescence is detected due to artefacts of the microscopy, cells internal fluorescence and noise. B) An example of green fluorescence image of surfaces with cells and patterned IB´s where the cell´s fluorescence is only visible as blurred stains. Scale bars indicates 500µm.

Although the fluorescence coming from cells is relatively intensive comparing to the background fluorescence (cells could be distinguished), the actual absolute intensity is much lower when compared with IB´s as presented in Figure A.6. We can conclude, that cell's fluorescence does not influence qualitatively our findings.

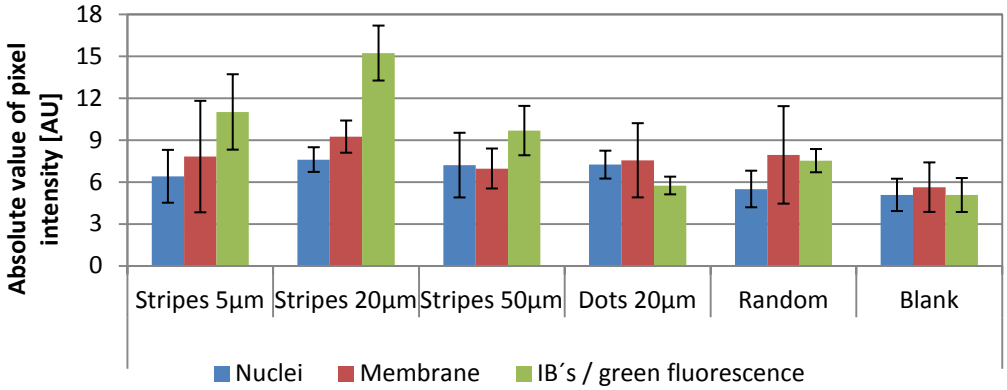

Figure A.6 Comparison of absolute values of green fluorescence intensities. Cells´ internal green fluorescence (values for Blank samples) has low absolute values and therefore is of minor significance in comparison with IBs fluorescence (rest of samples). It is worth noting, that for stripped patterns IBs cover roughly 50% of the surface, whereas for the dots this value is around 19%. In the case of random control, 100% of the surface is covered with IBs.

A.13. Evaporation-related phenomena

A.13.1. Disambiguation

Systematic experiments on the coffee-drop effect revealed that various deposit types can emerge during the evaporation, such as: rings, discontinuities, fingering instabilities, size segregation zones, etc [13]. As mentioned in Reference [14] during evaporation of a colloidal suspension over a surface three singularities can occur at the three-phase line (referred in literature also as contact line, pinning line): divergence of viscous stresses, divergence of evaporation and divergence of colloid concentration. This complex system is governed by many different variables and depending on their configuration, various phenomena can occur.

One has to keep in mind that, usually a scientific publication often describes only one specific combination of factors and the focus of a scientific publication is only on one of the aspects. Such a complex system makes cumbersome to investigate all the possible phenomena. Pinpointing these phenomena, explaining their mechanism and defining a range of variables that have predominant influence is one of the main goals of many authors. Table A.2 summarizes our efforts to gather all phenomena and deposition techniques that are reported and occur while the contact line is crossing the surface of a sample.

In fact, there is a multitude of similar mechanisms that can occur. Moreover, the fact that the science of the phenomena accompanying the evaporation is a quickly developing and rich field, in which many scientific groups are working simultaneously, the nomenclature developed to name all these modes and mechanisms is often misleading and confusing. This is the reason why in subject literature there can be found examples of acronyms that refer to the same or very similar phenomena:

- **Evaporation Induced Self-Assembly (EISA)** – this term refers to the process of self-assembling of 3D bulk aggregates of colloids during evaporation. Surfactants are needed to control the self-assembly, particles´ long range ordering. In this way high particle densities are obtained [15].
- **Evaporation Controlled Self-Assembly (ECSA)** – refers to the deposition of well ordered, self-assembled layers of colloids on surfaces during removing hem from the liquid (dip coating). Surfactants (e.g. CTAB) are required. Spongelike deposits can be obtained [15].
- **Evaporation Driven Self-Assembly (EDSA)**– similar to ECSA but without the use of surfactant and therefore resulting in unordered layers [16].
- **Controlled Evaporative Self-Assembly (CESA)** – called also CSA (Convective Self-Assembly), refers to a subset of EDSA in which well-controlled conditions (temperature, confined geometry) of colloid evaporation lead to stick-slip pinning

of the contact line during evaporation, resulting in self-assembled, regular and repetitive patterns (usually stripes). No surfactants are required [17].

Table A.2 Possible modes of colloid deposition during the movement of the contact line over a substrate.

Type of deposit	Evaporation	Colloids	Surfactants	Homogenous surface	Description	Mechanism/ driving force	Deposit	References
Langmuir--Bodgett monolayers	☒	☒	☑	☒/☑	Transfer of a mono layer of surfactant molecules self-assembled on liquid-air interface on the sample	Reduction of free energy of surfactants	Mostly monolayer of self-assembled surfactant molecules	[25,26]
Coffee stain rings	☑	☒/☑	☒	☒	Rim of deposit parallel to contact line, left by a drying drop	Fluidic flow caused by evaporation	Gradient parallel to the contact line.	[24,27]
Self-assembled periodic rings	☑	☑	☒	☒	Regular and periodic lines following a contact-line occurring during evaporation.	Periodical pinning of the rim of the evaporating liquid (CESA)	Regular pattern of lines parallel to the contact line	[13-37]
Fingering instabilities	☑	☑	☒	☑	Regular stains perpendicular to the contact line movement.	Convection and Marangoni effect leading to local contact line pinning.	Regular pattern of lines perpendicular to the contact line.	[17,21,22, 23]
Monoloayers at interfaces	☑	☑	☑	☑	High ordered layers of a nanoparticles.	Capillarity and reduction of free energy of surfactants.	Mono layer of self-assembled nanoparticles.	[19,20]
Central pillar	☑	☑	☒	☒	Formation of a single pilar in the center of drying drop.	The exact mechanism is unknown	Single pillar-like deposit in the centre of a drying drop.	[18]

A.13.2. Controlled Evaporative Self Assembly (CESA)

An interesting phenomena, denominated Controlled Evaporative Self Assembly (CESA) [27,28], results in ring-shaped regular patterns on horizontally placed substrates [29] or stripe patterns on vertical surfaces immersed in a colloidal suspension [30]. This self-assembly is due to (i) the periodic pinning of the contact line and (ii) accumulation of material at the contact line while it is stationary. In well-controlled conditions this method can lead to regular periodic pinning of the contact line and this stick-slip motion results in a regular pattern formation in a bottom-up manner (see Figure A.7). Several scientific groups have reported the production of well-defined patterns of various materials by successfully controlling the stick-and-slip motion in confined geometries [31]. However, there are numerous variables that play a role in this process and need to be controlled in order to obtain repeatable results:

Intrinsic variables:

- Solute concentration
- Solvent
- Composition of solute
- Weight of dispersed particles

Extrinsic variables:

- Surface chemistry
- Topography/roughness
- Particle geometry
- Temperature
- External fields (magnetic, electric, mechanical shear, etc.)

Moreover, the stochastic nature of the contact line pinning due to the inherent instability of the meniscus leads to difficulties in predicting the periodicity of the patterned structures [32].

Apart form experimental work, CESA has been mathematically modelled in an analytical [33] as well as a numerical [34] manner, giving promising results.

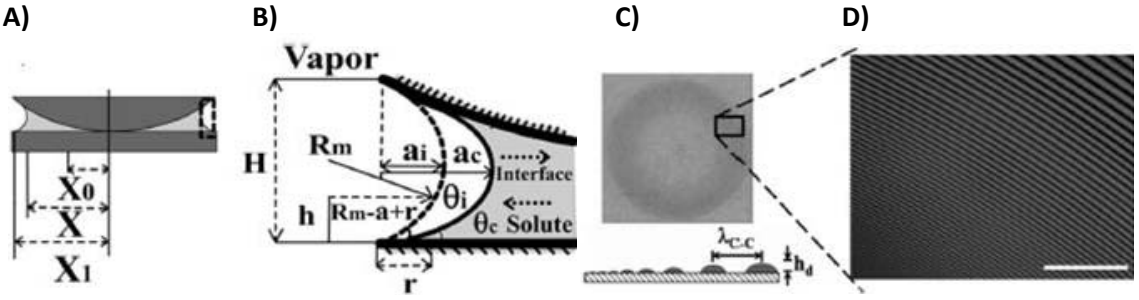

Figure A.7 Scheme and examples of CESA. A) Schematic cross-section of a capillary-held solution containing a solute placed in a "cylinder-on-flat" geometry. X_1, X, and X_0 are the radii of outermost, intermediate, and innermost rings from the sphere/flat contact centre, respectively. B) Close-up of the capillary edge is marked in the panel (A). C) Digital image of entire zone of concentric rings formed by the deposition of NPs in the geometry shown in (A). D) A small zone of the fluorescent image of NPs rings is shown. Scale bar indicates 200μm. Image reproduced from Reference [31].

Basing on CESA phenomena, a surface patterning device has been reported in which a wetted slide moves horizontally over the substrate, giving a homogenous and controllable speed over the substrate. Model and fluorescent particles have been deposited giving lines and a grid pattern at room temperature [35]. A similar method, denominated “flow coating”, has been used to produce nanowires from metallic quantum dots (QDs) [36] (see Figure A.8). Surfaces patterned in this way were reported to be used as templates [27,37].

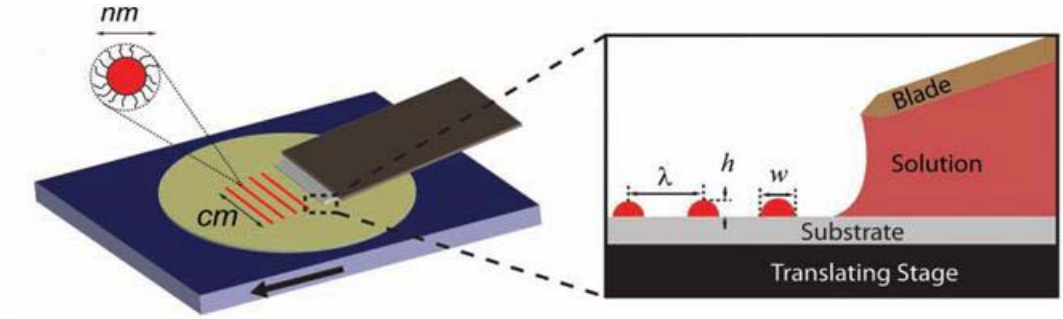

Figure A.8 Schematic diagram of the flow-coating apparatus for generating stripe patterns of metallic QDs on a silicon wafer. Image adapted from Reference [36].

Another interesting side effect of CESA is size chromatography – the segregation between colloidal particles, due to their size. Due to geometry of a pinned droplet´s contact line, smaller particles are located closer to the, rim than the bigger ones. This was observed as a clear separation of colloids, with two and three different populations of particles [38,39].

A.14. IBs suspension preparation for evaporation driven deposition

A.14.1. Preparation protocol

In order properly perform evaporation assisted pattern deposition homogenous and monodisperse suspensions are required. Thus, a preparation protocol was established in order to eliminate big agglomerates that could result low reproducibility and artefacts of the deposition methodology and provide repeatability between colloidal suspensions prepared with different IBs batches.

IB´s aliquots were resuspended in 4ml of MiliQ water. Different aliquots were joined in case higher concentration was required. The suspensnion was sonicated for 10 minutes and left for 48 hours at 4^0C to settle. After that time, the supernatant (ca. 3ml) was harvested from above the sediment and used as storage suspension. The working suspension was obtained from storage suspension by diluting it in MiliQ water to obtain the desired particle density and

confirming it by Nanoparticle Tracking Analysis (NTA). In case of mixed IBs (FGF and GFP) adequate amounts of each suspension were joined and diluted to obtain a desired particle concentration. Prior to the first usage the working solution was sonicated and purged for 10 minutes with argon for degasification. The working solutions of IB´s were routinely examined with Dynamic Light Scattering (DLS) and Nanoparticle Tracking Analysis in order to quantify their particle sizes and concentration.

A.14.2. Dynamic Light Scattering (DLS)

Dynamic light scattering is a technique that is used to determine the size distribution profile of small particles in suspension.

Its working principle is based on light scattering in all directions (Rayleigh scattering). If the light source is monochromatic and coherent, the scattering intensity fluctuates over time due to the fact that the small particles in solutions are undergoing Brownian motion. As the distance between the particles in the solution is constantly changing with time, the light undergoes either constructive or destructive interference by the surrounding particles. Information about the time scale of movement of the particles is contained in these intensity fluctuations. With this data, size distribution of particles can be calculated.

For determination of particle size distribution of different samples we have used a Zetasizer Nanoseries Nano-ZS (Malvern Instruments, U.K.). The samples (1.0ml) were measured directly without dilution at 298K. Three different experiments were performed in order to check the reproducibility of the results. Results are calculated based on the intensity of scattered light.

A.14.3. Nanoparticle Tracking Analysis (NTA)

This technique is based on a conventional optical microscope fitted with a scientific camera and a viewing unit. The particles in the sample are illuminated with a laser light source and the scattered light is captured by the camera and displayed on the connected personal computer running a Nanoparticle Tracking Analysis software. In this way the particles can be automatically tracked and sized. Results are displayed as a size distribution graph and can be exported in various formats including spreadsheets or video files.

Concretely, we have used LM20 unit (Nanosight, acquired by Malvern Instruments in 2013). In order to quantify the IBs concentration, 1.0ml of aqueous suspenions were prepared by diluting the working suspensions 1 to 1000. Samples were introduced into the flow chamber and the standard procedure was performed at 298K.

A.15. Atomic Force Microscopy

Atomic force microscopy (AFM) is a high resolution scanning probe microscopy technique that relies on the measurement of ultra-small forces (less than 1nN) present between a tip and a sample surface.

In AFM a sharp tip at the end of a flexible cantilever is brought in contact with, or near, the surface to be imaged. Information gathered by AFM is limited to a very reduced area of the sample (maximum scanned area is approximately 150 x 150µm), and only "flat" samples (no more than 20µm of roughness) can be analyzed.

The accurate control of the tip or sample positioning is carried out by several piezoelectric elements that facilitate the very precise scanning, while the relative displacement between the cantilever surface and the reference surface is determined by a laser reflected on the top of the cantilever whose movement is recorded on a position sensitive detector (PSD).

AFM can be operated using two different manners: contact and non-contact mode:

- Contact mode, in which the tip is dragged over the surface while keeping a constant contact with it, following the topography of the substrate. Moreover, information about the friction (lateral force) between the tip and the sample can also be obtained. However, this fact also turns to be one of the main disadvantage of this AFM mode as the friction of the tip might also damage the surface of soft samples if not precisely controlled.
- Non-contact mode, in which the cantilever is oscillated by a vibrating piezocrystal and changes on the amplitude of the oscillating movement are recorded while the surface is scanned. This mode is much less damaging than the previous one as the tip does not contact directly the sample surface, however no information about the friction forces of the substrate can be obtained.

Specifically, we have used 5500LS SPM AFM unit from Agilent Technologies. Samples have been imaged using non-contact mode using SSS-NCH tips (Nanosensors). The general characteristics of the tip are presented in Table A.3.

Table A.3 General characteristics of SuperSharpSilicon - Non-Contact/Tapping Mode - High Resonance Frequency tips (SSS-NCH, Nanosensors)

Property	Nominal value	Specified range
Radius curvature [nm]	2	< 5
Thickness [µm]	4	3.0-5.0
Mean width [µm]	30	30-45
Length [µm]	125	115-135
Force constant [N/m]	42	10-130
Resonance frequency [Hz]	330	204-497

A.16. A general pump protocol for simple patterns deposition

Here we will describe in the detail the general pump protocol used to deposit simple stripes from IBs suspensions using developed evaporation driven self-assembly methodology. The scheme protocol is explained in Section 3.3.3 (“Input and output parameters for a simple pattern deposition”) and presented in Figure 3.16.

Before deposition, EtOH and MiliQ water is run through tubing in order to ensure sterile conditions of deposition. Then an inlet tube is inserted into the cuvette with IB´s suspension and the outlet tube is inserted inside the cuvette close to the bottom. The system was left running before the deposition is performed to reach the desired temperature. We used a Watson Marlow pump (Figure 3.15) governed by an external PC unit with a FIALab software (FIALab Instruments). The deposition protocol usually consisted of three phases:

A) **Introduction of suspension.** In the first stage, the desired amount of suspenionn is introduced into the cuvette to cover the deposition area of sample. It is left to equilibrate for at least 5 minutes. A small amount of liquid is then pumped out to establish a new contact line, independent from the deposit formed during equilibration.
B) **Actual deposition protocol.** Consists of repetitive enabling/disabling of flow in order to govern the pattern geometry (stripes width, separation, material concentration)
C) **Excess liquid removal.** The remaining fluid, if any, is recollected and kept for reuse.

An example protocol is presented in Table A.4 . The deposited patterns obtained by this methodology are presented in Figure 3.18 and Figure 3.21.

The material is being deposited during the evaporation at the contact line. By governing the speed of the contact line travelling across the sample, control over the concentration of the deposited material, is achieved. The final speed of contact line is determined by:

- Cuvette geometry that defines liquid meniscus surface that can be varied, e.g. using V-shaped seal
- Evaporation speed which depend on the solvent type, particle concentration, temperature, surface tension, pressure, etc.
- Pump flow speed

However, the influence of the pump is predominant on the contact line speed. It can be expressed in units of speed (mm/min) of contact line movement, flow rate (ml/min) of liquid removed from cuvette or as an argument used in the pump protocol which is a number between 1 and 100 that determines the % of maximal pump efficacy, see Table A.4 . These

three representations are linearly dependent and can be used interchangeably (see calibration curves in Figure 3.17 and in Figure 3.19 B and C).

Table A.4 An example protocol for deposition simple stripe patterns using evaporation driven self-assembly methodology. This protocol will result in a deposition of 20 series, each with 4 stripes. Each stripe is deposited with disabled pump (flow 0 mm/min) and deposition times ranging from 60s to 10s.

Global Logon Peristaltic Pump1 CounterClockwise(%) 50 Delay (sec) 190 Peristaltic Pump1 Off Delay (sec) 450 Peristaltic Pump1 Clockwise(%) 50 Delay (sec) 1	A) Introduction of suspension
Loop Start (#) 20 Peristaltic Pump1 Clockwise(%) 20 Delay (sec) 1 Peristaltic Pump1 Off Delay (sec) 60 Peristaltic Pump1 Clockwise(%) 20 Delay (sec) 1 Peristaltic Pump1 Off Delay (sec) 40 Peristaltic Pump1 Clockwise(%) 20 Delay (sec) 1 Peristaltic Pump1 Off Delay (sec) 20 Peristaltic Pump1 Clockwise(%) 20 Delay (sec) 1 Peristaltic Pump1 Off Delay (sec) 10 Loop End	B) Deposition protocol (repeated in this case 20 times)
Peristaltic Pump1 Clockwise(%) 50 Delay (sec) 190	C) Excess liquid removal

A.17. Pump protocols for gradient development

In Table A.5, Table A.6 and Table A.7 are presented the actual protocols used to generate gradient patterns in genetic algorithms. Each profile consists of various lines, that are defined by time of deposition (in seconds) and speed of deposition (in mm/min). Order of these protocols corresponds to the fluorescence images and profiles from Figure 3.29 and Figure 3.30. In black are marked protocols that were used to initiate whole generation. In red are marked protocols that resulted in best fluorescence profiles. Best (red) protocols from one

generation became initiator (black) protocols in next one. Last red protocol (best in all generations) was used to produce gradients for cell motility study in Chapter 4.

Table A.5 Actual protocols for the 1st Generation of profiles. Time is presented in seconds and speed in ml/min. In black is marked protocol used to generate whole series and in red protocol resulting the best fluorescence profile of IBs deposit that was used to generate the next generation.

Protocol 1		Protocol 2		Protocol 3		**Protocol 4**		Protocol 5	
Time	Speed	Time	Speed	Time	Speed	Time	Speed	Time	Speed
2	0.3210	2	0.3210	2	0.3210	2	0.3210	2	0.3210
3	0.2165	3	0.2298	3	0.2544	3	0.2406	3	0.2427
5	0.1197	4	0.1506	3	0.1929	4	0.1616	4	0.1702
14	0.0470	7	0.0878	5	0.1368	7	0.0885	6	0.1071
51	0.0127	15	0.0436	7	0.0859	19	0.0336	11	0.0572
60	0.0025	41	0.0158	16	0.0404	60	0.0077	29	0.0221
10	0.0000	10	0.0000	10	0.0000	10	0.0000	10	0.0000
Protocol 6		Protocol 7		Protocol 8		Protocol 9		**Starting Protocol**	
Time	Speed	Time	Speed	Time	Speed	Time	Speed	Time	Speed
2	0.3210	2	0.3210	2	0.3210	2	0.3210	2	0.3210
3	0.2558	4	0.1778	3	0.2142	3	0.2529	2	0.2675
3	0.1951	9	0.0703	5	0.1297	3	0.1907	3	0.2140
5	0.1391	33	0.0196	9	0.0701	5	0.1345	4	0.1605
7	0.0879	60	0.0045	20	0.0328	8	0.0840	6	0.1070
15	0.0415	60	0.0008	56	0.0114	16	0.0393	12	0.0535
10	0.0000	10	0.0000	10	0.0000	10	0.0000	10	0.0000

Table A.6 Actual protocols for the 2nd Generation of profiles. Time is presented in seconds and speed in ml/min. In black is marked protocol used to generate whole series and in red protocol resulting the best fluorescence profile of IBs deposit that was used to generate the next generation.

Protocol 1		Protocol 2		Protocol 3		Protocol 4		Profile 5	
Time	Speed	Time	Speed	Time	Speed	Time	Speed	Time	Speed
2	0.3210	2	0.3210	2	0.3210	2	0.3210	2	0.3210
3	0.2235	3	0.2177	3	0.2088	3	0.2411	3	0.2505
5	0.1411	5	0.1329	5	0.1213	4	0.1659	4	0.1793
8	0.0783	9	0.0708	11	0.0611	6	0.1017	6	0.1144
18	0.0366	20	0.0316	25	0.0257	12	0.0529	10	0.0618
52	0.0124	60	0.0102	60	0.0079	32	0.0201	26	0.0243
10	0.0000	10	0.0000	10	0.0000	10	0.0000	10	0.0000
Protocol 6		Protocol 7		**Protocol 8**		**Starting Protocol**			
Time	Speed	Time	Speed	Time	Speed	Time	Speed		
2	0.3210	2	0.3210	2	0.3210	2	0.3210		
2	0.2603	3	0.2298	3	0.1952	3	0.2406		
3	0.1942	4	0.1506	6	0.0997	4	0.1616		
5	0.1293	7	0.0878	16	0.0408	7	0.0885		
9	0.0729	15	0.0436	49	0.0130	19	0.0336		
22	0.0298	41	0.0158	60	0.0030	60	0.0077		
10	0.0000	10	0.0000	10	0.0000	10	0.0000		

Table A.7 Actual protocols for the 3rd Generation of profiles. Time is presented in seconds and speed in ml/min. In black is marked protocol used to generate whole series and in red protocol resulting the best fluorescence profile of IBs deposit that was used to generate the next generation.

Starting Protocol		Protocol 1		Protocol 2		Protocol 3		Protocol 4	
Time	Speed	Time	Speed	Time	Speed	Time	Speed	Time	Speed
2	0.3210	2	0.3210	2	0.3210	2	0.3210	2	0.3210
3	0.1926	3	0.1926	4	0.1926	5	0.1926	6	0.1926
6	0.0963	6	0.0963	7	0.0963	9	0.0963	12	0.0963
16	0.0401	16	0.0401	19	0.0401	24	0.0401	32	0.0401
48	0.0107	48	0.0107	58	0.0107	72	0.0107	96	0.0107
49	0.0000	70	0.0000	84	0.0000	105	0.0000	140	0.0000
Protocol 5		Protocol 6		Protocol 7		Protocol 8		Protocol 9	
Time	Speed	Time	Speed	Time	Speed	Time	Speed	Time	Speed
2	0.3210	2	0.3210	2	0.3210	2	0.3210	2	0.3210
2	0.1926	3	0.1926	3	0.1926	4	0.1926	3	0.1926
4	0.0963	6	0.0963	7	0.0963	8	0.0963	5	0.0963
11	0.0401	18	0.0401	21	0.0401	26	0.0401	13	0.0401
34	0.0107	56	0.0107	67	0.0107	86	0.0107	36	0.0107
49	0.0000	84	0.0000	105	0.0000	140	0.0000	49	0.0000
Protocol 10		Protocol 11		Protocol 12					
Time	Speed	Time	Speed	Time	Speed				
2	0.3210	2	0.3210	2	0.3210				
3	0.1926	3	0.1926	3	0.1926				
6	0.0963	6	0.0963	6	0.0963				
16	0.0401	16	0.0401	16	0.0401				
48	0.0107	48	0.0107	48	0.0107				
84	0.0000	105	0.0000	140	0.0000				

A.18. Time-lapse confocal microscopy

In order to obtain confocal microscopy images, samples were mounted to an Attofluor cell chamber (A7816, Invitrogen). A Leica TCS SP5 AOBS spectral confocal microscope (Leica Microsystems, Mannheim, Germany) with a Plan-Apochromat 63x, 1.4 NA lens was used. IBs were excited with a 488 nm argon laser beam and detected at 500-537 nm. Images were captured every 30 minutes.

A.19. Bibliography

[1] Elizondo E., Larsen J., Hatzakis N.S., Cabrera I., Bjornhorn T., Veciana J., Stamou D., Ventosa N. “Influence of the preparation route on the supramolecular organization of lipids in a vesicular system”; *J. Am. Chem. Soc.* **2012**, Vol. 134(4), 1918−1921

[2] Kretschmann E., Reather H. “Radiative decay of nonradiative surface plasmon excited by light”; *Z.Naturf.* **1968**, Vol. 23A, 2135-2136

[3] Lide D.R., “CRC Handbook of Chemistry and Physics”, Internet Version **2005**

[4] Innes R.A., Sambles J.R. “Optical characterisation of gold using surface plasmon-polariton”, *J. Phys. F: Met. Phys.* **1987**, Vol. 17, 277-287

[5] Arnebrant T., Backstorm K., Jonsson B., Nylander T. “An Ellipsometry Study of Ionic Surfactant Adsorption on Chromium Surfaces”; *Journal of Colloid and Interface Science* **1989**, Vol. 128(2), 303-312

[6] http://www.lookchem.com/Cholesterol-3-D1/

[7] Cuypers P.A., Corsel J.W., Janssen M.P., Kop J.M.M., Hermens W.T., Hemkerg H.C. "The Adsorption of Prothrombin to Phosphatidylserine Multilayers Quantitated by Ellipsometry"; *Journal of Biological Chemistry* **1983**, Vol. 258(4), 2426-2431

[8] Thomas J.G., Baneyx F. “Roles of the Escherichia Coli Small Heat Shock Proteins Ibpa and ibpb in the rmal Stress Management: Comparison With Clpa, Clpb, and HtpG In Vivo”; *J. Bacteriol.* **1998**, Vol. 180, 5165-5172

[9] Garcia-Fruitos E., Gonzalez-Montalban N., Morell M., Vera A., Ferraz R.M., Aris A., Ventura S., Villaverde A. “Aggregation as Bacterial Inclusion Bodies Does Not Imply Inactivation of Enzymes and Fluorescent Proteins”; *Microbial Cell Factories* **2005**, Vol. 4(27)

[10] Carrio M., Gonzalez-Montalban N., Vera A., Villaverde A., Ventura S. “Amyloid-Like Properties of Bacterial Inclusion Bodies”; *J. Mol. Biol.* **2005**, Vol 347, 1025-1037

[11] Hoffmann F., van den Heuvel J., Zidek N., Rinas U. “Minimizing Inclusion Body Formation during Recombinant Protein Production in Escherichia coli at Bench and Pilot Plant Scale”; *Enzyme. Microb. Technol.* **2004**, Vol. 34, 235–241

[12] Chang J.C., Brewer G.J., Wheeler B.C. “A modified microstamping technique enhances polylysine transfer and neuronal cell patterning”; *Biomaterials* **2003**, Vol. 24, 2863-2870

[13] Deegan R.D. “Pattern formation in drying drops”; *Physical Review E* **2000**, Vol. 61, 475-485

[14] Berteloot G., Daerr A., Lequeux F., Limat L. "Dip coating with colloids and evaporation"; *Chemical Engineering and Processing: Process Intensification* **2013**, Vol. 68, 69–73

[15] Grosso D., Cagnol F., Soler-Illia G.J. de A.A., Crepaldi E.L., Amenitsch H., Brunet-Bruneau A., Bourgeois A., Sanchez C. "Fundaments of Mesostructuring through evaporation-induced self-assembly"; *Adv. Funct. Mater.* **2004**, Vol. 14, 309-322

[16] Maenosono S., Okubo T., Yamaguchi Y. "Overview of nanoparticle array formation by wet coating"; *Journal of Nanoparticle Research* **2003**, Vol. 5, 5-15

[17] Han W., Lin Z. "Learning from “Coffee Rings”: Ordered Structures Enabled by Controlled Evaporative Self-Assembly"; *Angew. Chem. Int. Ed.* **2012**, Vol. 51, 1534-1546

[18] Baldwin K.A., Fairhurst D.J. “The effects of molecular weight, evaporation rate and polymer concentration onpillar formation in drying poly(ethylene oxide) droplets”; *Colloids and Surfaces A: Physicochem. Eng. Aspects* **2014**, Vol 441, 867–871

[19] Xiong S., Dunphy D.R., Wilkinson D.C., Jiang Z., Strzalka J., Wang J., Su Y., dePablo J.J., Brinker C.J. "Revealing the Interfacial Self-Assembly Pathway of Large-Scale, Highly-Ordered, Nanoparticle/Polymer Monolayer Arrays at an Air/Water Interface"; *Nano Lett.* **2013**, Vol. 13(3), 1041–1046

[20] Bigioni T.P., Lin X.M., Nguyen T.T., Corwin E.I., Witten T.A., Jaeger H.M. "Kinetically driven self assembly of highly ordered nanoparticle monolayers"; *Nature Materials* **2006**, Vol. 5(4), 265-270

[21] Xu J., Xia J., Lin Z. "Evaporation-Induced Self-Assembly of Nanoparticles from a Sphere-on-Flat Geometry"; *Angew. Chem. Int. Ed.* **2007**, Vol. 46, 1860–1863

[22] Li B., Han W., Byun M., Zhu L., Zou Q., Lin Z. "Macroscopic Highly Aligned DNA Nanowires Created by Controlled Evaporative Self-Assembly"; *ACS Nano* **2013**, Vol. 7(5), 4326-4333

[23] Leizerson I., Lipson S.G., Lyushnin A.V. "Finger Instability in Wetting-Dewetting Phenomena"; *Langmuir* **2004**, Vol. 20, 291-294

[24] Deegan R.D. “Pattern formation in drying drops”; *Physical Review E* **2000**, Vol. 61, 475-485

[25] Chen X., Lenhert S., Hirtz M., Lu N., Fuchs H., Chi L. "Langmuir–Blodgett Patterning: A Bottom–Up Way To Build Mesostructures over Large Areas"; *Acc. Chem. Res.* **2007**, Vol. 40, 393-401

[26] Clemente-Leon M., Coronado E., Lopez-Munoz A., Repetto D., Catala L., Mallah T. "Patterning of Magnetic Bimetallic Coordination Nanoparticles of Prussian Blue Derivatives by the Langmuir−Blodgett Technique"; *Langmuir* **2012**, Vol. 28, 4525-4533

[27] Han W., Byun M., Li B., Pang X., Lin Z. "A Simple Route to Hierarchically Assembled Micelles and Inorganic Nanoparticles"; *Angew. Chem. Int. Ed.* **2012**, Vol. 51, 12588-12592

[28] Han W., Byun M., Lin Z. "Assembling and positioning latex nanoparticles viacontrolled evaporative self-assembly"; *J. Mater. Chem.* **2011**, Vol. 21, 16968–16972.

[29] Deegan R.D., Bakajin O., Dupont T.F., Huber G., Nagel S.R., Witten T.A. "Capillary flow as the cause of ring stains from dried liquid drops"; *Nature* **1997**, Vol. 389, 827–829

[30] Ghosh M., Fan F., Stebe K.J. "Spontaneous pattern formation by dip coating of colloidal suspensions on homogeneous surfaces"; *Langmuir* **2007**, Vol. 23, 2180–2183

[31] Han W., Lin Z. "Learning from <<Coffee Rings>>: Ordered Structures Enabled by Controlled Evaporative Self-Assembly"; *Angew. Chem. Int. Ed.* **2012**, Vol. 51, 1534-1546

[32] Watanabe S., Miyahara, M.T. "Particulate pattern formation and its morphology control by convective self-assembly"; *Advanced Powder Technology* **2013**, Vol. 24(6), 897-907

[33] Adachi E., Dimitrov A.S., Nagayama K. "Stripe Patterns Formed on a Glass Surface during Droplet Evaporation", *Langmuir* **1995**, Vol. 11, 1057-1060

[34] Frastia L., Archer A.J., Thiele U. "Dynamical Model for the Formation of Patterned Deposits at Receding Contact Lines"; *Phys. Rev. Lett.* **2011**, Vol. 106, 077801

[35] Prevo B.G., Velev O.D. "Controlled, Rapid Deposition of Structured Coatings from Micro- and Nanoparticle Suspensions"; *Langmuir* **2004**, Vol. 20, 2099-2107

[36] Kim H.S., Lee C.H., Sudeep P.K., Emrick T., Crosby A.J. "Nanoparticle Stripes, Grids, and Ribbons Produced by Flow Coating"; *Adv. Mater.* **2010**, Vol. 22, 4600–4604

[37] Byun. M., Han W., Li B., Xin X., Lin Z. "An Unconventional Route to Hierarchically Ordered Block Copolymers on a Gradient Patterned Surface through Controlled Evaporative Self-Assembly"; *Angew. Chem. Int. Ed.* **2013**, Vol. 52, 1122–1127

[38] Han W., Byunb M., Lin Z. “Assembling and positioning latex nanoparticles via controlled evaporative self-assembly”; *J. Mater. Chem.* **2011**, Vol. 21, 16968

[39] Wong T.S., Chen T.H., Shen X., Ho C.M. "Nanochromatography Driven by the Coffee Ring Effect" *Anal. Chem.* **2011**, Vol. 83, 1871–1873